



University of Sheffield

Doped Zeolite-Based Catalysts for Selective Glucose Isomerisation and Fructose Dehydration

A thesis submitted to The University of Sheffield for the degree of Doctor of
Philosophy in the Faculty of Science

Mohamed M. M. Kashbor

The University of Sheffield
Department of chemistry

July 2023

Declaration

I, the author, confirm that the Thesis is my own work. I am aware of the University's Guidance on the Use of Unfair Means (www.sheffield.ac.uk/ssid/unfair-means).

This work has not previously been presented for an award at this, or any other, university.

This work has been carried out at the University of Sheffield under the supervision of Dr. Marco Conte between September 2019 and July 2023.

04th July 2023

Signed.Mohamed.....

Department of Chemistry,
Dainton Building,
University of Sheffield
Brook Hill,
Sheffield, UK,
S3 7HF

Acknowledgement

In the first place, I would like to express my gratitude and appreciation to Allah, the Almighty, who has blessed me with the strength, patience, and guidance required to complete my doctoral studies.

I would like to express my sincere gratitude to my supervisor Dr Marco Conte for his support, advice, and guidance during my PhD journey. This project could not have been completed without his insight and knowledge of this research area. In addition to being enthusiastic and helpful, he was also an excellent supervisor, and I could not imagine a better one.

Appreciations are extended to the members of the Conte research group Dedi, James, Changyan, Baozhai, Rebecca, Mengyuan, Ghadeer and Bahhaj. It has been an absolute pleasure meeting you. I enjoyed all the time I spent in the UK with your company.

The project would not have been possible without the support of the technical staff in the Department of Chemistry, especially Simon Thorpe, Mahomed Okhai, Rob Hanson, Heather Grievson, Sharon Spey, and Khalid Doudin for their direct help and assistance in completing this research work.

Thanks also go to: Dr. James Railton and Dr. Craig Robertson (University of Sheffield) for XRD analysis, Mr. Dedi Sutarma (University of Sheffield) for chemisorption analysis, Dr. Adam Czajka (University of Sheffield) for TGA analysis, Dr. Naoko Sano (University of Newcastle) for XPS analysis, Mr. Ben Palmer and Ms. Abby Shipley (CBE, University of Sheffield) for textural properties analysis of materials, Dr. Diego Ganolio and Dr. Gainnotonio Cibin (Rutherford Appleton Laboratory) for EXAFS analysis, Prof. Xi Liu (Shanghai Jiao Tong University) for TEM measurements and data analysis, Dr. Luke Foster and Dr. Carmine D'Agostino (University of Manchester) for NMR diffusion studies and data analysis, and for their contribution to publications, Dr. Marco Conte (University of Sheffield) for data analysis for chemisorption, TGA, XRD, XPS and textural properties.

I am incredibly grateful to my family members for their endless love and encouragement, including my dearest parents, my beloved wife, my brother and all my sisters. Also, I would like to thank my close friends Khaled Elhmiadi and Yusef Elkeza for their inspirational words.

Last but not least, my sincere thanks are to the Libyan Ministry of Higher Education for their financial support to complete this research project.

List of publications and conferences.

Publications

1. **M. M. M. Kashbor**, D. Sutarma, J. Railton, N. Sano, P. J. Cumpson, D. Gianolio, G. Cibir, L. Forster, C. D'Agostino, X. Liu, L. Chen, V. Degirmenci and M. Conte, *Appl. Catal. A: Gen.*, 2022, **642**, 118689.
2. L. Forster, **M. M. M. Kashbor**, J. Railton, S. Chansai, C. Hardacre, M. Conte and C. D'Agostino, *J. Catal.*, 2023, **425**, 269–285.

Conferences

1. **Kashbor, M. M. M.**, and Conte, M, “Solubility of sugars: implications and limitations toward activity and selectivity of heterogeneous catalysts in the isomerisation of sugars”; Poster presented at: UK Catalysis Conference 2022, Holywell Park, Loughborough, United Kingdom, January 2022.

Abstract

Amidst depleting crude oil stocks and growing environmental concerns, eco-friendly manufacturing and sustainable energy alternatives are increasingly in demand. Biomass offers a promising and renewable energy source for the production of valuable fuels and chemicals such as 5-HMF, LA and their derivatives.

In recent decades, Sn-Beta has been extensively studied as a Lewis acid catalyst for biomass applications. Despite its high catalytic activity in glucose isomerisation (31% fructose yields in 30 minutes at 110 °C), Sn-Beta faces challenges for industrial feasibility due to a complex and time-consuming synthesis process, even at low Sn loading concentrations (< 2 wt.%). The use of fluoride anions as mineralizers in hydrothermal synthesis has environmental drawbacks and leads to the formation of micron-sized crystals, limiting intracrystalline diffusion. In this regard, this PhD project focused on a thorough investigation of active zeolite-based catalysts for glucose isomerisation and fructose dehydration. This involved the study of various metal-doped zeolite catalysts, using commercially available zeolites, particularly zeolite Y in its acidic form and doped with metals such Sn, Ga, Nb and Fe. The primary emphasis was placed on understanding the roles of various factors, such as Lewis and Brønsted acid sites, porosity, and solvent nature in these processes.

Prior to catalytic tests, the solubility of sugars was verified using an accurate HPLC method. By doing so, we aimed to identify any potential implications of this chemical property on catalytic activity and provide a reliable basis for accurate catalytic testing carried out afterwards. Our solubility measurements showed no detrimental impact on the catalytic activity obtained from glucose isomerisation and fructose dehydration under the reaction conditions studied.

Through a meticulous mass spectroscopic analysis, we detected two well-defined peaks of fragmentation pattern at $m/z = 217$ within the reaction mixture of our glucose isomerisation. These peaks directly corresponded to an anomeric mixture of methyl glucoside and fructoside, providing valuable insights into the composition of our glucose isomerisation reaction mixture.

In glucose isomerisation, the use of Sn- and Ga-doped zeolite Y, prepared via wetness impregnation protocol, in water as a solvent proved to be inactive due to strong solvent adsorption within the zeolite pores. However, these materials exhibited significant activity when methanol was used as a solvent. A remarkable glucose conversion of 90% and a high fructose selectivity of up to 55% were accomplished at 100 °C, under endogenous pressure, for 1-2 hours. Our investigation revealed a reaction pathway involving a hydride shift, facilitating the conversion of glucose into fructose and mannose and a Brønsted acid pathway, initiating the formation of methyl fructoside intermediate and its subsequent hydrolysis to fructose if water was added afterwards. While Brønsted acidity and porosity showed significant influence on the observed catalytic results, it was difficult to establish precise correlations between the catalytic performance and individual parameters. Therefore, it is imperative that various catalyst properties be explored in order to uncover and validate potential trends in their catalytic activity.

We conducted a screening of zeolite Y catalysts doped with various metals (such as Sn, Ga, Nb, and Fe) and metal oxides (such as CeO₂, Nb₂O₅, and TiO₂) for the selective dehydration of fructose in water. Our objective was to achieve enhanced production of 5-HMF, surpassing the reported literature yield values ($\leq 50\%$) under similar conditions. Among the tested catalysts, CeO₂/Y(80) and Nb₂O₅/Y(80) exhibited the highest 5-HMF yields, of approximately 40% under optimal reaction conditions

(140 °C, 2 hours, endogenous pressure, and a molar ratio of substrate to catalyst of 1:300). The lower 5-HMF yield was attributed to the formation of unwanted by-products such as levulinic acid, formic acid, and/or undesired insoluble humins.

Thesis contents

Declaration.....	i
Acknowledgement.....	ii
List of publications and conferences.	iv
Abstract.....	v
Thesis contents.....	1
CHAPTER 1: Introduction	5
1.1. Biomass as bio-renewable feedstocks for the production of platform chemicals.	5
1.2. Platform chemicals.	8
1.2.1. 5-Hydroxymethylfurfural (5-HMF).	9
1.2.2. Levulinic acid (LA).....	18
1.3. Relevance of glucose to fructose isomerisation.	21
1.4. Industrial production of fructose.....	23
1.4.1. Enzyme-catalysed reaction.	24
1.4.2. Homogeneous-catalysed reaction.	25
1.4.3. Heterogeneous-catalysed reaction.....	28
1.5. Zeolites.....	32
1.5.1. Structure of zeolites.	33
1.5.2. Porosity and shape selectivity.	36
1.5.3. Metal active species.	39
1.5.4. Acidity of zeolites.....	41
1.6. Common zeolite frameworks in glucose isomerisation.....	44
1.7. Project aims.....	53
1.8. References	55
CHAPTER 2: Experimental Methods and Techniques.....	71
2.1. Materials.....	71
2.1.1. Preparation of catalysts.....	71
2.2.2. Catalytic tests.....	72
2.2.3. Characterisation of Catalysts.....	72
2.2.4. Characterisation of reaction mixtures and standards.....	72
2.2. Synthesis of catalysts.	73
2.2.1. Wetness impregnation.....	73
2.2.2. Sol-gel.....	75
2.3. Catalytic tests for glucose to fructose isomerisation reaction.	77
2.3.1. One-pot reaction with water or methanol as a solvent.	77
2.3.2. Two-pot reaction with methanol and water as solvents.....	77

2.4 Synthesis of intermediates: alkyl pyranoside and/or alkyl furanoside.	77
2.5. Catalytic tests of fructose dehydration reaction to 5-hydroxymethylfurfural (HMF). ...	78
2.5.1. Dehydration of fructose over homogeneous catalysts.	78
2.5.2. Dehydration of fructose over heterogeneous catalysts.	78
2.6 Catalytic tests for the conversion of glucose and fructose to HMF over metal oxides.	79
2.7. Analytical techniques.	79
2.7.1. Characterisation of the reaction mixtures.	79
2.7.2. Characterization of the catalysts and structure-activity correlations.	92
2.8. References	104
3.1. Introduction.....	111
3.2. Purity and stability assessment of sugars.	113
3.2.1. Melting point measurements.	114
3.2.2. Thermogravimetric analysis (TGA).	115
3.2.3. ¹ H and ¹³ C Nuclear Magnetic Resonance Spectroscopy (NMR).	116
3.3. Development of HPLC diagram method for solubility determination.....	123
3.4. Solubility measurements of sugars in solutions.....	125
3.5. Conclusion.....	129
3.6. References	131
Chapter 4. Conversion of glucose to fructose over Sn and Ga-doped zeolite Y in methanol and water media.	135
4.1. Introduction.....	135
4.2. Catalytic activity of HY, Sn/Y and Ga/Y zeolites.	136
4.2.1. Catalytic tests in a one-step protocol using water or methanol as a solvent.	137
4.2.2. Catalytic tests in a two-step protocol by using methanol and water.	152
4.3. Control tests for solvent effect.	158
4.4. Control tests on the role of zeolite pores in glucose isomerisation.	160
4.5. Control tests for leaching and mass transfer.	163
4.7. Characterization of the catalysts and structure-activity correlations.	166
4.7.1. Acidity measurements.	166
4.7.2. X-ray photoelectron spectroscopy and inductively coupled plasma analysis. ...	169
4.7.3. High-angle annular dark-field imaging – scanning transmission electron microscopy.....	172
4.7.4. Powder X-ray diffraction.	174
4.7.5. Extended X-ray absorption fine structure and structure considerations.	176
4.8. Conclusion.....	179
4.9. References	181

Chapter 5. The role of zeolite acidity and porosity toward the catalytic activity of Sn-, Ga-, and Nb-doped zeolite Y, BEA, ZSM-5 and Al-MCM-41 in the isomerisation of glucose to fructose.	186
5.1. Introduction.....	186
5.2. Catalytic tests in a one-step protocol using water or methanol as a solvent.....	189
5.3. Catalytic tests in a two-step protocol by using methanol and water.....	193
5.4. Powder X-ray diffraction.....	197
5.5. Acidity measurements.....	201
5.5.1. Tentative acidity-activity correlations.	203
5.6. Porosity measurements.	207
5.6.1. Porosity-activity correlations.....	211
5.7. 3D acidity-porosity-activity correlations plots.	216
5.8. Conclusion.....	221
5.9. References	223
Chapter 6. Conversion of fructose to 5-hydroxymethylfurfural (5-HMF) over metals and metal oxides doped zeolite Y in water media.	226
6.1. Introduction.....	226
6.2. ¹ H-NMR characterisation of reaction mixtures.	230
6.3. Fructose dehydration to 5-HMF using hydrochloric acid as a homogenous catalyst.	235
6.4. Fructose dehydration to 5-HMF using metal-doped zeolites as heterogeneous catalyst.	239
6.4.1. Brønsted acidity measurements.	246
6.4.2. Powder X-ray diffraction.	248
6.5. Glucose and Fructose dehydration to 5-HMF using pure metal oxides as heterogeneous catalysts.	251
6.5.1. Glucose dehydration to 5-HMF.....	253
6.5.2. Fructose dehydration to 5-HMF.	256
6.5.3. Control test for external mass transfer limitations	259
6.6. Glucose and fructose dehydration to 5-HMF using metal oxide-doped zeolite Y as a heterogeneous catalyst.	261
6.6.1. Glucose dehydration to 5-HMF.....	262
6.6.2. Fructose dehydration to 5-HMF.	264
6.6.3. Control test on the synergistic effect of HY and Nb ₂ O ₅ /Y zeolite catalysts for glucose dehydration to 5-HMF.....	267
6.6.4. Powder X-ray diffraction.	268
6.7. Conclusion.....	270
6.8. References	273
Chapter 7. Conclusion and future work.	280

7.1. Conclusion.....	280
7.1.1 Solubility of sugars.....	280
7.1.2 Identification of reaction intermediates.....	281
7.1.3 Glucose to fructose isomerisation by Sn and Ga doped zeolites.....	281
7.1.4 Characterisation of zeolites for the glucose to fructose isomerisation.....	282
7.1.5 Synthesis of 5-HMF.....	283
7.1.6 Isomerisation and dehydration mediated by metal oxides.....	284
7.2. Future work.....	284
Appendix.....	288
A.1 Calibration Curves of Glucose, Fructose and Mannose in Aqueous Solution.....	288
A.2. ¹ H-NMR Spectra of Fructose Dehydration Reaction Mixture.....	290
A.3 Solubility Determination of Sugars by HPLC Diagram Method.....	291
A.4 Density Determinations of Saturated Sugar Solutions in Water and Alcohols.....	305
A.5 Catalytic Activity Data for Glucose Isomerisation Reaction in Yields.....	305
A.6 Powder X-ray Diffraction of Sn-, Ga-doped on SiO ₂ and Al ₂ O ₃	309
A.7 Diffuse Reflectance Infrared Fourier Transform (DRIFT) Spectroscopy Measurements.....	310
A.8 Unit cell calculations of powder X-ray patterns for HY, Sn/Y and Ga/Y zeolites.....	312
A.9 EXFAS data analysis for Sn/Y and Ga/Y zeolites.....	313
A.10 Powder X-ray Diffraction of Sn-, Ga- and Nb-doped Zeolite Y (5.1 and 30), zeolite beta (38), ZSM-5 (50) and MCM-41.....	315
A.11 Trends in Catalytic Activity as a Function of Acidity and Porosity.....	326
A.12 The Analysis of Pore Distribution.....	331
A.13 Catalytic Activity Data for Glucose and Fructose Dehydration Reaction in Yields.....	333
A.14 Unit cell calculations of powder X-ray patterns for HY, Sn/Y, Ga/Y, Nb/Y, and Fe/Y zeolites.....	335
A.15 Unit cell calculations of powder X-ray patterns for HY, TiO ₂ /Y, Nb ₂ O ₅ /Y, and CeO ₂ /Y zeolites.....	337
A.16 References.....	338

CHAPTER 1: Introduction

1.1. Biomass as bio-renewable feedstocks for the production of platform chemicals.

The development of alternative resources for the production of energy and materials have become increasingly important on a global scale in recent years¹. This has been prompted due to several factors, including the decrease in fossil fuel reserves, the growth in energy demand attributable to the rapid population expansion, and the prevalent concern about climate change²⁻⁴. For instance, the pollution generated from fossil fuel combustion is responsible for 4.2 million deaths and more than 100 million disability-adjusted life-years each year, which approximately corresponds to 8% of the total global deaths and 4% of global disability-adjusted life-years⁵. As a result, both industry and academia have committed significant efforts to replace the use of crude oil, natural gas, and coal with other bio-renewable commodities to generate heat and electricity, as well as to produce transportation fuels and building blocks used in the petrochemical production of olefins, aromatics, and thermoplastics⁶.

As a consequence, lignocellulosic biomass such as wood and Agricultural Residues (e.g., corn stover, wheat straw, and rice husks), and Leaves and Plant Residues (e.g., Grain Hulls) has attracted intensive attention in recent years to substitute fossil fuel resources, as it is a rich-carbon resource, typically around *ca.* 50%⁷. As shown in Figure 1.1, these materials are mainly composed of cellulose (40-60 wt%), hemicellulose (10-40 wt%), and lignin (15-30 wt%)⁸. Specifically, cellulose is a linear polysaccharide consisting of glucopyranosyl units as the main building block connected by β -1,4-glycosidic bonds¹. whereas hemicellulose comprises numerous hexose and pentose sugars, encompassing arabinose, galactose, glucose, mannose,

rhamnose, and xylose⁹. These polysaccharides can be depolymerised into sugars, which can be used to form fuels and value-added products such as furfural (Figure 1.2)¹⁰. Conversely, Lignin is a cross-linked aromatic polymer produced via the polymerisation of the substituted phenyl propylene units¹¹. The efficient cleavage of β -O-4 linkage in the aromatic units of lignin could lead to the depolymerisation of the biopolymer to aromatic monomers and dimers, which can be further converted into high-value chemicals¹².

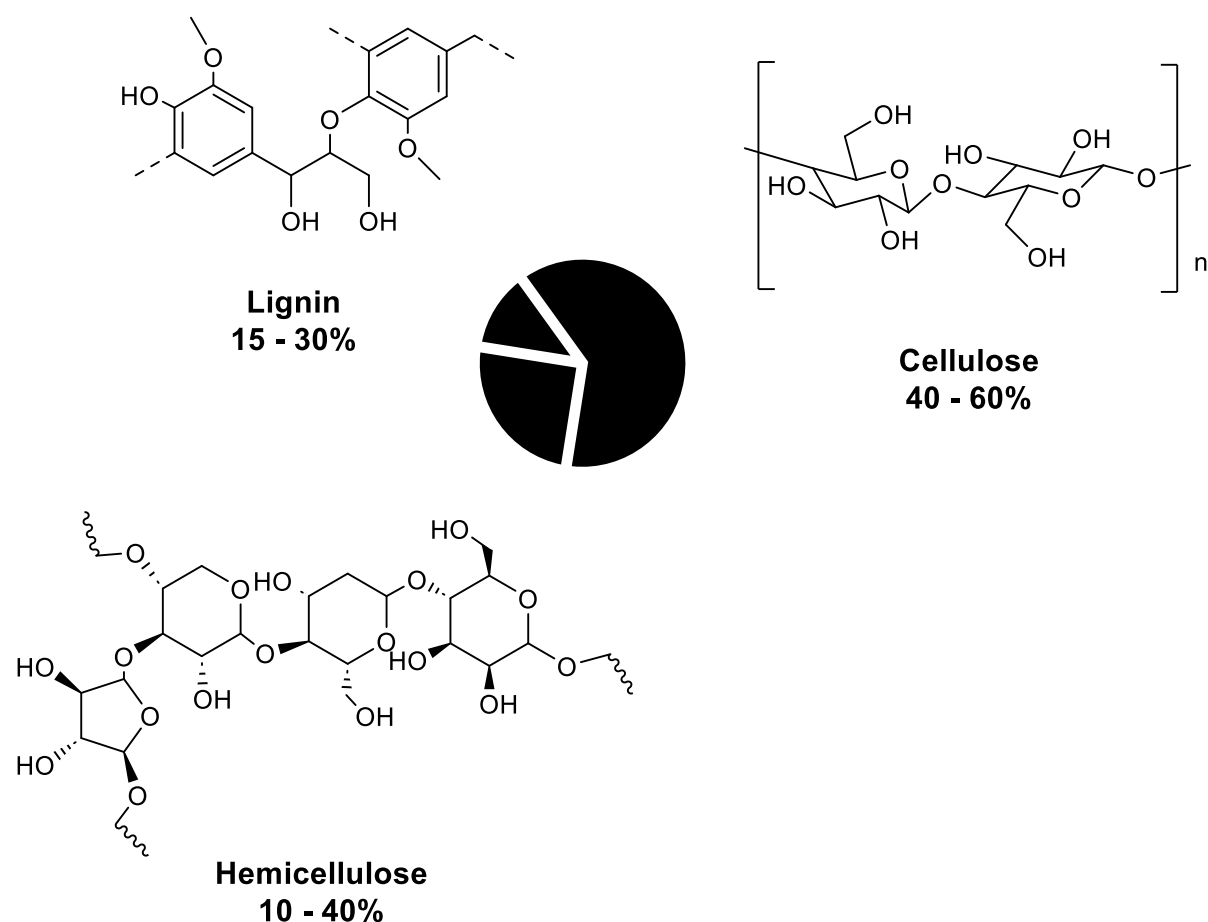


Figure 1.1. The composition of lignocellulosic biomass along with representative chemical structures of each component. A conceptual overview of hemicellulose and lignin is only provided by the above structures since those compounds are complex polymers with multiple types of subunits. The figure adapted from Robert M. O’Dea et al⁸.

The valorisation of lignocellulosic biomass feedstocks has notably received remarkable interest¹³, that is, the breakdown of these promising materials into the versatile platform chemicals required to produce valuable products, like fuels and chemical monomers^{14–16}. Despite the low price and high biomass availability, their degradation remains a substantial challenge¹⁰ and their use largely depends on the efficient conversion of the cellulosic raw material being used¹⁶. For instance, 5-hydroxymethylfurfural is an important platform chemical derived from sugars and can be converted into a wide range of essential value-added chemicals such as 2,5-furandicarboxylic acid¹⁷ and 2,5-dimethylfuran¹⁸ or even levulinic acid (Figure 1.2), which is one of the top 12 platform chemicals extracted from biomass feedstocks¹⁹

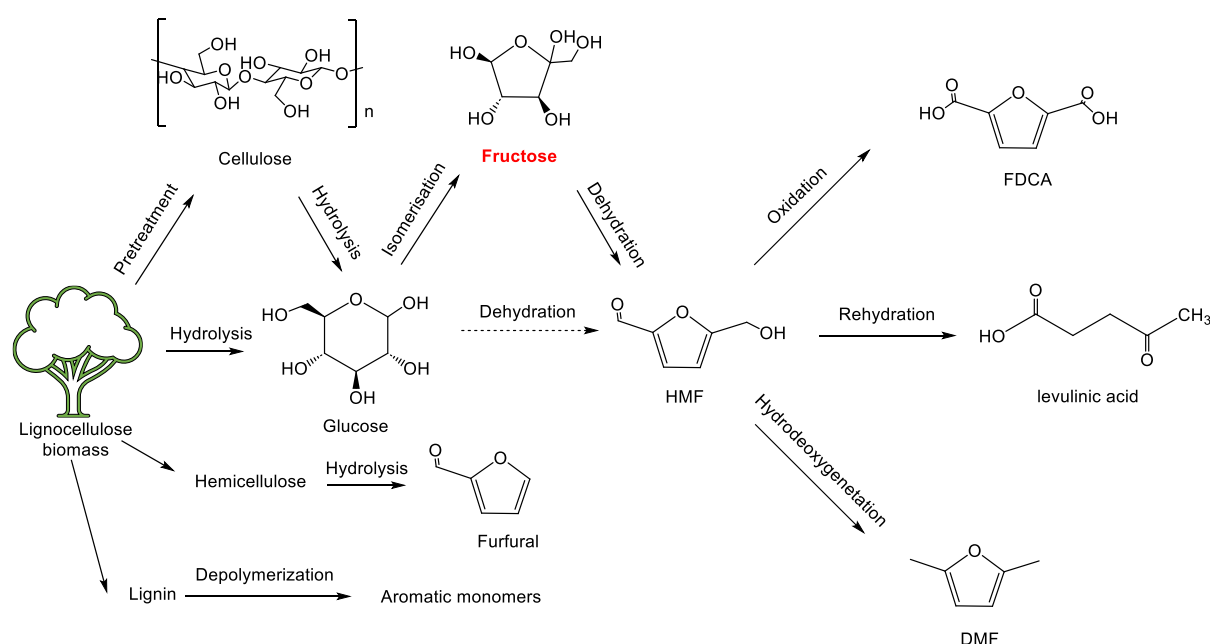


Figure 1.2. Biorefinery process of lignocellulosic biomass valorisation to platform chemicals such as 5-HMF and some of its derivatives via the formation of fructose intermediate. Furfural and aromatic monomers can also be obtained from hemicellulose and lignin, respectively. The figure adapted from Qidong Hou et al²⁰.

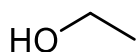
In general, the reaction pathway of biomass conversion to industrially viable chemicals involves sequential reaction steps, which begin from the hydrolysis of the cellulose and hemicellulose fractions into monomeric sugars, glucose (C-6) and xylose (C-5), respectively²¹. Glucose and xylose are then isomerised to fructose and xylulose, followed by the dehydration to the versatile platform chemicals of 5-hydroxymethylfurfural (5-HMF) and furfural serving as building blocks to form numerous products such as biofuels, biodegradable plastics, and biopharmaceuticals²².

1.2. Platform chemicals.

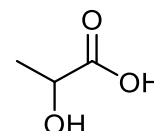
Platform chemicals are a class of materials derived from biomass and are important precursors in the production of a wide range of valuable chemicals and fuels²³. In 2010, the final list of the top 12 platform chemicals was released by the Department of Energy (DoE)²⁴, which includes ethanol, furfural, 5-hydroxymethylfurfural, 2,5-furandicarboxylic acid, glycerol, isoprene, succinic acid, 3-hydroxypropionic acid/aldehyde, levulinic acid, lactic acid, sorbitol, and xylitol (Table 1.1)²³.

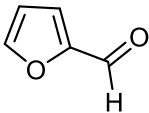
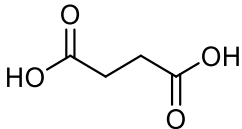
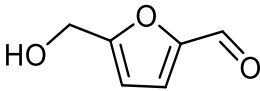
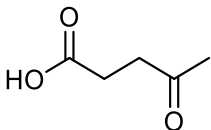
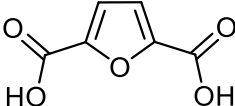
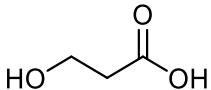
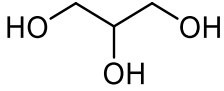
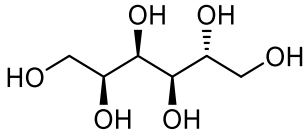
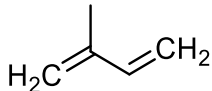
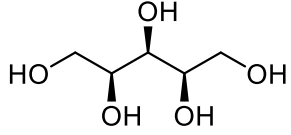
Table 1.1. The vertical order of the top 12 platform chemicals derived from biomass and their chemical structures²³, ranked by their importance as biorefinery target products²⁴.

Ethanol



Lactic acid



Furfural		Succinic acid	
5-Hydroxymethylfurfural		Levulinic acid	
2,5-furandicarboxylic acid		3-hydroxypropionic acid	
Glycerol		Sorbitol	
Isoprene		Xylitol	

1.2.1. 5-Hydroxymethylfurfural (5-HMF).

5-HMF is an attractive platform chemical that can be derived from the dehydration of hexose sugars such as glucose and fructose by losing three water molecules in an acidic catalysed reaction^{17,25}. However, due to its affordable cost and high availability, glucose is the preferred choice as a feedstock in this dehydration reaction. The conversion of glucose to 5-HMF is widely regarded as a tandem reaction, involving the isomerisation of glucose to fructose and the subsequent dehydration of fructose to 5-HMF. It is also widely accepted that the isomerisation reaction is the most important and rate-determining step in the formation process of 5-HMF²⁶. However, given the significance of these platform chemicals; we will first introduce them. Subsequently, the detailed relevance of the glucose isomerisation reaction will be described

afterwards (section 1.3). In this context, 5-HMF is a multifunctional heterocyclic furan molecule with a particular chemical structure composed of an aromatic aldehyde, aromatic alcohol, and a furan ring system²⁷, which allows the transformation of such versatile intermediate to fuels and other high-value chemicals²². For instance, 5-HMF can either be reduced to a diol or converted to a dicarboxylic acid via oxidation, both of which could be used for polymer synthesis. In addition, it is a relatively unsaturated aromatic molecule that can be transformed into fuels through the hydrogenation step. Furthermore, furans exhibit a heterocyclic structure in various biologically active molecules serving as pharmaceuticals²⁸. The Physicochemical characteristics of this important platform chemical are reported in Table 1.2

Table 1.2. physical and chemical properties of 5-Hydroxymethylfurfural (5-HMF)^{29,30}.

UPAC Name	5-(hydroxymethyl)-2-furaldehyde
Chemical Formula	C ₆ H ₆ O ₃
Physical state & colour	Crystal Solid/ Light Yellow (Tan)
Molecular weight	126.11 g·mol ⁻¹
Density	1.243 g·cm ⁻³ at 25 °C
Melting Point	28-34 °C
Boiling Point	114-116 °C at 1 mmHg
Flash Point	79 °C
Solubility in water at 25 °C	180 ± 10 g·L ⁻¹

In 1895, Dull et al. reported the first synthesis of 5-HFM through the thermal treatment of inulin in an oxalic acid solution as a catalyst³¹. Contemporaneously, Kiermayer described a similar approach to synthesising 5-HMF under pressure but using sugar

cane as a substrate¹³. In 1944, Haworth and Jones suggested the first mechanism for fructose dehydration reaction to 5-HMF. Since then, numerous vital reviews have been published in the literature concerning the synthesis of 5-hydroxymethylfurfural (5-HMF) using various catalytic systems and under different reaction conditions with the aim to develop an efficient and selective chemical route toward the formation of 5-HMF. An overview of the synthesis of 5-HMF over various catalytic systems using water as a reaction solvent is presented in Table 1.3.

Table 1.3. Summary of the synthesis of 5-Hydroxymethylfurfural from glucose and fructose using an array of homogenous and heterogenous catalysts in an aqueous solution.

Catalyst type	substrate	substrate loading (wt.%)	Catalyst (Si:Al molar ratio)	Catalyst loading (wt.%)	T/ °C	Time/h	Conversion (%)	5-HMF Yield (%)	Ref
Absence of catalyst	Glucose	10	None		140	3	8	4	32
Mineral acids		1.4 M	H ₃ PO ₄	0.14 M	180	20 min	-	12	28
Zeolites based catalysts		10	deAl-HY (15)	1.3	140	3	10	2	32
		10	deAl -Sn/Y (15)	1.3	140	3	35	6	32
		10	deAl -Ga/Y (15)	1.3	140	3	20	3	32
		3	H-Beta (12)	3	100	3	Trace	0	33
		0.6	Nb(0.05)-Beta (18)	0.1	180	24	47	22	34
		3	H-ZSM-5 (45)	3	100	3	Trace	0	33
		1.6	H-ZSM-5 (5)	1	170	2.5	42	9	35
		1.6	WO ₃ -ZSM-5 (5)	1	170	2.5	68	12	35
Metal oxides	1	Nb ₂ O ₅	10	120	3	100	16	36	

		1	Nb ₂ O ₅	10	120	3	100	12	37
		2	TiO ₂	1.6	140	6	80	28	38
		1	WO ₃	10	120	3	80	25	36
		1	Nb(0.2)-WO ₃	10	120	3	86	34	36
Other heterogeneous catalysts		2	Phosphated titania-silica (P-TiO ₂ -SiO ₂)	10	170	1	67	18	39
		10	Ytterbium MOFs Yb ₆ (BDC) ₇ (OH) ₄ (H ₂ O) ₄	0.3	140	24	28	20	40
Absence of catalyst		3	None		120	2	25	1	41
Mineral acids	Fructose	0.25 M	HCl	2 M	95	30 min	75	31	42
		11	CH ₃ COOH	100	200	20 min	92	58	43
		25	HOCCOOH	2 mol%	140	2	61	34	44
Zeolites based catalysts	Fructose	10	deAl-HY (15)	1.3	140	3	20	15	32
		10	deAl -Sn/Y (15)	1.3	140	3	53	35	32
		10	deAl -Ga/Y (15)	1.3	140	3	53	35	32
		3	HY (2.5)	0.3	120	2	12	1	41

		20	Sulfonic acid titania (TiO ₂ -SOH)	0.2	165	3	99	50	48
		0.5	Sulfonated porphyrin polymer (FePOP-1S)	0.5	160	2	95	35	47

The unique functional characteristic of 5-HMF grants its conversion to several interesting commodity chemicals via specific catalytic transformations⁴⁹ (Figure 1.3). For instance, 2,5-furan dicarboxylic acid (FDCA), recognised as one of the top 12 chemicals in the DoE list^{23,24} can be produced through the oxidation of 5-HMF¹⁷. This polymer precursor has the potential to substitute petroleum-based terephthalic acid, a commonly used component in the synthesis of a significant polyester such as polyethylene terephthalate (PET)⁵⁰. In addition, a series of promising liquid fuels, including 2,5-dimethylfuran (DMF)⁵¹, 2-methylfuran (MF)⁵², 5-methylfurfural (MFF)⁵³, 5-methyl-2-furanmethanol (MFM)⁵³, 2,5-bishydroxymethylfuran (BHMF)⁵⁴ and 2,5-dimethyltetrahydrofuran (DMTF)⁵⁵ can be obtained by catalytic transformations of 5-HMF^{18,56}. For example, DMF has particularly attracted much attention due to its numerous benefits, including an ideal boiling point of (92–94 °C) in terms of fuel stability under typical operating conditions in engines, high energy density (30 kJ·cm⁻³) enables the storage of a significant amount of energy per unit volume, high research octane number (RON=119) resulting in improved engine efficiency and performance, immiscibility with water, and ease to blend with gasoline or other fuels compared to ethanol⁵⁷.

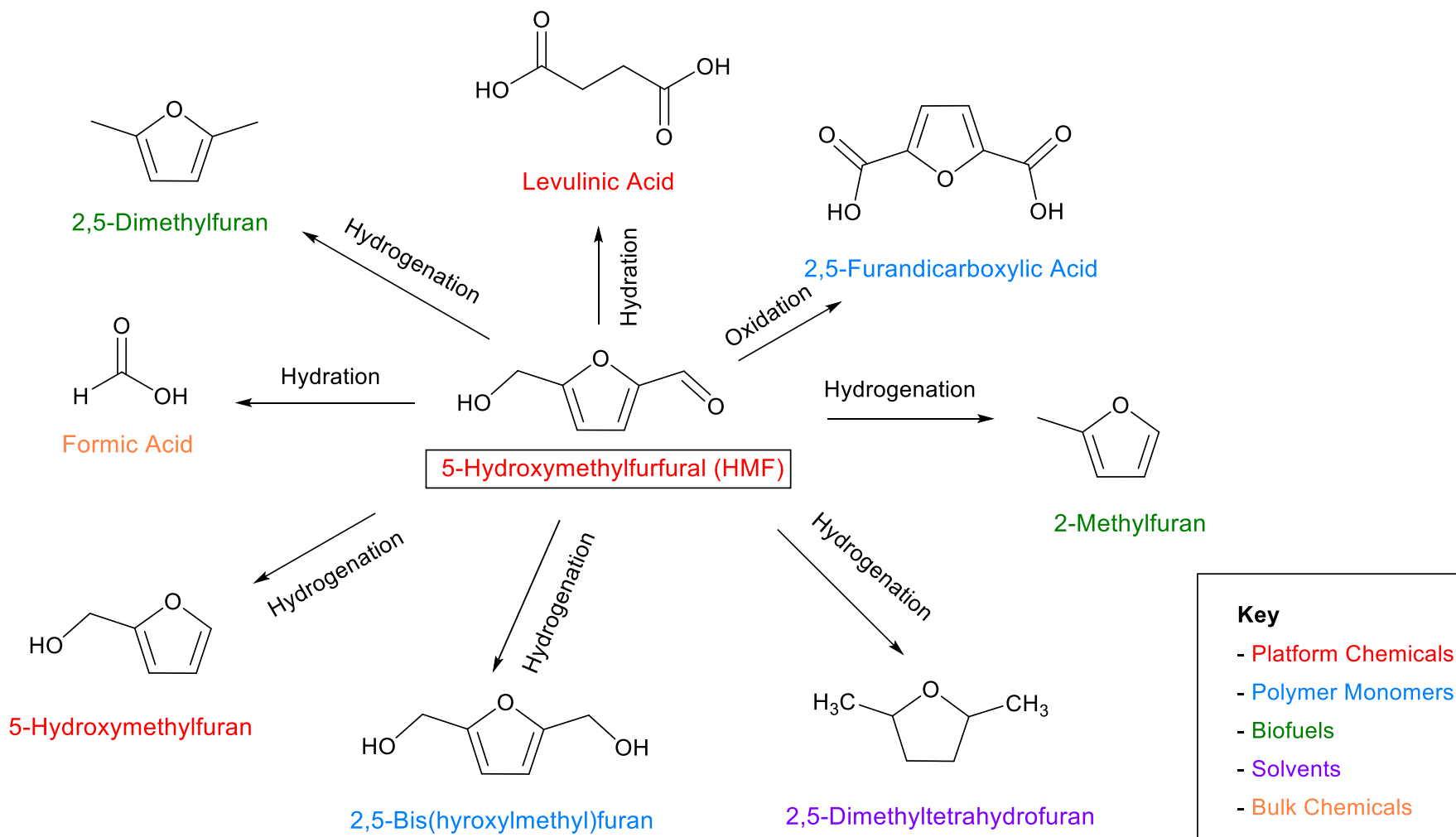


Figure 1.3. Transformation of 5-HMF to various furanic derivatives and other promising building blocks such as levulinic acid. The figure was adopted from Van Putten et al.⁴⁴

1.2.2. Levulinic acid (LA).

Levulinic acid (LA) is another prominent platform chemical that can be produced either from sugars like glucose and fructose through a series of transformation steps⁵⁸ or via subsequent rehydration of 5-HMF in the presence of acidic catalysed media⁵⁹. The isomerisation reaction of glucose to fructose also plays a critical role in the production of levulinic acid (LA) from glucose as a reaction feedstock. This step holds significant importance because fructose can be more easily transformed into LA compared to glucose. Given that glucose is less expensive and more abundant, the glucose isomerisation reaction becomes essential for the cost-efficient and effective production of LA from glucose⁶⁰. Due to the presence of a hydroxyl group and a carboxyl group within the molecular structure of this compound, LA can be easily converted into numerous fine chemicals⁶¹ (see Figure 1.4). For instance, essential molecules like succinic acid, diphenolic acid (DPA), methyltetrahydrofuran (THF)⁶², pyrrolidones⁶³, γ -valerolactone (GVL)⁶⁴ can be produced from levulinic acid through various type of reactions (Figure 1.4). These value-added compounds have been extensively used as polymers, biofuels, pharmaceuticals, plasticisers, herbicides, and solvents substituting petroleum-based chemicals due to their biocompatibility and biodegradability^{65,66}. Furthermore, levulinic ester (LE) such as methyl levulinate (ML), ethyl levulinate (EL), n-butyl levulinate (BL), etc., are other examples of the LA derivatives that have been widely used as fuel additives and bio-lubricants within the petrochemical sector⁶⁷.

Aside from levulinic acid, the rehydration of 5-HMF can also lead to the production of formic acid (FA), a commodity chemical that can be purified and sold directly. Furthermore, FA is commonly used as an acidulating textile agent, a decalcifier, an insecticide, and a refrigerant in the manufacturing process⁶⁸. In addition, the use of FA, which serves as an acid catalyst, a source of hydrogen (H_2), and a deoxygenation

agent in conjunction with fructose as a reagent, could also be utilised to produce the previously mentioned potential biofuel 2-Methylfuran (MF)⁵⁷

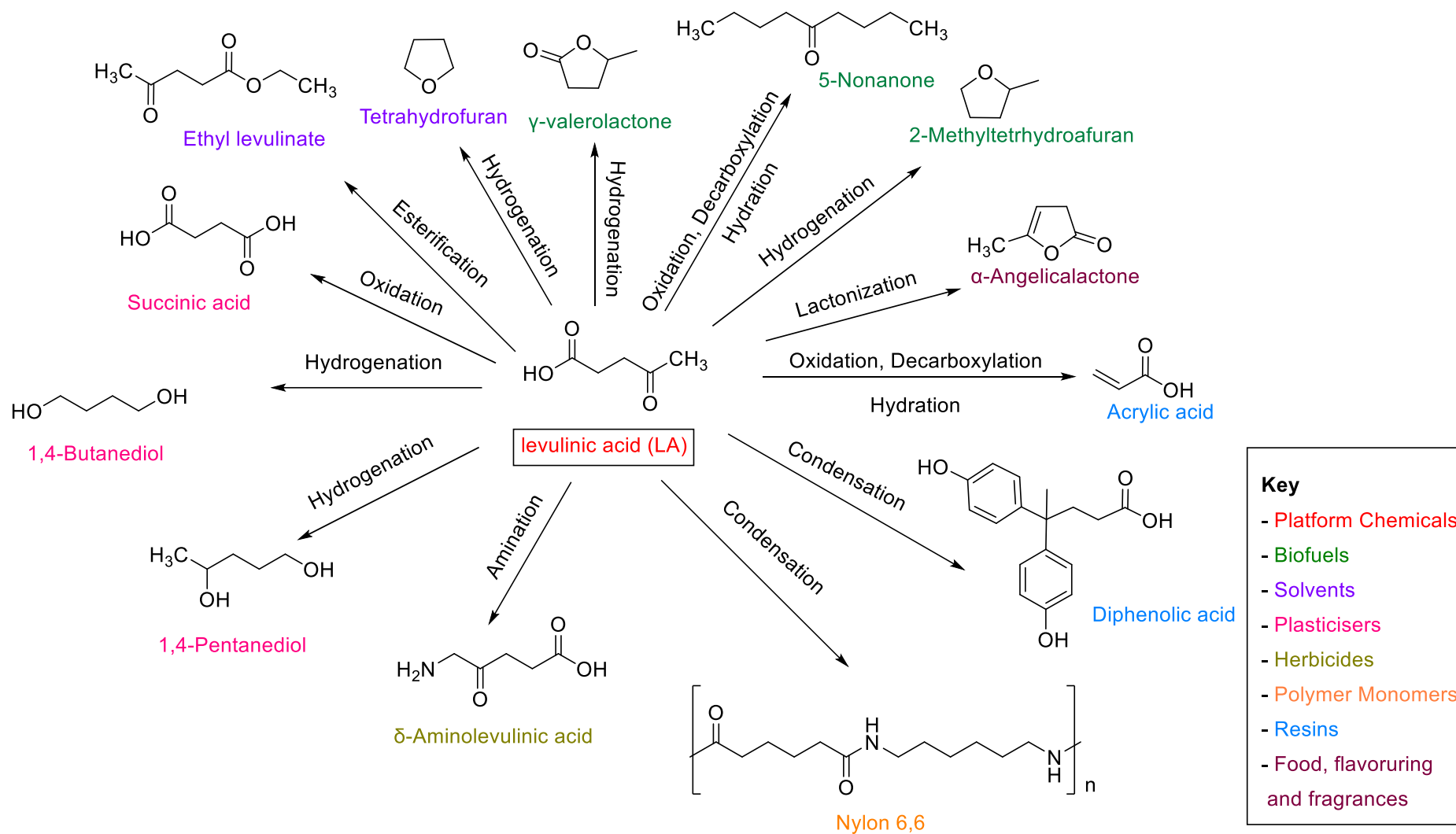


Figure 1.4. value-added chemicals derived from levulinic acid (LA), numerous useful commodities could be obtained from this platform chemical, which covers a wide range of industrial applications^{61,66}.

1.3. Relevance of glucose to fructose isomerisation.

The successful conversion of biomass feedstocks to platform chemicals such as 5-HMF and LA is crucially dependent on the efficient conversion of cellulosic feedstocks. For instance, Pentose (C5) sugars, like xylose, have been proposed as suitable candidates for this transformation process as a result of their high atom efficiency when converted to levulinic acid^{67,69}. However, the formation of an insoluble, undesirable by-product like humins can cause catalyst poisoning^{70,71}, reducing the industrial viability of the entire process.

Hexose (C6) sugar, such as glucose monomer, has also been suggested as a potential feedstock for the production of 5-HMF and LA. Glucose is a six-membered ring monosaccharide efficiently extracted from cellulose and hemicellulose by hydrolysis (Figure 1.2)^{72,73}. Therefore, it has been identified as the most abundant and cheap sugar in nature, with a price of 300 USD per ton⁷⁴ making it a preferred option for the synthesis of 5-HMF or even LA and FA. Nevertheless, glucose is a relatively inactive molecule due to the high stability of its 6-membered ring structure. Thus, the dehydration of glucose to 5-HMF is to some extent less favourable thermodynamically or occurs at a lower rate^{75,76}.

Fructose, a 5-membered ring molecule isomer of glucose, has been considered to serve as a substitute due to its less stable 5-membered ring structure, making it more reactive and capable of facilitating efficient dehydration reaction toward 5-HMF through the enolization of the open chain saccharide⁷⁷. It has been thermodynamically proven that the C-2-OH group within the fructose structure can be protonated subsequently in stabilising the furanic ring hence facilitating the dehydration step that leads to the production of 5-HMF⁷⁵. Despite this, fructose is known to be less abundant than glucose and finds many applications, such as a sweetener in the food industry⁷⁸

and as an excellent humectant in the skin and hair moisturising products⁷⁹, resulting in a higher relative cost (722 USD per ton⁸⁰ of fructose compared to glucose)⁷⁴. Therefore, the development of an efficient route to convert glucose into fructose is paramount since it becomes evident that this reaction is the rate-determining step for the production of platform chemicals such as 5-HMF and LA (Figure 1.5).

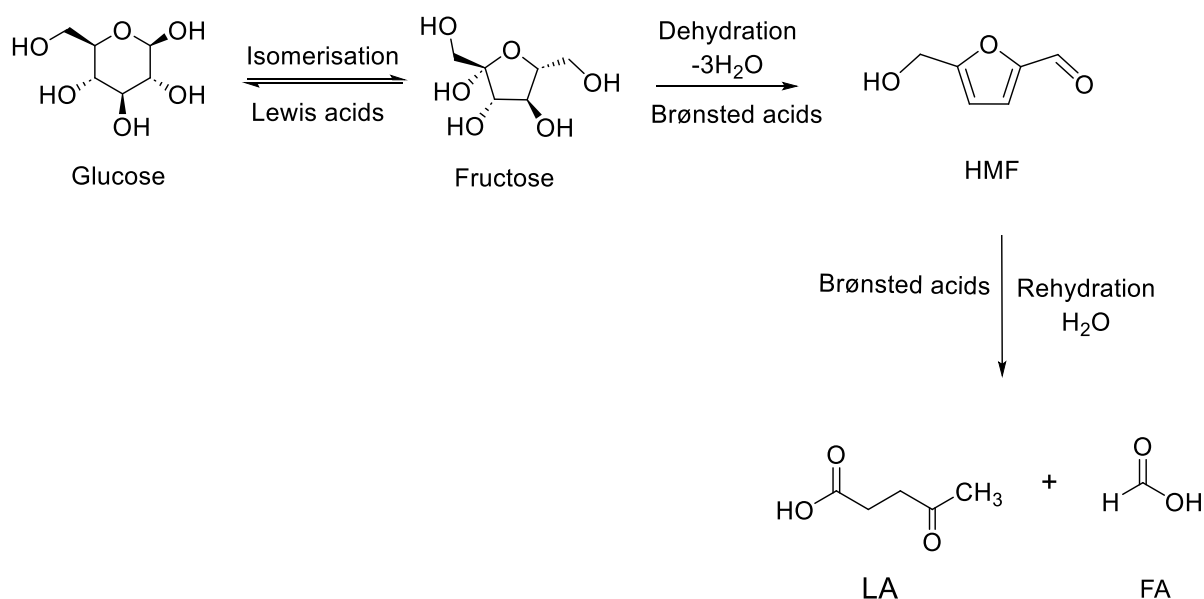


Figure 1.5. Overall schematic pathway of multi-step reaction from glucose as a biomass feedstock to platform chemicals such as 5-HMF, Levulinic acid, and formic acid in acid-catalysed media. Conversion of Glucose to fructose by isomerisation reaction over Lewis acidity, dehydration of fructose to 5-HMF over Brønsted acidity and subsequent rehydration of 5-HMF to levulinic acid and formic acid over Brønsted acidity⁶.

The chemical reaction of glucose to fructose isomerisation has been established for over 100 years and is recognised as an example of a Lobry de Bruyn-Alberda van Ekenstein transformation⁸¹. As shown in Figure 1.6, the isomerisation reaction typically occurs in three primary steps, which are the opening of the aldose glucopyranose ring, a 1,2-intramolecular hydrogen shift, and finally, the closing of the ketose fructofuranose ring^{6,82}.

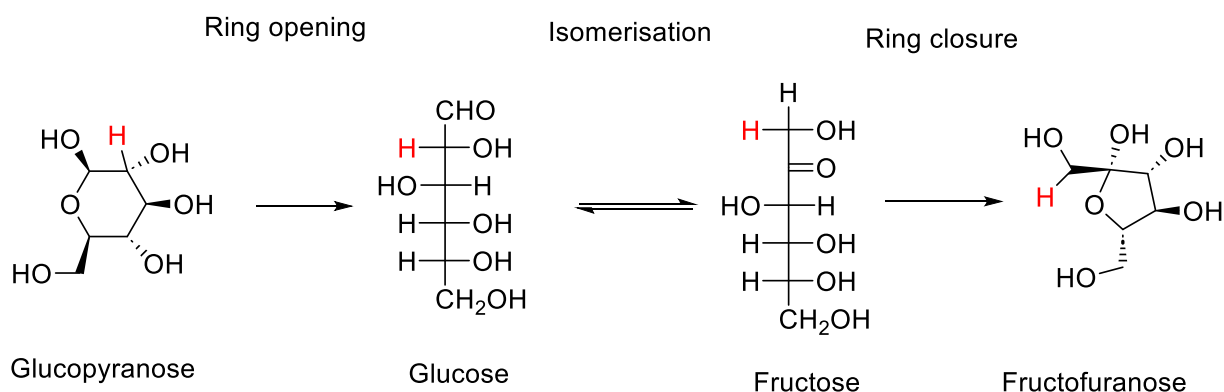


Figure 1.6. the main three stages of glucose to fructose isomerisation reaction, glucopyranose ring opening, isomerisation reaction of glucose into fructose occurred via hydrogen shift from C2 to C 1 position and at last, fructofuranose ring closure⁶.

1.4. Industrial production of fructose.

Since fructose is an essential component of the food industry, the process of an aldose to ketose isomerisation has already been carried out on a large industrial scale over the past decades using immobilised enzymes for bulk production of high fructose corn syrup (HFCS)⁸³, an aqueous mixture of glucose and fructose in various ratios⁸⁴. In addition to producing sweeteners, the interconversion reaction of glucose to fructose can also be used to produce a wide range of other chemicals and fuels derived from sugars, with fructose acting as an essential intermediate compound in the process. As a consequence, much effort has been committed to developing cost-effective and selective catalysts capable of converting glucose into a wide range of chemical compounds through fructose in recent years⁸⁵. Therefore, this section highlights an overview of previous and recent findings with regard to the isomerisation reaction of glucose to fructose over various catalytic systems and reaction conditions.

1.4.1. Enzyme-catalysed reaction.

Significant progress has been made in glucose isomerisation using enzymes such as glucose and xylose isomerases over the past several decades⁸⁶. The first study demonstrating enzymatic isomerisation of monosaccharides was conducted in 1952, where erythrose was converted into erythrulose in the presence of rabbit muscle⁸⁷. As early as 1953, Hochster and Watson discovered that a specific enzyme called xylose isomerase could catalyse the interconversion of the C5 sugars xylose to xylulose⁸⁸. According to the authors, xylose isomerase was only capable of isomerising xylose. However, Marshall and Kooi interestingly demonstrated that adjusting the reaction parameters such as incubation time, pH, and temperature enables the same xylose isomerase to catalyse the isomerisation of glucose to fructose⁸⁹. In addition, arsenate (AsO_4^{3-}) was required as an additive to facilitate the isomerisation reaction. In 1963, Yamanaka discovered glucose isomerase, an enzyme obtained from the D-xylose-grown cells of heterolactic acid bacteria and retained an 8-fold increase in specific activity after partial purification. Glucose isomerase enzyme, however, requires the presence of manganese ions (Mn^{2+}) to be active⁹⁰. At present, the reversible isomerisation of glucose to fructose is conducted on a commercial scale using glucose isomerase in an aqueous media⁹¹, which has an exceptionally high reaction specificity under acidic pH conditions and operates at relatively low temperatures (343 – 413 K). This leads to an equilibrium mixture of 50 wt.% glucose, 42 wt.% fructose and 8 wt.% other saccharides⁹². Although this enzymatic process has been established for decades now, there are still multiple drawbacks could not be addressed yet: 1) the need for large quantities of expensive enzymes, 2) the restricted operating temperature range due to the sensitivity of enzymes to reaction parameters, and 3) the possibility of biological contamination such as microbes growth in the system^{93,94}.

1.4.2. Homogeneous-catalysed reaction.

The use of homogeneous acid and base catalysts has been considered an alternative route to enzymes for the production of fructose from glucose⁹⁵. For instance, early investigations on homogeneous-catalysed glucose isomerisation involved the use of sodium hydroxide or calcium hydroxide as Brønsted solid bases. The reaction occurred via the formation of an ene-diol intermediate (see Figure 1.7), which produced a fructose yield in the range of 20 – 30%⁹⁶. This low yield of fructose is due to the fact that these inorganic bases have shown to be more attractive for converting glucose to side products of retro-aldolization by cation–ketose complexes, resulting in a low fructose yield^{97,98}. However, it was found that the addition of sodium borate ($\text{Na}_2\text{B}_4\text{O}_7$) alongside with alkaline solution of sodium hydroxide (0.5 M NaOH) significantly improved fructose yield (up to 90%), the enhanced yield of fructose can be explained by the formation of a borate ester complex $\text{B}(\text{OR})_3$, which plays a partial role in protecting the monosaccharides from alkaline degradation. Even so, a significant drawback of this process was the need for a high concentration of reagents even for a comparatively low concentration of glucose⁹⁹. Thus, making the process economically unattractive.

Furthermore, additional studies were conducted to increase fructose yield using sodium aluminate in the presence of arylboronates as an additive, and a fructose yield of around 60 – 70 % has been here reported^{100,101}. Likewise, using an aluminate solution could promote the base-catalysed conversion of glucose to fructose. Particularly, it has been found that the addition of aluminium oxide to a boiling solution of glucose-containing pyridine could significantly increase the reaction rate of the aldose–ketose transformation, yielding 50% fructose higher than that obtained with the conventional Lobry de Bruyn-Alberda van Ekenstein reaction¹⁰². Further, it was

observed that the fructose yield increased by 5-fold when alumina was added to the reaction mixture, which clearly indicates that alumina plays a crucial role in converting glucose into fructose in pyridine.

Conversely, amines with wide pKa values were incapable of forming cation-ketose complexes, providing the potential for greater optimisation of fructose selectivity. For instance, Liu et al. reported the use of organic amines such as morpholine, piperazine, ethylenediamine, triethylamine, piperidine, and pyrrolidine with pKa values in the range of 8.4–11.3. the results showed that these amine compounds lead to glucose conversions in the range of 43 - 62% with fructose yields in the range of 17 - 31% in water as a solvent after 30 minutes at a reaction temperature of 100 °C¹⁰³.

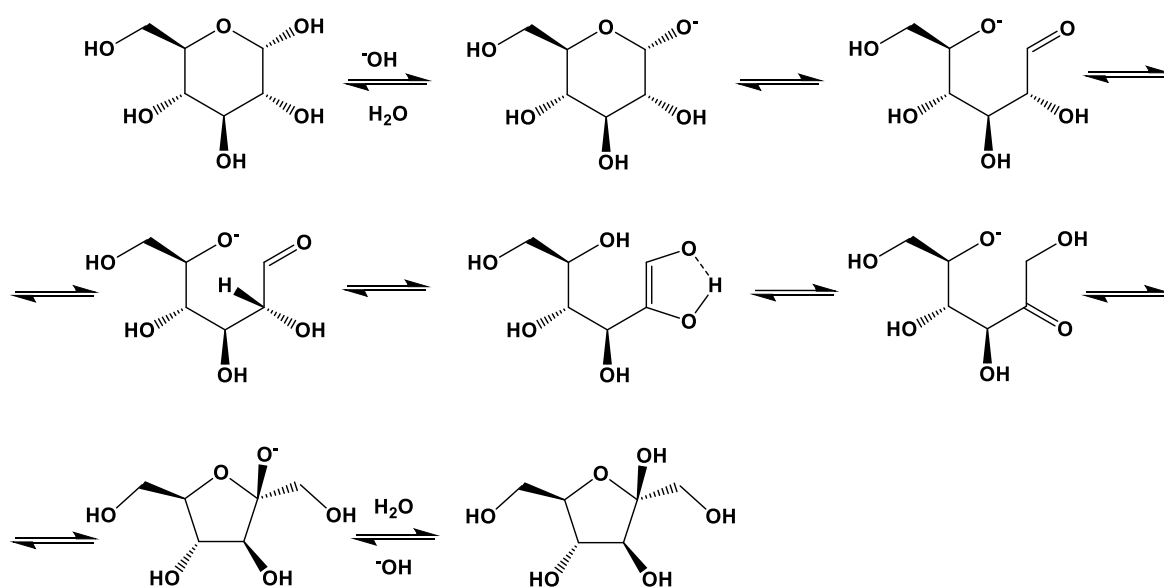


Figure 1.7. Proposed mechanism for isomerisation reaction of glucose to fructose via enediol intermediate catalysed through Brønsted bases in aqueous media. a proton transfer through an enolate intermediate is considered the rate-determining step in this reaction mechanism. However, the main disadvantage of using base catalysts is their potential to deprotonate the majority of the hydroxyl groups (OH) present in the glucose molecule. This can result in the enolate ions undergoing side reactions such as condensation and/or polymerization, which ultimately leads to the formation of complex mixtures and decrease the fructose selectivity¹⁰⁴.

In contrast, Lewis acids Homogeneous catalysts such as CrCl_2 , SnCl_4 , and AlCl_3 have been reported in a few works to be catalytically active in converting glucose into 5-HMF through fructose^{105–108}. For instance, in a study conducted by Li et al. aiming to catalyse the transformation of glucose to 5-HMF by using metal chloride of CrCl_3 as a catalyst in the ionic liquid solvent of (1-butyl-3-methylimidazolium chloride, [BMIm]Cl). It was, however, very difficult with this Lewis acid catalyst to control the formation of fructose in a relatively high yield¹⁰⁹. Furthermore, Jia et al. have recently reported the use of chromium trichloride hydrates ($\text{CrCl}_3 \cdot 6\text{H}_2\text{O}$) as a catalyst for the glucose-to-fructose isomerisation reaction in both aqueous and organic solvents, wherein fructose yields of 25% with glucose conversions in the range of 30-55% were obtained at a reaction temperature of 130 °C¹¹⁰. To gain more insight into the reaction mechanism, Mushrif et al. have used Ab initio molecular dynamics to elaborate on the mechanism of glucose isomerisation with a CrCl_3 catalyst in the presence of water¹¹¹. A proposal has been made that glucose can co-coordinate with the chromium chloride complex via substituting two water molecules, thereby supporting the claim that a partially hydrolysed chromium complex is formed before the conversion into fructose. In addition, it has been demonstrated by Tang et al. that AlCl_3 catalyses the isomerisation of glucose to fructose in an aqueous solution. Electrospray ionisation tandem mass spectrometry (ESIMS/MS) revealed that a ring-opening reaction occurred, leading to the coordination of acyclic glucose to the active aluminium species through the C1–O and C2–O positions, which in turn facilitated the formation of fructose via a 1,2-intramolecular hydride shift from the C2 to C1 positions of glucose¹¹². Even though both homogeneous base and acid catalysts show promising activity for the isomerisation of glucose into fructose, both of which are corrosive and not as environmentally friendly nor as cost-effective as solid catalysts, which can easily be

separated from the products, regenerated, and recycled back into the process¹¹³. From an economic point of view, homogeneous catalysts are less attractive for the isomerisation reaction of glucose to fructose, resulting in the need for the development of more suitable catalytic systems.

1.4.3. Heterogeneous-catalysed reaction.

In terms of fructose production, there is a great deal of potential for solid heterogeneous catalysts to replace conventional enzyme and homogeneous counterparts for large-scale industrial processes, including easy handling, sustainability, exceptional hydrothermal stability, wide operating temperature range, tuning of acid and base sites, high durability, and high impurity resistance^{104,114–116}. A wide variety of acid and base heterogeneous solid catalysts have so far been reported for the interconversion of glucose to fructose. For instance, Rebenfeld and Pacsu, late in 1953, reported using Amberlite IRA-400 (OH), a strong base anion-exchange resin, as a catalyst for the catalytic isomerisation of glucose to fructose. However, a fructose yield of 30% was only obtained¹¹⁷. In addition, Langlois and Larson showed that Dowex-1 and -2, other types of anion-exchange resins, could also be used as solid base catalysts to form fructose from glucose with a maximum yield of 32%¹¹⁸. Even though it was viable to achieve a reasonable fructose yield using these basic ion exchange resins, it should, however, be noted that undesirable products were also favoured. Furthermore, their stability is relatively low, and the removal of the adsorbed substrate on the active sites of the resin is rather difficult; thus, the regeneration of these catalysts is not possible, making the approach less attractive from an industrial perspective¹¹⁹.

On the other hand, bare metal oxides, such as ZrO₂ (tetragonal-monoclinic) and TiO₂ (rutile and anatase), can also catalyse the conversion of glucose to 5-HMF through

the formation of fructose intermediates in water at 200 °C. However, there were generally low yields of fructose ($\leq 15\%$) obtained from this catalytic process. From spectroscopic experiments, it was confirmed that glucose isomerisation takes place via base sites derived from metal oxides ZrO_2 and TiO_2 ¹²⁰. In addition, Nb_2O_5 exhibited high activity in the isomerisation reaction of glucose to fructose. This metal oxide, known for its water tolerance, possess both Lewis and Brønsted acidic characteristics, making them highly promising catalysts for the conversion of glucose to 5-HMF through the formation of fructose intermediates¹²¹. For instance, during the dehydration of glucose to 5-HMF, Nb_2O_5 exhibited remarkable catalytic activity in converting glucose to fructose, leading to a fructose selectivity of 60% for reactions carried out at a reaction temperature in the range of 160 – 180 °C after 30 min¹²². Furthermore, Hydrotalcites (HTs), an example of layered double hydroxides (LDH), have also been explored as a solid base catalyst for catalytic isomerisation of glucose to fructose. It was found that 90% selectivity toward fructose was obtained at a reaction temperature of 90 °C after 20 – 25 min when a commercial hydrotalcite catalyst (DHT-4A2) calcined at 400 °C and rehydroxylated was used. This was accompanied by low a glucose conversion of less than 15%¹²³. However, as the basicity of hydrotalcite largely depends on its layered structure, it can be altered by modifying the calcination and rehydration procedures. In this regard, as described by Jung et al., a series of hydrotalcite catalysts was prepared, including as-synthesized Mg–Al hydrotalcite, calcined Mg–Al hydrotalcite, and rehydrated Mg–Al hydrotalcite catalysts with a ratio of Mg/Al= 3. The HT_R catalyst exhibited abundant weak basic sites as a result of the exfoliation, and the vertical breaking of layers in the hydrotalcite structure through the rehydration procedure was shown to significantly enhance the catalytic activity of rehydrated Mg–Al hydrotalcite catalyst with glucose conversion of 50% and fructose

yield of 35% at a reaction temperature of 80 °C for 3 hours¹²⁴. A further study conducted by Essayem et al. showed that as-synthesised cetyltrimethylammonium cation mesoporous molecular sieves of the M41S family, including Si-MCM-48, Si-MCM-50, and Si-MCM-41 as hybrid catalysts used without any pre-treatment were highly capable of isomerising glucose to fructose, resulting in a fructose selectivity of 80% at glucose conversion of 20% being obtained at 100 °C in aqueous phase¹²⁵.

In addition to using solid bases, recent research has been focused on promoting the isomerisation of glucose into fructose using recyclable solid acid catalysts with Lewis acidic centres. As a result of this, solid acid metal (IV) phosphate catalysts with a high overall concentration of acidity and surface area (such as zirconium and tin phosphates) have been identified as selective and highly active catalysts for acid-catalysed isomerisation and dehydration reactions in the aqueous phase^{126,127}. In light of these perspectives, Huber et al. reported an array of zirconium- and tin-based phosphate catalysts for the conversion of glucose into levulinic acid through fructose intermediates. Zirconium phosphate catalysts containing more Brønsted acid sites showed at least 3-fold more activity than their tin phosphate catalysts toward the production of 5-HMF and levulinic acid. Conversely, tin (IV) phosphates, which possess more Lewis acid sites, favoured the isomerisation route to form fructose with a selectivity of 10 - 15% higher than with zirconium (IV) phosphate $\text{Zr}(\text{HPO}_4)_2$ and 40% glucose conversion¹²⁸. In the view of bifunctional catalysts, Akiyama et al. reported the catalytic activity of four types of MIL-101 derivatives composed of $-\text{NH}_2$, $-(\text{CH}_3)_2$, $-\text{NO}_2$, and $-\text{SO}_3\text{H}$, respectively, as an example of chromium-containing porous coordination polymers or metal-organic frameworks catalysts for the catalytic conversion of glucose to fructose in aqueous solution. The MIL-101- SO_3H catalyst revealed the highest fructose yield of 20% alongside glucose conversion of 78%

among all catalysts studied. It was also possible to achieve a 100% recovery of glucose and fructose, which indicates a very clean route for the reaction, which was claimed to be due to the reactive Lewis acidity of chromium open metal sites on the pore surface of MIL-101 catalyst¹²⁹. In view of its large pore size (2.9 - 3.4 nm), further investigation on the use of Cr-containing metal–organic frameworks (MOFs), denoted as MIL-101(Cr) for the catalytic isomerisation of glucose to fructose has also been explored in the recent years. It was found that the isolated Cr (III) species within MIL-101 act as Lewis acid sites and are responsible for facilitating the isomerisation of glucose to fructose in either aqueous, organic or their combination system¹³⁰. Similarly, Guo et al. have also found that a composite of MIL-101(Cr) and chromium hydroxide exhibits a superior performance (glucose conversion of 79% and fructose yield of 59%) toward the isomerisation of glucose to fructose at 100 °C for 24 h in the presence of ethanol via the formation of ethyl fructoside as an intermediate, which required a second step of hydrolysis in water at 100 °C for 24 h¹³¹.

More remarkably, it was first reported in 2010 by Davis et al., that Sn-containing beta zeolite acts as a Lewis acid catalyst and exhibits unprecedented high catalytic performance in catalysing glucose into fructose in aqueous media (fructose yield of 31% after 30 min at 110 °C)¹³². Beta zeolite, a 12-membered-ring zeolite framework with a large pore of 0.76 × 0.64 nm in diameter¹³³ was initially reported to be an excellent catalyst towards the Baeyer-Villiger oxidation of cyclic ketones to esters and lactones and the selective reduction of carbonyl compounds (Meerwein–Ponndorf–Verley Reaction) when incorporated by Sn species by Corma et al., about twenty years ago^{134,135}. In fact, the recent advances in Lewis acid containing zeolites as promising catalysts for transforming glucose to fructose will be explored in detail in this thesis work (section 1.6. in Chapter 1).

1.5. Zeolites

Zeolites are unique natural minerals that have been known for over 250 years. It was the Swedish mineralogist Axel F. Cronstedt who first discovered them in 1756¹³⁶. The term Zeolite was coined from two Greek words, “zeo”, which means “to boil”, and “lithos”, which means “stone”. According to Cronstedt's initial observations, these minerals boil when heated at high temperatures due to water boiling within their structure¹³⁷, hence the name. Zeolites are categorised as natural or synthetic based on their method of production¹³⁸. Natural zeolites are typically mined from the Earth's crust at an estimated rate of around one million tonnes in 2022¹³⁹. In contrast, synthetic zeolites are, as their name implies, synthesised explicitly to serve a specific purpose, most often through a hydrothermal process¹⁴⁰. Owing to their attractive characteristics, such as ion exchange capacities, efficient catalytic performance, low cost, and robustness¹⁴¹, zeolites have found a wide range of applications, including as water softeners in detergents due to their affinity for Ca^{2+} and Mg^{2+} ions¹⁴², and as adsorbents in the nuclear waste treatment to remove radioactive isotopes such as Sr^{2+} and Cs^+ ions¹⁴³. Catalytically, zeolites have also been commonly used in numerous important industrial processes, such as the well-known processes of fluid catalytic cracking¹⁴⁰ and hydrocracking¹⁴⁴, which are chemical conversion and thermal cracking processes involve the breakdown of heavy, less valuable hydrocarbons into lighter, more useful products¹⁴⁵. In addition to the continued development of these materials as sorbents and cracking catalysts, recent zeolite research has focused more on catalytic transformations of bio-based platform chemicals¹⁴⁶, catalytic transformations of C1 molecules, including CO, CO₂, CH₄, CH₃OH, and HCOOH¹⁴⁷, and CO₂ capture by adsorption technologies¹⁴⁸.

As of today, the International Zeolite Association (IZA) recognises a total of 253 framework types, each of which is identified by a unique three-letter framework code¹⁴⁹. Several factors contribute to the differences between the various frameworks, including the size and shape of channels, their dimensionality, their connectivity, and whether the channels are linked together to create large cavities, also referred to as super-cages.

Table 1.4. Five industrially relevant zeolite frameworks, along with their main structural characteristics¹⁴⁹.

Framework code	Representative example	Ring size (# T-atoms)	Pore size (Largest channel) Å × Å	Channel dimensionality (D)
FAU	Zeolite Y	12, 6, 4	7.4 × 7.4	3-Dimensional
BEA	Beta	12, 6, 5, 4	7.3 × 7.1	3-Dimensional
MOR	Mordenite	12, 8, 5, 4	7.0 × 6.5	1-Dimensional
MFI	ZSM-5	10, 6, 5, 4	5.6 × 5.3	3-Dimensional
FER	Ferrierite	10, 8, 6, 5	5.4 × 4.2	2-Dimensional

1.5.1. Structure of zeolites.

In general, zeolites are a class of microporous crystalline aluminosilicates consisting of structural units referred to as TO₄ (T = SiO₄ or AlO₄) linked by oxygen bridges and are called primary building units (PBUs). The different connections of these TO₄ tetrahedrons create various three-dimensional arrangements of channels and cages (polyhedral, cubic, hexagonal), which combine together to form distinct porous structures known as zeolite frameworks as secondary building units (SBUs)¹⁵⁰. As

shown in Figure 1.8, combining these two building blocks (i.e., the PBUs and SBUs) will result in the formation of a structure characterised by their diverse channels and chambers¹⁵¹. such an arrangement and size of the zeolite's channels and pores can significantly influence the accessibility of reactant molecules to active sites as well as the diffusion of products, therefore adversely affecting their catalytic performance.

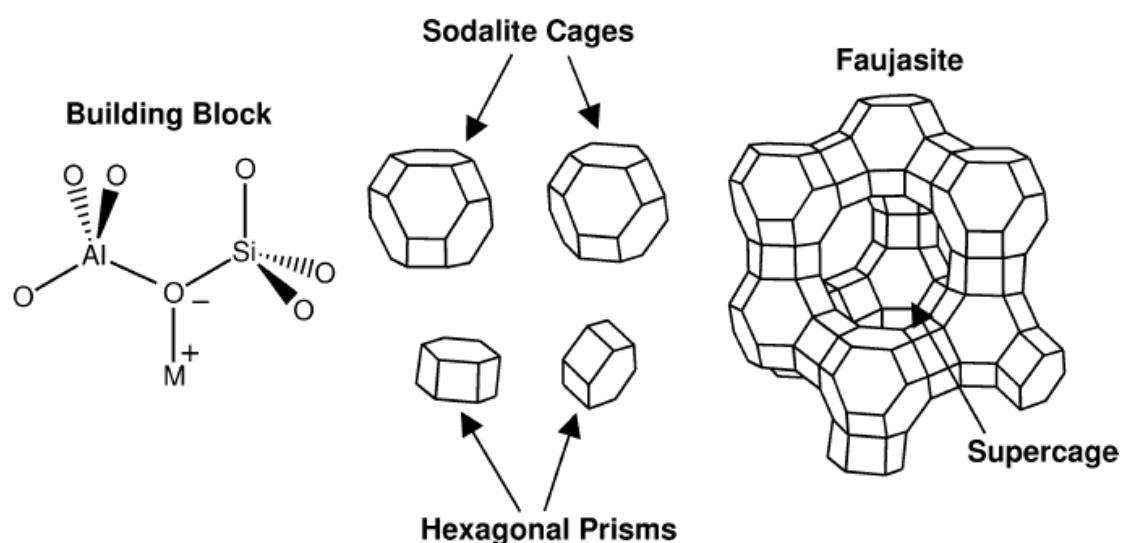


Figure 1.8. Schematic diagram of the structure of the most commonly used zeolite in this research, namely, zeolite Y. The structure consists of TO₄ tetrahedra units (T= Si, Al), linked via shared-corner oxygens and arranged geometrically to form sodalite cages and hexagonal prisms that subsequently combine to make a three-dimensional framework of zeolite. M⁺ is a charge-balancing cation, which is added to balance the negative charge associated with each Al³⁺ atom, yielding electrical neutrality¹⁵². The figure reproduced from Robert J. Davis with permission.

For instance, Osmundsen et al.¹⁵³ investigated the effect of structural type on the nature of active sites for the isomerisation of glucose to fructose in water using four different zeolite frameworks: Sn-BEA, Sn-MFI, Sn-MCM-41, and Sn-SBA-15. As a result, the characteristics of tin active sites differed significantly depending on the zeolite structure used. It was found that only Sn-BEA was able to efficiently catalyse the conversion of glucose to fructose with a conversion rate of 50%. In contrast, none

of the other catalysts could obtain conversion values higher than 5% in 48 h at a reaction temperature of 80°C. The low glucose conversion obtained by Sn-MFI could be explained by severe diffusion limitations induced by the narrow pore system and the large crystal size (Table 1.4). However, a similar explanation does not hold for mesoporous zeolites (Sn-MCM-41 and Sn-SBA-15), where diffusion should not have a significant impact. It could instead be resulting from the deactivation of the active sites as a result of their interaction with water. This would not be relevant in the case of the Sn active sites supported on the BEA and MFI zeolite frameworks, which are more resistant to deactivation by water due to their highly hydrophobic nature.

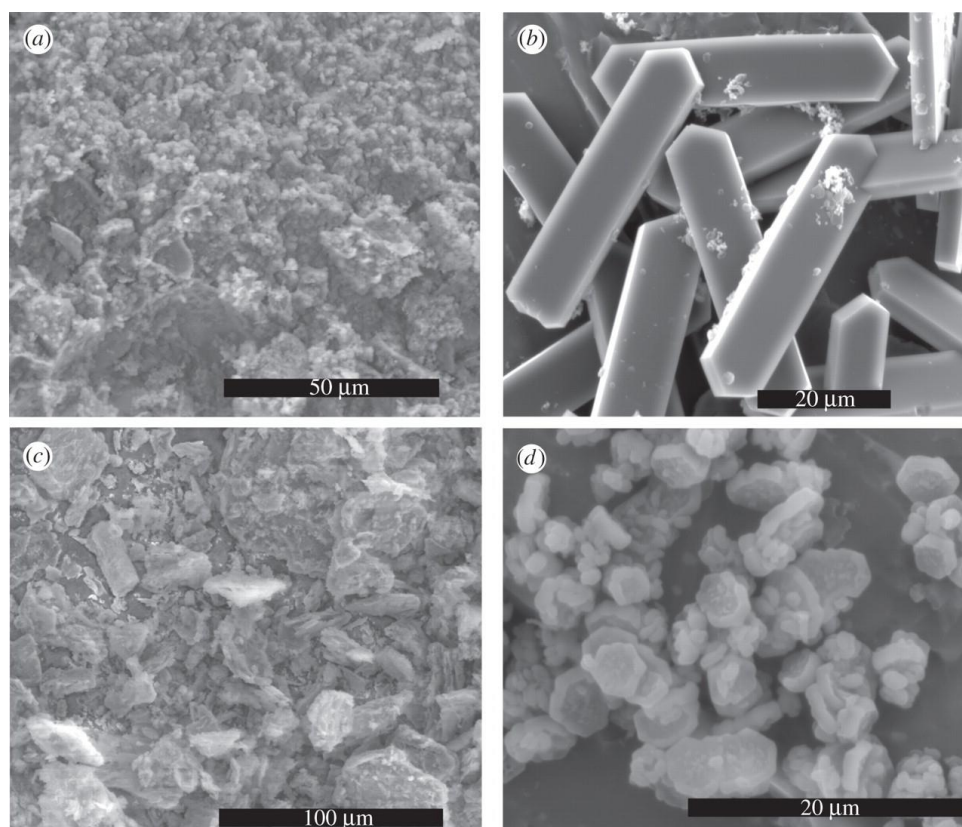


Figure 1.9. Representative SEM pictures of four stannosilicates samples. (a) Sn-BEA, (b) Sn-MFI, (c) Sn-MCM-41 and (d) Sn-SBA-15, demonstrating a distinct difference in morphology. The figure reproduced from Osmundsen et al.¹⁵³ with permission.

As can be seen in Figure 1.9, the SEM picture of the Sn-BEA crystal shows a very small spherical particle of less than 1 μm in size, whereas the Sn-MFI crystal has a sizeable coffin-shaped crystal size measuring more than 20 μm in length. The large particle size combined with the narrow pore system of the MFI structure means that severe diffusion limitations must be expected for this catalyst. Likewise, mesoporous zeolites appear to differ significantly; Sn-MCM-41 lacks a distinct particle shape, which is understandable given that the sample is amorphous. In contrast, the Sn-SBA-15 particle shape appears as hexagonal discs, which is highly consistent with the two-dimensional hexagonal ordering of the pores system in this catalyst¹⁵³.

1.5.2. Porosity and shape selectivity.

As zeolite structure reveals several discrete cavities (cages) and channels (pores) with an average size range between 0.3 to 1.5 nm¹⁵⁴, a specific pore system imposes steric constraints on the reaction, regulating the access of reactants and products through shape-selectivity phenomena. In general, if the size of pores is not large enough to facilitate the penetration of adsorbate molecules into their inner channel system, reactions will not occur, and in turn, the catalyst loses its activity¹⁵⁵. In terms of their pore sizes, zeolites can be classified as microporous (pore size less than 2 nm), mesoporous (pore size of 2-50 nm), and sometimes, macropores (pore size larger than 50 nm) materials¹⁵⁴. That said, these classifications are essential; however, there are also examples where the catalytic activity may take place on the external surface of the zeolite crystals. For instance, the hydro-isomerisation reaction of long-chain n-alkanes (carbon number > 12) on medium pore zeolites with one-dimensional pore channels (e.g., ZSM-22)¹⁵⁶.

Microporous zeolites have attracted more attention due to their size range, which promotes a wide range of crucial chemical reactions in industry, such as the above-described “fluidised catalytic cracking process” (Section 1.5)¹⁴⁰. These particular pore sizes can be generally constructed of eight, ten, twelve, and fourteen-membered rings. In particular, most of these zeolites fall into three main categories, which are small pore size zeolites with eight-membered rings and diameters of 0.3 - 0.45 nm such as Zeolite A, medium-pore size zeolites with ten-membered rings and diameters of 0.45 - 0.6 nm such as ZSM-5 zeolite, and large-pore size zeolites with twelve membered-rings and diameters of 0.6 - 0.8 nm such as Zeolite Y, X, beta and Mordenite (Figure 1.10).

For example, Guanna Li et al. conducted periodic DFT calculations to study the mechanism of glucose-to-fructose isomerisation reaction over tin-supported zeolite with various framework structures, including MOR, BEA, MFI and MWW¹⁵⁷. The primary focus was on the role of the Sn active sites and zeolite topology in the rate-determining step of the 1,2-intramolecular hydride shift. It was found that the difference in the size and shape of the zeolite pores possesses a minimal impact on the reactivity of the Sn active centres; they, however, have had a profound effect on the thermodynamic stability of the adsorbed *o-Glucose* and *o-Fructose* intermediates within the zeolite channels, which effectively reduces the accessibility of the lattice Sn sites.

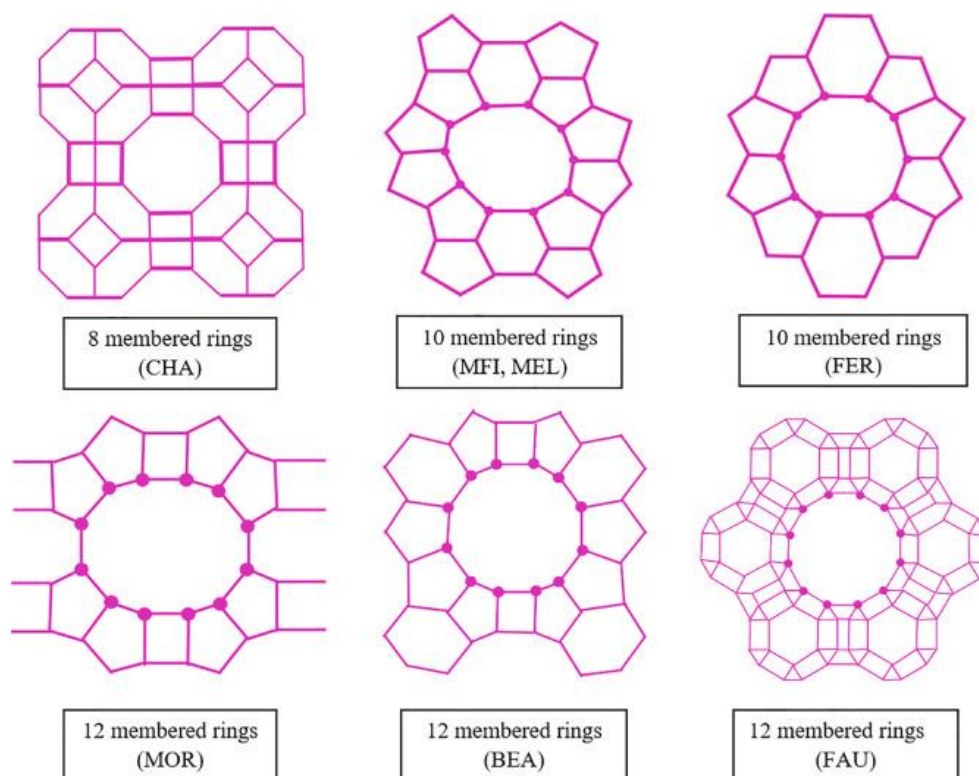


Figure 1.10. representative examples of the "n-membered" rings typically found in the structure of the zeolite. The figure reproduced from Nichaboon Chaihad et al. ¹⁵⁸. with permission.

Shape selectivity is another important characteristic of zeolites, which is derived from the size and geometry of their pore system¹⁵⁹. The fundamental concepts of this approach will be briefly discussed here:

i) Reactant shape selectivity (RSS).

In RSS, reactants of different sizes and shapes will have different levels of access to the internal active sites located in the porous network of zeolites, depending on their size. As a result, only species with a diameter similar to or smaller than the pores diameter of the zeolite will be able to enter the pores and react. The geometrical shape of the pore entrance and the diffusion properties of reactants within the pore govern this type of shape selectivity¹⁶⁰.

ii) Product shape selectivity (PSS).

In PSS, the shape and size of products control their diffusion outside the pores. In brief, products with geometric shapes equal to or smaller than the pore dimensions of the zeolite structure will smoothly diffuse out of the porous network, whereas zeolite frameworks with larger spatial dimensions will be trapped in the inner pore system. Major drawbacks driven by this type of shape selectivity are: (i) trapped products undergo further reactions and form undesired by-products. (ii) permanently trapped products inside the pores might quench the catalytic activity of the catalyst, resulting in catalyst deactivation¹⁶¹.

iii) Transition state shape selectivity (TSS).

In TSS, the available space around the active sites sterically controls the formation of bulky transition states in the zeolite cavities or channels. If the zeolite cavities or channels lack adequate space for the transition state, specific reactions may be prevented¹⁶².

1.5.3. Metal active species.

The substitution of heteroatoms within the zeolite framework has been shown to play an efficient role in tailoring the properties of microporous catalysts, including their acidity, pore structure, and crystal shape. The nature of the zeolite structure offers several possibilities for heteroatom substitution, whereby the heteroatom occupies tetrahedral coordination within its framework. This can either occur naturally in minerals or be achieved during the synthesis using a wide range of metals., such as main group elements (e.g., Sn, Ga, Ge, B) and transition metal elements (e.g., Ti, Fe, V, Cr, Mn)¹⁶³. The incorporation of heteroatom into the zeolites framework can be

accomplished during the zeolite crystal growth¹⁶⁴ or through a post-synthesis modification using procedures such as impregnation and ion exchange¹⁶⁵. When metals are introduced into the zeolite framework, different metal species are typically formed, wherein their type depends on factors beyond the zeolite structure alone. There are a number of parameters that are involved in determining the type, distribution, and number of atoms to be incorporated into the zeolite framework, including the solubility of the metal precursors, the specific chemical behaviour of the tetrahedral atoms of the precursor within the synthetic mixture, and most importantly, the capability of adding metal species fit the zeolites without distorting or collapsing their framework structures¹⁶⁶.

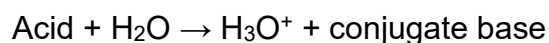
The introduction of these heteroatoms can be divided into two main categories; (i) they are introduced directly into the framework by substituting Al or, in some cases, Si atoms, which are referred to as (intra-framework species) or (ii) they are introduced inside the pores of the zeolite framework or on its external surface, which referred to as (extra-framework species)^{167,168}. Most zeolites possess the inherent capability to replace their tetrahedral Al³⁺ cations, and for atoms with lower charges, Si⁴⁺ cations can also be substituted¹⁶⁶.

As the nature of the active centres (e.g., metal or metal oxide species) is the most critical factor in the design of heterogeneous catalysts, there is no doubt that a comprehensive understanding of their characteristics, such as structure, chemical status and interactions with reactants and substrate materials, is crucial¹⁶⁹. For instance, as confirmed by isotopic labelling experiments conducted using ¹³C and ¹H NMR spectroscopy¹⁷⁰, Sn(IV) species incorporated into the well-known beta zeolites framework serves as Lewis acid centres, exhibiting remarkable activity to facilitate the ring-opening of glucose molecules and then coordinate with the lone electron pairs in

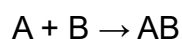
oxygen atoms (O1 and O2) at glucose aldehyde carbons before the isomerisation reaction takes place via a 1,2 intramolecular hydride shift from the C2 to C1 position in the ring-opened glucose chain. In light of these important observations, the type of acid sites found in zeolite catalysts is discussed in more detail in the following section.

1.5.4. Acidity of zeolites.

The most notable feature of zeolite materials is their unique tuneable acidity derived from the substituted heteroatoms. Both Lewis and Brønsted acidity can exist in zeolite structures¹⁷¹. The concept of acidity has been long recognised by various definitions; Arrhenius defined acids as substances that form hydronium ions H_3O^+ upon their dissociation in water¹⁷².



A more general concept has subsequently been established by Brønsted and Lowry, according to whom Brønsted acids act as proton donors and Brønsted bases as proton acceptors.



Where A performs as a proton donor and B as a proton acceptor.

Acidity originates in zeolite as a result of substituting the trivalent atom, commonly Al^{3+} species, for tetravalent Si^{4+} atoms, which generates a net negative charge on the zeolite framework that is compensated by alkaline or alkaline earth metal cation such as Na^+ , K^+ , Ca^{2+} and Mg^{2+} or H^+ . In the case of H^+ addition, Brønsted acidity typically is generated upon adding H^+ and, in sequence, forming hydroxyl groups in the zeolite channels. Therefore, Brønsted solid acid sites (BASs) consist of tetra-coordinated

aluminium sites with bridging OH groups in the framework. In other words, Brønsted acidity arises from the coordination of H₂O to free Al centres, which leads to the release of a proton (Figure 1.11)¹⁷³. As a consequence, Si:Al ratio plays a vital role in the strength of acid sites within the zeolite frameworks¹⁷⁴. As such, the lower the Si/Al ratio, the higher the acidity on the zeolite framework and vice-versa¹⁷⁵.

Lewis acidity is another type of acid sites found in zeolites that are generated due to the less coordinated metal centres within the framework of zeolite structures. As a result, any uncoordinated Al centre (Al-(O)₃) in zeolite frameworks is a Lewis acid site since it induces an electron deficiency, resulting in the capacity to accept electrons from a donor (Figure 1.11). The distribution of these extraframework cationic atoms is primarily determined by the distribution of anionic lattice atoms, which are therefore determined by the sitting of an aluminium framework¹⁷⁶. Thus, Brønsted and Lewis acidity accounts for the origin of the catalytic activity of zeolite catalysts.

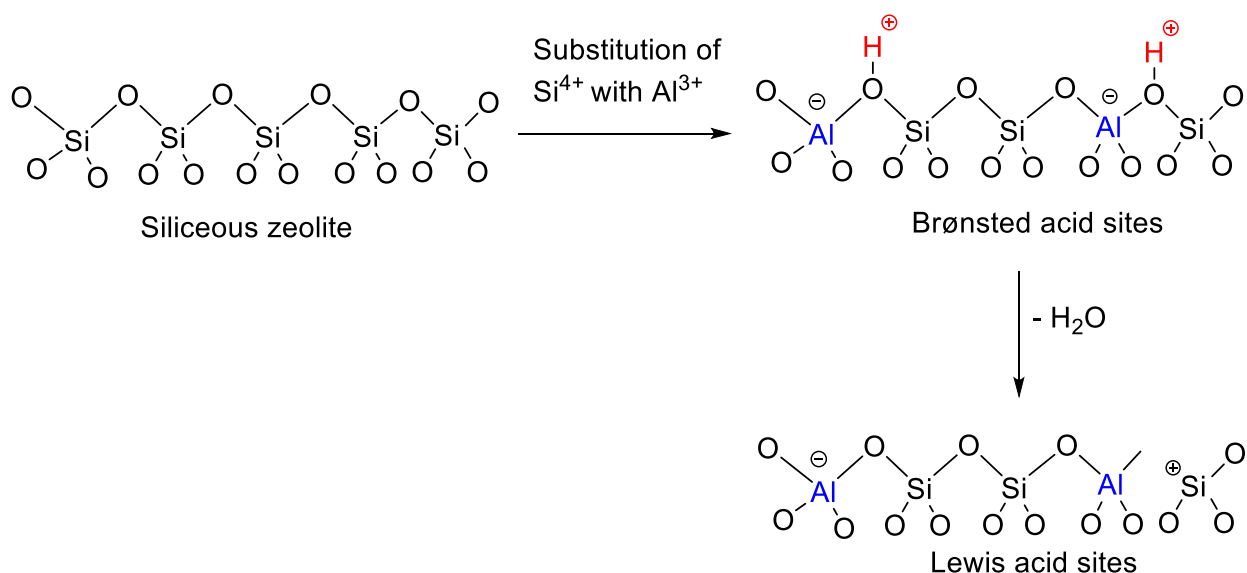


Figure 1.11. Schematic illustration for structures of Brønsted and Lewis acid sites. The Brønsted acid sites are defined as proton donors and associated with the presence of framework Al substitution in the zeolite structure; on the other hand, Lewis acidic sites are defined as electron-pair acceptors and formed due to metal lattice defects with the zeolite framework¹⁷⁷.

As Lewis and Brønsted acidity has shown promising levels of reactivity and stability for a wide range of biomass valorisation reactions, it is imperative to consider the role of these acid sites in the relevant reactions of glucose isomerisation and subsequent fructose dehydration. For instance, in the study of Lew et al., it was demonstrated that Sn-incorporated H-BEA catalysts combined with Amberlyst-131 could successfully be used to produce methyl furfural from glucose under various experimental parameters¹⁷⁸. The results revealed that Sn particles, together with the structure-acidity properties of H-BEA, play a significant role in promoting the isomerisation reaction. The glucose reaction with Amberlyst-131 alone (without Sn-BEA) led to the formation of ethyl glucopyranoside and ethyl glucofuranoside. In contrast, adding Sn/H-BEA material resulted in forming 5-(ethoxymethyl)furfural (EMF) with a yield of 30%. The reaction was typically demonstrated to take place via a two-steps protocol with first the isomerisation of glucose to fructose via the Lewis acid centre of Sn-modified H-BEA zeolite and then the etherification of formed fructose intermediates to the more desirable EFM by the Brønsted acid sites of Amberlyst-131. Similarly, Swift et al. developed a series of H-BEA-modified zeolite catalysts for the catalytic conversion of glucose to 5-HMF¹⁷⁹. The reaction was shown to proceed by a tandem mechanism, wherein the addition of Ti and Sn particles resulted in favourable Lewis/Brønsted acidic ratios capable of producing up to 60% of 5-HMF yields at 130 °C after 5 h in aqueous media. The study has also provided more understanding of the roles of the catalytic active sites during the reaction. A balanced ratio between Lewis and Brønsted acid sites was found to efficiently promote the glucose isomerisation and fructose dehydration reactions. This can be achieved by adjusting the Si/Al molar ratio or post-synthesis calcination treatment of the catalysts¹⁸⁰, though the actual behaviour of the material will be strongly dependent from the substrate in

use and the actual reaction conditions. Aside from the significance of acidic sites, the pores within the zeolite framework (a catalytic property discussed in section 1.5.2) also played an important role in forming 5-HMF. If reaction intermediates can be adsorbed within the pores without causing undesired cracking, the selectivity of the reaction will be energetically shifted towards 5-HMF¹⁸¹. A more recent study by Wang et al. revealed an increase in the furfural yield and a decrease in the 5-hydroxymethylfurfural (5-HMF) yield as a consequence of the decrease in the Brønsted acid site density of HY zeolite. In light of this, it is evident that controlling the catalyst acidity would significantly impact the distribution of products during glucose conversion to platform chemicals such as 5-HMF¹⁸² as explained in sections 1.3 and 1.4.3.

1.6. Common zeolite frameworks in glucose isomerisation.

As mentioned in section (1.4.3), Davis et al. in 2010 reported superior catalytic performance for Sn-beta zeolite, which serves as a solid Lewis acid for the aqueous isomerisation of glucose to fructose via 1,2-intramolecular hydride shift and the aqueous epimerisation of glucose to mannose through 1,2-intramolecular carbon shift (Figure 1.12). Specifically, 10 wt.% of a glucose solution containing Sn-Beta zeolite yielded approximately 46 wt.% glucose, 31 wt.% fructose, and 9 wt.% mannose after a reaction time of 30 min and 12 min at 383 K and 413 K, respectively using an M:S molar ratio of 1:50¹⁸³.

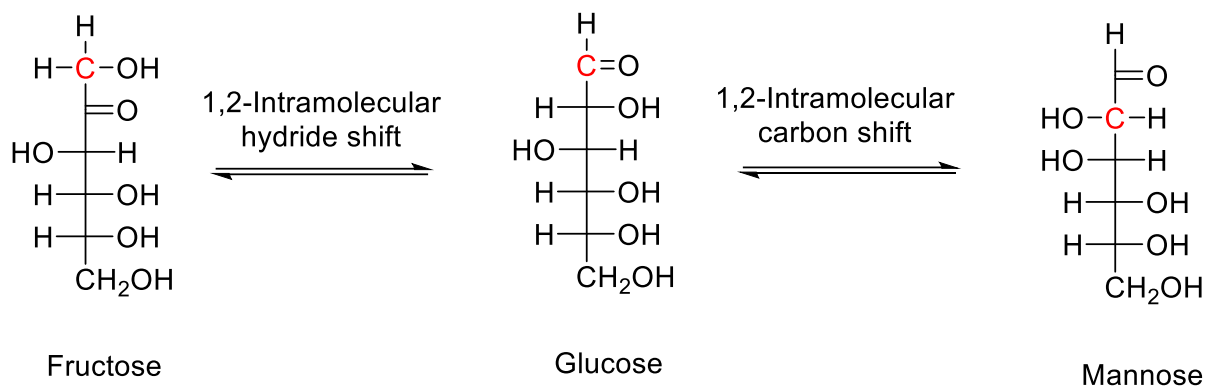


Figure 1.12. The schematic diagram for the glucose to fructose isomerisation reaction via 1,2-intramolecular hydride shift and the glucose to mannose epimerisation reaction via 1,2-intramolecular carbon shift¹⁷⁰.

According to Corma et al., this catalyst contains two types of Sn active sites (Figure 1.13), namely "open" and "closed", which correspond to partially hydrolysed Sn sites ((HO-Sn-OSi)₃) and non-hydrolysed, fully coordinated Sn sites (Sn-(OSi)₄)¹⁸⁴. Bermejo-Deval et al. investigated the role of these active sites theoretically using a small (T₄) cluster model of the active site with four tetrahedral atoms, which are assumed to be fully solvated by water. As a result, the closed sites had a reaction barrier 32 KJ/mol higher than the open sites, indicating that the open sites are more reactive sites and responsible for the catalytic isomerisation reaction of glucose to fructose¹⁷⁰. These open sites have also been demonstrated to be active in the Baeyer-Villiger oxidation of cyclic ketones and the Meerwein Ponndorf Verley reaction in previous studies¹⁸⁵.

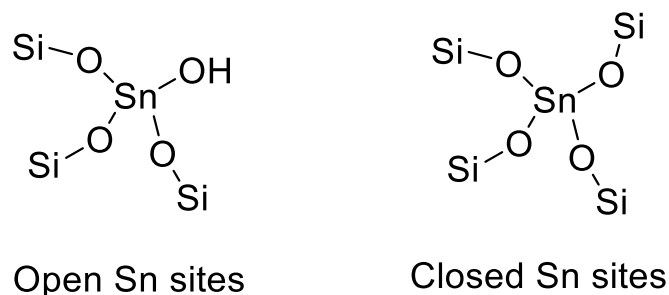


Figure 1.13. Structure of the open Sn site (partially hydrolysed) and the closed Sn active site (non-hydrolysed) in the zeolite frameworks. The open site contains silanol group Si-OH and (OSi)₃ groups connected to hydrolysed Sn-OH via oxygen molecules. Conversely, the closed site consists of an Sn site fully coordinated with (OSi)₄ groups¹⁸⁵.

Furthermore, isotope labelling experiments have been conducted to probe the reaction mechanism of glucose isomerisation using Sn-beta zeolite catalyst. It has been demonstrated that the reaction occurs via three main steps, including glucopyranose ring opening, which is mediated by the Sn active sites, the oxygen atom of the hydroxyl group is then coordinated to the C1 position of the glucose molecule, and the isomerisation is achieved via a 1,2-intramolecular hydride shift from C2 to C1 to form fructose. In this reaction mechanism, the hydride shift is considered the rate-determining step, which is responsible for converting the alpha-hydroxy aldehyde of the acyclic glucose chain into the alpha-hydroxy ketone of the acyclic fructose. The mechanism is then completed by the closure of the fructose ring.

Detailed characterisations of the Sn-zeolite also reveal that this hydride shift step is facilitated by the synergistic effect of Lewis acid Sn active sites and an adjacent proton donor. The latter can be either an internal silanol defect or a water molecule adsorbed on Sn sites¹⁸⁶. There is a difference in the nature of the reaction pathway between the base-catalysed reaction (Figure 1.14A). and the isomerisation reaction catalysed by Sn-beta zeolite (Figure 1.14B).

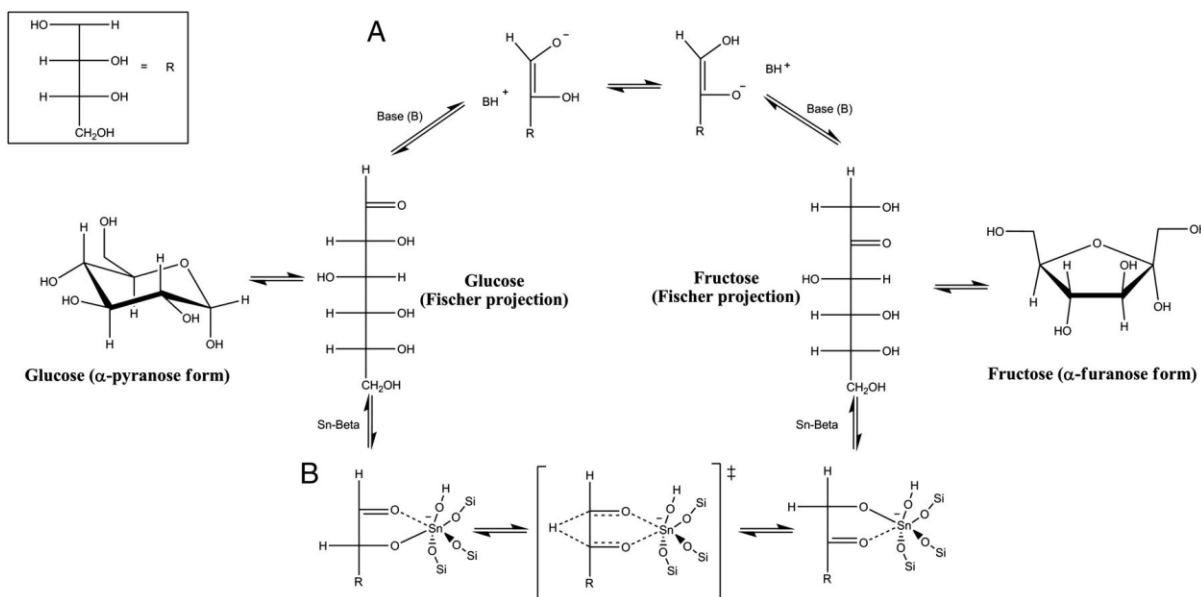


Figure 1.14. Glucose isomerisation mechanisms by **A)** base catalyst, which performs the aldose/ketose transformation via a 1,2-enediol intermediate, whereby the bonding electron pair at C2 moves through the carbon skeleton to C1 and **B)** Sn-Beta zeolite catalyst, which involves the formal transfer of a hydrogen atom from the C-2 to C-1 positions of the α -hydroxy aldehyde to form the corresponding α -hydroxy ketone via 1,2-intramolecular hydride shift mechanism. The figure is reproduced from Manuel Moliner et al.¹⁸³, with permission.

In addition, Davis et al. showed that extra-framework clusters referred to as (SnO_x) and located within the beta zeolite structure are capable of converting glucose to fructose in aqueous media. However, these species become inactive on external surfaces of crystallites and amorphous supports upon their contact with bulk water. Furthermore, extra-framework clusters have also been shown to serve as solid bases to catalyse the isomerisation reaction via Lobry de Bruyl-Alberda van Ekenstien rearrangements. As shown in (Figure 1.14A), the reaction mechanism involves a proton transfer step with an enolate intermediate formed by deprotonating the α -carbonyl in water¹⁷⁰.

As a result of the extensive research in the literature concerning the promising Sn-beta zeolite catalyst for the isomerisation of glucose to fructose during the past years, Lewis-acid-containing zeolites have attracted significant attention in order to design a

low-cost, highly active, highly selective, thermally stable, and reusable catalyst for the catalytic conversion of glucose to fructose. In this context, numerous zeolite-based catalysts have been synthesised and investigated for the glucose isomerisation reaction (Table 1.5). This inclination is due to their unique characteristics, including high thermal and mechanical stability, high surface area, adjustable pore sizes and shapes, and tuneable surface acidity. For instance, the use of zeolites Y and Beta in their acidic form (H^+) has been proposed for the isomerisation reaction of glucose to fructose by Saravanamurugan et al., who suggested a two-step reaction protocol using methanol and water as reaction solvents. The first step forms a methyl fructoside in methanol through the acid-mediated attack of this solvent to fructose, and the second step involves sequential hydrolysis of methyl fructoside intermediates by the step of water addition to form desirable fructose (Figure 1.15). A fructose yield of 55% was obtained over Ultra-stable Y zeolite in its protonated form, donated here as H-USY using this reaction protocol at 120 °C for a total reaction time of 2 h¹⁸⁷.

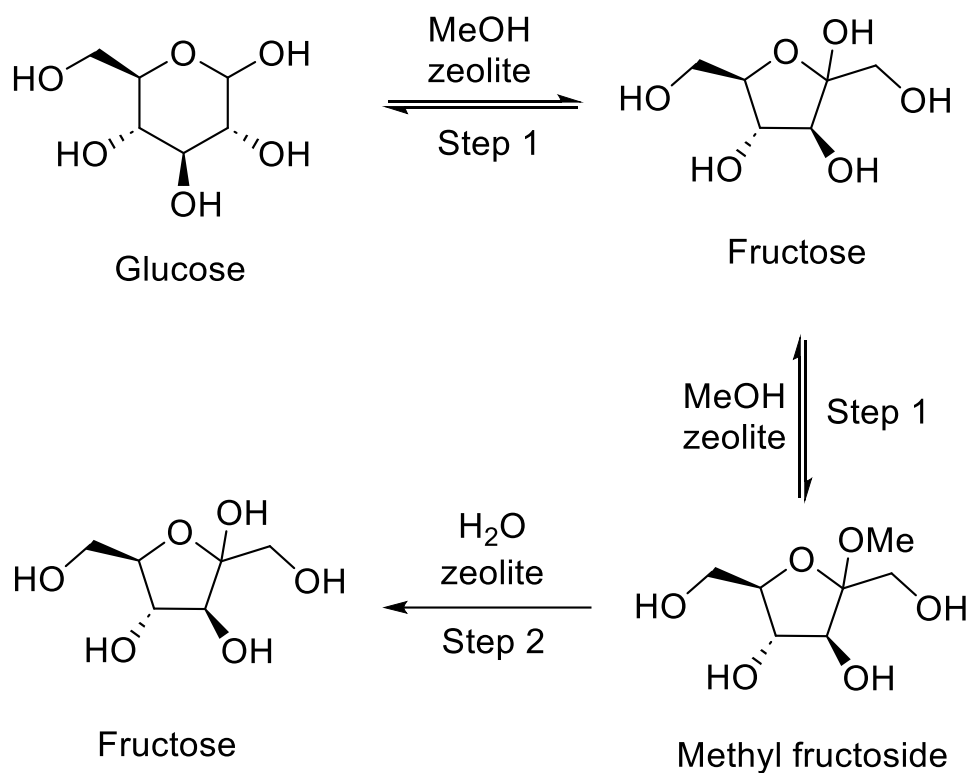


Figure 1.15. Reaction pathway of the catalytic isomerisation of glucose to fructose over acidic zeolites in alcohol and water media through the hydrolysis of an alkyl fructoside intermediate¹⁸⁷.

There have been additional studies on zeolite catalysts for catalysing the conversion of glucose to fructose under different reaction conditions. The catalytic activity of various zeolite-based catalysts reported in the literature along with the studied reaction parameters are provided in Table 1.5.

Table 1.5. Catalytic activity of various studied zeolite-based catalysts for the isomerisation reaction of glucose to fructose using different reaction conditions and media.

Catalyst (Metal loading)	SiO ₂ /Al ₂ O ₃ molar ratio	M:S molar ratio	T/ °C	Time/h	Solvent	Glucose conversion %	Fructose yield (%)	Ref
No catalyst	–	–	140	1.5	H ₂ O	5	1	183
Ti-BEA	25	1:50	140	1.5	H ₂ O	50	23	
Ti-MCM-41	pure SiO ₂	1:50	140	1.5	H ₂ O	23	7	
Sn-BEA	25	1:50	140	1.5	H ₂ O	80	24	
Sn-MCM-41	pure SiO ₂	1:50	140	1.5	H ₂ O	30	12	
Sn-BEA	25	1:50	110	0.5	H ₂ O	55	32	
Si-MCM-41	pure SiO ₂	1:5	100	2	H ₂ O	21	17	125
Si-MCM-48	pure SiO ₂	1:5	100	2	H ₂ O	3	2	
Si-MCM-50	pure SiO ₂	1:5	100	2	H ₂ O	16	14	
Ti-BEA	25	1:50	100	2	H ₂ O	8	11	188
Ti-BEA	25	1:50	100	2	CH ₃ OH	36	8	
NaA	2	1:5	95	1	H ₂ O	26	19	189

CsA	2	1:5	95	1	H ₂ O	34	22	
NaX	2.6	1:5	95	1	H ₂ O	20	17	
CsX	2.6	1:5	95	1	H ₂ O	25	19	
NaY	5.1	1:5	95	1	H ₂ O	9	6	
CsY	5.1	1:5	95	1	H ₂ O	10	6	
Sn-deAl-BEA (1wt.%)	25	1:5	110	2	H ₂ O	59	32	190
Mg-NaY (5 wt.%)	5.1	1:14	100	2	H ₂ O	28	23	113
Mg-NaY (10 wt.%)	5.1	1:7	100	2	H ₂ O	45	32	
Mg-NaY (15 wt.%)	5.1	1:5	100	2	H ₂ O	49	32	
Fe-BEA (0.06 wt.%)	25	1:10	150	1.5	H ₂ O	55	22	191
*Sn-ZSM-5 (4 wt.%)	30	1:30	110	2	C ₂ H ₅ OH + H ₂ O	55	44	192
HY	5.1	1:100	120	1	CH ₃ OH	44	16	187
*HY	5.1	1:100	120	2	CH ₃ OH + H ₂ O	46	20	
H-USY	12	1:100	120	1	CH ₃ OH	70	22	
*H-USY	12	1:100	120	2	CH ₃ OH + H ₂ O	72	55	
H-USY	60	1:100	120	1	CH ₃ OH	37	26	

*H-USY	60	1:100	120	2	CH ₃ OH + H ₂ O	37	24	32
H-BEA	25	1:100	120	1	CH ₃ OH	71	23	
*H-BEA	25	1:100	120	2	CH ₃ OH + H ₂ O	70	40	
H-BEA	38	1:100	120	1	CH ₃ OH	61	21	
H-BEA	38	1:100	120	2	CH ₃ OH + H ₂ O	57	29	
No catalyst	–	–	140	3	H ₂ O	5	0	
HY	30	1:50	140	3	H ₂ O	10	trace	
Sn-deAl-HY (2.9 wt.%)	30	1:70	140	3	H ₂ O	35	13	
Ga-deAl-HY (2.3 wt.%)	30	1:50	140	3	H ₂ O	17	5	

*Reactions were carried out via a two-step protocol as follows, step 1: in alcohol for one hour and Step 2: in water for an additional one hour at the specified reaction temperature.

Apart from the importance of catalyst selection, understanding the properties of our sugars is also a vital perspective. For instance, the solubility of glucose, fructose and mannose is another significant factor that should be verified since it can play a significant role in many aspects of a chemical reaction, including catalyst productivity ($\text{mol product kg catalyst}^{-1} \text{ h}^{-1}$) and data reproducibility and comparability among different laboratories and the development of catalysts by design. Therefore, implications of the solubility of the substrates towards catalyst productivity and catalytic performance will be studied in order to provide a robust platform for the reliability of catalytic tests that will be carried out afterwards. Furthermore, the isomerisation reaction can also be significantly influenced by other factors such as the solvent nature, reaction temperature and time. Such variables will also be systematically investigated in this thesis work.

1.7. Project aims.

In light of this background and context the objective of this research project is to:

1. Develop an efficient method, based on chromatography for the determination of glucose, fructose, and mannose solubility in different pure solvents in order to clarify the large discrepancies in solubility data reported in the literature and provide a reliable basis for the evaluation of catalytic tests will be performed in this thesis work.
2. Design and synthesise metal-doped zeolite catalysts for the isomerisation of glucose to fructose under mild conditions. Methods such as wet impregnation and sol-gel will be applied for catalyst preparation, and the effect of solvent nature, reaction temperature and time on the catalytic performance will be

discussed with the aim to achieve higher catalytic activity than currently reported in the literature.

3. Investigate the roles of Lewis and Brønsted acid sites in our catalysts, and identify, if possible, all reaction intermediates and associated reaction pathways in the catalytic conversion of glucose to fructose. Through the use of multiple zeolites with different pore sizes and non-porous materials such as SiO₂ and Al₂O₃, the relevance of pores for glucose isomerisation will also be evaluated.
4. Assess the structure and properties of the catalysts synthesized in this project using various methods and techniques, including back titration and NH₃ chemisorption for Lewis and Brønsted acidity, XRD for crystal structure, XPS for the oxidation chemical state of doped metal ions, HAADF-STEM for direct insights on the pore structure and metal distribution, BET for textural properties of these materials EXAFS for the coordination environment of metal atoms. Monitoring these materials' properties during the synthesis process is intended to produce a material with the most desirable characteristics and acquire data to identify structure-activity correlations.
5. Identify and evaluate the catalytic performance of various heterogeneous catalysts such as metal-doped zeolite, pure metal oxides, and metal oxide-doped zeolite with a view to developing highly efficient catalysts for the dehydration of glucose and fructose to 5-HFM in water under mild reaction conditions.

1.8. References

- 1 B. B. Hallac and A. J. Ragauskas, *Biofuel Bioprod Biorefin*, 2011, **5**, 215–225.
- 2 E. M. Rubin, *Nature*, 2008, **454**, 841–845.
- 3 G. Stephanopoulos, *Science (1979)*, 2007, **315**, 801–804.
- 4 A. J. Ragauskas, C. K. Williams, B. H. Davison, G. Britovsek, J. Cairney, C. A. Eckert, W. J. Frederick, J. P. Hallett, D. J. Leak, C. L. Liotta, J. R. Mielenz, R. Murphy, R. Templer and T. Tschaplinski, *AAAS*, 2006, **311**, 484–489.
- 5 K. Vohra, A. Vodonos, J. Schwartz, E. A. Marais, M. P. Sulprizio and L. J. Mickley, *Environ. Res.*, 2021, **195**, 110754.
- 6 J. Wang, J. Xi, Q. Xia, X. Liu and Y. Wang, *Sci. China Chem.*, 2017, **60**, 870–886.
- 7 N. L. Panwar, S. C. Kaushik and S. Kothari, *Renew. Sustain. Energy Rev.*, 2011, **15**, 1513–1524.
- 8 R. M. O’dea, J. A. Willie and T. H. Epps, *ACS Macro Lett.*, 2020, **9**, 476–493.
- 9 J. Arnling Bååth, A. Martínez-Abad, J. Berglund, J. Larsbrink, F. Vilaplana and L. Olsson, *Biotechnol. Biofuels*, 2018, **11**, 114.
- 10 P. Ning, G. Yang, L. Hu, J. Sun, L. Shi, Y. Zhou, Z. Wang and J. Yang, *Biotechnol. Biofuels*, 2021, **14**, 102.
- 11 C. Wang, S. S. Kelley and R. A. Venditti, *ChemSusChem*, 2016, **9**, 770–783.
- 12 X. Yu, Z. Wei, Z. Lu, H. Pei and H. Wang, *Bioresour. Technol.*, 2019, **291**, 121885.
- 13 K. Kohli, R. Prajapati and B. K. Sharma, *Energies (Basel)*, 2019, **12**, 233.

- 14 H. C. Ong, W. H. Chen, A. Farooq, Y. Y. Gan, K. T. Lee and V. Ashokkumar, *Renew. Sustain. Energy Rev.*, 2019, **113**, 109266.
- 15 W. Won and C. T. Maravelias, *Renew. Energ.*, 2017, **114**, 357–366.
- 16 C. M. Liu and S. Y. Wu, *Renew. Energ.*, 2016, **96**, 1056–1062.
- 17 M. Sajid, X. Zhao and D. Liu, *Green Chem.*, 2018, **20**, 5427–5453.
- 18 J. Shi, Y. Wang, X. Yu, W. Du and Z. Hou, *Fuel*, 2016, **163**, 74–79.
- 19 S. S. Chen, T. Maneerung, D. C. W. Tsang, Y. S. Ok and C. H. Wang, *Chem. Eng. J.*, 2017, **328**, 246–273.
- 20 Q. Hou, X. Qi, M. Zhen, H. Qian, Y. Nie, C. Bai, S. Zhang, X. Bai and M. Ju, *Green Chem.*, 2021, **23**, 119–231.
- 21 S. G. Wettstein, D. Martin Alonso, E. I. Gürbüz and J. A. Dumesic, *Curr. Opin. Chem. Eng.*, 2012, **1**, 218–224.
- 22 S. P. Teong, G. Yi and Y. Zhang, *Green Chem.*, 2014, **16**, 2015–2026.
- 23 S. Takkellapati, T. Li and M. A. Gonzalez, *Clean Technol. Environ. Policy.*, 2018, **20**, 1615–1630.
- 24 J. J. Bozell and G. R. Petersen, *Green Chem.*, 2010, **12**, 539–55.
- 25 P. Yang, Q. Xia, X. Liu and Y. Wang, *Fuel*, 2017, **187**, 159–166.
- 26 Z. Tang and J. Su, *Bioresources*, 2019, **14**, 5943–5963.
- 27 F. Menegazzo, E. Ghedini and M. Signoretto, *Molecules*, 2018, **23**, 2201.
- 28 T. Wang, M. W. Nolte and B. H. Shanks, *Green Chem.*, 2014, **16**, 548–572.

- 29 F. J. Morales, in *Process-induced food toxicants: occurrence, formation, mitigation and health risks*, eds. R. H. Stadler and D. R. Lineback, John Wiley & Sons, Inc., Hoboken, NJ, USA, 2008, pp. 135–174.
- 30 A. Jakob, M. Grilc, J. Teržan and B. Likozar, *Processes*, 2021, **9**, 924.
- 31 C. Thoma, J. Konnerth, W. Sailer-Kronlachner, P. Solt, T. Rosenau and H. W. G. van Herwijnen, *ChemSusChem*, 2020, **13**, 3544–3564.
- 32 R. Oozeerally, J. Pillier, E. Kilic, P. B. J. Thompson, M. Walker, B. E. Griffith, J. V. Hanna and V. Degirmenci, *Appl. Catal. A: Gen.*, 2020, **605**, 117798.
- 33 A. Takagaki, M. Ohara, S. Nishimura and K. Ebitani, *ChemComm.*, 2009, 6276–6278.
- 34 N. Candu, M. El Fergani, M. Verziu, B. Cojocaru, B. Jurca, N. Apostol, C. Teodorescu, V. I. Parvulescu and S. M. Coman, *Catal. Today*, 2019, **325**, 109–116.
- 35 O. V. Kislitsa, O. V. Manaenkov, E. A. Ratkevich, M. G. Sulman and Y. Y. Kosivtsov, *Chem. Eng. Trans.*, 2021, **88**, 295–300.
- 36 C. Yue, G. Li, E. A. Pidko, J. J. Wiesfeld, M. Rigutto and E. J. M. Hensen, *ChemSusChem*, 2016, **9**, 2421–2429.
- 37 K. Nakajima, Y. Baba, R. Noma, M. Kitano, J. N. Kondo, S. Hayashi and M. Hara, *J. Am. Chem. Soc.*, 2011, **133**, 4224–4227.
- 38 C. S. Lanziano, F. Rodriguez, S. C. Rabelo, R. Guirardello, V. T. Da Silva and C. B. Rodell, *Chem. Eng. Trans.*, 2014, **37**, 589–594.

- 39 C. Wang, Q. Zhang, T. You, B. Wang, H. Dai and F. Xu, *Bioresources*, 2018, **13**, 7873–7885.
- 40 D. L. Burnett, R. Oozeerally, R. Pertiwi, T. W. Chamberlain, N. Cherkasov, G. J. Clarkson, Y. K. Krisnandi, V. Degirmenci and R. I. Walton, *ChemComm.*, 2019, **55**, 11446–11449.
- 41 J. P. V. Lima, P. T. A. Campos, M. F. Paiva, J. J. Linares, S. C. L. Dias and J. A. Dias, *Chem*, 2021, **3**, 1189–1202.
- 42 B. F. M. Kuster, *Carbohydr. Res.*, 1977, **54**, 177–183.
- 43 Y. Li, X. Lu, L. Yuan and X. Liu, *Biomass Bioenergy*, 2009, **33**, 1182–1187.
- 44 R. J. Van Putten, J. C. Van Der Waal, E. De Jong, C. B. Rasrendra, H. J. Heeres and J. G. De Vries, *Chem. Rev.*, 2013, **113**, 1499–1597.
- 45 L. Wang, H. Guo, Q. Xie, J. Wang, B. Hou, L. Jia, J. Cui and D. Li, *Appl. Catal. A: Gen.*, 2019, **572**, 51–60.
- 46 E. I. García-López, F. R. Pomilla, B. Megna, M. L. Testa, L. F. Liotta and G. Marci, *Nanomater.*, 2021, **11**, 1821.
- 47 A. Modak, A. R. Mankar, K. K. Pant and A. Bhaumik, *Molecules*, 2021, **26**, 2519.
- 48 M. L. Testa, G. Miroddi, M. Russo, V. La Parola and G. Marci, *Mater.*, 2020, **13**, 1178.
- 49 F. Yang, Q. Liu, X. Bai and Y. Du, *Bioresour. Technol.*, 2011, **102**, 3424–3429.
- 50 A. Gandini, *Macromolecules*, 2008, **41**, 9491–9504.
- 51 Y. Román-Leshkov, C. J. Barrett, Z. Y. Liu and J. A. Dumesic, *Nature*, 2007, **447**, 982–985.

- 52 S. Iqbal, X. Liu, O. F. Aldosari, P. J. Miedziak, J. K. Edwards, G. L. Brett, A. Akram, G. M. King, T. E. Davies, D. J. Morgan, D. K. Knight and G. J. Hutchings, *Catal. Sci. Technol.*, 2014, **4**, 2280–2286.
- 53 M. Chatterjee, T. Ishizaka and H. Kawanami, *Green Chem.*, 2014, **16**, 4734–4739.
- 54 J. Mitra, X. Zhou and T. Rauchfuss, *Green Chem.*, 2015, **17**, 307–313.
- 55 J. Jae, W. Zheng, A. M. Karim, W. Guo, R. F. Lobo and D. G. Vlachos, *ChemCatChem*, 2014, **6**, 848–856.
- 56 N. A. Endot, R. Junid and M. S. S. Jamil, *Molecules*, 2021, **26**, 6848.
- 57 T. Thananattthanachon and T. B. Rauchfuss, *Angew. Chem.*, 2010, **122**, 6766–6768.
- 58 W. Wei, H. Yang and S. Wu, *Fuel*, 2019, **256**, 115940.
- 59 J. Horvat, B. Klaid, B. Metelko and V. Sunjid', *Tetrahedron Lett.*, 1985, **26**, 2111–2114.
- 60 D. Di Menno Di Bucchianico, Y. Wang, J. C. Buvat, Y. Pan, V. Casson Moreno and S. Leveneur, *Green Chem.*, 2022, **24**, 614–646.
- 61 K. Yan, C. Jarvis, J. Gu and Y. Yan, *Renew. Sustain. Energy Rev.*, 2015, **51**, 986–997.
- 62 L. Yan, Q. Yao and Y. Fu, *Green Chem.*, 2017, **19**, 5527–5547.
- 63 C. Moreno-Marrodan, F. Liguori and P. Barbaro, *Mol. Catal.*, 2019, **466**, 60–69.
- 64 S. Dutta, I. K. M. Yu, D. C. W. Tsang, Y. H. Ng, Y. S. Ok, J. Sherwood and J. H. Clark, *J. Chem. Eng.*, 2019, **372**, 992–1006.

- 65 G. Pasquale, P. Vázquez, G. Romanelli and G. Baronetti, *Catal. Commun.*, 2012, **18**, 115–120.
- 66 S. Dutta and N. S. Bhat, *ChemCatChem*, 2021, **13**, 3202–3222.
- 67 Y. Shao, K. Sun, L. Zhang, Q. Xu, Z. Zhang, Q. Li, S. Zhang, Y. Wang, Q. Liu and X. Hu, *Green Chem.*, 2019, **21**, 6634–6645.
- 68 D. J. Hayes, J. Ross, H. B. Hayes and S. Fitzpatrick, in *Biorefineries-Industrial Processes and Products*, eds. B. Kamm, P. R. Gruber and M. Kamm, Wiley-VCH Verlag GmbH, Weinheim, Germany, 2005, pp. 139–164.
- 69 B. Chamnankid, C. Ratanatawanate and K. Faungnawakij, *Chem. Eng. J.*, 2014, **258**, 341–347.
- 70 X. Hu, C. Lievens, A. Larcher and C. Z. Li, *Bioresour. Technol.*, 2011, **102**, 10104–10113.
- 71 M. A. Mellmer, J. M. R. Gallo, D. Martin Alonso and J. A. Dumesic, *ACS Catal.*, 2015, **5**, 3354–3359.
- 72 A. Onda, T. Ochi and K. Yanagisawa, *Green Chem.*, 2008, **10**, 1033–1037.
- 73 S. G. Aspromonte, A. Romero, A. v. Boix and E. Alonso, *Cellulose*, 2019, **26**, 2471–2485.
- 74 J. P. Lange, *Nat. Catal.*, 2021, **4**, 186–192.
- 75 A. A. Marianou, C. M. Michailof, A. Pineda, E. F. Iliopoulou, K. S. Triantafyllidis and A. A. Lappas, *Appl. Catal. A: Gen.*, 2018, **555**, 75–87.
- 76 J. R. Christianson, S. Caratzoulas and D. G. Vlachos, *ACS Catal.*, 2015, **5**, 5256–5263.

- 77 J. Faria, M. Pilar Ruiz and D. E. Resasco, *ACS Catal.*, 2015, **5**, 4761–4771.
- 78 J. Fu, F. Shen, X. Liu and X. Qi, *Green Energy Environ.*, 2023, **8**, 842–851.
- 79 C. G. Yoo, N. Li, M. Swannell and X. Pan, *Green Chem.*, 2017, **19**, 4402–4411.
- 80 C. E. Crestani, A. T. C. R. Silva, A. Bernardo, C. B. B. Costa and M. Giuliatti, *Chem Eng Commun.*, 2022, **209**, 869–881.
- 81 J. C. Speck, in *Adv Carbohydr Chem.*, ed. M. L. Wolfrom, Academic Press, 1958, vol. 13, pp. 63–103.
- 82 G. Li, E. A. Pidko and E. J. M. Hensen, *ACS Catal.*, 2016, **6**, 4162–4169.
- 83 V. J. Jensen and S. Rugh, in *Meth. Enzymol.*, Academic Press, 1987, vol. 136, pp. 356–370.
- 84 X. Han, Z. Feng, Y. Chen, L. Zhu, X. Li, X. Wang, H. Sun and J. Li, *Front. nutr.*, 2022, **9**, 829396.
- 85 S. Sharma, M.-L. Tsai, V. Sharma, P.-P. Sun, P. Nargotra, B. K. Bajaj, C.-W. Chen and C.-D. Dong, *Environments*, 2022, **10**, 6.
- 86 M. Moliner, Y. Román-Leshkov and M. E. Davis, *Proc. Natl. Acad. Sci. U.S.A.*, 2010, **107**, 6164–6168.
- 87 S. Akabori, K. Uehara and I. Muramatsu, *Proc. Jpn. Acad.*, 1952, **28**, 39–43.
- 88 R. M. Hochster and R. W. Watson, *J. Am. Chem. Soc.*, 1953, **75**, 3284–3285.
- 89 R. O. Marshall and E. R. Kooi, *Science (1979)*, 1957, **125**, 648–649.
- 90 K. Yamanaka, *Agric. Biol. Chem.*, 1963, **27**, 265–278.

- 91 S. H. Bhosale, M. B. Rao and V. V. Deshpande, *Microbiol. Rev.*, 1996, **60**, 280–300.
- 92 Y. Román-Leshkov, M. Moliner, J. A. Labinger and M. E. Davis, *Angew. Chem.*, 2010, **122**, 9138–9141.
- 93 S. Lima, A. S. Dias, Z. Lin, P. Brandão, P. Ferreira, M. Pillinger, J. Rocha, V. Calvino-Casilda and A. A. Valente, *Appl. Catal. A: Gen.*, 2008, **339**, 21–27.
- 94 S. Despax, B. Estrine, N. Hoffmann, J. Le Bras, S. Marinkovic and J. Muzart, *Catal. Commun.*, 2013, **39**, 35–38.
- 95 I. Delidovich, *Curr. Opin. Green Sustain. Chem.*, 2021, **27**, 100414.
- 96 J. B. Gottfried and D. G. Benjamin, *Ind. Eng. Chem.*, 1952, **44**, 141–145.
- 97 J. M. de Bruijn, A. P. G. Kieboom and H. van Bekkum, *Recl. Trav. Chim. Pays-Bas*, 1986, **105**, 176–183.
- 98 B. Yun Yang and R. Montgomery, *Carbohydr. Res.*, 1996, **280**, 27–45.
- 99 J. F. Mendicino, *J. Am. Chem. Soc.*, 1960, **82**, 4975–4979.
- 100 A. J. Shaw and G. T. Tsao, *Carbohydr. Res.*, 1978, **60**, 327–325.
- 101 A. J. Shaw and G. T. Tsao, *Carbohydr. Res.*, 1978, **60**, 376–382.
- 102 D. Ekeberg, S. Morgenlie and Y. Stenstrøm, *Carbohydr. Res.*, 2005, **340**, 373–377.
- 103 C. Liu, J. M. Carraher, J. L. Swedberg, C. R. Herndon, C. N. Fleitman and J. P. Tessonier, *ACS Catal.*, 2014, **4**, 4295–4298.
- 104 I. Delidovich and R. Palkovits, *ChemSusChem*, 2016, **9**, 547–561.

- 105 M. M. Özer, Y. Jia, Z. Zhang, J. R. Thompson and H. H. Weitering, *Science* (1979), 2007, **316**, 1594–1597.
- 106 S. Hu, Z. Zhang, J. Song, Y. Zhou and B. Han, *Green Chem.*, 2009, **11**, 1746–1749.
- 107 Y. Yang, C. Hu and M. M. Abu-Omar, *J. Mol. Catal. A Chem.*, 2013, **376**, 98–102.
- 108 K. R. Enslow and A. T. Bell, *Catal. Sci. Technol.*, 2015, **5**, 2839–2847.
- 109 H. Li, W. Xu, T. Huang, S. Jia, Z. Xu, P. Yan, X. Liu and Z. C. Zhang, *ACS Catal.*, 2014, **4**, 4446–4454.
- 110 S. Jia, K. Liu, Z. Xu, P. Yan, W. Xu, X. Liu and Z. C. Zhang, *Catal. Today*, 2014, **234**, 83–90.
- 111 S. H. Mushrif, J. J. Varghese and D. G. Vlachos, *Phys. Chem. Chem. Phys.*, 2014, **16**, 19564–19572.
- 112 J. Tang, X. Guo, L. Zhu and C. Hu, *ACS Catal.*, 2015, **5**, 5097–5103.
- 113 I. Graça, D. Iruretagoyena and D. Chadwick, *Appl. Catal. B: Environ.*, 2017, **206**, 434–443.
- 114 Y. C. Lin and G. W. Huber, *Energy Environ. Sci.*, 2009, **2**, 68–80.
- 115 R. Rinaldi and F. Schüth, *Energy Environ. Sci.*, 2009, **2**, 610–626.
- 116 C. Megías-Sayago, S. Navarro-Jaén, F. Drault and S. Ivanova, *Catalysts*, 2021, **11**, 1395.
- 117 L. Rebenfeld and E. Pacsu, *J. Am. Chem. Soc.*, 1953, **75**, 4370–4371.
- 118 US Patent, 2,746,889, 1956.

- 119 H. Li, S. Yang, S. Saravanamurugan and A. Riisager, *ACS Catal.*, 2017, **7**, 3010–3029.
- 120 M. Watanabe, Y. Aizawa, T. Iida, R. Nishimura and H. Inomata, *Appl. Catal. A: Gen.*, 2005, **295**, 150–156.
- 121 R. Khumho, S. Yousatit and C. Ngamcharussrivichai, *Catalysts*, 2021, **11**, 887.
- 122 K. M. Eblagon, A. Malaika, K. Ptaszynska, M. F. R. Pereira and J. L. Figueiredo, *Nanomater.*, 2020, **10**, 1–24.
- 123 J. Lecomte, A. Finiels and C. Moreau, *Starch/Staerke*, 2002, **54**, 75–79.
- 124 S. Yu, E. Kim, S. Park, I. K. Song and J. C. Jung, *Catal. Commun.*, 2012, **29**, 63–67.
- 125 R. O. L. Souza, D. P. Fabiano, C. Feche, F. Rataboul, D. Cardoso and N. Essayem, *Catal. Today*, 2012, **195**, 114–119.
- 126 S. M. Patel, U. V. Chudasama and P. A. Ganeshpure, in *Green Chem.*, Royal Society of Chemistry, 2001, vol. 3, pp. 143–145.
- 127 Y. Kamiya, S. Sakata, Y. Yoshinaga, R. Ohnishi and T. Okuhara, *Catal. Lett.*, 2004, **94**, 45–47.
- 128 R. Weingarten, Y. T. Kim, G. A. Tompsett, A. Fernández, K. S. Han, E. W. Hagaman, W. C. Conner, J. A. Dumesic and G. W. Huber, *J. Catal.*, 2013, **304**, 123–134.
- 129 G. Akiyama, R. Matsuda, H. Sato and S. Kitagawa, *Chem. Asian J.*, 2014, **9**, 2772–2777.

- 130 Q. X. Luo, Y. B. Zhang, L. Qi and S. L. Scott, *ChemCatChem*, 2019, **11**, 1903–1909.
- 131 Q. Guo, L. Ren, P. Kumar, V. J. Cybulskis, K. A. Mkhoyan, M. E. Davis and M. Tsapatsis, *Angew. Chem.*, 2018, **57**, 4926–4930.
- 132 M. Moliner, Y. Román-Leshkov and M. E. Davis, *Proc. Natl. Acad. Sci. U.S.A.*, 2010, **107**, 6164–6168.
- 133 T. O. Bok, E. P. Andriako, E. E. Knyazeva and I. I. Ivanova, *RSC Adv*, 2020, **10**, 38505–38514.
- 134 A. Corma, L. T. Nemeth, M. Renz and S. Valencia, *Nature*, 2001, **412**, 423–425.
- 135 A. Corma, M. E. Domine, L. Nemeth and S. Valencia, *J. Am. Chem. Soc.*, 2002, **124**, 3194–3195.
- 136 A. F. Masters and T. Maschmeyer, *Microporous Mesoporous Mater.*, 2011, **142**, 423–438.
- 137 N. E. R. Zimmermann and M. Haranczyk, *Cryst. Growth Des.*, 2016, **16**, 3043–3048.
- 138 E. T. C. Vogt, G. T. Whiting, A. Dutta Chowdhury and B. M. Weckhuysen, in *Adv. Catal.*, Academic Press Inc., 2015, vol. 58, pp. 143–314.
- 139 U.S. Geological Survey, *Mineral commodity summaries 2022*, Reston, VA, 2022.
- 140 C. S. Cundy and P. A. Cox, *Chem. Rev.*, 2003, **103**, 663–701.
- 141 R. W. Broach, D.-Y. Jan, D. A. Lesch, S. Kulprathipanja, E. Roland and P. Kleinschmit, in *Ullmann's Encyclopedia of Industrial Chemistry*, Wiley-VCH Verlag GmbH & Co. KGaA, Weinheim, Germany, 2012.

- 142 E. N. Coker and L. V. C. Rees, *Microporous Mesoporous Mater.*, 2005, **84**, 171–178.
- 143 M. W. Munthali, E. Johan, H. Aono and N. Matsue, *J. Asian Ceram. Soc.*, 2015, **3**, 245–250.
- 144 B. M. Weckhuysen and J. Yu, *Chem. Soc. Rev.*, 2015, **44**, 7022–7024.
- 145 E. T. C. Vogt and B. M. Weckhuysen, *Chem. Soc. Rev.*, 2015, **44**, 7342–7370.
- 146 T. Ennaert, J. Van Aelst, J. Dijkmans, R. De Clercq, W. Schutyser, M. Dusselier, D. Verboekend and B. F. Sels, *Chem. Soc. Rev.*, 2016, **45**, 584–611.
- 147 Q. Zhang, J. Yu and A. Corma, *Adv. Mater.*, 2020, **32**, 2002927.
- 148 F. Hussin and M. K. Aroua, *J. Clean. Prod.*, 2020, **253**, 119707.
- 149 Database of Zeolite Structures, <http://www.iza-structure.org/databases/>, (accessed 12 January 2023).
- 150 J. A. Boscoboinik, X. Yu, B. Yang, S. Shaikhutdinov and H. J. Freund, *Microporous Mesoporous Mater.*, 2013, **165**, 158–162.
- 151 W. Mozgawa and M. Król, *Chemik*, 2011, **65**, 667–674.
- 152 R. J. Davis, in *J. Catal.*, Academic Press Inc., 2003, vol. 216, pp. 396–405.
- 153 C. M. Osmundsen, M. Spangsberg Holm, S. Dahl and E. Taarning, in *Proc. Natl. Acad. Sci. U.S.A.*, Royal Society, 2012, vol. 468, pp. 2000–2016.
- 154 S. Ernst, *Angew. Chem.*, 2011, **50**, 5425–5426.
- 155 D. E. De Vos and P. A. Jacobs, in *Microporous Mesoporous Mater.*, 2005, vol. 82, pp. 293–304.

- 156 W. Huang, D. Li, X. Kang, Y. Shi and H. Nie, *Stud. Surf. Sci. Catal.*, 2004, **154**, 2353–2358.
- 157 G. Li, E. A. Pidko and E. J. M. Hensen, *Catal. Sci. Technol.*, 2014, **4**, 2241–2250.
- 158 N. Chaihad, S. Karnjanakom, A. Abudula and G. Guan, *Rapid Commun. Mass Spectrom.*, 2022, **1**, 167–183.
- 159 J. Weitkamp, S. Ernst and L. Puppe, in *Catalysis and Zeolites Fundamentals and Applications*, eds. J. Weitkamp and L. Puppe, Springer Berlin Heidelberg, Berlin, Heidelberg, First Edition., 1999, pp. 327–376.
- 160 A. Corma, *J. Catal.*, 2003, **216**, 298–312.
- 161 J. Hagen, *Industrial Catalysis: A Practical Approach*, Wiley-VCH Verlag GmbH & Co. KGaA, Weinheim, Germany, Third Edition., 2015.
- 162 S. M. Csicsery, *Zeolites*, 1984, **4**, 202–213.
- 163 T. Pang, X. Yang, C. Yuan, A. A. Elzatahry, A. Alghamdi, X. He, X. Cheng and Y. Deng, *Chin. Chem. Lett.*, 2021, **32**, 328–338.
- 164 M. J. Climent, A. Corma and S. Iborra, in *Zeolites and Catalysis*, eds. J. Čejka, A. Corma and S. Zones, Wiley-VCH Verlag GmbH & Co. KGaA, Weinheim, Germany, 2010, pp. 775–826.
- 165 V. Valtchev, G. Majano, S. Mintova and J. Pérez-Ramírez, *Chem. Soc. Rev.*, 2013, **42**, 263–290.
- 166 T. Tatsumi, in *Zeolites and Catalysis*, eds. J. Čejka, A. Corma and S. Zones, Wiley-VCH Verlag GmbH & Co. KGaA, Weinheim, Germany, 2010, pp. 713–743.

- 167 J.-L. Guth and H. Kessler, in *Catalysis and Zeolites*, eds. J. Weitkamp and L. Puppe, Springer Berlin Heidelberg, Berlin, Heidelberg, 1999, pp. 1–52.
- 168 G. H. Kühn, in *Catalysis and Zeolites*, eds. J. Weitkamp and L. Puppe, Springer Berlin Heidelberg, Berlin, Heidelberg, 1999, pp. 81–197.
- 169 Y. Pan, X. Shen, L. Yao, A. Bentalib and Z. Peng, *Catalysts*, 2018, **8**, 478.
- 170 R. Bermejo-Deval, M. Orazov, R. Gounder, S. J. Hwang and M. E. Davis, *ACS Catal.*, 2014, **4**, 2288–2297.
- 171 A. Zecchina, C. Lamberti and S. Bordiga, *Catal. Today*, 1998, **41**, 169–177.
- 172 A. Palčić and V. Valtchev, *Appl. Catal. A: Gen.*, 2020, **606**, 117795.
- 173 Z. Wang, Y. Jiang, O. Lafon, J. Trébosc, K. Duk Kim, C. Stampfl, A. Baiker, J. P. Amoureux and J. Huang, *Nat. Commun.*, 2016, **7**, 13820.
- 174 H. G. Karge, M. Hunger and H. K. Beyer, in *Catalysis and Zeolites*, Springer Berlin Heidelberg, Berlin, Heidelberg, 1999, pp. 198–326.
- 175 M. Moshoeshoe, M. Silas Nadiye-Tabbiruka and V. Obuseng, *Am. J. Mater. Sci.*, 2017, **2017**, 196–221.
- 176 E. A. Pidko, E. J. M. Hensen, G. M. Zhidomirov and R. A. van Santen, *J. Catal.*, 2008, **255**, 139–143.
- 177 E. Schulman, W. Wu and D. Liu, *Mater.*, 2020, **13**, 1822.
- 178 C. M. Lew, N. Rajabbeigi and M. Tsapatsis, *Ind. Eng. Chem. Res.*, 2012, **51**, 5364–5366.
- 179 T. D. Swift, H. Nguyen, Z. Erdman, J. S. Kruger, V. Nikolakis and D. G. Vlachos, *J. Catal.*, 2016, **333**, 149–161.

- 180 R. Otomo, T. Yokoi, J. N. Kondo and T. Tatsumi, *Appl. Catal. A: Gen.*, 2014, **470**, 318–326.
- 181 J. S. Kruger, V. Choudhary, V. Nikolakis and D. G. Vlachos, *ACS Catal.*, 2013, **3**, 1279–1291.
- 182 L. Wang, H. Guo, Q. Xie, J. Wang, B. Hou, L. Jia, J. Cui and D. Li, *Appl. Catal. A: Gen.*, 2019, **572**, 51–60.
- 183 M. Moliner, Y. Román-Leshkov and M. E. Davis, *Proc. Natl. Acad. Sci. U.S.A.*, 2010, **107**, 6164–6168.
- 184 M. Boronat, P. Concepción, A. Corma, M. Renz and S. Valencia, *J. Catal.*, 2005, **234**, 111–118.
- 185 Y. P. Li, M. Head-Gordon and A. T. Bell, *ACS Catal.*, 2014, **4**, 1537–1545.
- 186 G. Li, E. A. Pidko and E. J. M. Hensen, *ACS Catal.*, 2016, **6**, 4162–4169.
- 187 S. Saravanamurugan, M. Paniagua, J. A. Melero and A. Riisager, *J. Am. Chem. Soc.*, 2013, **135**, 5246–5249.
- 188 R. Gounder and M. E. Davis, *ACS Catal.*, 2013, **3**, 1469–1476.
- 189 C. Moreau, R. Durand, A. Roux and D. Tichit, *Appl. Catal. A: Gen.*, 2000, **193**, 257–264.
- 190 J. Dijkmans, D. Gabriëls, M. Dusselier, F. De Clippel, P. Vanelderen, K. Houthoofd, A. Malfliet, Y. Pontikes and B. F. Sels, *Green Chem.*, 2013, **15**, 2777–2785.
- 191 S. Xu, L. Zhang, K. Xiao and H. Xia, *Carbohydr. Res.*, 2017, **446–447**, 48–51.

192 R. Gautam, P. Pal and S. Saravanamurugan, *Chempluschem*, 2023, **88**,
2022002.

CHAPTER 2: Experimental Methods and Techniques.

2.1. Materials

All materials and chemicals were used as received from suppliers and without any further purification, and all purity values are reported in mass percentage unless otherwise specified under the relevant section headings.

2.1.1. Preparation of catalysts.

The materials and chemicals used for catalysts preparation include: gallium(III) nitrate hydrate ($\text{Ga}(\text{NO}_3)_3 \cdot x\text{H}_2\text{O}$, 99.90% trace metals basis, Acros), iron(III) chloride anhydrous (FeCl_3 , $\geq 98.50\%$, VWR international), Niobium(V) chloride (NbCl_5 , 99%, Sigma-Aldrich), Tin(IV) Chloride Pentahydrate ($\text{SnCl}_4 \cdot 5\text{H}_2\text{O}$, 98+%, Fisher), Aluminium oxide, gamma-phase ($\gamma\text{-Al}_2\text{O}_3$, 99.97% metals basis, Alfa Aesar), Silica, fumed (SiO_2 , 99.80%, Sigma-Aldrich), Cerium(IV) 2-methoxyethoxide ($\text{C}_{12}\text{H}_{28}\text{CeO}_8$, 18-20% w/w in 2-methoxyethanol, Alfa Aesar), Niobium(V) ethoxide ($\text{Nb}(\text{OCH}_2\text{CH}_3)_5$, 99.90% metals basis, Alfa Aesar), Titanium(IV) ethoxide ($\text{Ti}(\text{OC}_2\text{H}_5)_4$, Technical grade, Sigma-Aldrich), Aluminosilicate, Al-MCM-41 ($(\text{SiO}_2)_x (\text{Al}_2\text{O}_3)_y$, Sigma-Aldrich), Silica, mesostructured, MCM-41 type (SiO_2 , Sigma-Aldrich), Zeolite beta, ammonium ($680 \text{ m}^2 \cdot \text{g}^{-1}$, 25:1 $\text{SiO}_2:\text{Al}_2\text{O}_3$, Alfa Aesar), Zeolite beta, ammonium ($710 \text{ m}^2 \cdot \text{g}^{-1}$, 38:1 $\text{SiO}_2:\text{Al}_2\text{O}_3$, Zeolyst international), Zeolite Y, hydrogen ($730 \text{ m}^2 \cdot \text{g}^{-1}$, 5.1:1 $\text{SiO}_2:\text{Al}_2\text{O}_3$, Alfa Aesar), Zeolite Y, hydrogen ($780 \text{ m}^2 \cdot \text{g}^{-1}$, 30:1 $\text{SiO}_2:\text{Al}_2\text{O}_3$, Zeolyst international), Zeolite Y, hydrogen ($700 \text{ m}^2 \cdot \text{g}^{-1}$, 80:1 $\text{SiO}_2:\text{Al}_2\text{O}_3$, Zeolyst international), Zeolite ZSM-5, ammonium ($425 \text{ m}^2 \cdot \text{g}^{-1}$, 23:1 $\text{SiO}_2:\text{Al}_2\text{O}_3$, Alfa Aesar), Zeolite ZSM-5, ammonium ($425 \text{ m}^2 \cdot \text{g}^{-1}$, 50:1 $\text{SiO}_2:\text{Al}_2\text{O}_3$, Alfa Aesar).

2.2.2. Catalytic tests.

The materials and chemicals used for catalytic tests include 5-Hydroxymethylfurfural ($C_6H_6O_3$, 98%, Thermoscientific), D-(-)-Fructose ($C_6H_{12}O_6$, $\geq 99\%$, Fisher), D-(+)-Glucose ($C_6H_{12}O_6$, anhydrous, 99%, Alfa Aesar), D-(+)-Mannose ($C_6H_{12}O_6$, $\geq 99\%$, Alfa Aesar), Formic acid (CH_2O_2 , 99%, Acros), Levulinic acid ($C_5H_8O_3$, 98%, Sigma-Aldrich), Hydrochloric acid (HCl, 35%, VWR international) Cerium (IV) oxide (CeO_2 , 99.9% trace metals basis, Sigma-Aldrich), Lanthanum (III) oxide (La_2O_3 , $\geq 99.90\%$, Sigma-Aldrich), Molybdenum (VI) oxide (MoO_3 , 99.95% metal basis, Alfa Aesar), Niobium(V) oxide (Nb_2O_5 , 99.90% trace metals basis, Sigma-Aldrich), Titanium (II) oxide (TiO_2 , 99.5% metal basis, Fisher), Tungsten (VI) oxide (WO_3 , 99.8% metals basis, Thermoscientific), Ethanol (C_2H_6O , HPLC Grade, Fisher), Methanol (CH_4O , HPLC Grade, Fisher).

2.2.3. Characterisation of Catalysts.

The materials and chemicals used for the analysis of Catalysts include: Beta-Gallium(III) oxide ($\beta\text{-Ga}_2O_3$, $\geq 99.99\%$, Acros), Tin(IV) oxide (SnO_2 , 99.90%, Acros), Methyl Orange ($C_{14}H_{14}N_3NaO_3S$, ACS reagent, Dye content 85 %, Sigma-Aldrich), Potassium acid phthalate ($HKC_8H_4O_4$, ACS reagent, Sigma-Aldrich), Sodium carbonate (Na_2CO_3 , 99.80%, Honeywell), Sodium Hydroxide ($NaOH$, $\geq 98\%$, Fisher).

2.2.4. Characterisation of reaction mixtures and standards.

The materials and chemicals used for the analysis of reaction mixtures and standards include: acetonitrile (C_2H_3N , HPLC grade, Fisher), Deuterium oxide (D_2O , 99.9%, Sigma-Aldrich), Ethyl acetate ($C_4H_8O_2$, HPLC Grade, Fisher), Methyl β -D-

fructofuranoside (C₇H₁₄O₆, 98%, MuseChem), 1-propanol (C₃H₈O, HPLC grade, Fisher), Isopropanol (C₃H₈O, HPLC grade, Alfa Aesar).

2.2. Synthesis of catalysts.

2.2.1. Wetness impregnation.

Physicochemical parameters of heterogeneous catalysts can be substantially affected by their preparation methods¹. To this purpose, it is usually beneficial if supported metals and/or metal oxide as the active sites are present in a highly dispersed form over a support or within a framework.^{2,3} This will consequentially lead to a catalyst with a high surface area and, often to a maximum specific activity¹. To achieve this objective specifically for zeolite-based catalysts, the metal component is frequently deposited on a support surface with high porosity and thermal stability characteristics³. Standard preparation methods such as wetness impregnation (WI)⁴, Ion exchange (IE)⁵, and precipitation (i.e., coprecipitation, CP and deposition-precipitation, DP)⁶ are often used in the post-synthesis of supported catalysts. However, due to its simplicity in execution and economic advantages, wetness impregnation has been defined as the most straightforward and frequently applied technique to introduce metal centres into the zeolite crystals^{2,4,5}.

In wetness impregnation (WI), a metal precursor (e.g., a metal salt) is dissolved in a solvent, typically deionised water⁷. The support, a material possessing a high surface area and preferably thermostable (e.g., zeolites, metal oxides), is subsequently added to this solution with a certain amount depending on the desired metal loading. The resulting slurry is then gently dried through slow heating at a temperature below its boiling point. This will lead to the precursor being dispersed over a support by

concentration gradient effects. On completion, the catalyst is frequently calcined, to ensure stability, and it is converted, most often into a metal oxide⁸.

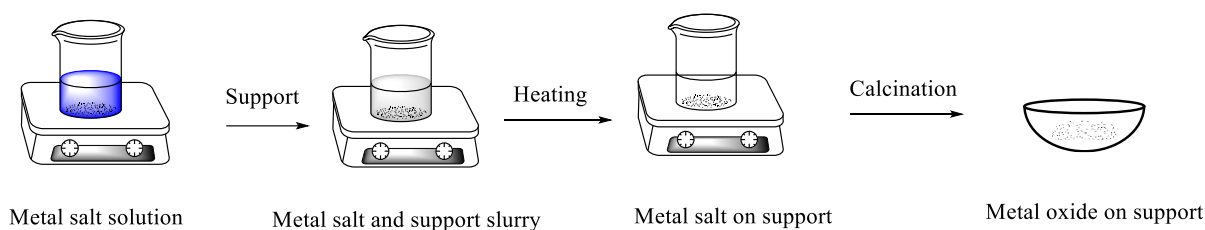


Figure 2.1. A schematic diagram shows the steps involved in the method of wetness impregnation as well as the formation of the metal and/or metal oxide on the support during some of these steps⁹.

The use of the impregnation technique was shown to produce active catalysts for converting sugars like glucose and/or fructose to a versatile platform chemical such as 5-hydroxymethylfurfural (5-HMF)^{10,11}. For instance, extensive investigations on the structural properties of the benchmarked tin containing beta zeolite “Sn-beta” have revealed that most Sn species were successfully incorporated into the beta zeolite framework by using this method^{12,13}. During this research, wetness impregnation was selected as the primary method for depositing metals/metal oxides as active sites on different zeolite supports. The choice was made as a result of its ease to conduct practically and the efficient metal dispersion that could be achieved upon using such a technique.

2.2.1.1. Preparation of Sn/Y, Ga/Y, Nb/Y and Fe/Y catalysts.

The preparation of catalysts used in this research, tin-, gallium-, niobium-, and iron-doped zeolite Y catalysts, denoted as Sn/Y, Ga/Y, Nb/Y and Fe/Y, respectively, is

described here. Specifically, catalysts were prepared using a wet impregnation protocol with water as the solvent for dissolving and incorporating metal precursors into the zeolite. Zeolite Y was used in its acidic form, here denoted as HY. The metal precursors used to prepare Sn/Y, Ga/Y, Nb/Y and Fe/Y were $\text{SnCl}_4 \cdot 5\text{H}_2\text{O}$, $\text{Ga}(\text{NO}_3)_3 \cdot x\text{H}_2\text{O}$, NbCl_5 and FeCl_3 , respectively.

Unless otherwise specified, all catalysts were prepared with a final metal loading of 1 wt %, where the desired amount of metal precursor was dissolved in water (25 mL) and mixed with zeolite Y (ca. 2 g) under vigorous stirring. The amount of zeolite was adjusted to compensate for the metal assay for each precursor. The resulting slurry was then heated to 80 °C and evaporated to dryness. Each catalyst was dried at 120 °C for 16 h and calcined at 550 °C for 4 h in static air (temperature ramp 20 °C min⁻¹).

In Chapter 5, a fixed 1 wt.% metal loading of Sn was locked and used to calculate the metal loading for Ga and Nb, leading to metal loading of 0.6 wt.% and 0.8 wt.% for both metals, respectively. Since the chapter focuses on investigating the roles of catalyst acidity on catalytic activity, it is crucial to account for the fact that 1 wt.% Sn, Ga and Nb have significantly different masses. This difference in mass will result in different amounts of catalyst being used when maintaining a constant M:S (metal to substrate) ratio. However, as we are testing the acidity of the zeolite, a different amount of zeolite will also have a different amount of total acidity in a solution, an additional potential variable that was considered, which could be relevant.

2.2.2. Sol-gel

Sol-gel is another well-known catalyst preparation technique commonly used for the preparation and deposition of metal active sites in the form of metal oxides¹⁴. Prior to

the step of metal oxide deposition on zeolite Y, metal oxides of titanium (TiO_2), niobium (Nb_2O_5) and cerium (CeO_2) were synthesised by using a sol-gel method adopted from Arif Rahman et al. ¹⁴. In a typical synthesis, desired amounts of metal ethoxide (i.e., Titanium(IV) ethoxide, Niobium(V) ethoxide and Cerium(IV) 2-methoxyethoxide) and 5 mL of ethanol were mixed in a beaker. The resulting solution was slowly added to 25 mL of deionised water under continuous stirring for 10 min. The solution was then added gently to 0.3 mL of concentrated HNO_3 (14 M). The resulting mixture was heated at 80 °C for 30 min under continuous stirring. A white milky solution was formed, which was then used to deposit metal oxide on zeolite Y.

The deposition of the prepared metal oxide on zeolite was carried out by dispersing 2 g of zeolite in 25 mL of water. This slurry was then gradually added to the previously prepared gel solution under constant stirring. The resultant slurry was kept under stirring for 2 hours and then dried at 100 °C for 4 hours. Catalysts were then calcined at 500 °C for 6 h (temperature ramp 10 °C min^{-1}).

All catalytic tests and synthesis in the following sections (2.3 – 2.6) were carried out using the same approaches. Unless otherwise specified, the catalytic tests were carried out in a sealed pressure tube (Ace-type GPE Scientific) at particular reaction temperatures set within each section. The tube containing the reaction mixture was inserted into a pre-heated, temperature-calibrated aluminium block for the desired reaction time and equipped with a magnetic stirrer operating at 700 rpm. After the desired reaction time, the mixture was quickly cooled down to room temperature by immersing the pressure tube in an ice bath. Control tests using fructose and mannose as the reaction substrate were carried out identically to those described for glucose. All catalytic tests were repeated three times to acquire the average and standard deviation of the sample of data.

2.3. Catalytic tests for glucose to fructose isomerisation reaction.

2.3.1. One-pot reaction with water or methanol as a solvent.

The catalyst was dispersed in solutions containing 4 mL of water or methanol and 125 mg of α -D-glucose ($31.25 \text{ g}\cdot\text{L}^{-1}$, 3.12 wt.%, $0.17 \text{ mol}\cdot\text{L}^{-1}$). The amount of catalyst, typically ca. 75 mg, was adjusted to a molar metal-to-glucose ratio of 1:100 with regard to the total amount of Ga or Sn in the zeolite. The reaction was carried out at a reaction temperature of 100 °C and a reaction time of 1 h.

2.3.2. Two-pot reaction with methanol and water as solvents

After the first step in methanol as a solvent, described in the previous section. The reaction mixture was cooled down again to room temperature using an ice bath, the vial was opened, and 4 mL of water was added to the reaction mixture. The vial was sealed, and the tube was reheated at 100 °C for 1 h.

2.4 Synthesis of intermediates: alkyl pyranoside and/or alkyl furanoside.

Methyl glucoside and fructoside intermediates were synthesised using MCM-41 and Al-MCM-41 mesoporous catalysts^{15,16}. Typically, these intermediates were synthesised by dispersing the catalyst in 4 mL aqueous solutions of α -D-glucose or D-(-)-Fructose ($31.25 \text{ g}\cdot\text{L}^{-1}$, 3.12 wt.%, $0.17 \text{ mol}\cdot\text{L}^{-1}$). The amount of catalyst, ca. 75 mg, was adjusted to an M:S molar ratio of 1:100. The synthesis was carried out at a reaction temperature of 100 °C and 120 °C for a reaction time in the range of 1 - 6 h.

2.5. Catalytic tests of fructose dehydration reaction to 5-hydroxymethylfurfural (HMF).

2.5.1. Dehydration of fructose over homogeneous catalysts.

In order to achieve selective fructose dehydration to HMF in an aqueous solution by the mean of a heterogeneous catalyst, a screening of the reaction parameters was first carried out by using HCl as a homogeneous Brønsted catalyst. A kinetic study was conducted at a reaction temperature of 100 °C for a time range of 10 – 360 min, and with a fructose to HCl molar ratio of 1:5 – 1:0.2. Typically, a 5 mL aqueous solution ($100 \text{ g}\cdot\text{L}^{-1}$, 10 wt.%, $0.56 \text{ mol}\cdot\text{L}^{-1}$) of fructose was mixed with the desired amount HCl at various fructose/HCl molar ratios.

2.5.2. Dehydration of fructose over heterogeneous catalysts.

Dehydration of fructose to HMF over various undoped and metal-doped zeolite Y as heterogeneous catalysts was performed under particular reaction conditions screened in section (2.5.1). More specifically, the catalyst was dispersed in a 5 mL aqueous solution ($100 \text{ g}\cdot\text{L}^{-1}$, 10 wt.%, $0.56 \text{ mol}\cdot\text{L}^{-1}$) of fructose. The desired amount of catalyst was adjusted to an M:S molar ratio in the range of 1:3 – 1:300 concerning the total amount of metal (i.e., Ga, Sn, Nb, and Fe) or metal oxides (e.g., TiO_2 , Nb_2O_5 , and CeO_2) in the zeolite. The catalytic tests were carried out at a reaction temperature of 100 °C and/or 140 °C and a reaction time of 2 - 6 h.

2.6 Catalytic tests for the conversion of glucose and fructose to HMF over metal oxides.

The catalyst was dispersed in a 5 mL aqueous solution ($100 \text{ g}\cdot\text{L}^{-1}$, 10 wt.%, $0.56 \text{ mol}\cdot\text{L}^{-1}$) of glucose or fructose. The desired amount of catalyst was adjusted to an M:S molar ratio of 1:10 with respect to the total amount of metal of the metal oxides studied (i.e., MoO_3 , La_2O_3 , CeO_2 , Nb_2O_5 , TiO_2 , and WO_3). The reactions were conducted at a reaction temperature of $140 \text{ }^\circ\text{C}$ and for a reaction time of 2 h.

2.7. Analytical techniques.

2.7.1. Characterisation of the reaction mixtures.

Due to the importance of identifying and quantifying the potential products and intermediates of our glucose to fructose isomerisation reaction as well as glucose and fructose dehydration reaction to 5-hydroxymethylfurfural (5-HMF). A range of analytical techniques, including High-Performance Liquid Chromatography – Evaporative Light Scattering Detector (HPLC-ELSD), High-Performance Liquid Chromatography – Mass Spectrometry (HPLC-MS), and Proton nuclear magnetic resonance ($^1\text{H-NMR}$) were used for the characterisation of the mixture solutions of all reactions carried out in this thesis work. In particular, HPLC-ELSD analysis was carried out for the identification and quantification of the components of reaction mixtures from glucose isomerisation; HPLC-MS analysis was mainly performed to confirm the presence of alkyl glucoside and/ or alkyl fructoside as potential intermediates in the reaction mixture of glucose isomerisation, and $^1\text{H NMR}$ was used for the identification and quantification of the components of the reaction mixture from glucose and fructose dehydration reactions to 5-hydroxymethylfurfural. Given the importance of these

characterisation techniques, the working principle of these analytical tools will be briefly discussed in the following sections.

2.7.1.1. High-Performance Liquid Chromatography – Evaporative Light Scattering Detector (HPLC-ELSD).

Column chromatography is a specific form of separation where the compounds to be separated, or in analytical terms 'resolved', are distributed between a mobile phase (eluent) and a stationary phase (packing material of the column in our case). The separation, identification, and quantification of different components in a mixture can be achieved using this technique¹⁷. In principle, the chromatographic process occurs due to repeated sorption onto and desorption from the stationary phase by sample components as they cross the column bed. The separation between individual components arises from differences in their distribution coefficients between the two phases¹⁸. In liquid chromatography, the separation of analyte molecules is based on their differential partitioning between two non-miscible phases, the stationary phase, and the mobile phase. Several interactions between the analyte, the stationary and mobile phases, such as ionic interactions, ion-dipole interactions, hydrogen bonds, and hydrophobic interactions (e.g., van der Waals and London dispersion forces), can govern the separation step. A reverse-phase was used in our HPLC analysis of sugar samples. In this mode, the sugar molecules are separated based on their hydrophobicity when they partition between a non-polar stationary phase and a polar mobile phase; thereby, an increase in the retention time could be observed for the less polar analytes¹⁹.

The essential components of a conventional HPLC system (see figure 2.2) consist of the mobile phase drawn from a reservoir via a pump, which drives the mobile phase through the column by controlling the flow rate and generating sufficient pressure in the range of 30 - 400 bar²⁰. An autosampler is often used to inject the sample into the column, typically placed within a column oven. The column is considered to be the heart of the chromatographic system, where the separation of analytes occurs. Most HPLC columns are made of an external part made of stainless steel in order to stand the pressures involved, with column lengths of 30 – 300 mm, internal diameters of 2.0–4.6 mm, and typically packed with 3 – 10 µm porous particles that are made up of silica, polystyrene-divinyl-benzene synthetic resin, alumina, or other types of ion-exchange resin, and chemically modified with long-chain alkyl groups (e.g., C18, C8, C4) to create a non-polar surface in the case of the reverse-phase column²¹. A column oven is used to maintain a constant column temperature. The detector is positioned directly after the column to respond to changes in column effluent composition during the chromatographic run. A data system collects the detector output and processes the data¹⁸.

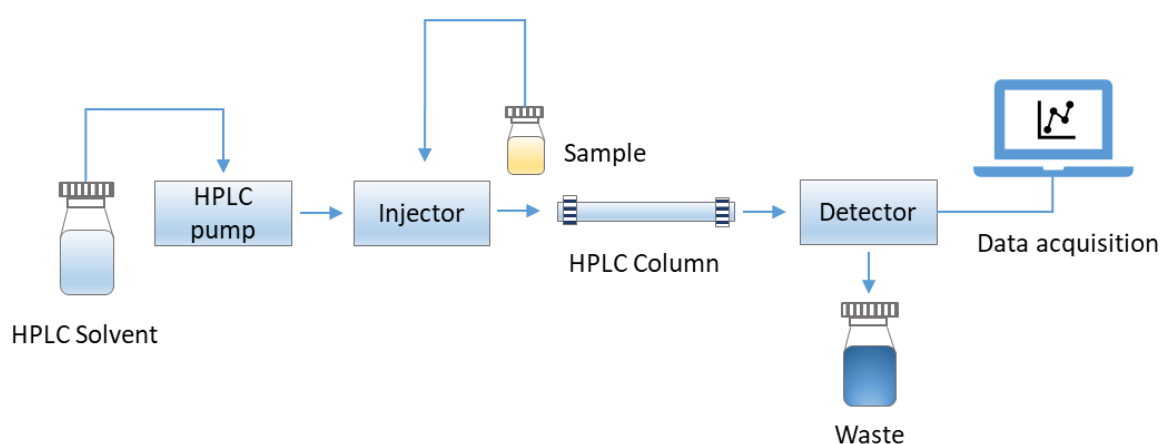


Figure 2.2. The schematic diagram demonstrates the working principle of the High-Performance Liquid Chromatography (HPLC) system¹⁸.

The peak area (i.e., the intensity of a signal) or the height if peaks are particularly sharp are directly proportional to the concentration of a compound injected into the instrument. These characteristics are typically originated from a response from a detector. This response must be related to the concentration or amount of the analyte of interest in order to obtain quantitative data, wherein a calibration must therefore be performed using either external or internal standard methods, both of which are performed using a calibration curve.

An ELSD detector was selected in this work amongst other types of detection systems such as differential refractive index (RI), charged aerosol detection (CAD) and electrochemical detectors (ECD), which have limitations including poor sensitivity, specificity, and selectivity depending on temperature, composition, flow rate, and incompatibility with gradient elution of detection. The evaporative light scattering detector (ELSD) is not affected by these limitations since it is based on the universal ability of small solid particles to cause photon scattering²². In particular, the principle of these aerosol-based HPLC detectors (Figure 2.4) is to convert the eluents (sample dissolved in mobile phase) from the HPLC column and carries by an inert carrier gas such as nitrogen to form a fine spray via a nebuliser. This spray is then heated to evaporate the mobile phase. Light is then focused on the remaining small solid particles, and scattered light is detected where the particle size achieved by the nebulisation and evaporation process can be affected by gas pressure and flow rate, sample concentration and the solvent used as the eluent²³.

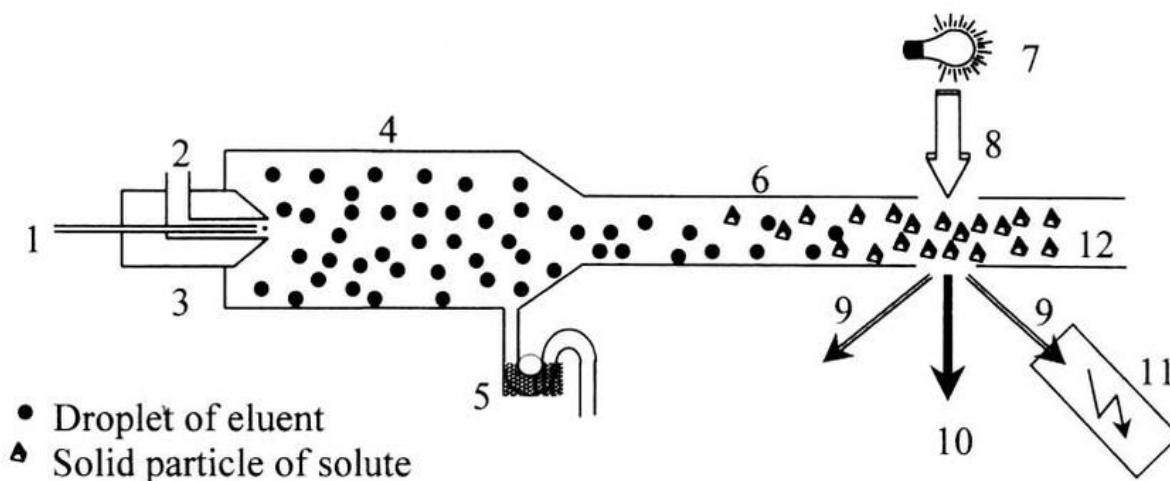


Figure 2.3. Schematic representation of the evaporative light scattering detector, which is composed of 1: Effluent; 2: Nebulizing gas; 3: Concentric nebuliser; 4: Nebulizing chamber; 5: Liquid waste (settled droplets); 6: Heated drift tube; 7: Light source; 8: Light beam; 9: Diffracted light; 10: Transmitted light; 11: Photomultiplier; 12: Gas exhaust. Figure reproduced from Philippe Christen²⁴ with permission.

Additionally, an ELSD detector can detect most compounds that are less volatile than the mobile phase, and it does not rely on the optical properties of the analytes²⁵. Despite all these advantages, there is still a scientific disagreement in the literature about the fit of data obtained by this detector to a calibration curve, which was essential for this study to quantify chromatogram results. In more detail, some literature confirms that data achieved by ELSD suffer from the lack of linearity between mass and signal intensity, or in other words, between the analyte concentration and the area under the peak of that analyte. At the same time, other literature reported a linear correlation²⁶⁻²⁸. Due to this uncertainty, we have always ensured to be in a linearity range when carrying out our quantitative determinations.

In a typical analysis, high-performance liquid chromatography was used for the characterisation of glucose isomerisation reaction mixture and the solubility measurements of sugars, using a Shimadzu UFLC XR chromatographer. A method for

a satisfactory resolution of the reaction mixture and identification of impurities made use of a Phenomenex Rezex RCM-Monosaccharide Ca^{++} column 300 by 7.8 mm column temperature of 60 °C and a mobile phase consisting of purified water running an isocratic elution program at a flow rate of 0.6 mL·min⁻¹ over 25 minutes and an injection volume (HPLC loop) of 10 µL.

2.7.1.2. High-Performance Liquid Chromatography – Mass Spectrometry (HPLC-MS).

The use of the mass spectroscopy technique can deliver valuable information for the molecular and structural identification of analytes of interest by measuring their mass-to-charge ratios (m/z)²⁹. A conventional mass spectrometer device comprises three main parts: ionisation sources, mass analysers and detectors. The molecule of interest must be first ionised in order to be detected and thus originating a mass-to-charge ratio (m/z) to be measured. The molecular ions are subsequently separated based on their m/z ratios, and their signals are then recorded as a function of scan time³⁰.

The generation of ions is considered to be the first and most fundamental step in mass spectrometric analysis. The analyte molecules must first be ionised (i.e., become charged) to allow separation from other charged species in the mass analyser²⁹. Various methods can be applied to achieve successful ionisation for the analytes of interest³¹. However, electrospray ionisation (ESI) and matrix-assisted laser desorption/ionisation (MALDI) are the most extensively employed methods for characterising and identifying a wide range of molecules³². In this section, the ionisation method of electrospray ionisation (ESI), which was used for mass spectrometric analysis during this thesis work, will be discussed in detail.

Electrospray ionisation (ESI) is a soft and widespread ionisation technique that is best utilised for thermally labile and at least moderately polar organic analytes³³, without the prerequisite of any chemical derivatisation and/or extraction processes from polar solutions³². This ionisation technique is currently the most often used technique associated with the mass spectrometry method; this is due to the possibility of coupling with liquid separation techniques, such as liquid chromatography (LC) and/or capillary electrophoresis (CE)³⁴. In ESI, an electric field is used to promote the transfer of ions from the solution to the gas phase³⁵. In brief, a sample solution is first infused into the ESI chamber using a heated glass or metal capillary³⁶. As a high voltage is introduced to the sample solution, a spray of charged droplets will then be formed at the end of the heated capillary. Once the ionisation temperature exceeds the solvent's boiling point, the solvent will progressively be evaporated, and ultimately the droplets will be dissociated into a stream of molecular ions. Then, the charged molecules will be crossed into the MS analysers operated under a high vacuum to separate them according to their mass-to-charge ratio (m/z)³⁷, as shown in Figure 2.5.

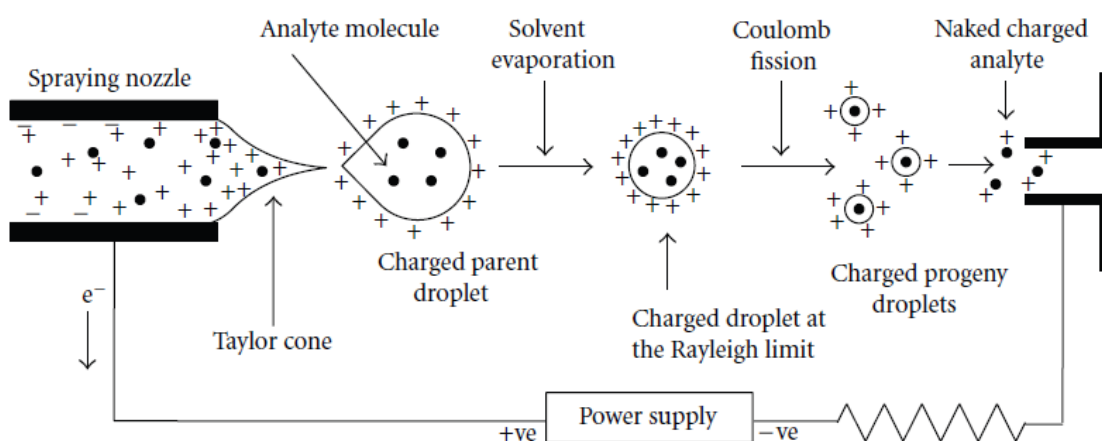


Figure 2.4. The schematic diagram represents the electrospray ionisation process. In the step of producing charged droplets, the analyte solution is pumped through the high-voltage capillary, which causes an electrochemical reaction of the solvent to take place that leads to an electron flow to or from the heated capillary, depending on its polarity³⁸. Figure reproduced from Shibdas Banerjee³⁹ with permission.

Ion modes can either be positive or negative, typically depending on the analyte's proton affinity. Any molecule with base-like functional groups can be simply ionised in the positive ion mode by creating adducts with proton(s). Conversely, molecules with acid-like characteristics typically give better ionisation spectra in the negative ion mode³³. Therefore, the optimum ionisation mode selection relies on the Brønsted-Lowry acid-base theory^{40,41}. The type of ions generated in the ionisation source can be frequently singly or multiply protonated $[M + zH]^{z+}$ ions in the positive ion mode or singly deprotonated $[M - H]^{-}$ ions, which are known to be dominant in the negative ion mode³³. For example, cationised molecules such as H^{+} , NH_4^{+} , Na^{+} or K^{+} are deliberately used during the ESI process because they typically give no fragmentation rather than the loss of the cation in the MS spectra³³. However, for compounds like carbohydrates, their fragmentation could also be significantly different from that of $[M + H]^{+}$ ions, which in turn will provide valuable structural information⁴².

The typical HPLC-MS analysis for the identification of intermediates of glucose to fructose isomerisation reaction was carried out by using an Agilent 1260 Infinity liquid chromatographer coupled with an Agilent 6530 Q-ToF mass spectrometer. The chromatographer was equipped with an Agilent Zorbax Extend-C18 column, and the separation of the compounds was carried out by using a water/formic acid (0.1%) and acetonitrile mobile phase with a gradient of acetonitrile from 5% to 15% in 15 minutes. A flow rate of 0.4 mL min^{-1} and an injection volume (sampling loop) of $1.0 \text{ }\mu\text{L}$ were used.

2.7.1.3. Proton and Carbon nuclear magnetic resonance spectroscopy (^1H - and ^{13}C -NMR).

Nuclear magnetic resonance spectroscopy (NMR) has proven to be one of the most sensitive and powerful techniques for investigating molecular structural information at

the atomic level of a sample⁴³. The fundamental concept of this spectroscopic technique depends on exploiting changes in the orientation of nuclear spin. In terms of quantum mechanics, spin is an essential characteristic of all elementary particles, such as protons, neutrons, and electrons⁴⁴. In more detail, NMR studies the magnetic properties of nuclei. Radiofrequency energy absorption may occur when nuclei are placed in a static magnetic field and exposed to a second oscillating magnetic field⁴⁵.

Figures 2.5 and 2.6 show that a charged spinning nucleus can be treated as a magnetic moment (μ). If an external magnetic field (B_0) is present, this may induce two nuclear spin states known as $(+1/2)$ and $(-1/2)$ ⁴⁶. The magnetic moment of the low-energy spin state $(+1/2)$ is oriented parallel to the external magnetic field, whereas that with a high-energy state $(-1/2)$ is oriented perpendicular to the direction of the external magnetic field⁴⁷. The energy difference between these two spin levels relies on the strength of the external magnetic field⁴⁶.

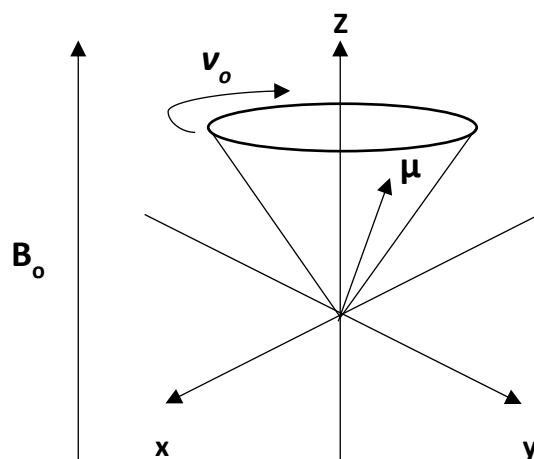


Figure 2.5. Representation of a processing proton in a stationary magnetic field B_0 ⁴⁷.

Transitions of these two spin energy states occur at the Larmor frequency ω_0 ⁴⁸:

$$\omega_0 = \gamma B_0 / 2\pi \quad \text{Eq.2.1}$$

The proportionality factor gamma is called the magnetogyric ratio and is a specific constant for the isotope of each element⁴⁸.

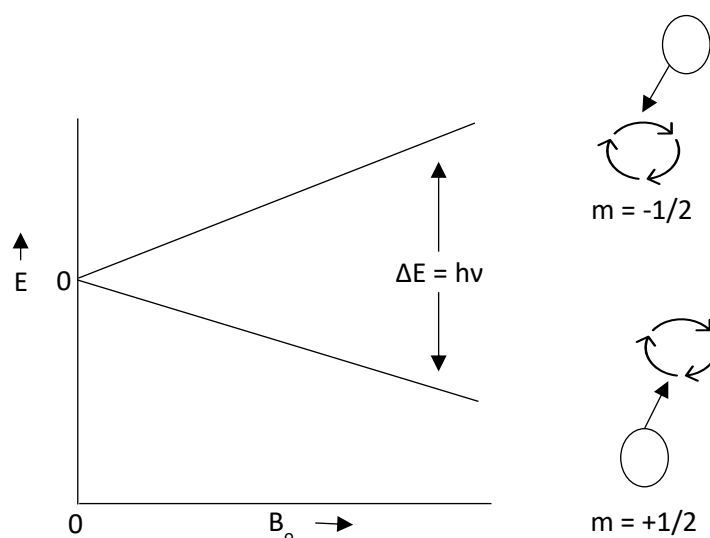


Figure 2.6. Schematic diagram of the energy difference ΔE between the spin energy states, which can be described in terms of frequency unit ν as $\Delta E = h\nu$, wherein h is Planck's constant, which is equal to $6.6256 \times 10^{-34} \text{ J}\cdot\text{s}$ ⁴⁸.

The signal in the NMR spectroscopic analysis results from the difference in the energy absorbed by the spins that generate a transition from the low energy states to the high energy state. Therefore, the signal is proportional to the difference in population between these two energy states. NMR is a relatively sensitive spectroscopic technique, though another contributor to the sensitivity of NMR originates from the resonance or energy exchange at a particular frequency between the spins and the spectrometer⁴⁸.

¹H-NMR spectra were collected using a Bruker Advance IIIHD 400 spectrometer, operating at 400 MHz, whereas ¹³C-NMR were collected using DEPTQ analysis measured at 100.2 MHz with a Bruker Advance III HD Spectrometer, using 896 transients, spectral width of 296 ppm, FID size 64k points and a recycle delay of 4s. Samples for both ¹H and ¹³C-NMR analysis were prepared by adding 100 μL of the reaction mixture to an NMR tube and dissolving it in 600 μL deuterium oxide (D₂O). Then, 50 μL of 0.1 M ethyl acetate (CH₃COOC₂H₅) was subsequently added as an internal standard.

2.7.1.4. Equations for the Calculations of Catalytic Activity.

The catalytic activity of our catalysts for all reactions carried out during this thesis was mainly assessed by calculating the molar conversion of the reagents, product distribution, carbon mass balance, and product yield. For instance, the characterisation of glucose to the fructose reaction mixture was carried out based on HPLC calibration curves of sugars (Figures A1 – A3 in Appendix A.1). In contrast, ¹H-NMR was used for reagent molar conversion, product distribution, and carbon mass balance calculations for the dehydration reactions of glucose and fructose to 5-HMF (Figure A4 in Appendix A.2)

The molar conversion was calculated as Eq.2.3:

$$C(\text{mol}\%) = \frac{n_{R,\text{consumed}}}{n_{R,0}} \cdot 100 \quad \text{Eq.2.2}$$

where $n_{R,0}$ is the number of moles of reagent at the start of the reaction, and $n_{R,\text{consumed}}$, is the number of moles of reagent consumed during a reaction after a time t .

n_{R} consumed was calculated by using the formula Eq.2.4:

$$n_{R,consumed} = n_{R,0} - n_{R,L} \quad \text{Eq.2.3}$$

where $n_{R,L}$ is the number of moles of reagent left in the reaction mixture after a reaction time t .

For the calculation of the *observed* molar selectivity S for a product i , this was calculated as the molar ratio between the product i and the sum in j of the moles of all the other products detected in the reaction mixtures Eq.2.4

$$S_i(\text{mol } \%) = \frac{n_i}{\sum_j n_j} \cdot 100 \quad \text{Eq.2.4}$$

As in our case, glucose, methyl fructoside, fructose and mannose were the only components observed in glucose isomerisation, whereas fructose dehydration showed products of 5-HMF, levulinic acid and formic acid. The observed selectivities of methyl fructoside (S_{MeF}), fructose (S_F), and mannose (S_M) for glucose isomerisation reaction as well as 5-HMF (S_{5-HMF}), levulinic acid (S_{LA}) and formic acid (S_{FA}) for fructose dehydration were calculated using Eq.2.5 - Eq.2.10.

$$S_F(\text{mol } \%) = \frac{n_F}{n_F + n_{MeF} + n_M} \cdot 100 \quad \text{Eq.2.5}$$

$$S_M(\text{mol } \%) = \frac{n_M}{n_M + n_{MeF} + n_F} \cdot 100 \quad \text{Eq.2.6}$$

$$S_{MeF}(\text{mol } \%) = \frac{n_{MeF}}{n_{MeF} + n_F + n_M} \cdot 100 \quad \text{Eq.2.7}$$

$$S_{5-HMF}(\text{mol } \%) = \frac{n_{5-HMF}}{n_{5-HMF} + n_{LA} + n_{FA}} \cdot 100 \quad \text{Eq.2.8}$$

$$S_{LA}(\text{mol } \%) = \frac{n_{LA}}{n_{LA}+n_{5-HMF}+n_{FA}} \cdot 100 \quad \text{Eq.2.9}$$

$$S_{FA}(\text{mol } \%) = \frac{n_{FA}}{n_{FA}+n_{5-HMF}+n_{LA}} \cdot 100 \quad \text{Eq.2.10}$$

The carbon mass balance (*CMB*) was calculated as the ratio between the number of carbon atoms (mol) in all of the observed components of the reaction mixture, divided by the initial number (mol) of carbon atoms for the reagent at reaction time zero (Eq. 2.11) of glucose isomerisation and (Eq. 2.12) for fructose dehydration.

$$CMB(\%) = \frac{6C \cdot n_{G,L} + 6C \cdot n_{MeF} + 6C \cdot n_F + 6C \cdot n_M}{6C \cdot n_{G,0}} \cdot 100 \quad \text{Eq.2.11}$$

$$CMB(\%) = \frac{6C \cdot n_{F,L} + 6C \cdot n_{5-HMF} + 5C \cdot n_{LA} + 1C \cdot n_{FA}}{6C \cdot n_{F,0}} \cdot 100 \quad \text{Eq.2.12}$$

Note: although in the case of glucose isomerisation, the number of carbon atoms in methyl fructoside is 7, the calculation accounts for 6 carbon atoms, as these originate from glucose, to which the calculation analysis is, as such this is the *CMB* with respect to glucose and not to methanol, which is also one of the solvents of the reaction mixture.

For the yields, *Y*, combining Eq.2.2, Eq.2.4 and Eq.2.11, these are:

$$Y_i(\%) = C(\text{mol } \%) \cdot \frac{S_i(\text{mol } \%)}{100} \cdot \frac{CMB(\%)}{100} \quad \text{Eq.2.13}$$

2.7.2. Characterization of the catalysts and structure-activity correlations.

In order to study and identify possible structure-activity correlations, our catalysts were systematically investigated using various acidity measurements and techniques like XPS, ICP-MS, XRPD, HAADF-STEM and EXAFS.

2.7.2.1. Acidity Determinations.

Acidity measurements were carried out by using back titration for total Brønsted acidity and NH₃ chemisorption for the combination of Brønsted and Lewis acidity.

In a typical experiment, total Brønsted acidity was measured according to a protocol used by Tantisriyanurak and referenced therein⁴⁹. 100 mg of catalyst was stirred in a sealed container with 10 mL of standardised NaOH (0.135 M) at 40 °C overnight. The solution was then recovered, and the catalyst residue was washed with 10 mL of de-ionised water, which was collected by filtration. The filtrate, together with the solution, was back titrated with standardised HCl (0.128 M) using methyl orange as an indicator. NaOH and HCl were standardised using potassium acid phthalate (HKC₈H₄O₄) and sodium carbonate (Na₂CO₃) respectively⁵⁰.

The typical NH₃ chemisorption experiments were conducted using a Micromeritics ASAP 2020 instrument equipped with a Chemi 2020 Kit to determine NH₃ adsorption isotherms based on volumetric gas sorption at different pressures, according to the protocol reported by Ding *et al.*,⁵¹. Using the volume of adsorbed gas and converting it to moles at standard temperature and pressure allows us to quantitatively measure the amount of strong Brønsted and both strong and weak Lewis acid sites in the materials. About 500 mg of the catalyst was evacuated at 150 °C for 2 h, followed by

adsorption measurements at 35 °C to promote the adsorption to both strong and weak sites at gas pressures from 100 to 700 mm Hg.

2.7.2.2. Porosimetry and BET surface area.

Brunauer–Emmett–Teller (BET) theory is a widely used characterisation technique for calculating surface area and pore size⁵². This method is used to estimate the amount of gas molecule adsorbed on a solid surface of the adsorbent material that correlated to the surface area, especially in the case of porous materials⁵³. The BET theory is an extension of the Langmuir theory, but with the assumption that gas molecules form multilayer adsorption instead of monolayer adsorption assumed in Langmuir theory^{54,55}. The BET equation is expressed as Eq. 2.14.

$$\frac{\frac{P}{P^0}}{n\left(1-\frac{P}{P^0}\right)} = \frac{1}{n_m C} + \frac{C-1}{n_m C} \left(\frac{P}{P^0}\right) \quad \text{Eq. 2.14}$$

where P/P_0 is the relative pressure of the equilibrium gas pressure P and the saturation pressure of an adsorbed substance at the adsorption temperature P^0 , n is the specific quantity of the adsorbed gas molecules at the relative pressure P/P^0 , n_m is the monolayer capacity of adsorbed gas, and C is the BET constant^{54,55}.

In a typical experiment, the pore size was measured using a Micromeritics 3Flex gas sorption system operating with liquid nitrogen at 77 K. In particular, the samples (ca. 100 mg) were degassed at 180 °C for 48 h before analysis. The BET surface area was calculated from the adsorption isotherm using a 20-points method with relative pressure P/P^0 in the range of (0.00 – 0.30) and 0.162 nm² as the surface area for gaseous molecular nitrogen⁵⁶.

The determination of pore size distribution was conducted via Barrett-Joyner-Halenda (BJH) model using desorption points⁵⁷, which is based on Kelvin's equation (Eq.2.15) that was used in the determination of the pore radius (r), which gas molecules adsorbed on⁵⁸.

$$r = \frac{2\gamma V}{RT \ln\left(\frac{P}{P^0}\right)} \quad \text{Eq. 2.15}$$

where γ is the gas-liquid surface tension, V is the molar volume of the adsorbed liquid, R is the gas constant, T is the temperature in Kelvin, and P/P^0 is the relative pressure of the equilibrium gas pressure P and the saturation pressure of an adsorbed liquid⁵⁸.

2.7.2.3. X-ray powder diffraction (XRPD).

X-ray powder diffraction (XRPD) is a technique used to identify the crystalline structure or phase composition of powdered materials⁵⁹. This technique is the result of constructive interference of a monochromatic (within experimental error) X-ray radiation when being scattered or reflected by a crystalline sample. Constructive interference is produced upon the interaction of the incident rays with the crystalline sample when conditions satisfy Bragg's Law (Eq. 2.16)⁶⁰.

$$n\lambda = 2d \sin \theta \quad \text{Eq. 2.16}$$

where n is any integer, λ is the wavelength of the incident-beam X-ray, d is the spacing between crystal planes (d spacing), and θ is the angle between the crystal plane and

the diffracted beam. According to Bragg's Law, the wavelength of electromagnetic radiation is correlated to the diffraction angle at which a diffraction peak is detected and the lattice spacing in a crystalline sample.

In the case of samples in powder form, the sample is irradiated within a range of incident angles, in such a way that all possible directions for the diffraction of the lattice should be attained. From Bragg's law, it is then possible to convert the incident and diffraction angles in d-spacing, bearing in mind that each crystalline sample has its unique d-spacing and structure.

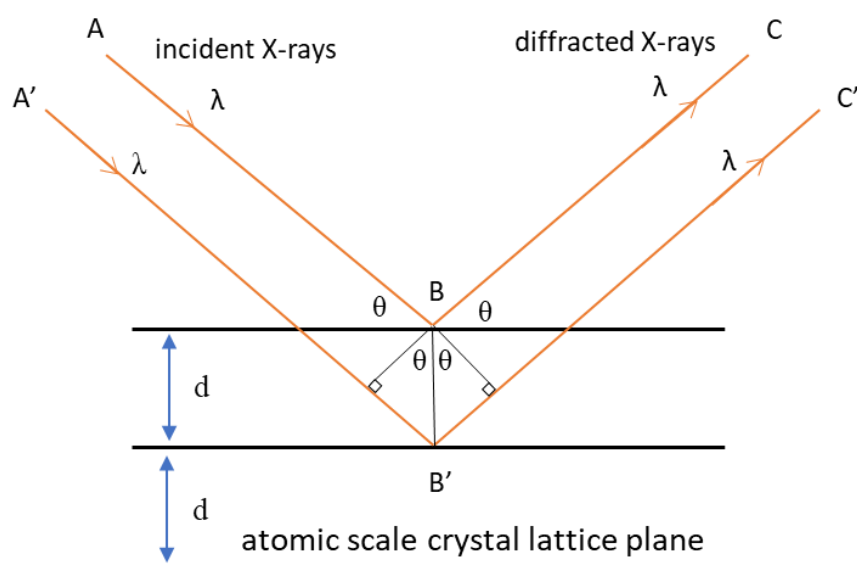


Figure 2.6. Schematic representation of the XRD process occurs according to Bragg's theory. The angle between incident beams and the normal to the lattice (θ) can be used to determine inter-layer spacing (d)⁶⁰.

X-ray powder diffraction (XRPD) patterns were acquired using a Bruker D8 Advance diffractometer equipped with a LynxEye detector. The samples were deposited over an amorphous silicon sample holder. The instrument was operated at 40 kV and 40

mA by selecting the CuK α radiation (1.5406 Å) as an X-ray source. The samples were analysed in the 2 θ range of 5-60° for a scan time of 60 min. Analysis of the patterns was carried out using X-Pert Pro software. The goodness of fit between experimental and simulated XRPD patterns was evaluated via χ^2 -test⁶¹ using Rietveld refinement⁶² as a full-pattern fit algorithm. Initial atomic coordinate values to perform the fit were obtained using crystallographic information files (CIF) available at the Database of Zeolite Structures (IZA-SC)⁶³.

2.7.2.4. X-ray photoelectron spectroscopy (XPS).

X-ray photoelectron spectroscopy (XPS) is a powerful surface analysis technique that is widely used to provide information on the elemental composition as well as the surface chemical state of elements (Li and heavier)⁶⁴ of a material at surface level (typically probes up to 10 nm in the depth of the specimen)^{65,66}. This technique involves the determination of the kinetic energy of electrons (i.e., photoelectrons) that are emitted from a sample due to the irradiation of the sample using single-energy X-ray photons⁶⁴.

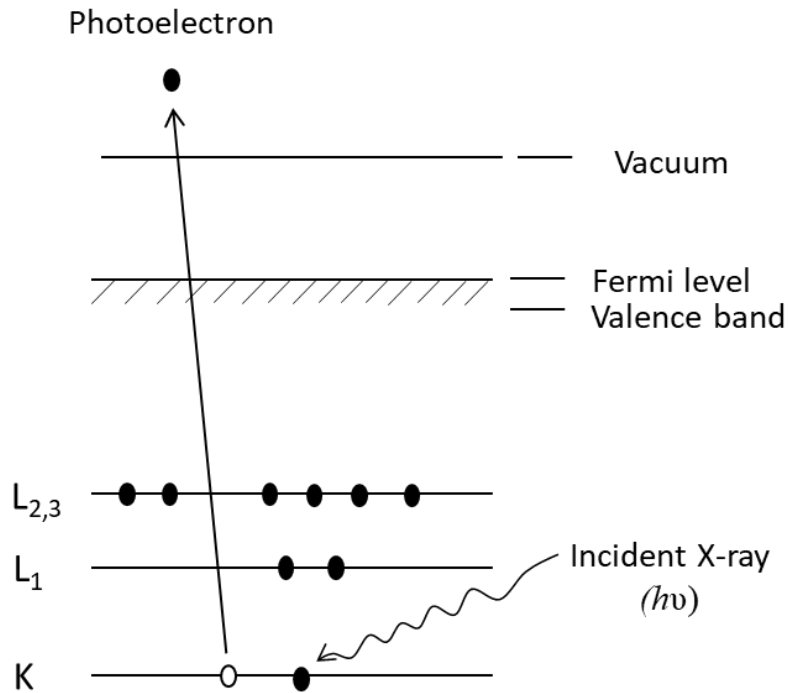


Figure 2.7. Schematic diagram of the photoemission process involved in the XPS technique. An electron can be ejected when an atom or molecule absorbs an X-ray photon. The surface elements and chemical states could be identified by detecting the kinetic energy (E_k) of the emitted electrons⁶⁴.

The photoelectron energy emitted from the sample is characteristic of each element.

The ejected photoelectrons' electron binding energy (E_b) is typically measured by the determined kinetic energy (E_k), Equation 2.17⁶⁴.

$$E_k = h\nu - E_b - \varphi \quad \text{Eq. 2.17}$$

where E_k is the kinetic energy of emitted electron; E_b is the binding energy of the emitted electron; h is Planck's constant; ν is the frequency of incident X-ray, and φ is the work function of the spectrometer.

In a typical experiment, X-ray photoelectron spectroscopy (XPS) was performed with a Kratos Axis Nova spectrometer using a monochromatic AlK α X-ray source (225 W) with an analyser pass energy of 160 eV for survey scans and 20 eV for high-resolution scans. Three positions per sample were analysed using charge neutralisation. All XPS spectra were charge corrected by setting the C1s C-C/H component to 284.8 eV⁶⁷.

2.7.2.5. High-angle annular dark-field imaging – Scanning transmission electron microscopy (HAADF-STEM).

Scanning transmission electron microscopy technique (STEM) is a type of transmission electron microscopy (TEM), defined as one of the most used techniques for imaging characterisation at atomic-scale resolution⁶⁸. Unlike conventional TEM, in STEM, the imaging process is achieved by adjusting the microscope lenses to create a focused electron beam into a spot, which is then scanned across a specimen in a raster pattern, where various signals are collected point-by-point at this stage to produce an image⁶⁹.

High-angle annular dark field (HAADF) is a powerful detection technique used widely in scanning transmission electron microscopy (STEM) analysis, which offers a more direct interpretation of images for crystalline materials compared to other TEM detection techniques⁷⁰, as the intensity of images is sensitive to the atomic number (Z)⁷¹. Wherein for high atomic-number materials, more electrons are scattered at a higher angle due to increased electrostatic interactions between the nucleus and the electron beam, making HAADF detect a more significant signal from the elements with higher atomic numbers, leading to a brighter image. The images using this detector are acquired in scanning transmission mode by collecting the high angle scattered intensity ($\gg 10$ mrad)⁶⁸ at each probe position. HAADF provides incoherent images

due to incoherent elastically scattered electrons⁷², which means these images do not suffer from 'contrast reversals' due to the change in the specimen's thickness and defocus of the specimen⁷³.

This technique has a wide range of applications for studying the porous materials at the atomic scale and the characterisation of zeolite structures like pores structure of hierarchical micro- and meso-porous zeolite frameworks and the analysis of active metal centres in zeolites⁶⁸. Consequently, the HAADF-STEM technique was used in our research to gain high-resolution images that provide helpful information for visualising metal nanocatalysts in zeolites, such as the size and the size distribution of metal particles.

In a typical experiment, samples were prepared for transmission electron microscopy (TEM) analysis by dispersing and sonicating the catalyst powders in high-purity ethanol for ca. 10 min and allowing a drop of the suspension to dry on a Cu grid. HAADF-STEM images were acquired using an FEI Talos F200X operating at 200 keV under STEM mode. The frequency count for the particle size distribution for Sn/Y was obtained from a set of 200 particles. Data analysis and fitting of the particle size distributions were carried out using OriginPro 2022 software.

2.7.2.6. Extended X-ray absorption fine structure (EXAFS).

Extended X-ray absorption fine structure (EXAFS) spectroscopy is a type of X-ray absorption technique typically referring to the XAS spectrum region of 40-1000 eV after the absorption edge⁷⁴. EXAFS measurements are of interest as they can provide precise information on the types and number of neighbour atoms to the absorbing atom in the material⁷⁵.

In principle, EXAFS occurs due to an electron being interfered with itself. This excited electron scatters elastically off the neighbouring atoms (e.g., O) at a distance of R from the absorbing atom (e.g., Sn and Ga), causing fine structure oscillations. Further scattering amplitude probability, such as inelastic photoelectron scattering, loss of energy, or even failure of scattering, could also occur. This can be expressed with a proportionality constant $f(k)^{75}$:

$$\chi(k) = f(k) \cos(2kR) \quad \text{Eq. 2.18}$$

However, in view of multiple nearby atoms (i) as well as the difference in the number of the same atom surrounding the absorbing atom (N), there will be essentially a sum of all diverse scattering possibilities, so Eq. 2.18 can be rewritten as follows:

$$\chi(k) = \sum_i N_i f_i(k) \cos(2kR_i) \quad \text{Eq. 2.19}$$

Additional considerations to the above equation (Eq. 2.18) have been made over literature^{74,76} in view of the following factors **a)** the expression of the equation as a spherical wave instead of a plane wave, **b)** the mean free path of the photoelectron $\lambda(k)$ that arises from constructive and destructive interference, which are due to the energy removal and the change in wavelength for the scattered photoelectron, and **c)** the MSRD effect “mean square relative displacement” (σ^2), which is the sum of the thermal and static disorder.

The mean square relative displacement is the variance of the displacement, which typically falls in the range of $\sim 0.002 \text{ \AA}^2$ to $\sim 0.03 \text{ \AA}^2$. MSRD with a value larger than the

above-specified range suggests disorder/ amorphous in the crystal structure of the measured material⁷⁵. In view of all the above factors, and to obtain a formula that contains all of the relevant vital elements, which any correct theory must have, and also to provide an appropriate method for the fitting of local atomic structure nearby the absorber atom to the EXAFS experimental data, the standard EXAFS equation (Eq. 2.20) can be rearranged and written as the following⁷⁵:

$$\chi(k) = S_0^2 \sum_i N_i \frac{f_i(k)}{kR_i^2} e^{\frac{2R_i}{\lambda(k)}} e^{-2k^2\sigma_i^2} \sin(2kR_i + \delta_i(k)) \quad \text{Eq. 2.20}$$

In a typical experiment, extended X-ray absorption fine structure (EXAFS) spectra were collected at the Sn K-edge (29200 eV) and Ga K-edge (10367 eV). The measurements were carried out using a fixed-exit double-crystal Si(311) monochromator and Pt-coated branch of collimating mirrors for Sn, while Si(111) and Cr-coated branch were used for Ga. The beam size at the sample position was approximately 1×1mm. All samples were prepared in the form of pellets (13 mm diameter) using 200 mg of sample powder to maximise the edge jump (0.25 for Ga and 0.56 for Sn), maintaining a total transmission higher than 10%. The measurement was performed at room temperature in transmission mode using 3 ion chambers filled with different gas mixtures optimised for best detection efficiency at the two edges (for Sn K-edge I_0 : 50 mbar Kr/He $I_{t,ref}$: 200 mbar Kr/He, for Ga K-edge I_0 : 40 mbar Ar/He $I_{t,ref}$: 200 mbar Ar/He 10% absorption on I_0 and 70% absorption on $I_{t,ref}$). The spectra were collected in quick EXAFS mode by continuously scanning the monochromator with a constant energy step size of 0.3 eV. The scan covered an energy range from –200 to +1000 eV concerning the edge position, corresponding to a k-range of ca 16

Å⁻¹. For each sample, 10 scans were acquired and subsequently merged to improve the signal-to-noise ratio. Data were normalised using the program Athena⁷⁷, with a linear pre-edge and 2nd order polynomial post-edge. After background subtraction, the resulting $\chi(k)$ functions were k^3 -weighted and Fourier transformed in a range from 2.5 to 15.5 Å⁻¹. Fits were performed with Artemis software part of IFEFFIT suite⁷⁸; phases and amplitudes were calculated with FEFF code⁷⁴.

2.7.2.7. Inductively coupled plasma-mass spectrometry (ICP-MS).

Inductively coupled plasma mass spectrometry (ICP-MS) is an analytical technique that is extensively used in the determination of elements at trace levels in various sample matrices⁷⁹. In this context, ICP-MS was used in this research to determine the content of metal dopant (e.g., Sn and Ga) in the reaction mixture to investigate the effect of metal leaching during the reaction if present.

In principle, ICP uses a high frequency inductively coupled plasma as an atomizing source. The plasma is typically generated and sustained by argon gas flow⁸⁰, which has ionisation properties that allow the simultaneous ionisation of most of the periodic table elements, making the multi-element analysis possible⁸¹. In more detail, the sample is usually introduced to the plasma as liquid or solution⁸⁰. The solution is pumped into a nebuliser to generate an aerosol, then sprayed into a spray chamber that removes the large aerosol droplets (>10 µm)⁸² for the plasma. The nebuliser gas then directed the aerosol via the spray chamber to the plasma. The plasma is a highly energised and electrically neutral gas composed of ions, electrons, and neutral particles and has a temperature in the range of 5000-9000K⁸⁰. It involves the spontaneous emission of photons from atoms and ions that have been excited in a radiofrequency (RF) present in an induction coil⁸³. The sample aerosol in plasma is

then desolvated, vaporised, atomised, and ionised⁷⁹. The analyte atoms are then promoted from the ground to excited states using the additional energy imparted by the collisional excitation within the plasma⁸⁴. Ions are then extracted from the plasma, and their beam is guided toward the mass analyser using an ion optics system. Finally, their amount is measured at a specific mass-to-charge ratio (m/z)⁷⁹.

In a typical experiment, the determination of metal content was carried out using an Agilent 7500CE ICP-MS instrument which was calibrated up to 10 parts per billion (ppb) using solutions prepared by dilution from stock solutions containing 1000 parts per million (ppm) of the metal standards. The concentrations of metal ions in the samples were calculated against a calibration graph.

2.7.2.8. Thermogravimetric analysis (TGA).

Thermogravimetric analysis proves to be a valuable technique for gaining insights into the thermal behaviours of a material when exposed to heating under predetermined heating rate and temperature conditions. In this technique the weight change of a sample is typically determined as a function of a controlled change of temperature over time⁸⁵. For the context of our research, TGA was used to determine the total moisture and impurities content of our sugar samples⁸⁶. The TGA analysis of glucose, fructose, and mannose (Figure 3.1) was conducted to estimate the potential presence of moisture content in these sugars. This was accomplished by measuring the mass loss upon heating the samples at 180 °C (heating rate of 5 °C·min⁻¹) under a flow of nitrogen, followed by maintaining the temperature for a period of 30 min using a PerkinElmer Pyris 1 TGA analyzer.

2.8. References

- 1 C. Perego and P. Villa, *Catal. Today*, 1997, **34**, 281–305.
- 2 Israf Ud Din, Q. Nasir, M. D. Garba, A. I. Alharthi, M. A. Alotaibi and M. Usman, *Mini-Rev. Org. Chem.*, 2021, **19**, 92–110.
- 3 F. Pinna, 1998, **41**, 129–137.
- 4 Y. Yamada, T. Akita, A. Ueda, H. Shioyama and T. Kobayashi, *Rev. Sci. Instrum.*, 2005, **76**, 062226.
- 5 N. Kosinov, C. Liu, E. J. M. Hensen and E. A. Pidko, *Chem. Mater.*, 2018, **30**, 3177–3198.
- 6 P. Munnik, P. E. De Jongh and K. P. De Jong, *Chem. Rev.*, 2015, **115**, 6687–6718.
- 7 R. J. White, R. Luque, V. L. Budarin, J. H. Clark and D. J. Macquarrie, *Chem. Soc. Rev.*, 2009, **38**, 481–494.
- 8 M. Conte, J. A. Lopez-Sanchez, Q. He, D. J. Morgan, Y. Ryabenkova, J. K. Bartley, A. F. Carley, S. H. Taylor, C. J. Kiely, K. Khalid and G. J. Hutchings, *Catal. Sci. Technol.*, 2012, **2**, 105–112.
- 9 L. Sun, L. Jiang, X. Hua, Y. Zheng, X. Sun, M. Zhang, H. Su and C. Qi, *J. Alloys Compd.*, 2019, **811**, 152052.
- 10 A. A. Marianou, C. M. Michailof, A. Pineda, E. F. Iliopoulou, K. S. Triantafyllidis and A. A. Lappas, *Appl. Catal. A: Gen.*, 2018, **555**, 75–87.
- 11 X. Song, J. Yue, Y. Zhu, C. Wen, L. Chen, Q. Liu, L. Ma and C. Wang, *Ind. Eng. Chem. Res.*, 2021, **60**, 5838–5851.

- 12 A. Kohler, W. Seames, I. Foerster and C. Kadrmas, *Catalysts*, 2020, **10**, 1–16.
- 13 B. Tang, W. Dai, G. Wu, N. Guan, L. Li and M. Hunger, *ACS Catal.*, 2014, **4**, 2801–2810.
- 14 A. Rahman, M. Nurjayadi, R. Wartilah, E. Kusriani, E. A. Prasetyanto and V. Degermenci, *Int. J. Technol.*, 2018, **9**, 1159–1167.
- 15 B. Viswanathan and B. Jacob, *Catal. Rev. - Sci. Eng.*, 2005, **47**, 1–82.
- 16 A. M. Van Der Heijden, F. Van Rantwijk and H. Van Bekkum, *J. Carbohydr. Chem.*, 1999, **18**, 131–147.
- 17 M. Martin and G. Guiochon, *J. Chromatogr. A*, 2005, **1090**, 16–38.
- 18 L. R. Snyder, J. J. Kirkland and J. W. Dolan, *Introduction to Modern Liquid Chromatography*, John Wiley & Sons, Inc., Hoboken, NJ, USA, Third Edition., 2011.
- 19 V. R. Meyer, *Practical High-Performance Liquid Chromatography*, John Wiley & Sons, Cornwall, Great Britain, Fifth Edition., 2013.
- 20 J. De Vos, K. Broeckhoven and S. Eeltink, *Anal. Chem.*, 2016, **88**, 262–278.
- 21 P. Žuvela, M. Skoczylas, J. Jay Liu, T. Baczek, R. Kaliszan, M. W. Wong and B. Buszewski, *Chem. Rev.*, 2019, **119**, 3674–3729.
- 22 C. Ma, Z. Sun, C. Chen, L. Zhang and S. Zhu, *Food Chem.*, 2014, **145**, 784–788.
- 23 M. Dreux and M. Lafosse, in *Carbohydrate Analysis High Performance Liquid Chromatography and Capillary Electrophoresis*, ed. Z. el Rassi, Journal of Chromatography Library , 1st Edition., 1995, vol. 58, pp. 515–540.

- 24 P. Christen and J.-L. Veuthey, *Curr. Med. Chem.*, 2001, **8**, 1827–1839.
- 25 P. Shanmugavelan, S. Y. Kim, J. B. Kim, H. W. Kim, S. M. Cho, S. N. Kim, S. Y. Kim, Y. S. Cho and H. R. Kim, *Carbohydr. Res.*, 2013, **380**, 112–117.
- 26 N. Adnani, C. R. Michel and T. S. Bugni, *J. Nat. Prod.*, 2012, **75**, 802–806.
- 27 V. S. Nayak, Z. Tan, P. M. Ihnat, R. J. Russell and M. J. Grace, *J. Chromatogr. Sci.*, 2012, **50**, 21–25.
- 28 V. L. Cebolla, L. Membrado, J. Vela and A. C. Ferrarido, *J. Chromatogr. Sci.*, 1997, **35**, 141–150.
- 29 A. El-Aneed, A. Cohen and J. Banoub, *Appl. Spectrosc. Rev.*, 2009, **44**, 210–230.
- 30 J. R. Yates, C. I. Ruse and A. Nakorchevsky, *Annu. Rev. Biomed. Eng.*, 2009, **11**, 49–79.
- 31 T. Gruending, S. Weidner, J. Falkenhagen and C. Barner-Kowollik, *Polym. Chem.*, 2010, **1**, 599–617.
- 32 R. Cozzolino and B. De Giulio, *Eur. J. Lipid Sci. Technol.*, 2011, **113**, 160–167.
- 33 A. Steckel and G. Schlosser, *Molecules*, 2019, **24**, 611.
- 34 T. R. Covey, B. A. Thomson and B. B. Schneider, *Mass Spectrom. Rev.*, 2009, **28**, 870–897.
- 35 J. B. Fenn, M. Mann, C. K. Meng, S. F. Wong and C. M. Whitehouse, *Science (1979)*, 1989, **246**, 64–71.

- 36 C. Markert, M. Thinius, L. Lehmann, C. Heintz, F. Stappert, W. Wissdorf, H. Kersten, T. Benter, B. B. Schneider and T. R. Covey, *Anal. Bioanal. Chem.*, 2021, **413**, 5587–5600.
- 37 T. Chen, Q. Yao, R. R. Nasaruddin and J. Xie, *Angew. Chem.*, 2019, **131**, 12093–12103.
- 38 N. B. Cech and C. G. Enke, *Mass Spectrom. Rev.*, 2001, **20**, 362–387.
- 39 S. Banerjee and S. Mazumdar, *Int. J. Anal. Chem.*, 2012, **2012**, 1–40.
- 40 G. J. van Berkel and V. Kertesz, in *Electrospray and MALDI Mass Spectrometry*, John Wiley & Sons, Inc., Hoboken, NJ, USA, 2012, pp. 75–122.
- 41 E. P. L. Hunter and S. G. Lias, *J. Phys. Chem. Ref. Data.*, 1998, **27**, 413–656.
- 42 N. E. Es-Safi, L. Kerhoas and P. H. Ducrot, *Rapid Commun. Mass Spectrom.*, 2007, **21**, 1165–1175.
- 43 M. K. Singh and A. Singh, in *Characterization of Polymers and Fibres*, Elsevier, 2022, pp. 321–339.
- 44 J. H. F. Bothwell and J. L. Griffin, *Biol. Rev.*, 2011, **86**, 493–510.
- 45 R. A. Graaf, *In Vivo NMR Spectroscopy*, John Wiley & Sons Ltd., The Atrium, Southern Gate, Chichester, West Sussex, PO19 8SQ, UK, Third Edition., 2019.
- 46 James Keeler, *Understanding NMR Spectroscopy*, John Wiley & Sons Ltd., Cambridge. The UK, 2nd Edition., 2010.
- 47 V. P. B. Grover, J. M. Tognarelli, M. M. E. Crossey, I. J. Cox, S. D. Taylor-Robinson and M. J. W. McPhail, *J. Clin. Exp. Hepatol.*, 2015, **5**, 246–255.

- 48 Harald Günther, *NMR Spectroscopy: Basic Principles, Concepts and Applications in Chemistry*, Wiley-VCH Verlag GmbH & Co. KGaA, Boschstr. 12,69496, Weinheim, Germany, Third Edition., 2013.
- 49 S. Tantisriyanurak, H. N. Duguid, L. Peattie and R. Dawson, *ACS Appl. Polym. Mater.*, 2020, **2**, 3908–3915.
- 50 C. Tyl and G. D. Sadler, in *Food analysis*, Springer, 2017, pp. 389–406.
- 51 M. Conte, B. Xu, T. E. Davies, J. K. Bartley, A. F. Carley, S. H. Taylor, K. Khalid and G. J. Hutchings, *Microporous Mesoporous Mater.*, 2012, **164**, 207–213.
- 52 D. Dollimore, P. Spooner and A. Turner, *Surf. technol.*, 1976, **4**, 121–160.
- 53 P. Sinha, A. Datar, C. Jeong, X. Deng, Y. G. Chung and L. C. Lin, *J. Phys. Chem. C*, 2019, **123**, 20195–20209.
- 54 F. Ambroz, T. J. Macdonald, V. Martis and I. P. Parkin, *Small Methods*, 2018, **2**, 1800173.
- 55 K. E. Hart, L. J. Abbott and C. M. Colina, *Mol. Simul.*, 2013, **39**, 397–404.
- 56 Y. S. Ding, X. F. Shen, S. Sithambaram, S. Gomez, R. Kumar, V. M. B. Crisostomo, S. L. Suib and M. Aindow, *Chem. Mater.*, 2005, **17**, 5382–5389.
- 57 I. C. Medeiros-Costa, C. Laroche, J. Pérez-Pellitero and B. Coasne, *Microporous Mesoporous Mater.*, 2019, **287**, 167–176.
- 58 A. Mohammed, A. U. Ahmed, H. Ibraheem, M. Kadhom and E. Yousif, in *AIP Conference Proceedings*, 2022, vol. 2450, p. 020007.
- 59 D. J. Morgan, *Clay Miner.*, 1990, **25**, 544–545.
- 60 E. S. Ameh, *Int. J. Adv. Manuf. Technol.*, 2019, **105**, 3289–3302.

- 61 F. Sánchez-Bajo and F. L. Cumbreira, *J. Appl. Crystallogr.*, 1999, **32**, 730–735.
- 62 R. J. Hill and L. M. D. Cranswick, *J. Appl. Crystallogr.*, 1994, **27**, 802–844.
- 63 Database of Zeolite Structures, <http://www.iza-structure.org/databases/>, (accessed 12 November 2022).
- 64 D. R. Baer and S. Thevuthasan, in *Handbook of Deposition Technologies for Films and Coatings: Science, Applications and Technology*, Elsevier, 2009, pp. 749–864.
- 65 A. Neville, R. R. Mather and J. I. B. Wilson, in *Plasma Technologies for Textiles: A Volume in Woodhead Publishing Series in Textiles*, Elsevier Ltd, 2007, pp. 301–315.
- 66 R. R. Mather, in *Surf. Mod. Text.*, Elsevier Inc., 2009, pp. 296–317.
- 67 D. Briggs and G. Beamson, *Anal. Chem*, 1992, **64**, 1729–1736.
- 68 W. Wan, J. Su, X. D. Zou and T. Willhammar, *Inorg. Chem. Front.*, 2018, **5**, 2836–2855.
- 69 S. J. Pennycook, *Ultramicroscopy*, 1989, **58**, 58–69.
- 70 H. Vanrompay, A. Skorikov, E. Bladt, A. Béché, B. Freitag, J. Verbeeck and S. Bals, *Ultramicroscopy*, 2021, **221**, 113191.
- 71 J. Y. Zhang, J. Hwang, B. J. Isaac and S. Stemmer, *Sci. Rep.*, 2015, **5**, 12419.
- 72 B. Fultz and J. M. Howe, in *Transmission Electron Microscopy and Diffractometry of Materials*, Springer Berlin Heidelberg, Berlin, Heidelberg, 2008, pp. 583–609.
- 73 B. Mendis, *Microscopy and Microanalysis*, 2010, **16**, 1948–1949.

- 74 J. J. Rehr and R. C. Albers, *Rev. Mod. Phys.* , 2000, **72**, 621–653.
- 75 E. A. Stern, D. E. Sayers and F. W. Lytle, *Phys. Rev. B.*, 1975, **11**, 4836–4846.
- 76 D. E. Sayerst, E. A. Sterntf and F. W. Lytle, *Phys. Rev. Lett.*, 1971, **27**, 1204–1207.
- 77 A. J. Dent, G. Cibin, S. Ramos, A. D. Smith, S. M. Scott, L. Varandas, M. R. Pearson, N. A. Krumpa, C. P. Jones and P. E. Robbins, *J. Phys. Conf. Ser.*, 2009, **190**, 012039.
- 78 B. Ravel and M. Newville, *J. Synchrotron Radiat.*, 2005, **12**, 537–541.
- 79 S. C. Wilschefski and M. R. Baxter, *Clin. Biochem. Rev.*, 2019, **40**, 115–133.
- 80 C. G. Novaes, M. A. Bezerra, E. G. P. da Silva, A. M. P. dos Santos, I. L. da S. Romão and J. H. Santos Neto, *Microchem. J.* , 2016, **128**, 331–346.
- 81 P. J. Potts, in *Treatise on Geochemistry: Second Edition*, Elsevier Inc., 2013, vol. 15, pp. 171–180.
- 82 B. L. Sharp, *J. Anal. At. Spectrom.*, 1988, **3**, 613–652.
- 83 E. Paredes, J. Bosque, J. M. Mermet and J. L. Todolí, *Spectrochim Acta Part B At Spectrosc*, 2010, **65**, 908–917.
- 84 X. Hou and B. T. Jones, *Encyclopedia of analytical chemistry*, 2000, **11**, 9468–9485.
- 85 S. Ebnesajjad, in *Handbook of Adhesives and Surface Preparation: Technology, Applications and Manufacturing*, ed. S. Ebnesajjad, William Andrew imprint of Elsevier, 1st Edition., 2011, pp. 31–48.
- 86 S. Ceylan and Y. Topçu, *Bioresour. Technol.*, 2014, **156**, 182–188.

Chapter 3: Solubility of Glucose, Fructose and Mannose in Water and Alcohol Media.

3.1. Introduction

Solubility is an important characteristic that determines a substance's ability to dissolve in a specific solvent¹, which is often not significantly considered in many publications²⁻⁵. In contrast, it can have significant implications on catalyst productivity, that is, the amount of product that can be obtained per amount of catalyst per time. Furthermore, it might also lead to an inaccurate determination of the catalytic activity of the materials being studied.

In particular, for scale-up production, the higher the concentration of sugar in the solution, the greater the expected productivity per volume of the reaction mixture of isomers at the end of the reaction. This is relevant because for the isomerisation reaction of glucose to fructose, not all zeolites (either doped or undoped) are active in water⁶, whereas glucose and its isomers are significantly less soluble when moving from water to methanol or a longer chain of alcohols. For instance, the solubility of glucose decreases from ca. 480 g·L⁻¹ in water⁷ to ca. 23 g·L⁻¹ in methanol⁸. This justifies an increase in reaction temperature (usually in the range of 100 °C) not only to accelerate the reaction and activate the catalyst but also to allow for a greater amount of sugar to be solubilized under reaction conditions.

Furthermore, sugar solubility data are essential for another reason. In order to obtain accurate calculations for conversion or selectivity, a closed carbon mass balance is required. However, despite the large number of papers addressing the isomerisation of sugars, many practical experimental details have not been clearly documented in

the literature or simply disregarded as “data obtained from calibration curves”^{9–11}. Many, if not most, measurements of reaction mixtures are carried out after the reaction has cooled down at room temperature from a surfactant solution that has been recovered and separated from a solid catalyst. Whereas this is the most obvious choice, it may induce errors in calculations, especially for reaction mixtures in which the initial amount of sugar is higher than its solubility limit at room temperature. Sampling a surfactant solution of a sugar that is only partially solubilized could lead to a significant error in the conversion calculation and selectivity for our class of reactions. Especially if the reaction did not proceed, and the detection of a small amount of glucose left in the solution would be the result of a limited solubility instead of the reactivity of this species. Thus, hampering the reproducibility of data among different laboratories and the development of catalysts by design.

For example, substrate A has an actual solubility of 40 g·L⁻¹ and 60 g·L⁻¹ in water at room temperature and 100 °C, respectively. A solution is prepared by mixing 60 g of A in 1 L of water. A reaction was carried out using an inactive catalyst (no conversion of A can be triggered by this catalyst) at 100 °C where all the substrate A is soluble, and then the reaction mixture is cooled down to room temperature after the reaction is concluded. At this temperature, the solubility of A decreased from 60 g·L⁻¹ to 40 g·L⁻¹, which means this reaction mixture contains a solution of A with a real concentration of 40 g·L⁻¹ and a precipitate of 20 g of A accumulated. The characterisation result (HPLC or NMR etc.) will show a solution of A of 40 g·L⁻¹ provided the catalyst is nonactive, however, it is expected to have an artificial concentration of 60 g·L⁻¹. As a result, an artefact conversion of 33% instead of 0% will be concluded based on the characterisation data. Therefore, misusing the correct solubility will lead to a

conversion higher than expected and is likely to result in a wrong interpretation of the catalytical performance especially when a new catalyst is under investigation.

Thus, this chapter aims to assess and identify **1)** the purity and stability of glucose, fructose, and mannose by the mean of melting point measurements, thermogravimetric analysis (TGA), and ^1H and ^{13}C nuclear magnetic resonance (NMR) Spectroscopy. **2)** the development of a reliable HPLC analysis method for the determination of glucose, fructose, and mannose solubility in different pure solvents. **3)** a more comprehensive and flexible data set of sugar solubility, alongside their experimental errors, expressed in different concentration units, that can help to clarify the large discrepancies in solubility data reported in the literature which prompted us to experimentally determine solubility values to be used for this thesis work.

3.2. Purity and stability assessment of sugars.

Prior to the solubility determination of glucose, fructose, and mannose, it is crucial to evaluate their purity by estimating the presence of impurities and moisture contents in the sugar samples. For instance, sugar impurities can significantly alter the reaction rate by either acting as a catalyst and increasing the rate or reacting with the sugar and decreasing the rate. Impurities in sugars can also leach out into the reaction solution, change its pH and, in turn, neutralize the acidic environment required for biomass conversion. Also, the formation of by-products can be promoted via the reaction of sugar impurities with reactants, intermediates, or products. Furthermore, impurities in initial reactants could be carried over to the final product, affecting their quality and purity¹²⁻¹⁴. Given this relevance, the purity of sugars was thoroughly assessed using an array of analytical techniques, which are reported below.

3.2.1. Melting point measurements.

Melting point is widely used to estimate the purity of chemicals in their solid state¹⁵. Pure crystalline compounds generally tend to have a sharp melting point range. In other words, the temperature difference at which compounds begin to melt and are completely melted is relatively narrow (≤ 5 °C)¹⁶. The presence of impurities, even in a small quantity (≤ 500 ppm)¹⁷, would decrease the melting points, broaden their range¹⁶, and, more importantly, affect their solubility data¹⁸. In view of this, the melting points of glucose, fructose, and mannose, in their solid form were determined by visual observation using a melting-point apparatus instrument (Table 3.1).

Table 3.1. Melting point range for glucose, fructose, and mannose. The initial value represents the temperature at which the sugar began melting, and the second value corresponds to the temperature at which the sugars were fully melted. The temperature increase during the measurements was controlled at a ramp rate of 5 °C/min.

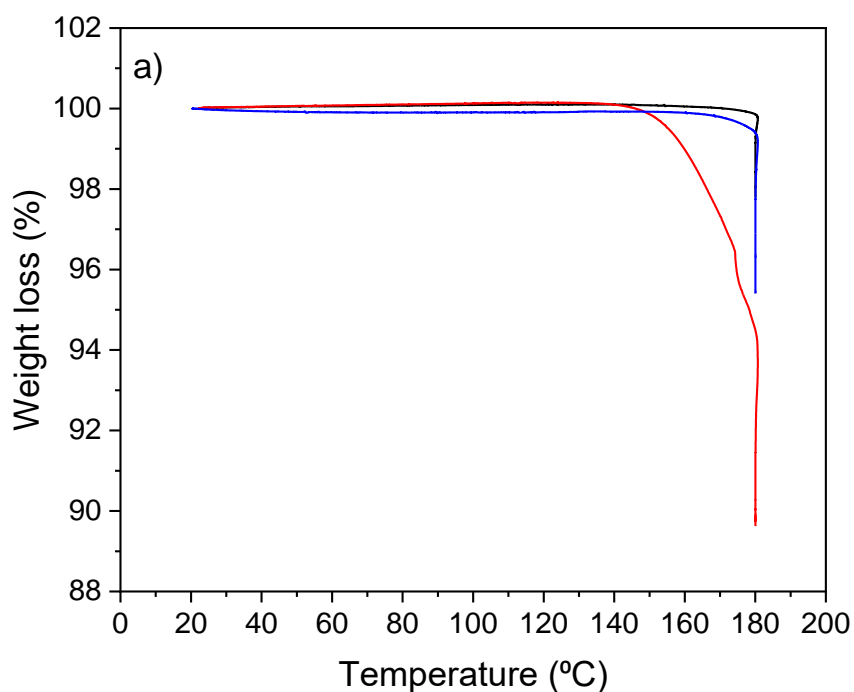
Sugar	Melting point range (°C \pm 1)	Melting point values in literature (°C)
Glucose	147 – 151	148 – 150
Fructose	103 – 105	102 – 104
Mannose	130 – 133	132

As shown in Table 3.1, glucose melts at the highest temperature of all sugars studied, with a melting point range of 147 – 151 °C. Mannose, on the other hand, has a melting point temperature in the range of 130 - 133 °C. At the same time, fructose showed the lowest melting point with a temperature range of 103 - 105 °C. In addition, the measured melting point values obtained herein were highly in agreement with the data reported in the literature (Glucose: 148 – 150 °C, Fructose: 102 – 104 °C, and Mannose: 132 °C)^{19,20} and accurately matched the melting point data provided by

chemical suppliers, which indicates that our sugar samples of glucose, fructose and mannose are relatively pure.

3.2.2. Thermogravimetric analysis (TGA).

Thermogravimetric analysis is a technique in which the weight change of a sample is determined as a function of a controlled change of temperature with time²¹. Using such a method, the total moisture and impurities content of a sample can be estimated²². TGA analysis of glucose, fructose, and mannose (Figure 3.1) was carried out to quantify moisture content in sugars by measuring the mass loss upon heating the samples at 180 °C (heating rate of 5 °C·min⁻¹) under a flow of nitrogen and then holding the temperature for a period of 30 min.



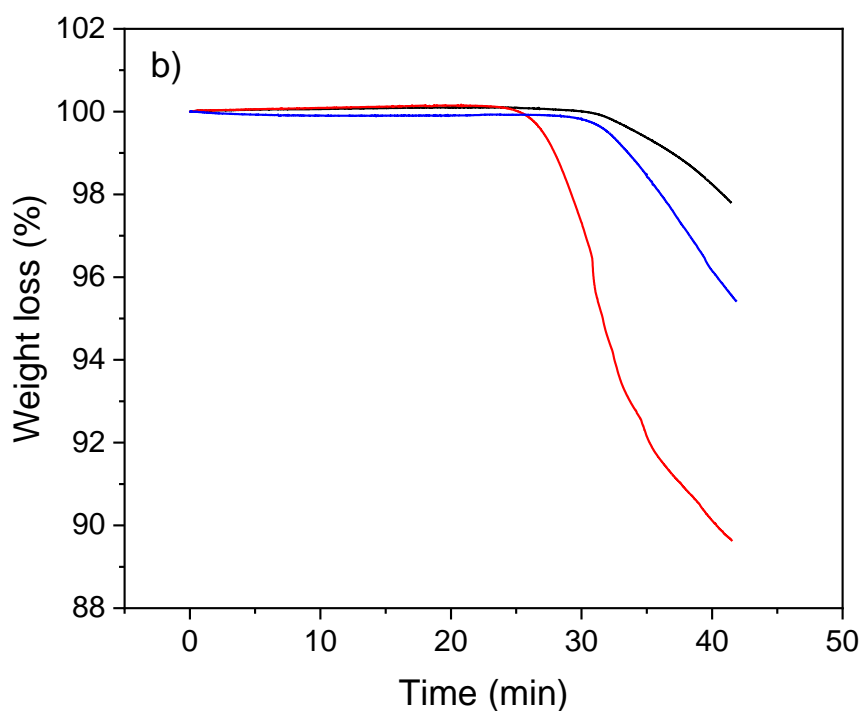


Figure 3.1. The weight change (TGA curves) as a function of **a)** temperature and **b)** time as a function of time (right) for glucose, fructose, and mannose.

As can be seen from the TGA measurements, no weight loss (i.e., compatible with the background of the baseline) was detected in the analysis of glucose, fructose, and mannose. Thus, indicating that all sugar samples were not containing any appreciable amount of moisture and as such not affecting our M:S ratio during the catalytic test. In addition, all samples were found to be melting. As a consequence, this is likely to explain the drop in remaining mass observed during the 10 min isothermal.

3.2.3. ^1H and ^{13}C Nuclear Magnetic Resonance Spectroscopy (NMR).

The anomeric equilibrium of sugars is another significant characteristic that can affect their solubility and stability in solution²³. The anomeric equilibrium of sugars refers to

the process by which the alpha (α) and beta (β) anomers of a sugar molecule are interconverted in an aqueous solution²⁴ (Figure 3.2). Essentially, the alpha and beta anomers are two stereoisomers of the same sugar molecule, which differ only in the configuration of their hydroxyl groups at the anomeric carbon. In the β -anomer, the hydroxyl group (-OH) attached to the first carbon atom is positioned upward, unlike in the α -anomer, which is positioned in a downward direction. As a consequence of this structural difference, there are differences in the intramolecular hydrogen bonding patterns of the two glucose anomers²⁵.

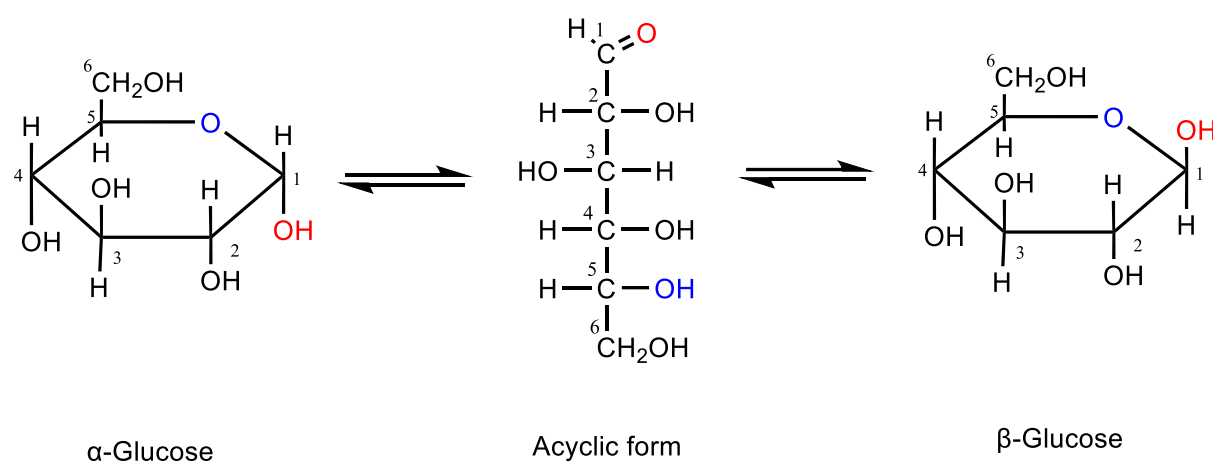


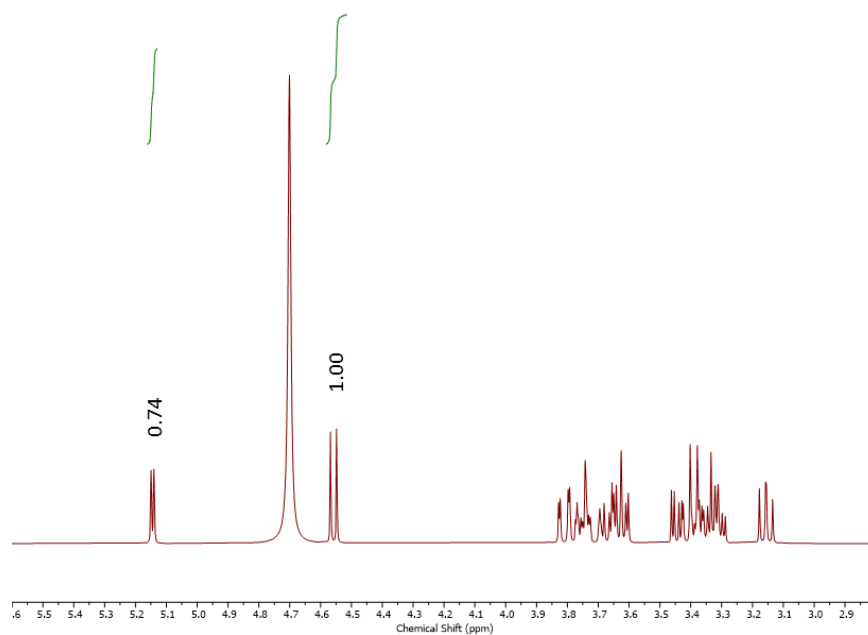
Figure 3.2. Schematic representation of anomeric forms of cyclic glucose in solution in equilibrium obtained by the mean of mutarotation reaction through the acyclic form, which is defined as the gradual change in rotation to an equilibrium point.

For example, the beta (β) form of glucose is more stable in water than the alpha (α) form²⁶. This could be explained by strong solvation effects²⁷; that is, the beta anomer possesses a more extended conformation that allows it to be capable of forming more hydrogen bonds with water molecules. In contrast, the alpha anomer exhibits a more compact conformation that makes it less capable of interacting with water molecules.

The β -anomer may preferably be solvated because it fits neatly into a tridymite ice lattice, with the water-water hydrogen bonds being replaced by glucose-water hydrogen bonds²⁸. This results in the β -anomer being more stable and with a longer lifetime in solution than the α -anomer. In addition, the change in anomeric equilibrium could also influence the solubility of sugars. For instance, it has been demonstrated in previous studies that β -glucose exhibits a higher solubility as compared to α -glucose in an aqueous solution^{29,30}. This could be due to its more significant degree of hydration, which results from the hydroxyl group on the first carbon atom (C1) being oriented in a way that allows the formation of more hydrogen bonds with water molecules^{31,32}.

In view of this, the anomeric equilibrium composition of aqueous glucose, fructose and mannose solutions has been determined from the ^1H and ^{13}C NMR chemical shifts of the individual anomers in D_2O at 20 °C. The peak assignments of glucose, fructose, and mannose were carried out according to previously published literature studies^{33–36}. The anomeric ratios of all sugars studied were determined by measuring the intensity of the signals of $\alpha\text{-H-1}/\beta\text{-H-1}$ in ^1H NMR spectrums and $\alpha\text{-C-1}/\beta\text{-C-1}$ in ^{13}C NMR spectrums (Figures 3.3 – 3.5).

¹H NMR of Glucose



¹³C NMR of Glucose

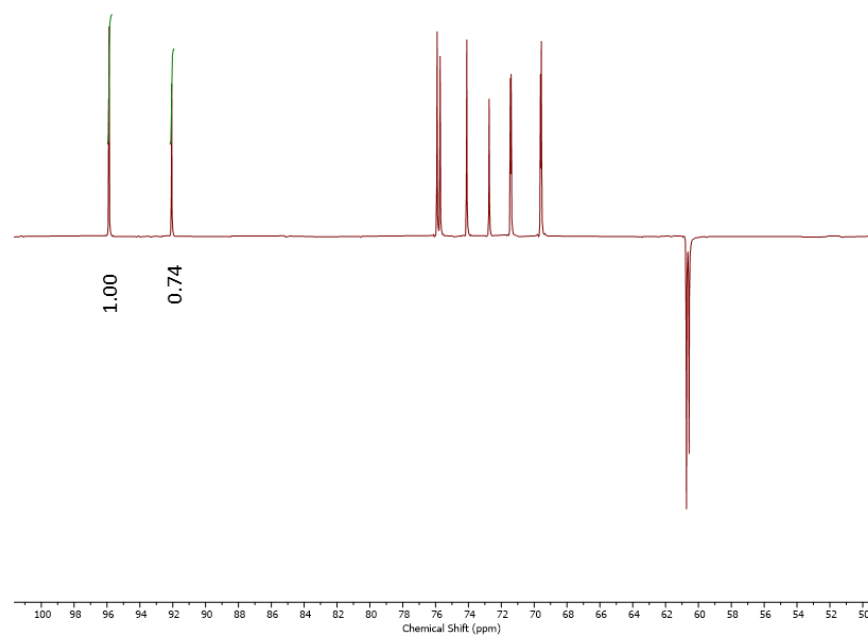
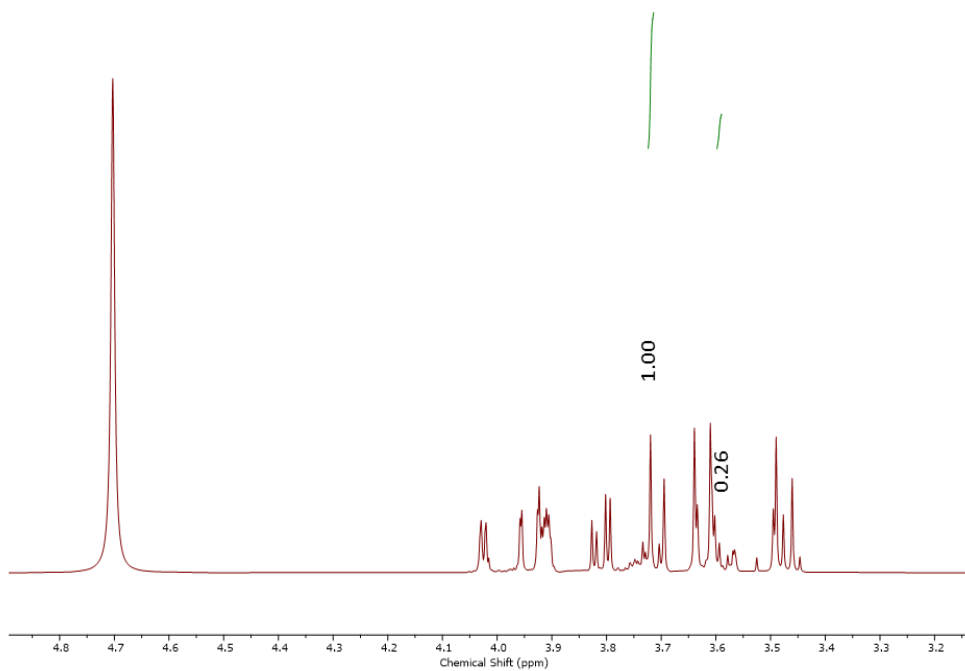


Figure 3.3. ¹H and ¹³C NMR spectra at 400 and 100.2 MHz, respectively for D-Glucose equilibrated in D₂O (0.55 M) at 20 °C, showing the α- and β-anomeric distribution at equilibrium.

^1H NMR of Fructose



^{13}C NMR of Fructose

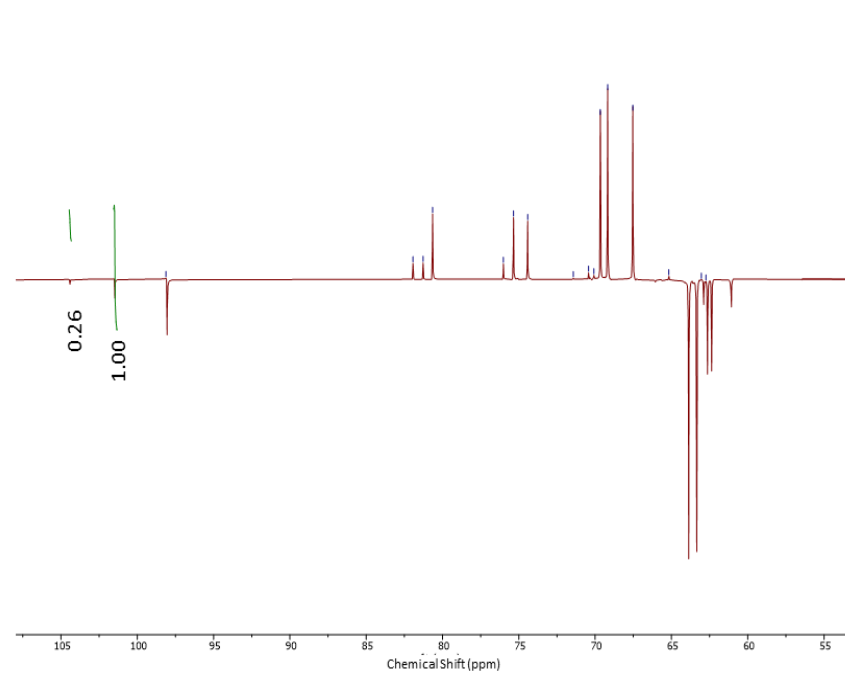


Figure 3.4. ^1H and ^{13}C NMR spectra at 400 and 100.2 MHz, respectively for D-Fructose equilibrated in D_2O (0.55 M) at 20 °C, showing the α - and β -anomeric distribution at equilibrium.

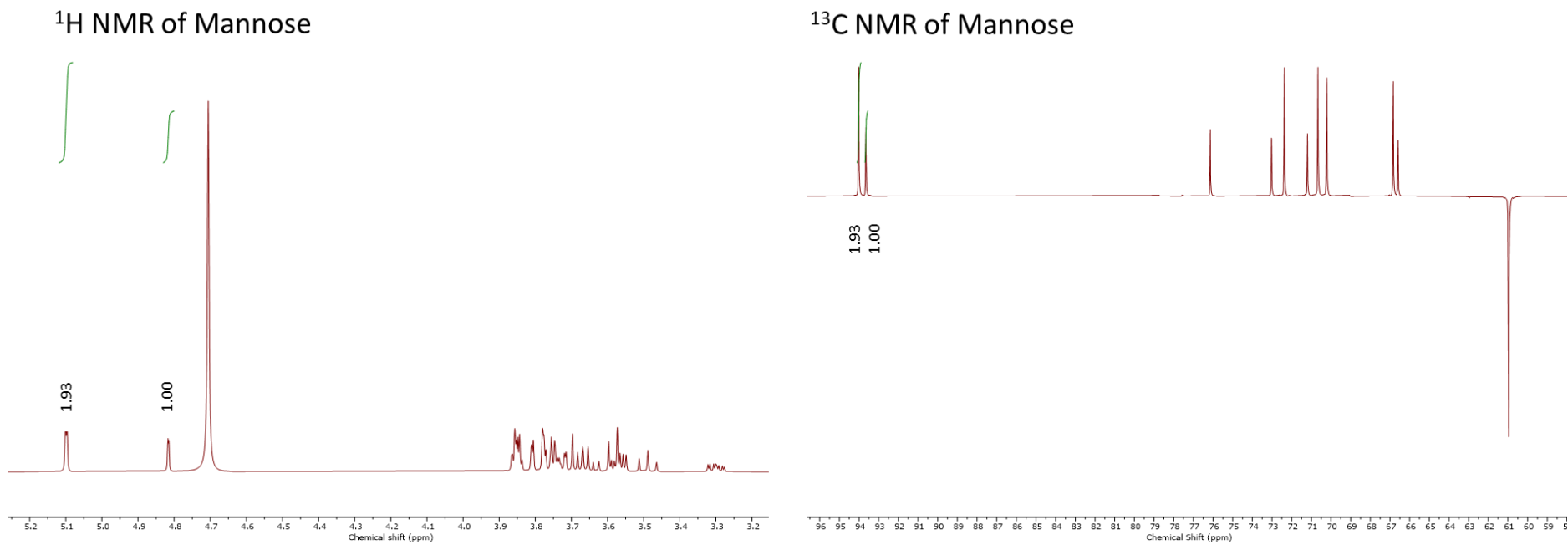


Figure 3.5. ¹H and ¹³C NMR spectra at 400 and 100.2 MHz, respectively for D-Mannose equilibrated in D₂O (0.55 M) at 20 °C, showing the α- and β-anomeric distribution at equilibrium.

The results of the anomeric composition of glucose, fructose, and mannose, alongside their proton and carbon NMR chemical shifts, are reported in Table 3.2.

Table 3.2. Measured anomeric composition (α and β), together with their proton (^1H) and carbon (^{13}C) NMR chemical shift values (δ , ppm), of glucose, fructose, and mannose aqueous solutions in D_2O at 20 °C.

Sugar anomer	^1H 1 chemical shift (ppm)	^{13}C 1 chemical shift (ppm)	β : α molar ratio	percentage concentrations (%)	
				α -anomer	β -anomer
α -Glucose	5.14	92.01	1:0.74	42	58
β -Glucose	4.55	95.87			
α -Fructose	3.59	105.00	1:0.26	21	79
β -Fructose	3.71	102.00			
α -Mannose	5.10	94.01	1:1.39	58	42
β -Mannose	4.81	93.64			

As can be seen, in the case of glucose, the β -anomer had a higher percentage concentration of 58% at equilibrium, compared to 42% of the α -anomer in D_2O at 20 °C. In contrast, mannose showed an opposite anomeric distribution, with the α -anomer being more predominant than the β -anomer with an anomeric distribution of 58% and 42% for α -anomer and β -anomer, respectively, at equilibrium. On the other hand, fructose revealed that the β -anomer was the dominant species, exhibiting a percentage concentration of 79% as compared to 21% of the α -anomer at equilibrium. In all cases, the results were reasonably consistent with the expected equilibrium compositions previously reported in the literature (Glucose: α/β equilibrium of 36:64³³, Fructose: α/β equilibrium of 18:82³⁷, Mannose: α/β equilibrium of 64:36)³⁸.

3.3. Development of HPLC diagram method for solubility determination.

The solubility of common sugars like glucose, fructose and mannose has been widely reported in the literature. However, there is significant variation in the literature concerning the solubility values derived from different methods, ranging from the isothermal and gravimetric methods to the refractive index³⁹⁻⁴¹. For instance, fructose solubility at room temperature has been reported to be 121 g·L⁻¹ when measured by the isothermal method⁴² and 142 g·L⁻¹ when measured by gas chromatography⁸. To date, isothermal and refractometric methods have been commonly preferred for solubility determination, either due to the accuracy of the isothermal³⁹ and gravimetric methods⁴¹ or the rapid analysis and low cost associated with the refractometric method⁴⁰. Despite these advantages, there are also some limitations to be considered, including the lengthy process and solute dependent of the isothermal methods and the gravimetric method^{39,41} and the lack of accuracy of refractive indexes⁴³ when compared to other methods, such as liquid chromatography combined with evaporative light scattering detector, which is a powerful and more accurate technique for this purpose but was only used by limited researchers⁴⁴. In view of this and through the use of high-performance liquid chromatography (HPLC) equipped with an evaporative light scattering detector (ELSD), we applied a regression method applicable to any solute and any solvent (Figure 3.3) and (Figures A5 – A18 in Appendix A.3) to accurately determine the solubility of glucose, fructose, and mannose in water and various alcohols such as methanol, ethanol, 1-propanol, and isopropanol at room temperature.

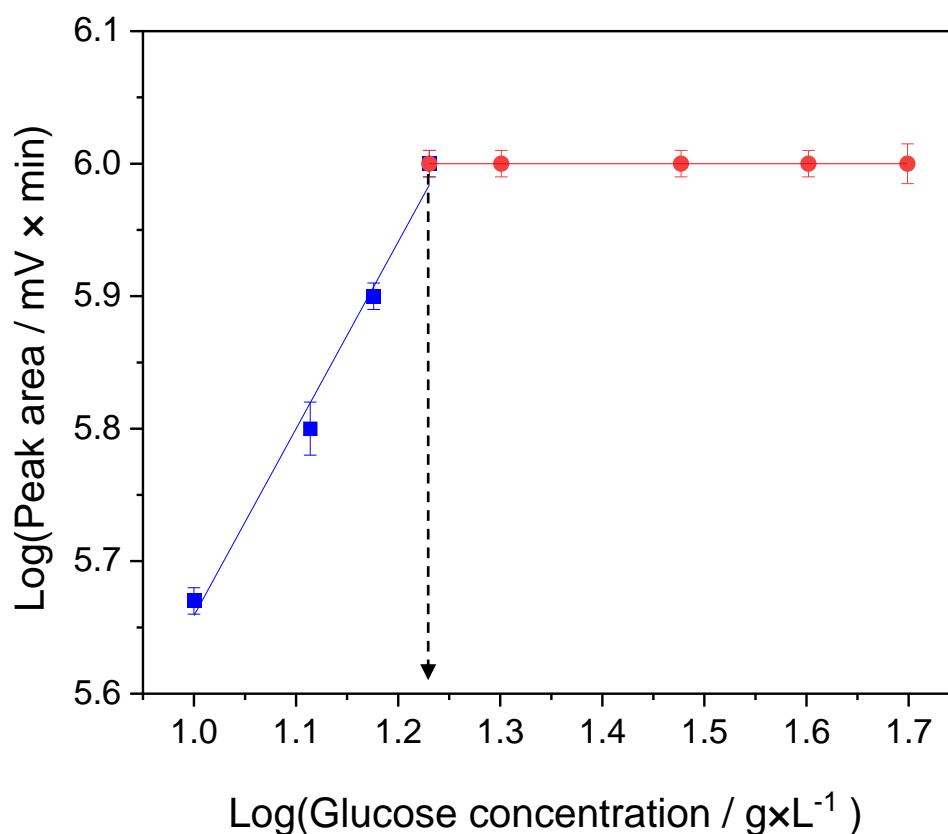


Figure 3.3. A representative example of the working principle of solubility determination by chromatography (e.g., Glucose in methanol 10 – 50 g·L⁻¹). A linear correlation between an HPLC signal and the sample concentration is expected within the solubility limit (■), whereas a constant saturation value should be detected upon saturation and by analysing the surfactant solution (●). The intersection of these two regression lines determines the solubility of a compound.

Regression parameters of 1.41 and 4.25 for the slope and intercept respectively of the regression line before the saturation point (blue line), as well as regression parameters of 0.00 and 6.00 for the slope and intercept respectively of the regression line after the saturation point (red line), were obtained and used in the calculation of solubility values.

3.4. Solubility measurements of sugars in solutions.

As described in the previous section (section 3.3), we could successfully build solubility diagrams up to the saturation point of a solution to systematically measure the solubility of glucose, fructose, and mannose in water, methanol, ethanol, 1-propanol and isopropanol at 20 °C. In particular, peak areas were plotted against sugar concentrations in order to obtain a calibration curve. Two linear regressions, $y = a x + b$, were observed and used to fit the data to their formulas, wherein the slope a and intercept b were calculated through OriginLab software using equations (3.1 and 3.2), respectively.

$$a = \frac{\sum (x_i - \bar{x})(y_i - \bar{y})}{\sum (x_i - \bar{x})^2} \quad Eq. 3.1$$

$$b = \bar{y} - a\bar{x} \quad Eq. 3.2$$

The solubility was then determined using the regression parameters of the two lines observed upon saturation point, as in Equation 3.3.

$$Solubility = \frac{b_2 - b_1}{a_1 - a_2} \quad Eq. 3.3$$

Where b_1 and b_2 are the intercept values of the regression line before and after the saturation point, respectively, whereas a_1 and a_2 are the slope values of these two lines, the measured solubility values of glucose, fructose, and mannose expressed in grams of sugar per 1 L of solution ($\text{g}\cdot\text{L}^{-1}$) are reported in (Table 3.3).

Table 3.3. Solubility data of glucose, fructose, and mannose in water, methanol, ethanol, 1-propanol and isopropanol measured at 20 °C and expressed in weight-to-volume values (g·L⁻¹). Glucose showed the lowest solubility values among other sugars in all solvents.

Sugar	Solubility of Sugars (g·L ⁻¹)				
	Water	Methanol	Ethanol	1-propanol	Isopropanol
Glucose	505 ± 2	17 ± 4	2 ± 1	2 ± 1	2 ± 1
Fructose	732 ± 3	111 ± 3	10 ± 3	5 ± 2	4 ± 2
Mannose	639 ± 2	108 ± 5	8 ± 3	4 ± 2	3 ± 1

As expected, all sugars studied were highly soluble in water, with solubility values of 505, 732, and 639 g·L⁻¹ for glucose, fructose, and mannose, respectively. However, this was significantly decreased when alcohols were used as solvents. For instance, glucose showed a solubility value of 17 g·L⁻¹ in methanol, which is consistent, within the experimental error, with 23 g·L⁻¹ obtained by Montañés et al. using Gas chromatography at 22 °C⁸. On the other hand, Mannose and fructose were relatively soluble in methanol, resulting in solubility values in the range of 110 g·L⁻¹, with fructose solubility being, within the experimental error, in agreement with 121 g·L⁻¹ measured by an isothermal method at 25 °C⁴². Furthermore, when longer carbon chain alcohols, such as ethanol, 1-propanol, and isopropanol, were used as solvents, the solubility showed another dramatic decrease, indicating that solubility decreased with the increase in the length of the alcohol carbon chain. Specifically, glucose, fructose, and mannose demonstrate solubility values of 2, 10, and 8 g·L⁻¹ in ethanol, compatible with data reported by Montañés et al. using gas chromatography at 22 °C⁸. Furthermore, using 1-propanol and isopropanol resulted in much lower solubility values (≤ 5 g·L⁻¹) than in ethanol. Among all sugars tested, fructose exhibited the highest solubility values in all solvents, followed by mannose and glucose in decreasing order of

solubility. The solubility of these sugars decreases in the order of water \geq methanol \geq ethanol \geq 1-propanol \geq isopropanol.

Despite the usefulness of investigations concerning the measurement of sugar solubility, there are many relevant details that are not reported in many published works^{8,44,45}. Furthermore, in order to compare our data with those reported in the literature, which makes use of an array of different (and often non-consistent) units our solubility data were expressed in various modes (Table 3.4), including weight percentage (wt %), molar fractions, molality ($\text{mol}\cdot\text{Kg}^{-1}$), molarity ($\text{mol}\cdot\text{L}^{-1}$) and grams of sugars per 100 mL of solvent. It should be noted, though, that, in order to express the solubility data in different concentration units, the density of saturated sugar solutions needs to be determined. As a result, the density of saturated sugar solutions in water, methanol, ethanol, 1-propanol, and isopropanol, together with the density of these solvents in their pure forms, were measured and reported in (Table A1 in Appendix A.4).

Table 3.4. Solubility of glucose, fructose, and mannose in water and alcohol, measured at 20 °C and expressed, alongside their experimental errors, in four other different concentration units.

Solvent	Sugar	Weight percentage (wt %)	Mole fraction ($\times 10^{-2}$)	Molality ($\times 10^{-2}$ mol·Kg ⁻¹)	Molarity ($\times 10^{-2}$ mol·L ⁻¹)	Mass of solute (g)/100 mL solvent
Water	Glucose	44.4 ± 0.2	7.4 ± 0.7	44.3 ± 0.1	280 ± 1	80 ± 1
	Fructose	61.4 ± 0.4	14 ± 3	88.2 ± 0.1	41 ± 2	159 ± 1
	Mannose	54.1 ± 0.3	11 ± 2	65.4 ± 0.1	36 ± 1	118 ± 1
Methanol	Glucose	2.3 ± 0.5	0.4 ± 0.1	13.80 ± 0.03	10 ± 2	2 ± 1
	Fructose	14.3 ± 0.4	2.9 ± 0.6	92.33 ± 0.02	62 ± 2	13 ± 1
	Mannose	13.8 ± 0.6	2.8 ± 0.9	89.59 ± 0.04	60 ± 3	12 ± 1
Ethanol	Glucose	0.3 ± 0.1	0.07 ± 0.01	1.51 ± 0.01	1.1 ± 0.6	0.2 ± 0.1
	Fructose	1.4 ± 0.4	0.4 ± 0.1	7.68 ± 0.02	6 ± 2	1.0 ± 0.5
	Mannose	1.1 ± 0.4	0.3 ± 0.1	5.78 ± 0.02	4 ± 2	0.8 ± 0.5
1-propanol	Glucose	0.2 ± 0.1	0.08 ± 0.01	1.36 ± 0.01	1.0 ± 0.6	0.2 ± 0.1
	Fructose	0.7 ± 0.3	0.24 ± 0.05	39.80 ± 0.01	3 ± 1	0.5 ± 0.3
	Mannose	0.6 ± 0.3	0.18 ± 0.04	29.84 ± 0.01	2 ± 1	0.4 ± 0.3
Isopropanol	Glucose	0.2 ± 0.1	0.08 ± 0.01	1.30 ± 0.01	1.0 ± 0.6	0.2 ± 0.1
	Fructose	0.6 ± 0.3	0.21 ± 0.05	3.41 ± 0.01	3 ± 1	0.4 ± 0.3
	Mannose	0.4 ± 0.1	0.14 ± 0.02	2.27 ± 0.01	2 ± 1	0.3 ± 0.2

This can provide a complete overview of the solubility data and improve the reproducibility and reliability of data across different studies and researchers.

3.5. Conclusion

The solubility of reactants, intermediates, and products can play a crucial role in many aspects of a chemical reaction, including catalyst productivity and the reproducibility of data. It can affect the rate at which reagents (e.g., glucose) reach the catalytic site, which, in turn, affects the reaction rate and productivity. Furthermore, errors in the calculations of conversion and selectivity due to solubility could significantly limit the reproducibility of data among different laboratories and the development of catalysts by design.

Prior to the solubility determinations, the purity and stability of glucose, fructose and mannose were assessed by the mean of melting point measurements, thermogravimetric analysis (TGA), and ^1H and ^{13}C nuclear magnetic resonance spectroscopy (NMR) analysis in order to detect the presence of moisture and impurities, as well as to determine the alpha (α) and beta (β) anomeric equilibrium composition, which all could significantly affect the reliability of the measured solubility values. All sugars studied showed to be highly pure with an expected anomeric ratio.

An efficient HPLC analysis method based on the saturation point of sugar solutions was developed to accurately determine the solubility of glucose, fructose and mannose in water, methanol, ethanol, 1-propanol and isopropanol at room temperature. All sugars showed high solubility in water ($\geq 500 \text{ g}\cdot\text{L}^{-1}$). In contrast, when alcohols were used as solvents, the solubility was significantly affected to a different

extent with solubility values of ($\leq 20 \text{ g}\cdot\text{L}^{-1}$), except for those of fructose and mannose in methanol, which were reasonably soluble with solubility in the range of $110 \text{ g}\cdot\text{L}^{-1}$.

The solubility data, along with their experimental errors, were further expressed in different concentration units, including weight percentage (wt %), molar fractions, molality ($\text{mol}\cdot\text{Kg}^{-1}$), molarity ($\text{mol}\cdot\text{L}^{-1}$) and mass of solute (i.e., sugar) per 100 mL of solvent ($\text{g}\cdot 100\text{mL}$) in order to provide a more detailed and flexible collection of data regarding the solubility of sugar in different solvents, which will allow the ease of data reproducibility and comparability, as well as to provide a robust platform for the reliability of catalytic tests that will follow in chapters 4 and 5 for the isomerisation of glucose to fructose.

3.6. References

- 1 S. Stegemann, F. Leveiller, D. Franchi, H. de Jong and H. Lindén, *Eur. J. Pharm. Sci.*, 2007, **31**, 249–261.
- 2 S. Saravanamurugan, M. Paniagua, J. A. Melero and A. Riisager, *J. Am. Chem. Soc.*, 2013, **135**, 5246–5249.
- 3 S. Despax, B. Estrine, N. Hoffmann, J. Le Bras, S. Marinkovic and J. Muzart, *Catal. Commun.*, 2013, **39**, 35–38.
- 4 P. Zhu, S. Meier and A. Riisager, *Catal. Sci. Technol.*, 2022, **12**, 5332–5338.
- 5 M. Yabushita, N. Shibayama, K. Nakajima and A. Fukuoka, *ACS Catal.*, 2019, **9**, 2101–2109.
- 6 N. Rajabbeigi, A. I. Torres, C. M. Lew, B. Elyassi, L. Ren, Z. Wang, H. Je Cho, W. Fan, P. Daoutidis and M. Tsapatsis, *Chem. Eng. Sci.*, 2014, **116**, 235–242.
- 7 S. H. Yalkowsky, Y. He and P. Jain, *Handbook of Aqueous Solubility Data*, CRC Press, 2nd Edition., 2016.
- 8 F. Montañés, A. Olano, E. Ibáñez and T. Fornari, *AIChE Journal*, 2007, **53**, 2411–2418.
- 9 S. Xu, L. Zhang, K. Xiao and H. Xia, *Carbohydr. Res.*, 2017, **446–447**, 48–51.
- 10 M. Moliner, Y. Román-Leshkov and M. E. Davis, *Proc. Natl. Acad. Sci. U.S.A.*, 2010, **107**, 6164–6168.
- 11 I. Graça, D. Iruretagoyena and D. Chadwick, *Appl. Catal. B: Environ.*, 2017, **206**, 434–443.

- 12 J. Pang, M. Zheng, R. Sun, L. Song, A. Wang, X. Wang and T. Zhang, *Bioresour. Technol.*, 2015, **175**, 424–429.
- 13 F. Li, J. Yan, X. Zhang, N. Wang, H. Dong, L. Bai and H. Gao, *Ind. Eng. Chem. Res.*, 2021, **60**, 11241–11250.
- 14 E. Soszka, O. Sneka-Płatek, E. Skiba, W. Maniukiewicz, A. Pawlaczyk, J. Rogowski, M. Szyrkowska-Jóźwik and A. M. Ruppert, *Fuel*, 2022, **319**, 123646.
- 15 A. R. Katritzky, R. Jain, A. Lomaka, R. Petrukhin, U. Maran and M. Karelson, *Cryst. Growth Des.*, 2001, **1**, 261–265.
- 16 S. Dent, *Purity and Identification of Solids Using Melting Points*, Portland, OR, USA, 2006.
- 17 E. F. Joy, J. D. Bonn and A. J. Barnard, *Thermochim Acta*, 1971, **2**, 57–68.
- 18 M. Karthikeyan, R. C. Glen and A. Bender, *J. Chem. Inf. Model.*, 2005, **45**, 581–590.
- 19 M. Hurttä, I. Pitkänen and J. Knuutinen, *Carbohydr. Res.*, 2004, **339**, 2267–2273.
- 20 X. Hu, Y. Shi, P. Zhang, M. Miao, T. Zhang and B. Jiang, *Compr Rev Food Sci Food Saf*, 2016, **15**, 773–785.
- 21 S. Ceylan and Y. Topçu, *Bioresour. Technol.*, 2014, **156**, 182–188.
- 22 S. Ebnesajjad, in *Handbook of Adhesives and Surface Preparation: Technology, Applications and Manufacturing*, ed. S. Ebnesajjad, William Andrew imprint of Elsevier, 1st Edition., 2011, pp. 31–48.

- 23 Y. Z. Chua, H. T. Do, A. Kumar, M. Hallermann, D. Zaitsau, C. Schick and C. Held, *Food Biophys.*, 2022, **17**, 181–197.
- 24 S. Srisa-Nga and A. E. Flood, *Asian Pacific Confed. Chem. Eng. Congr. Progr. Abstr*, 2004, **113**, 1–10.
- 25 J. F. Lopes and E. M. S. M. Gaspar, *J. Chromatogr. A*, 2008, **1188**, 34–42.
- 26 C. Araujo-Andrade, F. Ruiz, J. R. Martínez-Mendoza and H. Terrones, *J. Mol. Struct. - Theochem*, 2005, **714**, 143–146.
- 27 C. Molteni and M. Parrinello, *J. Acta Crystallogr. B*, 1993, **364**, 33.
- 28 M.A. Kabayama and D. Patterson, *Can. J. Chem.*, 1958, **36**, 563–573.
- 29 G. Leontarakis, P. Tsavas, E. Voutsas, K. Magoulas and D. Tassios, *J. Chem. Eng. Data.*, 2005, **50**, 1924–1927.
- 30 C. E. Perles and P. L. O. Volpe, *J. Chem. Educ.*, 2008, **85**, 686.
- 31 Q. Lin, S. Liao, L. Li, W. Li, F. Yue, F. Peng and J. Ren, *Green Chem.*, 2020, **22**, 532–539.
- 32 R. Häkkinen and A. Abbott, *Green Chem.*, 2019, **21**, 4673–4682.
- 33 A. Kosaka, M. Aida and Y. Katsumoto, *J. Mol. Struct.*, 2015, **1093**, 195–200.
- 34 M. U. Roslund, P. Tähtinen, M. Niemitz and R. Sjöholm, *Carbohydr. Res.*, 2008, **343**, 101–112.
- 35 J. C. Edwards, J. M. Hunter and B. V. Nemzer, *J. Food Res.*, 2014, **3**, 115.
- 36 T. Barclay, M. Ginic-Markovic, M. R. Johnston, P. Cooper and N. Petrovsky, *Carbohydr. Res.*, 2012, **347**, 136–141.

- 37 L. HYVÖNEN, P. VARO and P. KOIVISTOINEN, *J Food Sci*, 1977, **42**, 657–659.
- 38 D. J. Wilbur, C. Williams and A. Allerhand, *J Am Chem Soc*, 1977, **99**, 5450–5452.
- 39 A. M. Peres and E. A. Macedo, *Ind. Eng. Chem. Res.*, 1997, **36**, 2816–2820.
- 40 L. A. Alves, J. B. Almeida E Silva and M. Giuliatti, *J. Chem. Eng. Data.*, 2007, **52**, 2166–2170.
- 41 G. Leontarakis, P. Tsavas, E. Voutsas, K. Magoulas and D. Tassios, *J. Chem. Eng. Data.*, 2005, **50**, 1924–1927.
- 42 E. A. Macedo and A. M. Peres, *Ind. Eng. Chem. Res.*, 2001, **40**, 4633–4640.
- 43 Q. Wang and Y. Fang, *J. Chromatogr. B*, 2004, **812**, 309–324.
- 44 X. Gong, S. Wang and H. Qu, *Chin. J. Chem. Eng.*, 2011, **19**, 217–222.
- 45 R. J. Van Putten, J. G. M. Winkelman, F. Keihan, J. C. Van Der Waal, E. De Jong and H. J. Heeres, *Ind. Eng. Chem. Res.*, 2014, **53**, 8285–8290.

Chapter 4. Conversion of glucose to fructose over Sn and Ga-doped zeolite Y in methanol and water media.

4.1. Introduction

Sugar isomerisation is a reaction that, if fully exploited, could greatly expand the potential application of biomass for the production of high-value chemicals and fuels^{1,2}. Biomass contains a significant amount of sugar aldoses, mainly aldohexoses, such as glucose, galactose, xylose, arabinose, and ribose, which are capable of being converted into their five-membered ring ketoses. This is particularly important since carbohydrate-based materials account for the majority (up to 60%) of biomass-derived feedstock³. In this regard, the catalytic conversion of glucose to fructose is considered one of the most significant sugar transformations⁴. Since fructose is an effective potential precursor for the production of industrially important chemicals such as 5-hydroxymethylfurfural and levulinic acid, which, in turn, can be used as building blocks in the polymer and biofuel industries, respectively⁵.

To date, the use of Sn-doped zeolites^{6,7} has displayed considerable promise in facilitating the catalytic isomerisation of glucose to fructose, particularly when Sn-active species are doped on zeolites with large pores such as zeolite beta^{8,9} (section 1.6). This reactivity has been associated with the formation of Lewis acid sites (Sn^{4+})⁶ and/or extra-framework SnO_x clusters present in the pores of zeolite beta, potentially affecting the step of metal incorporation⁹. In contrast, due to its highly Lewis acidic nature¹⁰, Ga^{3+} has increasingly been considered an active metal centre for this class of reaction¹¹. This is widely believed to be a critical parameter in the isomerisation reaction of glucose to fructose since it facilitates the 1,2-intramolecular hydride shifts from C2 to C1 carbons in glucose to form desired fructose (Figure 4.2)^{12,13}. In principle,

this metal is also capable of replacing aluminium species located within zeolite frameworks, resulting in a highly dispersed metal species form¹⁴. Therefore, it could result in the formation of both intra- and extra-framework species after being incorporated into a zeolite framework¹⁵, such as the commercially available zeolites, e.g., zeolite Y¹⁶, which is much easier and more straightforward to prepare compared to beta-zeolite.

The objectives of this part of the experimental work are, to **1)** synthesise Sn and Ga-doped zeolite Y and test their catalytic performances, together with the acidic undoped zeolite Y, in order to determine the importance of Lewis acid active sites formed by the doping of Sn and Ga alongside Brønsted acid sites when solvents such as water, methanol, and their combinations are used for the isomerisation reaction of glucose; **2)** detect the potential presence of alkyl-sugar species, namely methyl fructoside, after reaction in methanol, which, if present, can be deliberately used later in order to enhance the synthesis of fructose through the hydrolysis step of this intermediate in water; **3)** confirm possible reaction pathways of the glucose isomerisation reaction; **4)** identify structure-activity correlations using a wide range of characterisation techniques, including chemisorption, diffraction methods and spectroscopy techniques such as X-ray photoelectron spectroscopy and Extended X-ray absorption fine structure.

4.2. Catalytic activity of HY, Sn/Y and Ga/Y zeolites.

In this section, undoped acidic zeolite Y and doped with Sn or Ga - here abbreviated as HY, Sn/Y and Ga/Y, respectively, were synthesised according to the protocol described in section 2.2.1, and their catalytic activity for the isomerisation reaction of

glucose to fructose was systematically determined under various reaction conditions (see section 2.3), (range of 80 °C – 120 °C, endogenous pressure and a reaction time in the range of 1 – 2 h).

4.2.1. Catalytic tests in a one-step protocol using water or methanol as a solvent.

It has been observed that the presence of water as a reaction solvent either in a single-step protocol or in combination with methanol prior to the reaction leads to a lack of any product formation under the reaction conditions used. It is not unprecedented for zeolite to exhibit no reactivity during the catalytic conversion of glucose to fructose when water is used as a solvent¹⁷. This might be due to site-blocking mechanisms that have been proposed to explain this behaviour, which could be in the form of strong adsorption inside zeolite pores¹⁸.

On the other hand, HY, Sn/Y and Ga/Y (Table 4.1) showed high catalytic activity when using methanol as the reaction solvent under reasonably mild reaction conditions (reaction temperature in the range of 80 °C – 120 °C, endogenous pressure for 1 h). Specifically, as the reaction proceeds at 80 °C, an equilibrium trend was observed for the glucose to fructose isomerisation pathway with conversion rates of approximately *ca.* 50% (K_{eq} values for this isomerisation reaction are in the range of 1.1 at 60 °C¹⁹); in contrast, a reaction temperature of 120 °C revealed a nearly quantitative conversion rate of glucose with product selectivities of *ca.* 31%, 42%, and 27% for fructose, methyl fructoside, and mannose, respectively, when reaction carried out over Ga/Y zeolite (Figure 4.1). Thus, implying an increase in the value of the equilibrium constant or the existence of alternative reaction pathways. However, carbon mass balance also decreased significantly at higher temperatures, most likely as a consequence of the formation of insoluble undesirable humins²⁰.

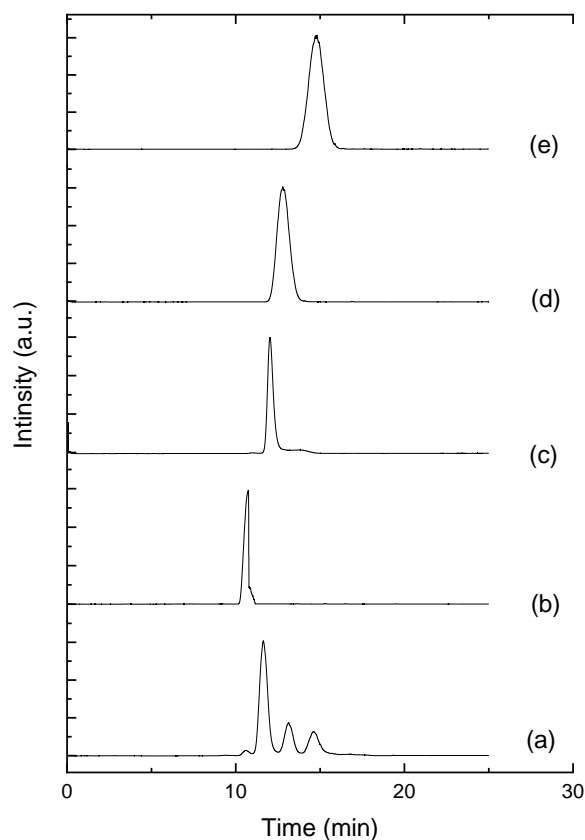


Figure 4.1. HPLC chromatograms for (a) representative reaction mixture for the isomerization reaction of glucose to fructose by using methanol as a solvent, and Ga/Y as a catalyst, (b) glucose $t_R = 10.9$ min, (c) methyl fructoside $t_R = 11.9$ min, (d) mannose $t_R = 12.8$ min, (e) fructose $t_R = 14.8$ mins standards, and. The reaction mixture comprises glucose, methyl fructoside, mannose and fructose.

It has also been observed that the formation of alkyl fructose (most likely methyl fructoside, see section 4.2.1.1) is strongly favoured at low temperatures (ca. 70 %). However, when the temperature reached 120 °C, this intermediate can undergo an increase in production, accompanied by a higher consumption rate. Consequently, its visibility diminished as it underwent decomposition of approximately 40-50% to yield fructose at around 30%. However, higher temperatures led to an increased amount of unwanted by-product mannose being formed (up to ca. 20-30%). From our data, we could conclude that a reaction temperature of 100 °C represents the most efficient

compromise between high glucose conversion (> 90%) and carbon mass balance (also > 90%) (see Table 1) and yield values (Table A2 in Appendix A.5).

Table 4.1. Catalytic results of HY, Sn/Y and Ga/Y catalysts for the isomerisation reaction of glucose in methanol. The reactions were performed using 125 mg of the glucose in 4 mL of CH₃OH at the specified reaction temperature for 1 h and endogenous pressure using a constant M:S molar ratio of 1:100. Conversion and selectivity values were calculated using (Equations 2.2 – 2.9 in Chapter 2). Experimental error is expressed as the standard deviation of three replicated measurements.

T (°C)	Catalyst	Glucose Conversion (%)	Selectivity ^(a) (%)			CMB ^(c) (%)
			Fructose	MeF ^(b)	Mannose	
120	HY	94 ± 1	26 ± 1	48 ± 1	27 ± 1	76 ± 5
100	HY	90 ± 1	30 ± 2	35 ± 2	36 ± 1	99 ± 6
90	HY	70 ± 2	21 ± 2	66 ± 2	14 ± 1	95 ± 4
80	HY	49 ± 5	15 ± 6	80 ± 5	6 ± 1	97 ± 2
120	Sn/Y	96 ± 1	26 ± 1	51 ± 0	24 ± 1	67 ± 5
100	Sn/Y	95 ± 1	28 ± 1	40 ± 1	32 ± 1	84 ± 4
90	Sn/Y	71 ± 3	20 ± 1	69 ± 2	11 ± 1	93 ± 4
80	Sn/Y	50 ± 1	26 ± 1	68 ± 1	6 ± 1	100 ± 3
120	Ga/Y	98 ± 1	31 ± 1	42 ± 1	27 ± 1	50 ± 6
100	Ga/Y	94 ± 2	27 ± 2	42 ± 1	31 ± 2	91 ± 6
90	Ga/Y	62 ± 1	22 ± 3	71 ± 4	8 ± 1	92 ± 4
80	Ga/Y	55 ± 4	17 ± 2	77 ± 3	6 ± 1	98 ± 3

^(a) Observed selectivity

^(b) MeF = (Methyl Fructoside)

^(c) CMB = (Carbon mass balance)

Despite this solvent exhibits enhanced reactivity, its utilization for this reaction still needs to be thoroughly assessed. For example, the use of alcohol has the potential to enhance glucose conversion due to possible solvent effects. However, this solvent can also result in the formation of alkyl fructoside intermediates²¹. This could, therefore, lead to the presence of two different reaction routes: the first is the isomerisation

reaction of glucose to fructose facilitated via Lewis acid active sites (Figure 4.2), whereas the second is the formation of either methyl glucoside and/or methyl fructoside intermediates, which mediated through Brønsted acid active sites (Figure 4.5a and 4.5b).

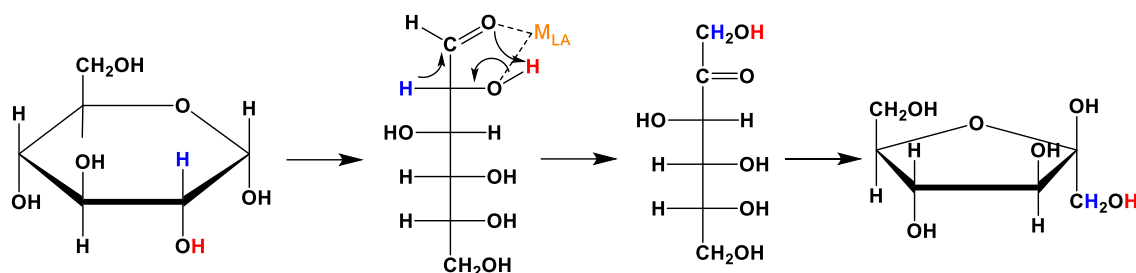


Figure 4.2. Proposed reaction mechanism of glucose isomerisation catalysed via Lewis acid centres (scheme adapted from Román-Leshkov et al¹²). Following the ring opening, a Lewis acid metal site coordinates the two oxygens in the carbonyl and adjacent OH groups. This would result in a hydride (H atom in red) migrating to the aldehydic carbon in the form of a CH₂OH group and a carbonyl (resulting in a ketone). The open configuration of fructose will then be closed to form a ring-shaped structure.

4.2.1.1. Presence of alkyl-sugar species as a potential intermediate in glucose isomerisation in methanol.

It is important to note that, so far, it has been controversial to determine if alkyl-sugar species are formed upon the isomerisation of sugars like glucose in alcohol. For example, according to Adachi, Bermejo-Deval, and Davis^{9,18,22}, no alkyl fructoside was observed following the reaction in methanol; instead, glucose, fructose, and mannose were only detected. In contrast, Saravanamurugan¹⁶ made the claim, unsupported by concrete evidence that alkyl fructoside was detected in the reaction mixture after the reaction in methanol, which was deliberately used afterwards to form fructose through the hydrolysis of this intermediary in water.

As a consequence of the disagreement in the literature regarding the formation of alkyl fructoside as a potential product of the isomerisation reaction of glucose, we set out to confirm the presence of this intermediate in our reaction mixture. HPLC-MS methods were used to characterise the reaction mixture (Figure 4.4). We identified a compound with a molecular ion (including Na^+ as a part of the ionisation process) of an $m/z = 217$, which is in agreement with either methyl glucoside or methyl fructoside ($[\text{C}_7\text{H}_{14}\text{O}_6\text{Na}]^+ = 194 + 23 = 217 \text{ a.m.u}$), whose fragmentation patterns are compatible with those found in the standard solution of the methyl fructoside intermediate (Figure 4.3). Despite this, it should be noted that glucose and fructose can also adopt equivalent MS fragmentation patterns after the loss of a $[\text{OCH}_3]^+$ fragment²³. In this regard, the chromatographic retention times were compared (Figure 4.1) using the same standard of methyl fructoside (MuseChem), which confirmed, within experimental error, that methyl fructoside (measured at $> 50 \text{ mol}\%$) is indeed formed in the reaction mixture.

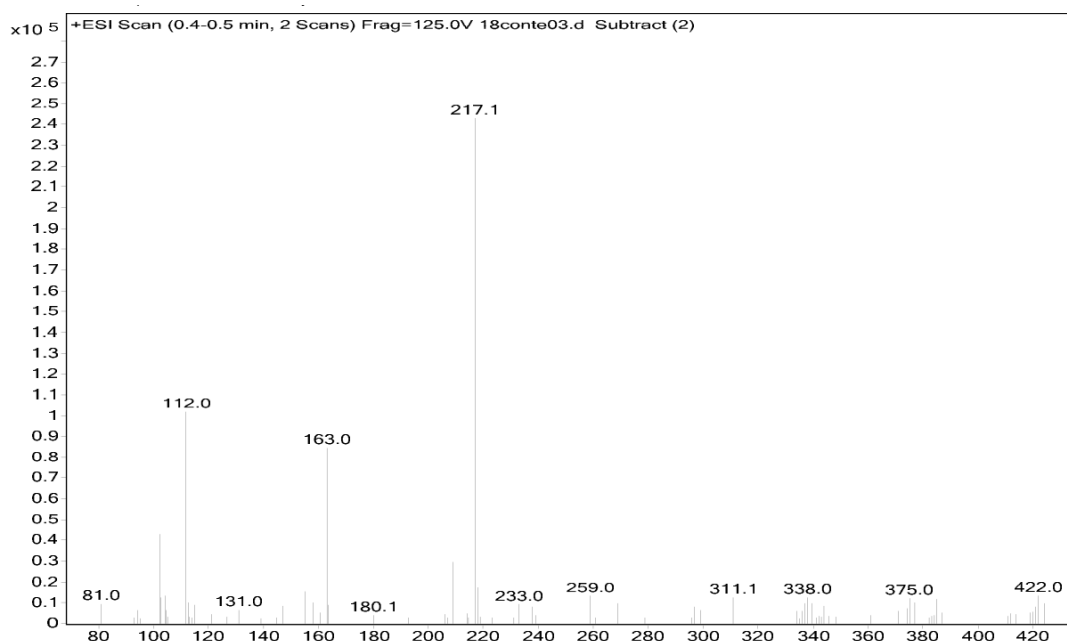


Figure 4.3. Mass spectrum from HPLC-MS of a methyl fructose standard (Methyl β -D-fructofuranoside, MuseChem, 98%), in acetonitrile. $m/z = 217$ corresponds to the molecular

ion + Na adducts $[C_7H_{14}O_6Na]^+$, and the fragment at $m/z = 163$ corresponds to the loss of 3 water molecules from this adduct.

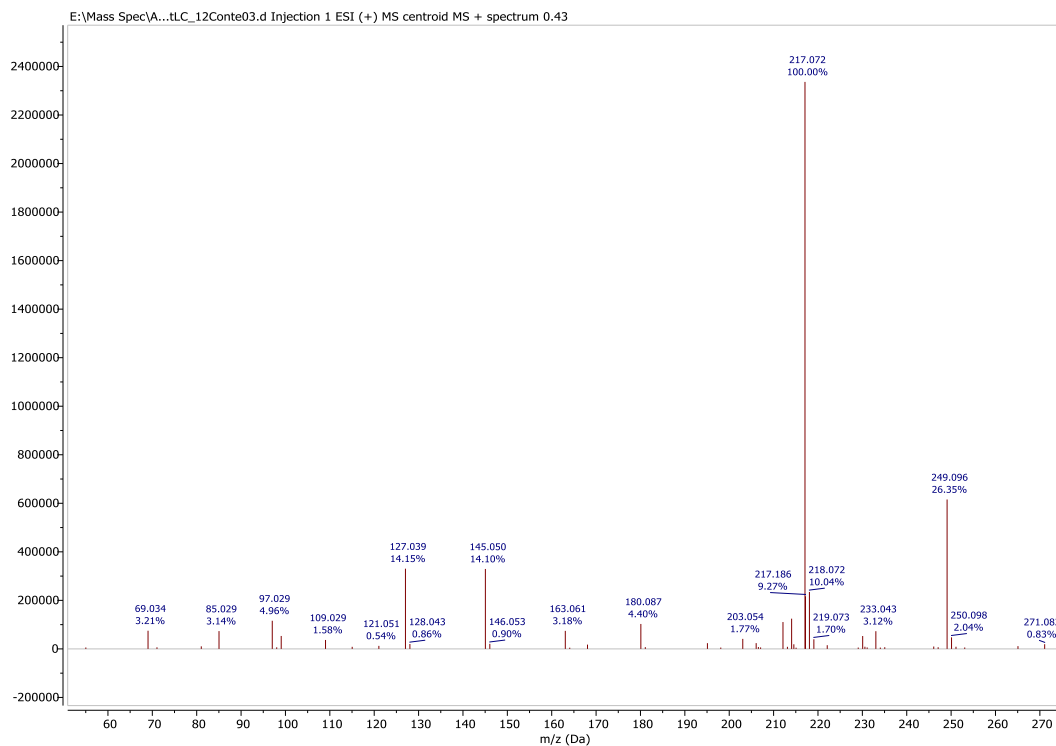


Figure 4.4. Mass spectrum from HPLC-MS from methyl fructose peak of a typical reaction mixture of glucose in methanol in the presence of zeolite HY for a reaction carried out at 100 °C for 1h and endogenous pressure. $m/z = 217$ corresponds to the molecular ion + Na adducts $[C_7H_{14}O_6Na]^+$, and the fragment at $m/z = 163$ corresponds to the loss of 3 water molecules from this adduct.

Additional mass spectroscopic investigations were carried out with the aim to differentiate between alkyl glucoside and fructoside and to gather more information on the formation conditions of these important intermediates by using catalysts with different acidity levels and adjusting the reaction temperatures and times. In view of this, methyl glucoside and methyl fructoside intermediates were synthesised according to the protocol reported in (section 2.4), and then their formation characteristics were identified using HPLC-MS described in (section 2.7). The results showed no methyl glucoside formation when pure silica MCM-41 was used as a

catalyst (Table 4.2 and Figure 4.6). Conversely, when the synthesis was carried out with aluminosilicates zeolite, donated here as Al-MCM-41, the glucose conversion was nearly quantitative (Table 4.2 and Figure 4.5) and produced mainly methyl glucoside. This can be explained by the presence of Al species within the second catalyst, acting as a source of Brønsted acid sites (BASs)²⁴, which is considered to be a crucial factor for this kind of synthesis^{25,26}. Furthermore, 120 °C is a more efficient reaction temperature for the synthesis of methyl glucoside, yielding 100% after 1 hour, compared to just 60% after the same reaction time at 100 °C.

In contrast, it was possible to synthesise methyl fructoside from fructose with both the acidic aluminosilicates zeolite (Al-MCM-41) and non-acidic pure silica zeolite (MCM-41) using methanol as a reaction solvent. In particular, the synthesis results revealed that the formation of methyl fructoside exhibited considerably faster rates when using aluminosilicate zeolite compared to pure silica zeolite (Table 4.2 and Figure 4.7). When the Al-MCM-41 catalyst was used, the formation rate of methyl fructoside approached nearly 100% within 1 hour at either 100 or 120 °C, whereas pure silica MCM-41 required a time range of 3 - 6 h to achieve the same yield at these reaction temperatures. This effect of temperature and time on the synthesis of methyl fructoside was not observed with Al-MCM-41 (Table 4.2 and Figure 4.7).

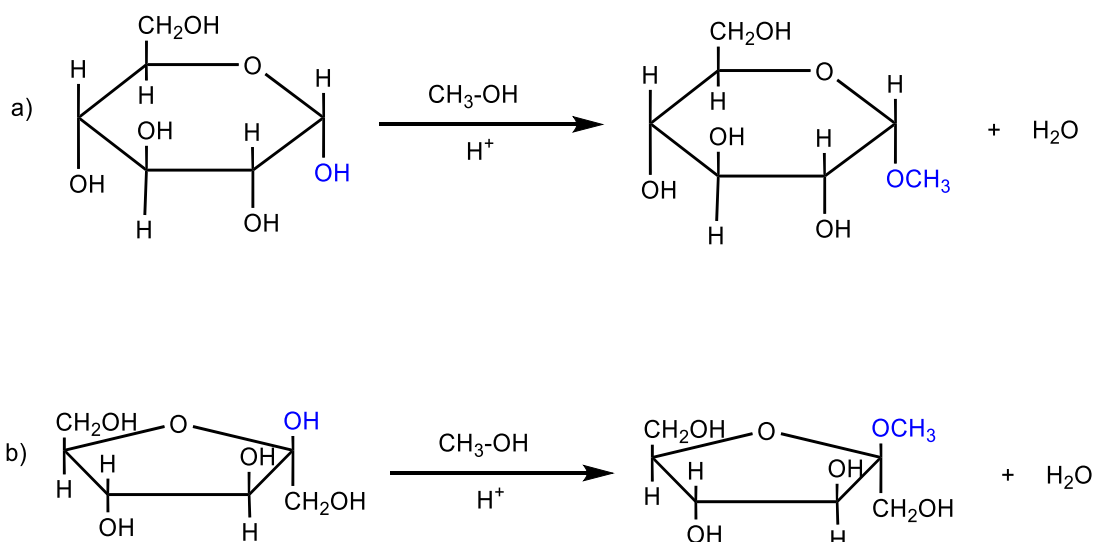


Figure 4.5. Acid-mediated synthesis of (a) methyl glucoside and (b) methyl fructoside through the addition of methanol. Compounds in cyclic forms, with methyl glucoside produced by adding OCH₃ to the carbonyl group (aldehyde) of glucose and methyl fructoside formed via the addition of OCH₃ to the carbonyl group (ketone) of fructose.

Table 4.2. Summary of the reaction equilibria for the synthesis of methyl glucoside and methyl fructoside in methanol under different reaction conditions.

Substrate	Catalyst	Temperature (°C)	Time (h)	Expected Product (wt.%)
Glucose	MCM-41	100	6	Methyl glucoside (0 wt.%)
	MCM-41	120	6	Methyl glucoside (0 wt.%)
	AI-MCM-41	100	2	Methyl glucoside (100 wt.%)
	AI-MCM-41	120	1	Methyl glucoside (100 wt.%)
Fructose	MCM-41	100	6	Methyl fructoside (100 wt.%)
	MCM-41	120	2	Methyl fructoside (100 wt.%)
	AI-MCM-41	100	1	Methyl fructoside (100 wt.%)
	AI-MCM-41	120	1	Methyl fructoside (100 wt.%)

The reactivity of fructose was generally higher compared to glucose, which was in part unexpected in this context. This is because, in principle, aldehydes are inherently more electrophilic and, thereby, more reactive toward nucleophilic addition reactions than

ketones²⁷. However, it is possible to explain this trend of reactivity because fructose has a 5-membered ring structure, which is naturally more reactive than the 6-membered ring structure of glucose^{28,29}.

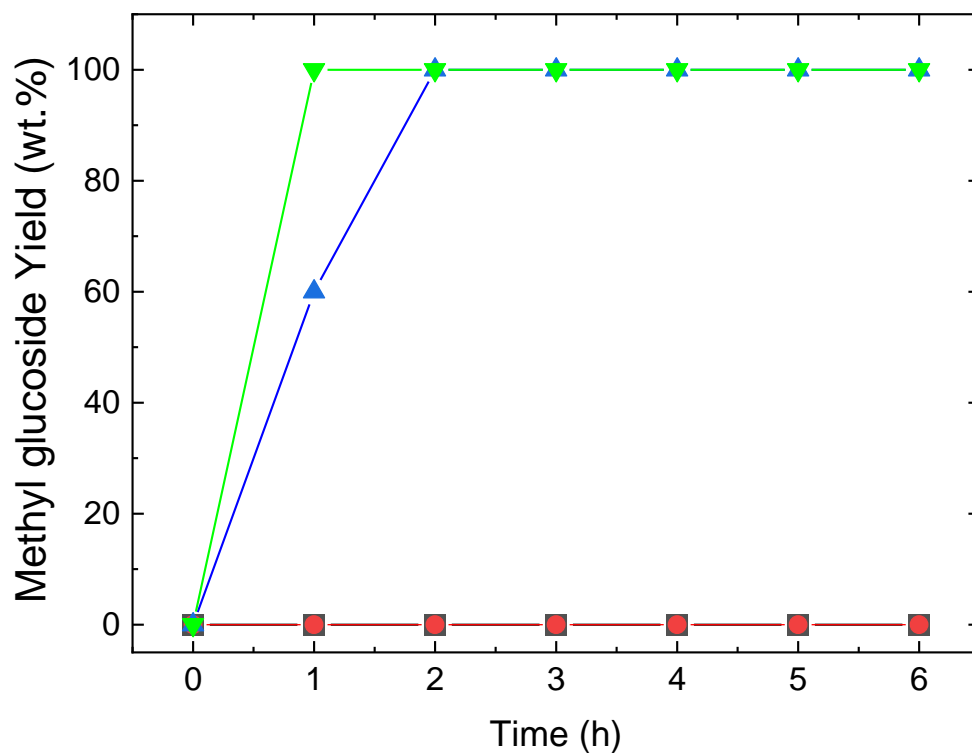


Figure 4.6. Time evolution of the synthesised methyl glucoside under different synthesis parameters using non-acidic MCM-41 at 100 °C (■), non-acidic MCM-41 at 120 °C (●), acidic Al-MCM-41 at 100 °C (▲) and acidic Al-MCM-41 at 120 °C (▼) for synthesis time in the range of 1 - 6 h.

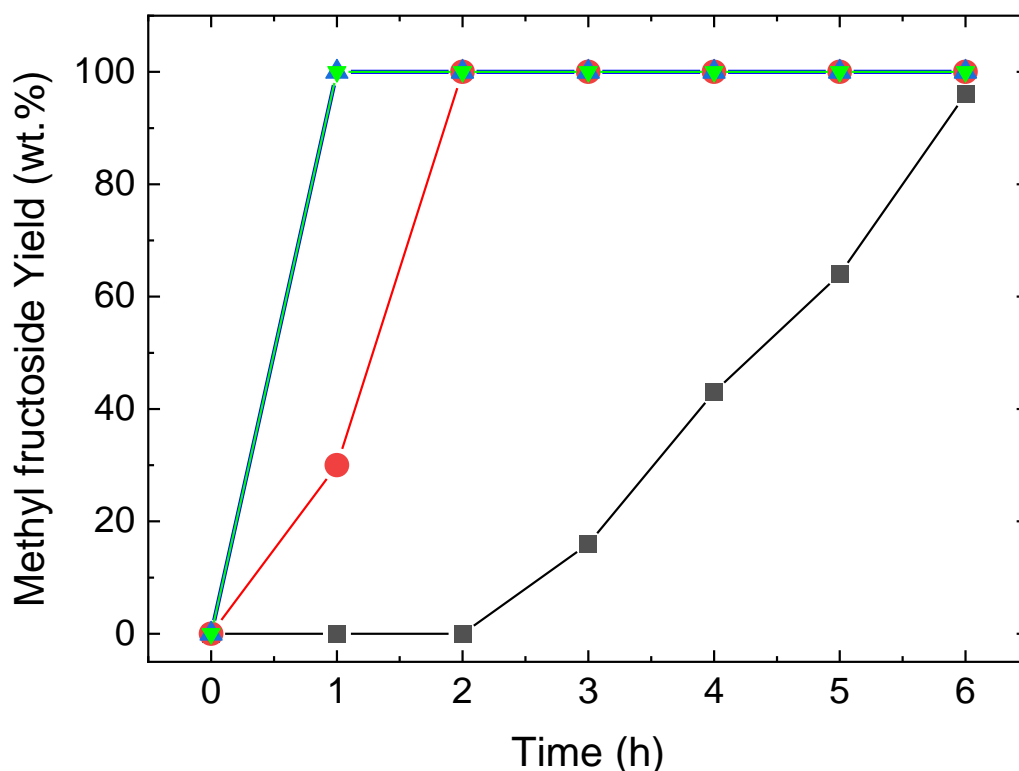


Figure 4.7. Time evolution of the synthesised methyl fructoside under different synthesis parameters using non-acidic MCM-41 at 100 °C (■), non-acidic MCM-41 at 120 °C (●), acidic Al-MCM-41 at 100 °C (▲) and acidic Al-MCM-41 at 120 °C (▼) for synthesis time in the range of 1 - 6 h.

As a part of our intensive investigation regarding the presence of methyl glucoside and methyl fructoside in our reaction mixture, we conducted an in-depth data analysis of the mass spectroscopic fragmentation patterns for our synthesised methyl glucoside and fructoside. In particular, we simultaneously analyse the MS fragmentation patterns of each step of the LC part. Our robust data analysis allowed us to identify two distinct peaks for the fragmentation patterns of $m/z = 217$, corresponding to an anomeric mixture of methyl glucoside and fructoside. The first peak highlighted in yellow, with an LC retention time of nearly 0.45 min, is definitely compatible with the standard methyl fructoside. In contrast, the second peak highlighted in purple, with an LC

retention time of approximately 0.6 min, more likely corresponds to the presence of methyl glucoside (Figures 4.8 and 4.9).

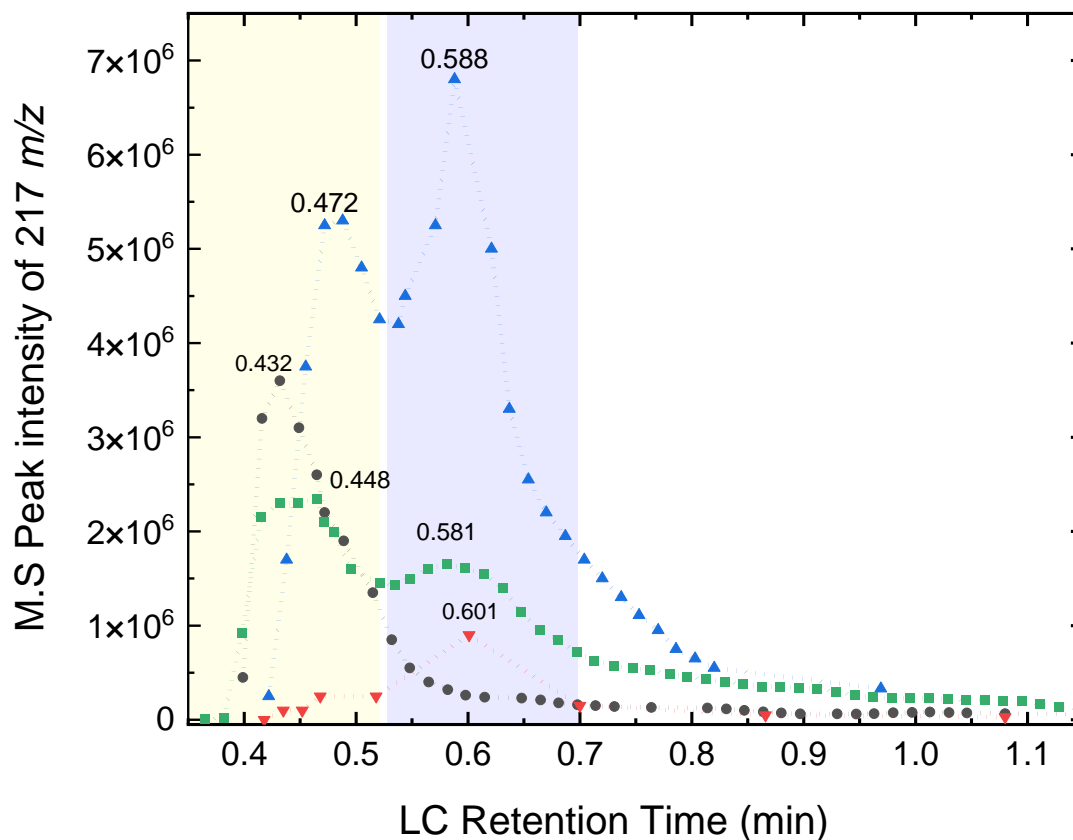


Figure 4.8. Mass spectroscopy peak intensity of 217m/z of a standard of methyl fructoside (●), synthesised methyl glucoside by MCM-41 (▼), synthesised methyl fructoside by MCM-41 (▲), and reaction mixture of glucose isomerisation over Sn/Y zeolite (■). Two distinct peaks for this fragmentation pattern were observed, corresponding to methyl glucoside and fructoside within our samples.

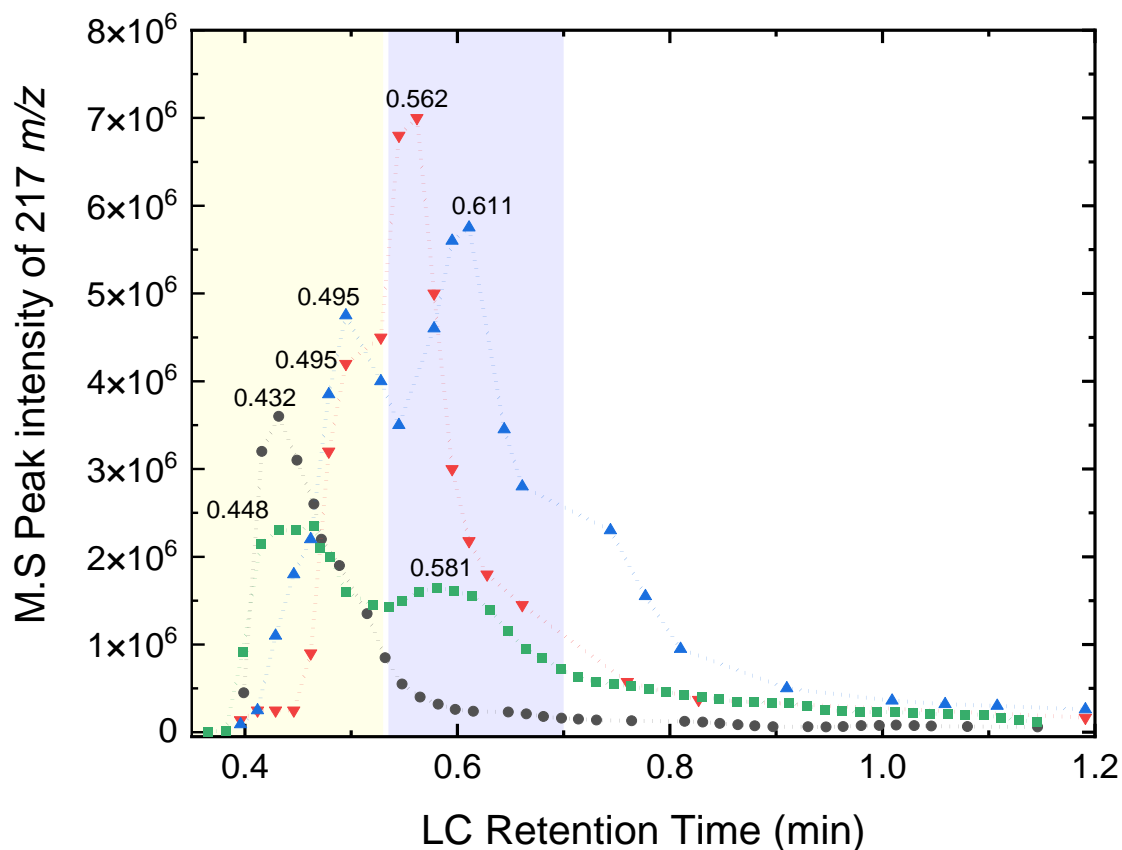


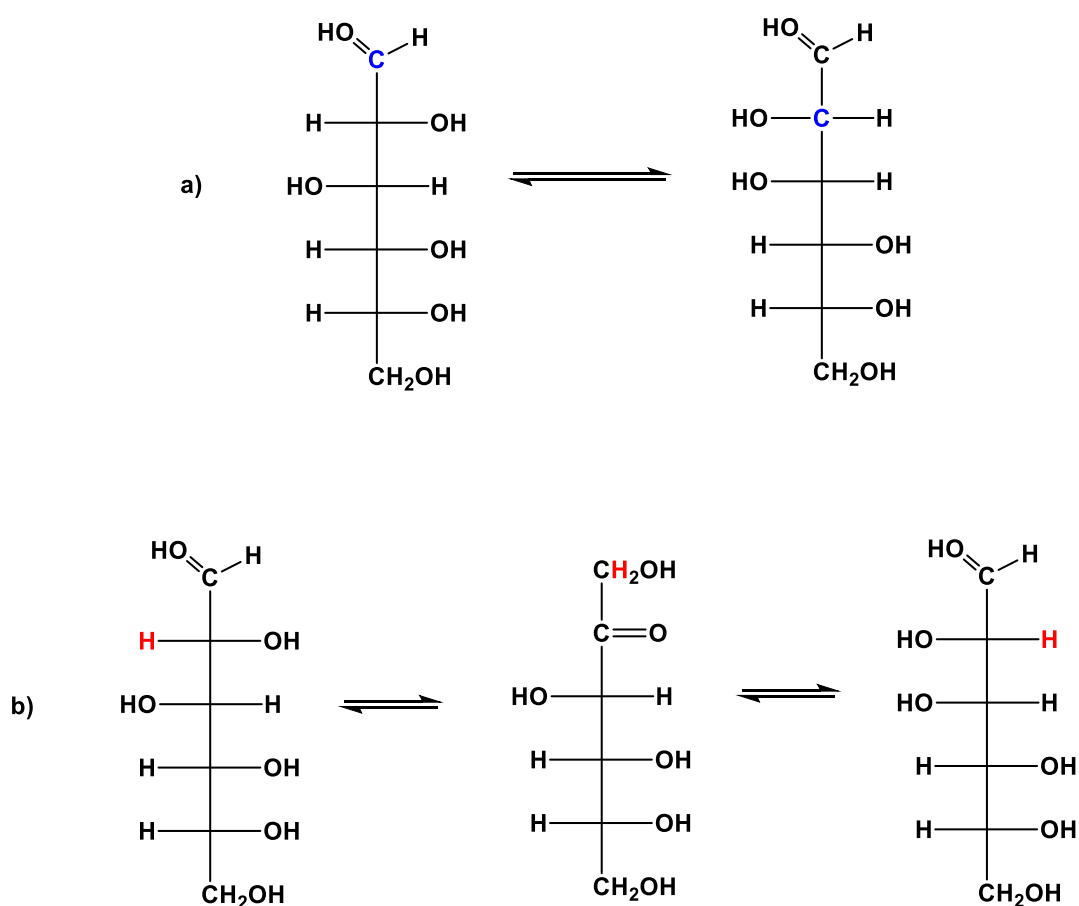
Figure 4.9. Mass spectroscopy peak intensity of $217m/z$ of a standard of methyl fructoside (●), synthesised methyl glucoside over Al-MCM-41 (▼), synthesised methyl fructoside Al-MCM-41 (▲), and reaction mixture of glucose isomerisation over Sn/Y zeolite (■). Two distinct peaks for this fragmentation pattern were observed, corresponding to methyl glucoside and fructoside within our samples.

The evolution of the intensity of the same peak per time of methyl glucoside and fructoside with actual reaction mixture and standard methyl fructoside revealed that the actual reaction mixture (green line) obtained by our catalysts contains both methyl glucoside and methyl fructoside with more methyl fructoside being formed.

Therefore, the results confirm that at least two distinct mechanisms are involved in the isomerisation reaction: a Lewis-mediated glucose-to-fructose isomerisation and a Brønsted-catalysed pathway toward the formation of methyl fructoside and methyl glucoside intermediates. Therefore, it is evident that an accurate characterisation of a

reaction mixture is a valuable tool to unveil reaction mechanisms and, in turn, to promote the rational design of catalysts.

Mannose has also been detected in significant amounts (quantified at 25 mol%) within the reaction mixture of our glucose isomerisation. In fact, mannose is an epimer of glucose, meaning they differ only in one stereogenic centre due to chiral inversion. It has been postulated that this epimerisation reaction can be triggered in two possible pathways: either through a carbon shift from the C1 to C2 position of glucose³⁰ (Figure 4.10a) or via a sequential hydride shift from the C2 to C1 position of fructose to form mannose³¹ (Figure 4.10b).



Figures 4.10. (a) Postulated production of mannose from glucose by a 1,2-intramolecular carbon shift from C1 to C2 positions; (b) Proposed formation of mannose through two sequential hydride shifts: the first one, from C2 to C1 of glucose to form fructose, then an additional hydride shift from C1 to C2 of fructose to form mannose.

In view of the co-existence of these multiple equilibria (Figure 4.11), we conducted control tests using fructose and mannose as substrates in methanol (Table 4.3) in order to determine which of these two reaction mechanisms is involved in our case.

Table 4.3. Catalytic data of HY, Sn/Y, and Ga/Y for the conversion of fructose and mannose as substrates in methanol. Reaction conditions: 125 mg of substrate in 4 mL of methanol at 100 °C for 1 h and endogenous pressure using a constant M:S molar ratio of 1:100.

Catalyst	Substrate	Conversion (%)	Selectivity (%)		
			Me-fructoside	Glucose	Mannose
HY	Fructose	100	100	0	0
Sn/Y	Fructose	100	100	0	0
Ga/Y	Fructose	100	100	0	0
			Me-fructoside	Glucose	Fructose
HY	Mannose	90	82	18	0
Sn/Y	Mannose	93	84	16	0
Ga/Y	Mannose	91	85	15	0

First of all, it was possible to detect the full conversion of fructose to methyl fructoside. This indicates that in the reaction involving glucose as a substrate, fructose is first formed (Lewis catalysed pathway), which is then converted into its fructoside form (Brønsted catalysed pathway).

Furthermore, the presence of mannose as a substrate leads to the formation of both glucose and methyl fructoside. However, based on the reaction using fructose as a substrate, methyl fructoside can be produced directly from fructose. As a consequence, it can be concluded that of the two reaction mechanisms for the formation of mannose: (i) direct conversion of glucose to mannose via carbon shift, or (ii) the indirect formation of mannose from glucose via hydride shift from fructose, our data support the second mechanism, since the first route would not lead to the formation of alkyl fructoside.

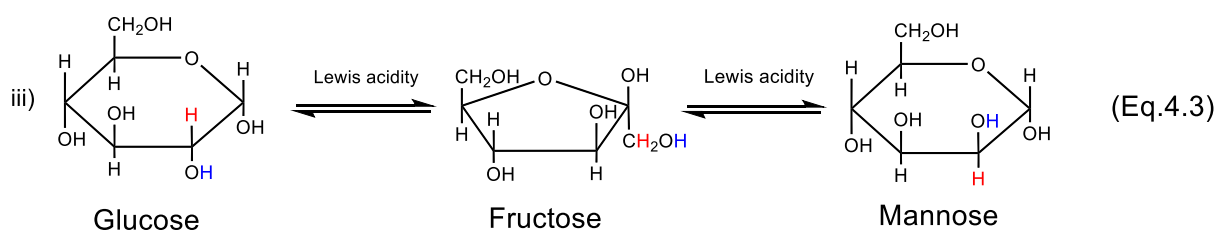
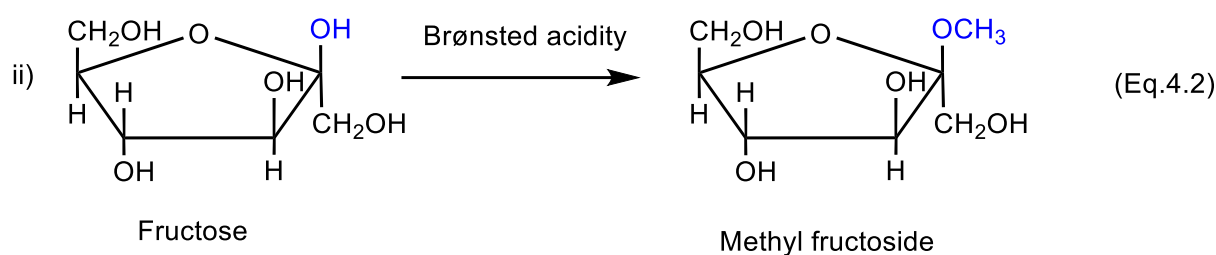
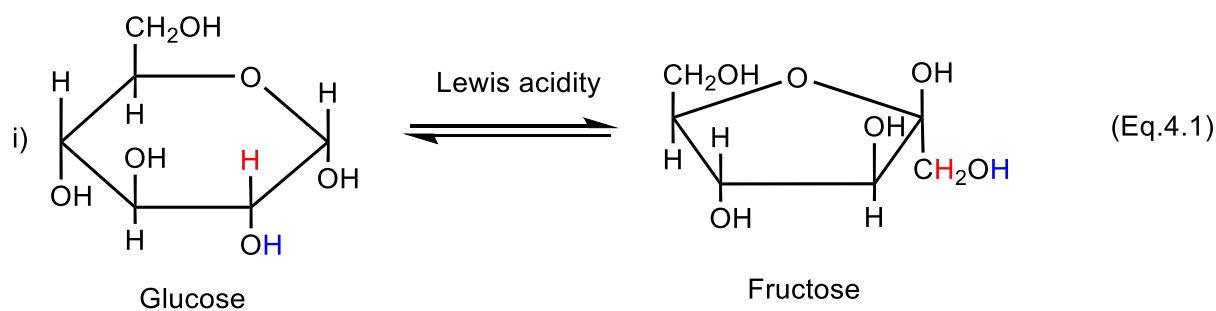


Figure 4.11. Multiple equilibria schematics for the isomerisation reaction of glucose to fructose in methanol mediated by either Lewis or Brønsted acid sites (Eqs. 4.1 - 4.3).

Given these mechanisms and the product distribution observed, it is apparent that any Lewis acid effects caused by Ga or Sn dopants are insignificant in comparison to pre-existing Al centres, with methyl fructoside being a predominant component of the product distribution as a consequence of Brønsted acidity domains. However, the by-products obtained from Ga/Y appear to be different, probably facilitating the formation of more of the unwanted humins at 120 °C since no 5-HMF was observed within the reaction conditions studied.

4.2.2. Catalytic tests in a two-step protocol by using methanol and water.

Since the formation of methyl fructoside was verified during the acid-mediated attack of methanol on fructose in our reaction mixture, we considered a sequential hydrolysis step of this intermediate with water to promote the production of fructose¹⁶. Furthermore, it should be highlighted that this step is also catalysed by Brønsted acid sites. The detailed catalytic results of our materials after this water treatment are provided in (Table 4.3) and (Table A3 in Appendix A.5). We have also confirmed that the reaction reached equilibrium after 1 hour.

Table 4.3. Catalytic data of HY, Sn/Y and Ga/Y catalysts for the isomerisation reaction of glucose in methanol followed by the step of water addition using a two-step protocol. The tests were conducted using 125 mg of the substrate in 4 mL of methanol at specified reaction temperatures for 1 h and endogenous pressure and then 4 mL of water was added for an additional 1 h at a constant M:S molar ratio of 1:100. Experimental error is expressed as the standard deviation of three independent measurements.

T (°C)	Catalyst	Conversion (mol %)	Selectivity ^(a) (mol %)			CMB ^(c) (%)
			Fructose	MeF ^(b)	Mannose	
120	HY	92 ± 1	54 ± 1	18 ± 1	28 ± 1	80 ± 4
100	HY	86 ± 2	40 ± 2	26 ± 2	34 ± 1	93 ± 5
90	HY	69 ± 1	25 ± 6	61 ± 4	14 ± 1	93 ± 3
80	HY	42 ± 4	21 ± 1	66 ± 1	4 ± 1	100 ± 2
120	Sn/Y	93 ± 1	56 ± 1	20 ± 1	25 ± 1	65 ± 6
100	Sn/Y	90 ± 3	50 ± 2	25 ± 4	25 ± 1	77 ± 4
90	Sn/Y	70 ± 1	23 ± 1	67 ± 1	10 ± 1	84 ± 4
80	Sn/Y	47 ± 3	26 ± 5	72 ± 5	3 ± 1	97 ± 2
120	Ga/Y	96 ± 1	67 ± 1	14 ± 1	21 ± 2	63 ± 4
100	Ga/Y	91 ± 4	55 ± 1	20 ± 2	25 ± 2	93 ± 5
90	Ga/Y	56 ± 2	26 ± 4	68 ± 4	7 ± 1	94 ± 3
80	Ga/Y	54 ± 6	20 ± 1	77 ± 1	2 ± 1	87 ± 5

^(a) Observed selectivity.

^(b) MeF = (Methyl Fructoside).

^(c) CMB = (Carbon mass balance).

It is evident that the step of water addition in the two-step reaction protocol has a significant impact on the formation of fructose through the consumption of methyl fructoside. From our data we observe an apparent decrease in methyl fructoside intermediate that is consistent with the formation of desirable fructose, resulting in the formation of ca. 40–70 % of fructose for reactions carried out at 100 and 120 °C (Table 4.3) and fructose yields of approximately 50 % (Table A3 in Appendix A.5). In addition, this water treatment showed no impact on the conversion rate of glucose with all three catalysts. This indicates that the reaction was at equilibrium after the first step in methanol, and all changes in selectivity observed are due exclusively to this hydrolysis step. This conclusion was confirmed by the determination of kinetic profiles for HY, Sn/Y and Ga/Y catalysts in methanol and after the step of water addition for a reaction time in the range of 0 – 2 h (Figures 4.11 to 4.13) and (Table A4 in Appendix A.5).

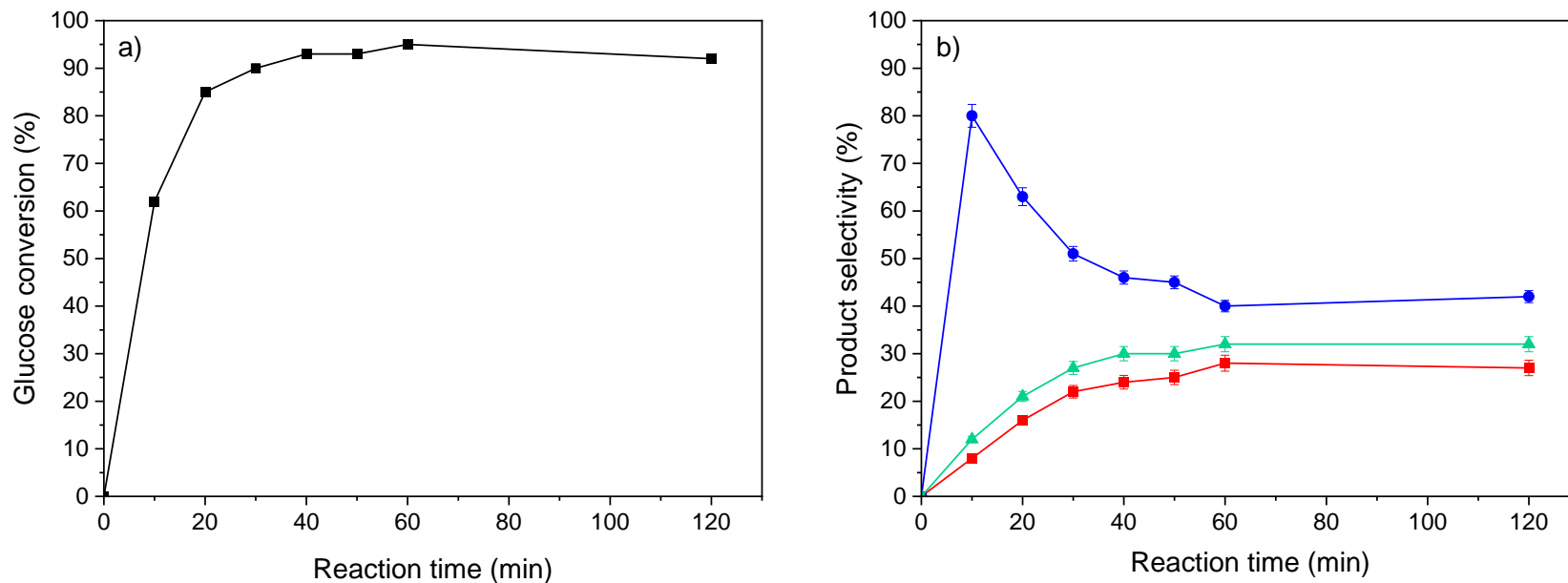


Figure 4.11. a) Kinetic profile for the glucose conversion (■), and b) product selectivity of the reaction mixture composed of fructose (■), methyl fructoside (●), and mannose (▲) catalysed by zeolite HY at 100 °C in methanol. The reactions were conducted using 125 mg of the substrate in 4 mL of methanol for 1 h and endogenous pressure using a constant M:S molar ratio of 1:100.

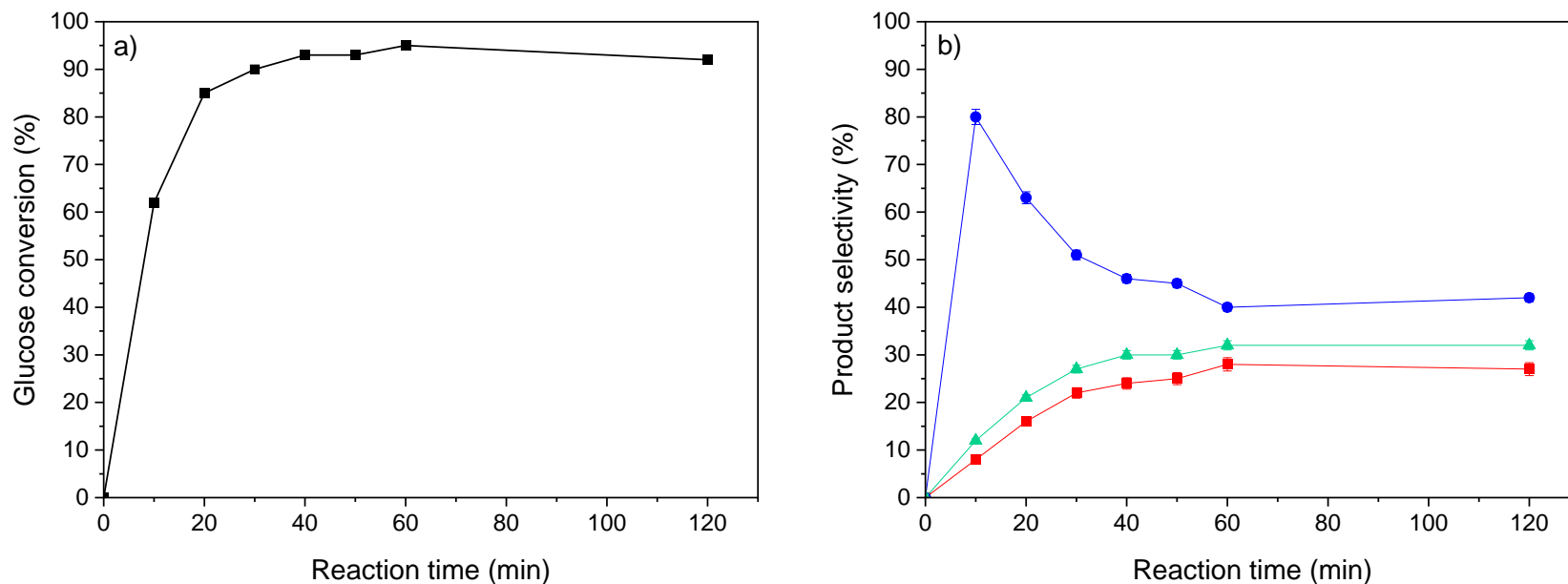


Figure 4.12. a) Kinetic profile for the glucose conversion (■), and b) product selectivity of the reaction mixture composed of fructose (■), methyl fructoside (●), and mannose (▲) catalysed by Sn/Y catalyst at 100 °C in methanol. The reactions were conducted using 125 mg of the substrate in 4 mL of methanol for 1 h and endogenous pressure using a constant M:S molar ratio of 1:100.

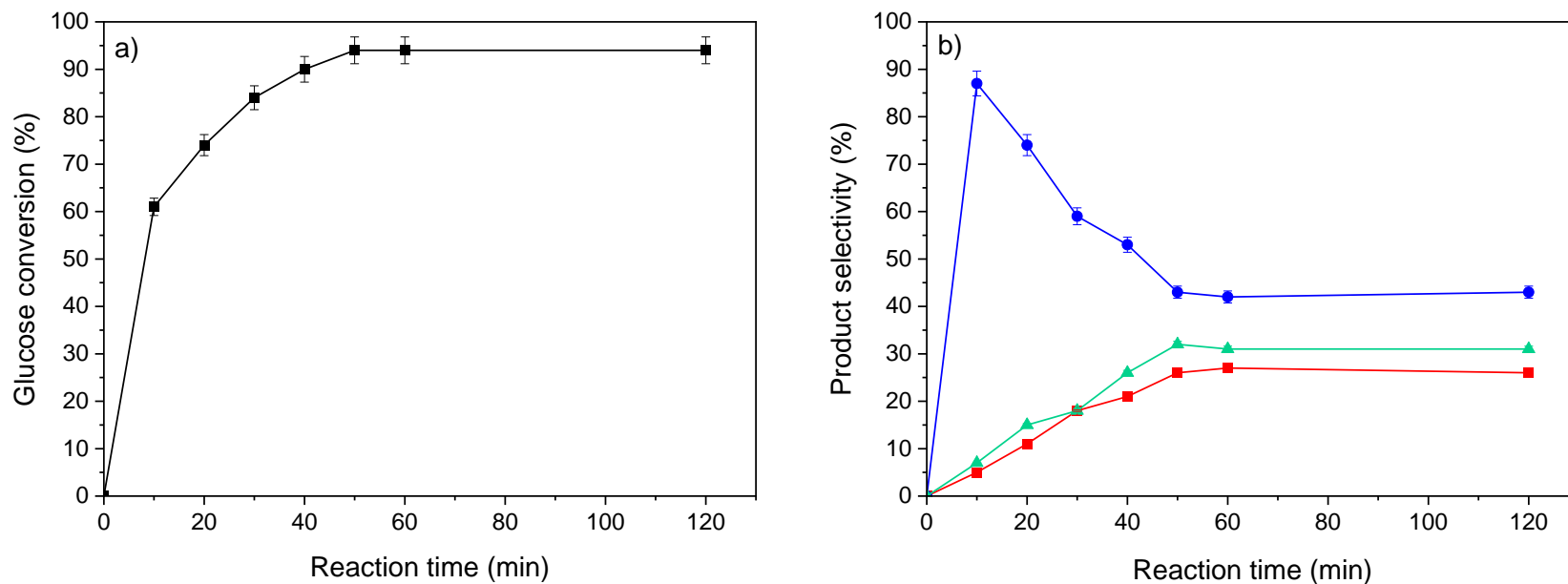


Figure 4.13. a) Kinetic profile for the glucose conversion (■), and b) product selectivity of the reaction mixture composed of fructose (■), methyl fructoside (●), and mannose (▲) catalysed by Ga/Y catalyst at 100 °C in methanol. The reactions were conducted using 125 mg of the substrate in 4 mL of methanol for 1 h and endogenous pressure using a constant M:S molar ratio of 1:100.

Both reactions were nearly completed within 1 h. This indicates that the reaction in methanol was therefore completed after 1 h and subsequent changes in product selectivity following the addition of water are unlikely to be due to an insufficient reaction time in the first step of the reaction. Furthermore, the second step of water addition demonstrated no significant effect on the selectivity of mannose for the three catalysts (either in terms of its production or consumption). It is important to also note that the conversion of glucose for reactions carried out at 100 and 120 °C is exceedingly high (> 90 %) and the reaction is considered near-quantitative. Whereas for reactions carried out at 80 °C and 90 °C, the conversion rate of glucose remained constant in the range of 60 %, regardless of water presence. Consequently, it can be concluded that this solvent has no influence on the equilibria (primarily epimerisation) of the species involved in the reaction but has a profound effect on the hydrolysis reaction of alkyl fructoside intermediate to desirable fructose.

Given the significant role that the methyl fructoside intermediate has been shown to play in fructose formation, additional enhancements to achieve improved fructose selectivity could involve increasing the temperature during the reaction step following water addition, increasing $[H^+]$ by lowering the pH of the solution to promote the hydrolysis of alkyl fructoside or using a zeolite with increased Brønsted acidity. However, these approaches can also negatively affect the overall reaction in terms of fructose yield. For example, an increase in reaction temperature might also lead to the formation of more undesirable humins, whereas an increase in Brønsted acidity can also enhance the propensity of the reaction to undergo dehydration, ultimately resulting in a reduction in fructose production. Therefore, a meticulous identification and assessment of potential reaction conditions will be imperative for optimization purposes and will serve as a basis for future work.

4.3. Control tests for solvent effect.

It has been demonstrated previously that reaction solvents influence a number of key factors, including the adsorption of reactive species, the solubility of reagents, and the catalytic cycle through the interactions with species involved in that catalytic cycle. In this context, The potential solvent effects on the catalytic performance of our catalysts for the isomerisation reaction of glucose to fructose were investigated using NMR relaxation measurements through an external collaboration work³².

As shown in (section 4.2.1), no glucose conversion was observed for the reactions using water as a solvent, which was confirmed to be due to site blockage of active sites on the zeolite surface by the strong adsorption of water molecules. This adverse effect is believed to be a result of the presence of water within the pores of the zeolite, filling them in such a way as to impede sugar molecules from entering the pores and, in turn, suppressing the reaction to occur. Alternatively, high Lewis acidity, which is a key characteristic of zeolite reactivity in the isomerisation of glucose to fructose - could be counterproductive if water is strongly co-ordinated with Lewis acid active sites through electron-rich oxygen atoms, which would prevent coordination of reactive species, therefore inhibiting catalytic activity³³.

In contrast, glucose conversion of approximately 100% was instead obtained in methanol and ethanol as solvents. In particular, with methanol, all catalysts exhibited a relatively equal product distribution of methyl fructoside, fructose, and mannose, most likely due to a dominant Brønsted reaction pathway resulting in a slight preference for the formation of methyl fructoside intermediate (*ca.* 30 % - 35 %), compared to the expected products of the isomerisation reaction (i.e., fructose and mannose). On the other hand, the presence of ethanol as a solvent led to the formation

of a significant amount of desired fructose ($\geq 50\%$), facilitated via a reaction pathway dominated by Lewis acid centres (Figure 4.14).

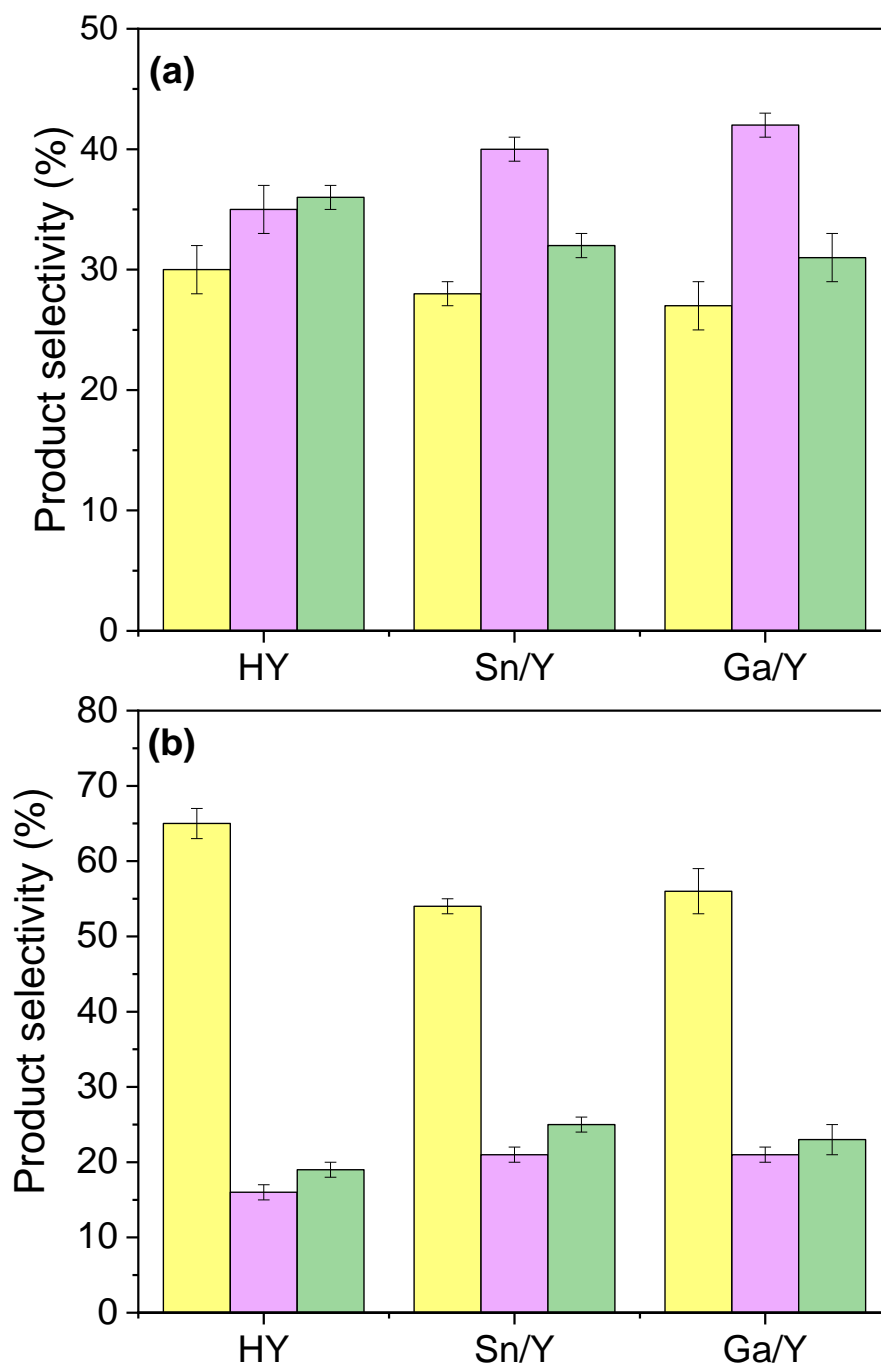


Figure 4.14. Product selectivity of fructose (■), alkyl fructoside (i.e., methyl and ethyl) (■), and mannose (■) as measured from the catalytic isomerisation of glucose into fructose using HY, Ga/Y and Sn/Y zeolite catalysts at 100 °C and endogenous pressure (a) in methanol and (b) in ethanol as solvents after a reaction time of 1 h. Glucose conversion of approximately 90 % and 100 % were achieved in methanol and ethanol, respectively³².

The NMR relaxation time measurements showed that the interaction strengths of the reaction solvents with the catalyst surfaces are found to be in the following order: water > ethanol > methanol for all the zeolites studied. Specifically, water adsorbs quite strongly to the zeolite pores, preventing reactant molecules from reaching the Lewis acid active sites and, in turn, suppressing the isomerisation reaction from occurring. Methanol, instead, has relatively weak adsorption to the surface of the zeolite; hence, reactant molecules can migrate into the pores of the zeolite, allowing the conversion of glucose to fructose and/or mannose via the Lewis acid active sites; the formed sugars can furthermore react at Brønsted acid centres located on the external surface of the zeolite framework and form methyl fructoside as a result of the relatively low uptake of methanol in comparison with that of ethanol. On the other hand, Ethanol adsorbs more strongly, but not up to a point to prevent the reaction from taking place, and yet strong enough to promote a larger uptake of sugar into the zeolite pores, hence the solvated sugars mainly interact with the Lewis acid active sites and are prevented from participating in further reactions at Brønsted acid active sites located on the outer surface of the zeolite, resulting in the formation of fructose as the major product³².

4.4. Control tests on the role of zeolite pores in glucose isomerisation.

In order to support these different hypotheses, and the conclusion was drawn from the NMR relaxation time measurements, Sn- and Ga-doped on SiO₂ and Al₂O₃ were synthesised and tested together with their undoped SiO₂ and Al₂O₃ in their bulk, i.e., non-porous forms in order to mimic the external surface of zeolites and determine the effects of site-blocking versus pore occupancy. In light of the catalyst preparation method used, namely, wet impregnation followed by a calcination step, we anticipate that SnO₂ and Ga₂O₃ clusters are expected to be formed on the surfaces of SiO₂ and

Al₂O₃¹⁵ (Figures A19 and A20 in Appendix A6). However, as these supports are non-porous, diffusion effects would be minimised. Therefore, we can precisely explain the differences in reaction reactivity of glucose isomerisation as non-porous materials would only be subjected to site-blocking effects. Unlike zeolite, which could be affected by both site blocking and pore occupancy.

In view of this, the catalytic tests of Sn/SiO₂, Sn/Al₂O₃, Ga/SiO₂, Ga/Al₂O₃, as well as SiO₂ and Al₂O₃, were carried out for the isomerisation reaction of glucose to fructose in the presence of water, methanol and ethanol as reaction solvents, and the catalytic data of this control test are provided (Table 4.4).

Table 4.4. The catalytic activity of Sn/SiO₂, Ga/SiO₂, Sn/Al₂O₃, and Ga/Al₂O₃ and their supports: SiO₂ and γ -Al₂O₃ for the isomerisation of glucose to fructose in water, methanol, and ethanol solvents. The reactions were carried out using a solution containing 125 mg of glucose in 4 mL of solvents at 100 °C and endogenous pressure using a metal loading for Sn and Ga was 1 wt. %, and a constant M:S molar ratio of 1:100.

Catalyst	Solvent(s)	Conversion (%)	Selectivity (%)			CMB (%)
			Fructose	Mannose	Fructoside	
SiO ₂	H ₂ O	0	n.d.	n.d.	n.d.	100
SiO ₂	CH ₃ OH	0	n.d.	n.d.	n.d.	100
SiO ₂	CH ₃ CH ₂ OH	0	n.d.	n.d.	n.d.	100
Sn/SiO ₂	H ₂ O	0	n.d.	n.d.	n.d.	100
Sn/SiO ₂	CH ₃ OH	23 ± 2	47 ± 3	53 ± 3	n.d.	96 ± 1
Sn/SiO ₂	CH ₃ CH ₂ OH	21 ± 1	78 ± 1	23 ± 1	n.d.	88 ± 2
Ga/SiO ₂	H ₂ O	0	n.d.	n.d.	n.d.	100
Ga/SiO ₂	CH ₃ OH	11 ± 1	54 ± 1	46 ± 2	n.d.	100 ± 2
Ga/SiO ₂	CH ₃ CH ₂ OH	19 ± 2	67 ± 3	33 ± 2	n.d.	100 ± 1
Al ₂ O ₃	H ₂ O	0	n.d.	n.d.	n.d.	100
Al ₂ O ₃	CH ₃ OH	13 ± 2	56 ± 1	44 ± 1	n.d.	100 ± 1
Al ₂ O ₃	CH ₃ CH ₂ OH	23 ± 4	56 ± 2	44 ± 2	n.d.	88 ± 4
Sn/Al ₂ O ₃	H ₂ O	0	n.d.	n.d.	n.d.	100

Sn/Al ₂ O ₃	CH ₃ OH	30 ± 2	56 ± 3	44 ± 3	n.d.	91 ± 3
Sn/Al ₂ O ₃	CH ₃ CH ₂ OH	27 ± 1	51 ± 1	49 ± 1	n.d.	83 ± 2
Ga/Al ₂ O ₃	H ₂ O	0	n.d.	n.d.	n.d.	100
Ga/Al ₂ O ₃	CH ₃ OH	19 ± 2	50 ± 1	50 ± 1	n.d.	90 ± 2
Ga/Al ₂ O ₃	CH ₃ CH ₂ OH	23 ± 2	43 ± 3	57 ± 3	n.d.	92 ± 2

n.d. = not detected.

Similar to microporous zeolites, none of these non-porous catalysts, neither doped nor undoped, displayed any reactivity in the presence of water as a reaction solvent. Notably, a similar lack of reactivity was observed in previous studies conducted by Davies et al., who studied the catalytic performance of external SnO₂ clusters doped on zeolite beta³⁴. The results of our tests indicate that this phenomenon would be more general and not limited to specific zeolites, SnO_x clusters, or any particular interactions between Sn and zeolites.

In particular, pure SiO₂ showed no catalytic activity in the presence of methanol as a solvent. In contrast, this had increased significantly to 23 % and 11 % with Sn/SiO₂ and Ga/SiO₂ catalysts, respectively. Furthermore, since no alkyl fructoside is formed regardless of the reaction conditions used, we can conclude that the formation of this intermediate is inhibited due to the lack of Brønsted acid active centres, which is an essential characteristic present in all zeolite-based catalysts used within this reaction (i.e., HY, Sn/Y, and Ga/Y).

Pure Al₂O₃, on the other hand, showed activity in the range of 15%. This is, in fact, a result of the presence of Lewis acid sites in this bare oxide. Further enhancement of the activity was obtained by the incorporation of Sn and Ga species, resulting in similar approaches to those of doped non-porous SiO₂. In all cases, non-porous support displayed significantly lower activity (at least 5 - 10 times less) than that of microporous

zeolite HY. As a result, it can be concluded that, for zeolites, the presence of pores plays a significant role in driving the reaction, and the isomerisation reaction of glucose does indeed take place within the pores.

In comparison to methanol, ethanol as a solvent produced similar results; however, since this solvent has a small site-blocking effect, pore occupancy will be a dominant factor in the reactivity of porous zeolite. It should also be noted that no alkyl fructoside (formed by Brønsted acidity) was found, but only fructose and mannose were found to be produced by Lewis acidity.

In general, conversion values are comparable to or even higher than those obtained with methanol. Since ethanol has a lower protic and nucleophilic potential than methanol, it will have a much smaller site-blocking effect within the pores of the zeolites than water or methanol. It is also pertinent to note that specific considerations regarding the potential nucleophilic effects of these solvents on our substrates were beyond the scope of this study and, hence, are not being addressed further. However, this could provide the basis for future investigations in this regard.

4.5. Control tests for leaching and mass transfer.

Leaching is a phenomenon that may occur in heterogeneous catalysis systems, involving the dissolution of the active species from the heterogeneous catalyst into the reaction media. In view of this, control tests for metal leaching of Sn and Ga species were carried out, even if our reaction seems to be dominated by Brønsted acidity¹⁰. The results of ICP analysis of the reaction mixtures revealed an extremely small amount of metal leaching at each reaction step. Following both steps of methanol and subsequent water addition a mass loss of approximately 0.1% was detected for Ga (relative to the total amount of Ga species present in the catalyst), whereas Sn/Y had

relative metal losses of 1.2% and 1.7% of Sn, after the step using methanol and the sequential step of water addition, respectively. In order to eliminate the effect of these trace amounts of metals in the solution, we conducted control tests using reaction mixtures containing $\text{SnCl}_4 \cdot 5\text{H}_2\text{O}$ and $\text{Ga}(\text{NO}_3)_3 \cdot x\text{H}_2\text{O}$ precursors. The catalytic tests were performed using identical amounts of metal leaching detected by ICP analysis (approximately corresponding to metal to substrate molar ratio of $1:10^2$ for Ga and $1:10^4$ for Sn). However, no catalytic activity was observed in these catalytic tests. Consequently, these small amounts of metal leaching do not have any significant effect either on the durability of our materials or the reaction in the solution.

Table 4.5. Relative leaching loss measured by the mean of ICP-MS using the reaction mixtures of the active metal, Sn or Ga, with respect to a 1 wt% metal loading for Sn/Y, Ga/Y after reactions carried out in methanol and/or reactions carried out in methanol followed by the step of water addition. The experimental error is reported as the standard deviation of three repeated measurements.

Catalyst	Catalytic step	Relative Sn metal loss (%)	Relative Ga metal loss (%)
Sn/Y	After methanol	1.2	-
Ga/Y	After methanol	-	< 0.1
Sn/Y	After methanol and sequential water addition	1.7	-
Ga/Y	After methanol and sequential water addition	-	0.14

External diffusion is the phenomenon of the mass transfer of a reagent from its phase (either a gas or a liquid, in our case) to the catalyst's surface. A control test on the effect of the stirring rate and the amount of catalyst to conversion is systematically investigated to rule out the effect of external diffusion limitation. In this regard, Control tests with different mixing stirring rates in the range of 100 - 1000 rpm revealed no effect on catalytic performance. Alternatively, changing the M:S molar ratio from 1:10

to 1:1000 showed significantly different results (Figure 4.17). In particular, glucose conversion is increased per increasing number of active centres in the M:S range of 1:1000 - 1:100, thus confirming the reaction is carried out under a kinetic regime, and the effects of external diffusion limitation (mass transfer) are negligible. However, an increase in the M.S ratio ranges from 1:50 to 1:10 resulted in constant glucose conversions of 98%. This could be attributed to either diffusion limitations or the possibility that a maximum glucose conversion has already been reached by equilibrium. The latter explanation appears more reliable since the conversion rate reaches 100% within the experimental error. Overall, an M:S molar ratio of 1:100 promotes the highest glucose conversion but still preserves a kinetic regime.

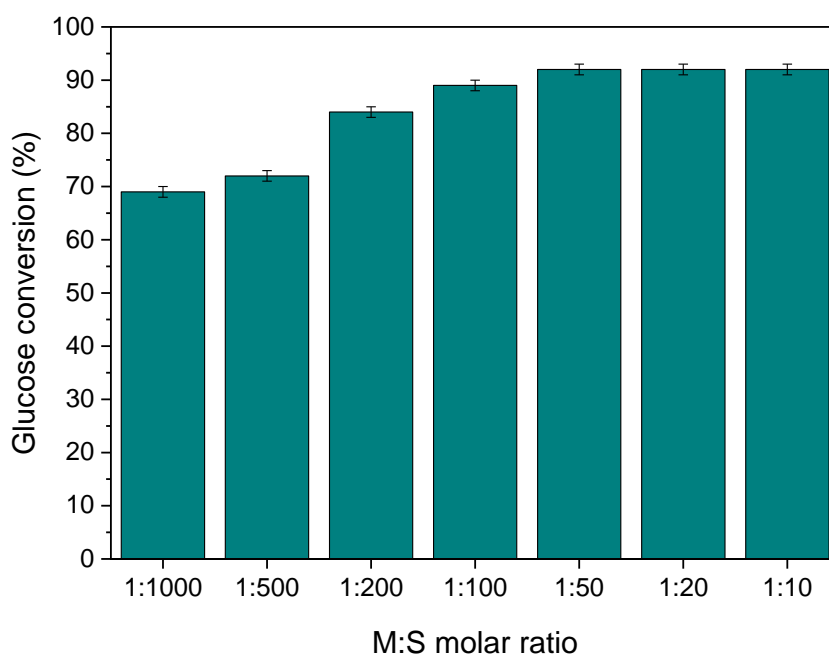


Figure 4.17. Representative diffusion (external mass transfer) control test for the effect on glucose conversion by changing an M:S molar ratio for a reaction carried out in methanol at 100 °C using Ga/Y zeolite. The tests were performed using 125 mg of the substrate in 4 mL of methanol for 1 h. Metal catalyst loading 1 wt% was kept constant, and the amount of catalyst varied.

4.7. Characterization of the catalysts and structure-activity correlations.

As a result of the several reaction routes observed for the production of fructose from the isomerisation of glucose (Eqs. 4.1-4.3), which either involve hydride shifts or an acid-base reaction pathway and occur inside or outside the pores of the zeolite frameworks. In this regard, our catalytic data prompted us to investigate and determine potential structure-activity correlations for all catalysts used. As a consequence, a wide range of acidity measurements and techniques, including back titration and NH_3 chemisorption for Lewis and Brønsted acidity, BET for textural properties, N_2 adsorption-desorption for pore structure, XPS for the oxidation chemical state of doped metal ions, HAADF-STEM for surface morphology, XRPD for crystal structure, and EXAFS for the coordination environment of metal dopants were used.

4.7.1. Acidity measurements.

As a result of the significant role acidity has played in the data obtained so far, a thorough characterisation of the materials was performed for both Brønsted acidity and Lewis acidity. In this regard, an acid/base back-titration (described in section 2.7.2.1 in Chapter 2) was carried out for the determination of the total Brønsted acidity, whereas an NH_3 chemisorption experiment was conducted in order to measure the total Brønsted and Lewis acidity (Table 4.6 and Figure 4.18). Despite the simplicity of the back-titration method, it is a straightforward and statistically robust technique still used, though mainly to determine the acidity of microporous polymers^{35,36}. Specifically, measuring the number of protons recovered from the titration over a strong base to a particular endpoint³⁷ corresponds to Brønsted acidity in our case.

Table 4.6. Acidity data and textural properties of HY, Sn/Y and Ga/Y: (a) total Brønsted acidity measured via acid/base back-titration; (b) combination of Brønsted and Lewis acidity determined by NH₃ chemisorption; (c) surface area through 20 points BET method using N₂ adsorption and (d) microporous volume measured via BJH method using N₂ adsorption.

Catalyst	B acidity^(a) (mmol g⁻¹)	B + L acidity^(b) (mmol g⁻¹)	S^(c) (m² g⁻¹)	V_{micro}^(d) (mL g⁻¹)
HY	1.78	2.93	797	0.26
Sn/Y	1.72	2.85	691	0.21
Ga/Y	1.70	2.78	695	0.21

As demonstrated in (section 1.5.4), Brønsted acidity can be derived through the presence of OH groups through silanol units (SiOH) or hydrated Al centres³⁸. Lewis acidity, on the other hand, can be derived from coordinatively unsaturated metal centres (e.g., Al, Sn, or Ga in our case)³⁹. Back titration measurements revealed an apparent decrease in the values of total Brønsted acidity following the step of metal doping. This decrease showed consistency, in principle, with a decrease in Brønsted acidity associated with the formation of basic SnO₂ and Ga₂O₃ metal oxides. It should be noted, however, that the difference between these acidity values (1.78 to 1.70 mmol g⁻¹) was found to be within the experimental error of our titration procedure (ca. 0.02 mmol g⁻¹). Therefore, we do not consider this difference to be statistically significant.

The total Brønsted and Lewis acidity, determined rather through NH₃-chemisorption, also decreased with Sn- and Ga-doped catalysts compared to the acidity of the parent zeolite. A straightforward comparison of Brønsted acidity obtained by acid/base back-titration and the combination of Brønsted and Lewis acidity obtained by NH₃-chemisorption is not easily possible, although our results indicate that there is no apparent difference between our catalysts in terms of Lewis acidity. Both sets of acidity data are found to be consistent with one another, despite NH₃ chemisorption providing

information on the total acidity of the sample (i.e., Brønsted and Lewis acid centres) when, in contrast, the back-titration measures only total Brønsted acid sites. Indeed, back-titration measurements have always revealed lower acidity values than those determined using the NH_3 -chemisorption technique.

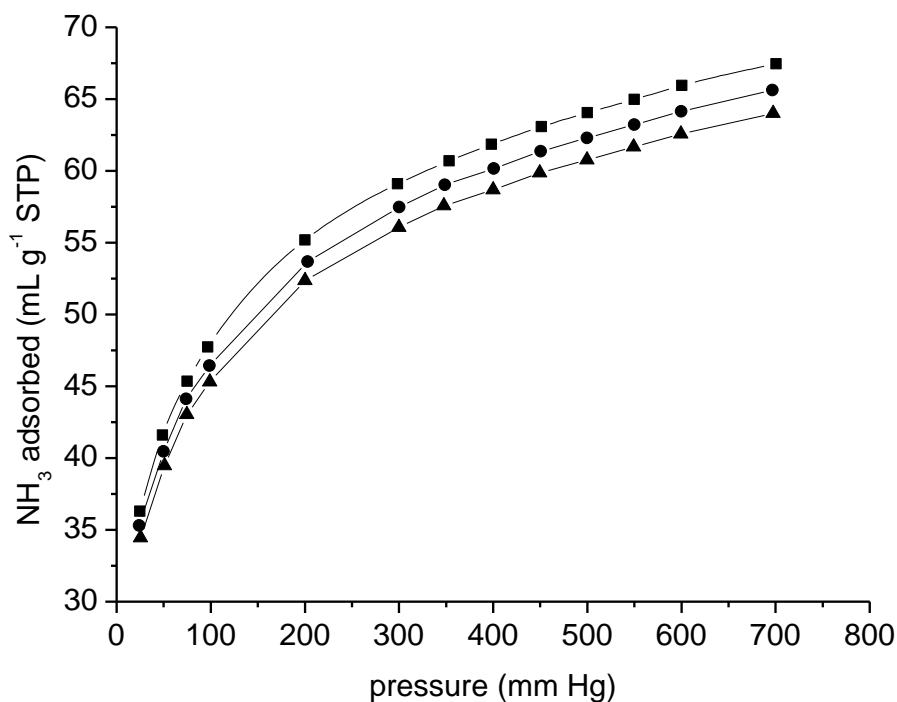


Figure 4.18. Adsorption isotherms for the combination of Brønsted and Lewis acidity of NH_3 over (■) HY zeolite, (●) Sn/Y zeolite, and (▲) Ga/Y zeolite. Samples were pre-treated by evacuation at 150 °C for a time of 2 h and adsorption measurements carried out at 35 °C. NH_3 volumes were normalised as standard temperature and pressure per gram of sample.

Given the importance of Brønsted and Lewis acid sites in the isomerisation of sugars, our materials were further characterised using diffuse reflectance infrared Fourier transform (DRIFT) spectroscopy with pyridine as an adsorbent in order to differentiate between strong and weak Brønsted and Lewis acid sites. From the DRIFT peak intensities, Lewis to Brønsted ratios (L/B) of 0.95, 0.89, and 1.2 were estimated for HY, Sn/Y, and Ga/Y, respectively (Figure A21 in Appendix A.7), in agreement with the

acidity data obtained by acid/base Back-titration and NH_3 -chemisorption. That is a relatively small increase in the Lewis acidity of the Ga/Y zeolite catalyst⁴⁰.

As a complement to these data, our materials were subjected to BET surface area and micropore volume measurements (Table 4.6) in order to determine whether major changes had occurred in the density of acid sites. However, the differences appear to be insignificant. In addition, both total surface area and micropore volume were found to be slightly decreased upon metal doping, consistent with the catalyst preparation method used³⁹.

4.7.2. X-ray photoelectron spectroscopy and inductively coupled plasma analysis.

To support the acidity results described above, we performed X-ray photoelectron spectroscopy in order to measure both the oxidation chemical state and the amount of dopant Sn and Ga species in our catalysts.

As indicated in the spectra of the Sn/Y sample, two peaks were observed with binding energies of 495.4 eV and 486.7 eV, which could be assigned to Sn $3d_{5/2}$ and Sn $3d_{3/2}$, respectively. This chemical state is highly consistent with that of SnO_2 ⁴¹ (Figure 4.19). In contrast, the XPS spectra of Ga revealed an apparent peak with a binding energy of 1117.8 eV that corresponds to Ga $2p_{3/2}$. This result is consistent with that of Ga_2O_3 or Ga with a high oxidation state⁴² (Figure 4.20). In both Sn and Ga, the observed oxidation chemical states demonstrated high consistency with the method of preparation (i.e., wetness impregnation followed by a calcination step in the air)³⁹. It is also important to note that although the uncoordinated, or surface coordinatively unsaturated species of Sn^{4+} and Ga^{3+} are both Lewis acid sites, SnO_2 and Ga_2O_3 are, in principle, basic in nature. This, in fact, could explain the slight decrease in acidity observed in our measurements.

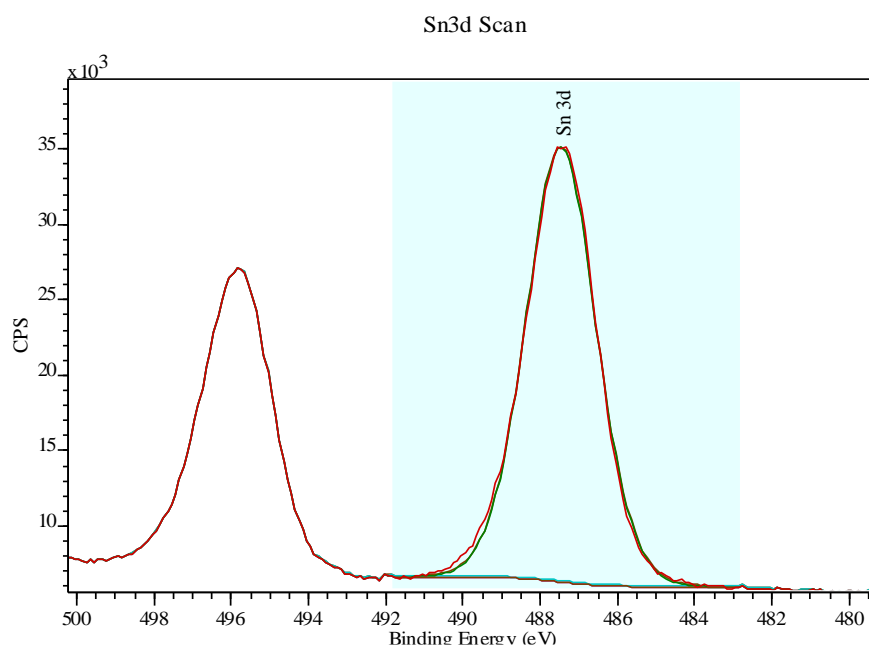


Figure 4.19. XPS spectrum (red line) and peak fitting (green line) for the Sn3d signal in Sn/Y. The signal of Sn is compatible with SnO₂ having binding energies for Sn 3d_{3/2} and Sn 3d_{5/2} of 495.7 eV and 487.4 eV, respectively.

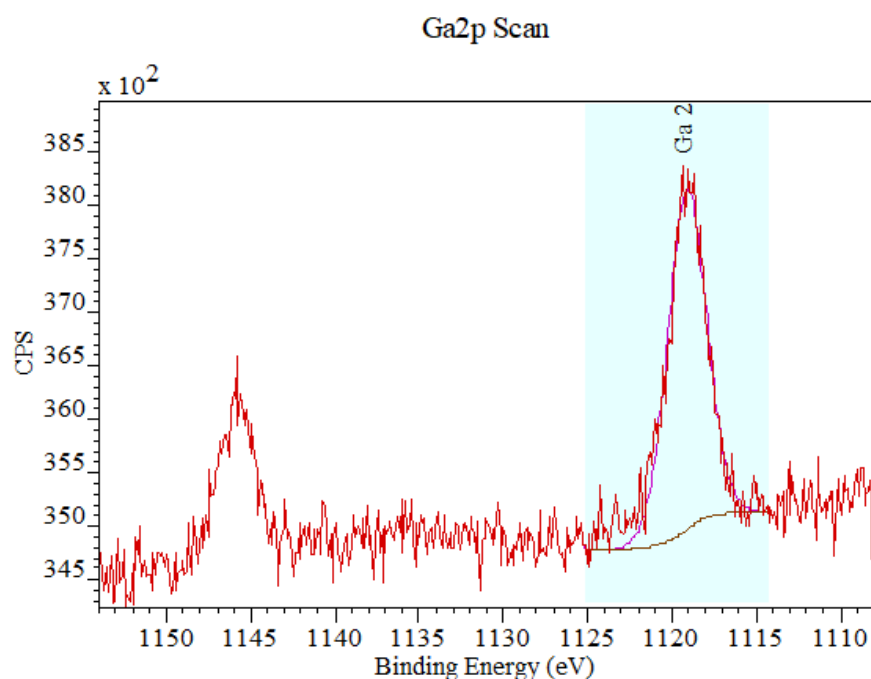


Figure 4.20. XPS spectrum (red line) and peak fitting (green line) for the Ga_{2p} signal in Ga/Y. The signal of Ga is compatible with Ga₂O₃ having binding energies for Ga 2p_{3/2} of 1118.8 eV.

On the other hand, the quantitative analysis of the surface composition (Table 4.7) revealed that the two catalysts are quite different. In particular, Sn species were detected in a relatively large amount, 1.8 at%. In contrast, Ga species were detected in a much smaller amount of 0.1 at%, close to the limit of detection.

Table 4.7. Atomic surface composition of HY, Sn/Y and Ga/Y zeolites reported in at%. Carbon is an incidental component, and the presence of all the other elements is consistent with the metal precursors used and the elemental composition of the zeolite framework.

Catalyst	At (%)							
	C	O	Sn	Si	Al	Ga	N	Cl
HY	11.0	56.8	0.0	30.8	1.3	0.0	0.1	0.0
Sn/Y	9.5	57.3	1.8	30.5	1.0	0.0	0.0	0.0
Ga/Y	10.0	59.6	0.0	29.0	1.0	0.1	0.2	0.0

As a result of comparing these amounts with their expected bulk compositions of 1 wt% for both Sn and Ga centres, 1 wt% would be equivalent to *ca.* 0.5 mol% in the case of Sn and 0.9 mol% in the case of Ga for the entire bulk material (as compensation for this difference, all catalytic tests were carried out at a constant M:S molar ratio). Therefore, under the assumption that Sn and Ga were uniformly distributed inside the pores of the zeolite and on its external surface, A higher at% or mol% of Ga compared to Sn would be expected to be detected. Due to the fact that XPS is a surface-sensitive analytical technique capable of an average penetration depth in the range of 5 - 10 nm⁴³, the extremely weak signal observed for Ga could be due to these species being highly dispersed inside the zeolite pores, whereas Sn is predominantly distributed on the external surface of the zeolite crystals.

4.7.3. High-angle annular dark-field imaging – scanning transmission electron microscopy.

To gather direct evidence supporting the conclusions derived from the XPS analysis, which indicated Sn (as SnO₂ clusters) was primarily present on the outer surface of the zeolite crystal, and Ga (as Ga₂O₃ clusters) was mainly present within the pores of the zeolite framework, our catalysts were further analysed by means of high-angle annular dark-field imaging – scanning transmission electron microscopy (HAADF-STEM)⁴⁴. As can be seen in Figures 4.21A and 4.21B, it is evident that the Sn/Y catalyst consists of defined SnO₂ clusters located at the exterior surface of the zeolitic crystal, with an average particle size which is determined to be 4.2 nm. On the other hand, Ga/Y exhibited an absence or only occasional presence of Ga₂O₃ clusters (Figures 4.22A and 4.22B), which leads us to the conclusion that Ga must be either highly dispersed or present within the zeolite pores.

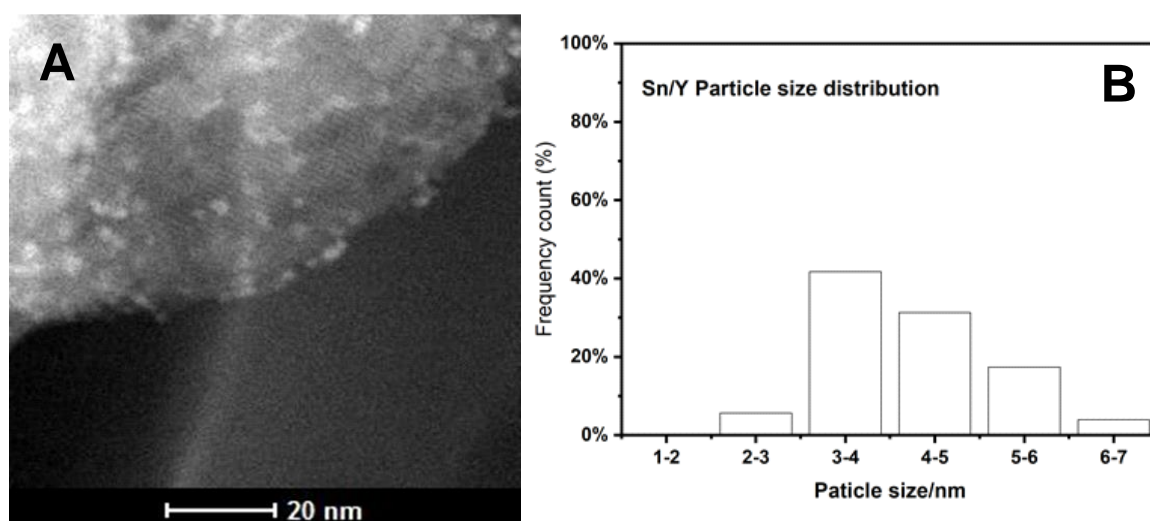


Figure 4.21. (A) HAADF-STEM image of Sn/Y zeolite prepared using a wetness impregnation procedure with 1 wt% as metal loading of Sn. The fringe-like structure on the support represents zeolite channels, and the particles along the edges (outside the crystal) are SnO₂-like nanoparticles. **(B)** The distribution of particle sizes of SnO₂ with an average particle size of 4.2 nm.

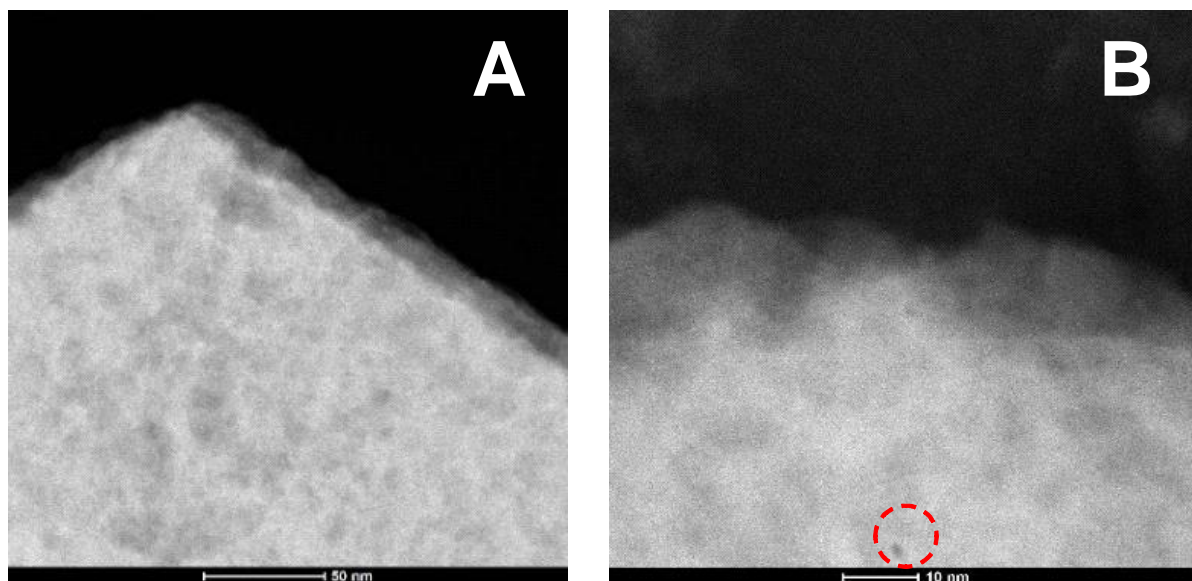


Figure 4.22. HAADF-STEM image of Ga/Y zeolite prepared using a wetness impregnation protocol with 1 wt% as metal loading of Ga. **(A)** Metal or metal nanoparticles are not observed externally in zeolite crystals, or **(B)** only occasionally (dark spot inside the dashed red circle).

Having obtained a highly dispersed metal using a straightforward impregnation procedure is quite surprising and could offer a wide range of potential implications beyond the current thesis work. A similar phenomenon has been observed infrequently, as in the preparation of Fe-doped mesoporous silica SBA-15⁴⁵ or zeolite HZSM-5⁴⁶, which were only produced by means of vacuum synthesis techniques and with the use of alkali metals as promoters, which are significantly different from the protocol used in this thesis work, that is, performed at atmospheric pressure with no addition of alkali metals. This significant difference does not, however, appear to be a major factor in the reaction. Consequently, it can be concluded that most of the activity originates from the acidity of the zeolites. However, it is imperative to understand the potential effects of added dopant metals. For example, it is important to consider carefully speculations made on the catalytic activity of metal species such as Sn and Ga active centres originating from their Lewis acidity characteristic when moving from a homogeneous catalytic system^{10,12,13} to a heterogeneous counterpart; Therefore,

retention of the catalytic activity might not be maintained. Although this could still have an effect on selectivity.

4.7.4. Powder X-ray diffraction.

As part of a comprehensive structural investigation of our materials, powder XRD patterns were obtained for HY, Sn/Y and Ga/Y catalysts (Figure 4.23) to characterise the crystalline structure of the prepared catalysts and to determine if the zeolite has undergone any ion exchange or distortion due to the preparation protocol. A Rietveld refinement⁴⁷ was performed (Table A6 in Appendix A.8). As shown in the XRD patterns, Sn/Y and Ga/Y exhibit nearly identical PXRD patterns and no significant contraction in the unit cell volume has been observed as a consequence of the variations in the unit cell volume of the parent zeolite HY (determined as 14363 Å³). In view of this, it is unlikely for Sn or Ga to be incorporated into the zeolite framework as a substitution for Al - at least within the resolution of the acquired PXRD patterns.

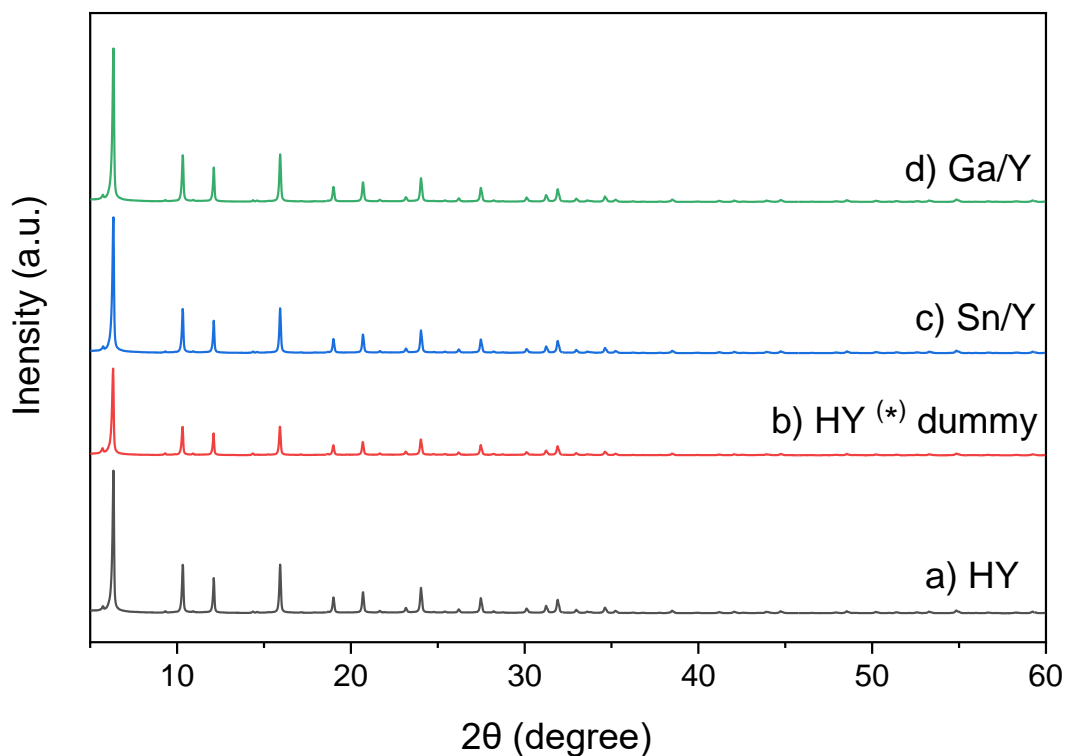


Figure 4.23. XRD patterns of zeolites: **a)** HY as delivered, **b)** HY treated for metal deposition but without metal dopant, **c)** Sn/Y and **d)** Ga/Y. All zeolites exhibit a nearly identical pattern and show no evidence of Sn and Ga metal or metal oxide clusters.

It is important to note that even though Sn and Ga centres were demonstrated to be present as SnO₂ and Ga₂O₃ (Sections 4.7.2 and 4.7.3), there were no distinctive reflections associated with these metal oxide clusters observed. For SnO₂⁴³, these were expected to be at 26.6°, 37.8° and 51.8° 2θ, for the reflections of (110), (200) and (211), respectively, and in the case of β-Ga₂O₃⁴⁸. These were expected to be at 31.2°, 35.9° and 38.1° 2θ, for the reflections (222), (400) and (411), respectively. This is consistent with data obtained from HAADF-STEM, and a particle size of less than 4 – 5 nm, or highly dispersed metal species⁴⁹.

Apart from determining the basic structure and bulk chemical composition, obtaining the unit cell parameter (derived from XRD data) of Sn and Ga-doped zeolite Y catalysts prepared via the wetness impregnation technique is vital to understanding the

interactions between the metal and zeolite framework. Several studies have demonstrated that metal might be deposited over the surface of zeolite or trapped within its framework, wherein the two types of metal-zeolite interactions result in different catalytic performances^{50,51}. The substitution of metal in place of Al sites within the zeolite matrix is generally indicated by the expansion or contraction of the unit cell depending on the size of the metal (in our case, Sn and Ga) compared to Al. For instance, due to the larger size of Sn in its ionic form and coordination when compared to Al, increasing the volume expansion of the unit cell indicates that this metal has been successfully incorporated into the structural matrix⁵². A unit cell expansion, however, was not observed with our Sn/Y catalyst (Table A6 in Appendix A.8), indicating that the Sn species of our catalyst prepared by wetness impregnation were not embedded into the framework of these zeolite catalysts but rather were supported on their surface or within their pores/channels.

4.7.5. Extended X-ray absorption fine structure and structure considerations.

In order to confirm and reinforce the data and conclusions derived from HAADF, STEM and XRD regarding the structural characteristics of Sn/Y and Ga/Y zeolites, our materials were also studied using an extended X-ray absorption fine structure (EXAFS) technique^{53,54}.

First of all, the EXAFS measurements demonstrated that the signal for Ga/Y was much stronger as compared to that for Sn/Y, in agreement with data from the ICP-MS, which indicated that Ga had a much higher mol% than Sn. As a consequence, the differences in the fitting of the two species are most likely due to a difference in the distribution of metals within the catalysts investigated.

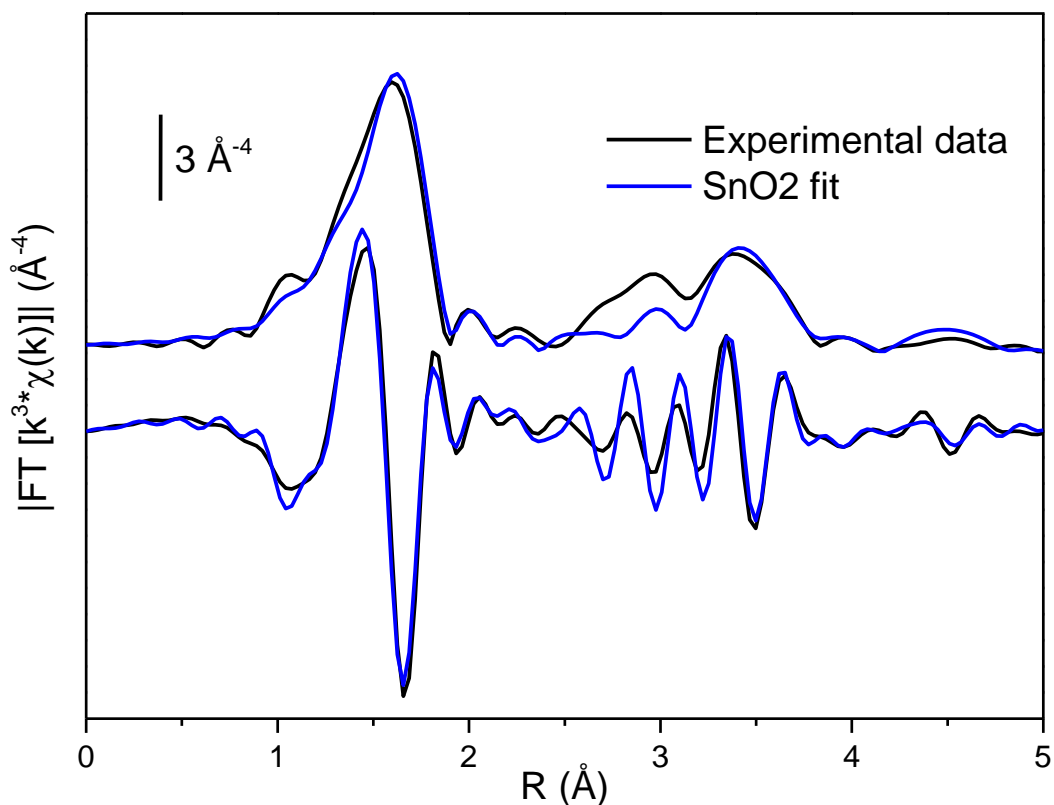


Figure 4.24. EXAFS Fourier transform for Sn/Y zeolite (black line). Modelled spectra of SnO₂ clusters independent of the Zeolite structure are depicted in blue lines. An excellent fit in agreement with slightly amorphous SnO₂ was observed.

Specifically, a fitting of the Sn/Y catalyst versus the standard SnO₂ was performed⁵⁵, and the EXAFS interpolation results have been confirmed to be compatible with SnO₂ crystallographic structure (Figure 4.24 and Table A7 in Appendix A.9). One notable difference observed in our catalysts, that is, their outer Sn shells exhibit a higher Debye-Waller factor as compared to bulk SnO₂ (0.0089 Å²), as shown in Table A7 in Appendix A.9. It appears that SnO₂ clusters in Sn/Y have shown a slightly higher disordered/amorphous structure than that of the bulk oxide. Since SnO₂ in its bulk form has a highly ordered structure, it is expected that the value for the photoelectron mean Sn-Sn path in the second shell would be in the range of 0.003-0.005 Å².

In terms of Ga/Y, the results showed to be quite different from those of comparable HAADF-STEM data. In consequence, the results of EXAFS were either fitted based on the assumption

of the presence of β -Ga₂O₃ clusters or Ga incorporated into the zeolite framework. As we move towards the Ga edge and observe the data, the absence of a second shell is evident in the EXAFS Fourier transform signal, potentially supporting the presence of β -Ga₂O₃ clusters. Conversely, the first shell is compatible with the presence of 4 - 6 oxygen atoms, as would be expected from the incorporation of Ga within the zeolite framework⁵⁶. It is not possible to obtain a satisfactory fit with the scattering path that involves Ga-Ga atoms from the crystal structure of β -Ga₂O₃⁵⁷ (Figure 4.25).

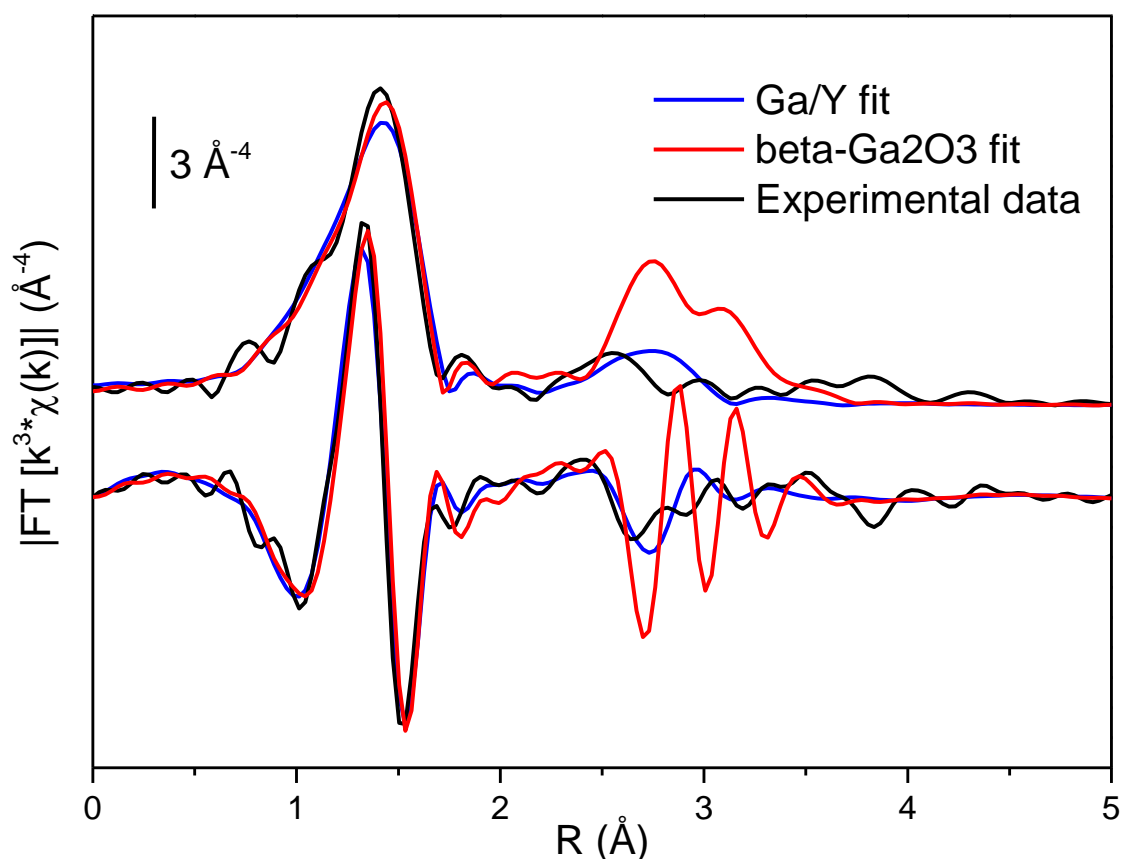


Figure 4.25. EXAFS Fourier transform for Ga/Y zeolite (black line). Modelled spectra: of β -Ga₂O₃ clusters independent of the zeolite structure (red line) and Ga species within the zeolite framework (blue line). A better fit of the experimental data is achieved in the latter case.

A significant improvement in fit could be observed with the attempt to substitute Ga in the zeolite framework (Figure. 4.25, Table A8 in Appendix A.9). The distances appear to correspond to the higher atomic weight of Ga in comparison to Si/Al, showing a first shell distance nearly identical to the length of the Ga-O bond in β -Ga₂O₃. In contrast,

the intensity and phase of the second shell are better reflected, with both being similarly shifted with the same amount (+0.2 Å). As well, here, the Debye-Waller factor appears to be relatively high (0.02 Å²), indicating the presence of a strain/disorder in the structure.

4.8. Conclusion

This study has demonstrated that the isomerisation of glucose is a complicated reaction involving the interconversion of multiple species as well as the production of a methyl fructoside intermediate and mannose in the presence of methanol as a reaction solvent.

It was found that our materials, namely HY, Sn/Y, and Ga/Y, exhibited similar catalytic performance in converting glucose to fructose, methyl fructoside, and mannose with different temperatures in the range of 80 - 120°C and using either one-step reaction protocol in methanol or two-step reaction protocol in methanol followed by the subsequent addition of water as solvents. Despite the fact that increasing the reaction temperature improved dramatically glucose conversion to over 90% and fructose selectivity above 50%, the reduced carbon mass balance suggested the formation of more by-products, most likely humins. As a result of these factors, 100°C was found to be the optimal reaction temperature.

In the presence of methanol as a solvent, significant amounts of methyl fructoside intermediates were formed through a reaction pathway mediated via Brønsted acid centres. In catalytic reactions with fructose and mannose as substrates in the presence of methanol, all catalysts produced a reaction mixture composed of glucose, methyl fructoside, fructose and mannose. In addition, we demonstrated that glucose, fructose, and mannose are all in equilibrium with fructose through 1,2-intramolecular

hydride shifts promoted via Lewis acid active sites present in the catalyst. As a consequence, three reaction pathways are involved in the catalytic conversion of glucose to methanol: (i) a Lewis acid pathway that converts glucose to fructose and then in mannose, (ii) the reversible reaction, and (iii) a Brønsted acid pathway that facilitates the conversion of fructose to methyl fructoside.

In contrast, when the reactions were performed with water following methanol, the presence of this solvent could enhance the hydrolysis reaction of the methyl fructoside intermediate to desirable fructose while simultaneously suppressing the catalytic performance of all zeolite catalysts for the isomerisation reaction of glucose to fructose. Most likely, this is a consequence of water being strongly adsorbed within the zeolite pores or due to a site-blocking of Lewis acid active centres that facilitate the isomerisation reaction of glucose to fructose. Nevertheless, the addition of water following the reaction in methanol led to an increased conversion of methyl fructoside into fructose under all our conditions. This indicates that a Brønsted acid pathway dominates this reaction, which could probably explain the similar catalytic results obtained with all catalysts studied.

Ga/Y and Sn/Y were shown to be significantly different in structure, with Sn/Y being mainly composed of SnO₂ clusters located on the external surface of the zeolite crystals and Ga/Y comprised of highly dispersed Ga species inside the pores. Therefore, the Brønsted acid reaction pathway discussed in the earlier section (section 4.2.1) might not necessarily take place or be restricted by the zeolite pores, and this will provide a basis for further studies to investigate the importance of pores in this reaction when water is not the initial solvent.

4.9. References

- 1 I. Delidovich and R. Palkovits, *ChemSusChem*, 2016, **9**, 547–561.
- 2 P. Gallezot, *Chem. Soc. Rev.*, 2012, **41**, 1538–1558.
- 3 S. Dutta, *ChemSusChem*, 2012, **5**, 2125–2127.
- 4 V. Choudhary, A. B. Pinar, R. F. Lobo, D. G. Vlachos and S. I. Sandler, *ChemSusChem*, 2013, **6**, 2369–2376.
- 5 B. Kamm, *Angew. Chem.*, 2007, **46**, 5056–5058.
- 6 R. Bermejo-Deval, R. S. Assary, E. Nikolla, M. Moliner, Y. Román-Leshkov, S.-J. Hwang, A. Palsdottir, D. Silverman, R. F. Lobo, L. A. Curtiss and M. E. Davis, *Proc. Natl. Acad. Sci. U.S.A.*, 2012, **109**, 9727–9732.
- 7 N. Rai, S. Caratzoulas and D. G. Vlachos, *ACS Catal.*, 2013, **3**, 2294–2298.
- 8 M. Moliner, Y. Román-Leshkov and M. E. Davis, *Proc. Natl. Acad. Sci. U.S.A.*, 2010, **107**, 6164–6168.
- 9 R. Bermejo-Deval, M. Orazov, R. Gounder, S. J. Hwang and M. E. Davis, *ACS Catal.*, 2014, **4**, 2288–2297.
- 10 H. Nguyen, V. Nikolakis and D. G. Vlachos, *ACS Catal.*, 2016, **6**, 1497–1504.
- 11 R. Oozeerally, J. Pillier, E. Kilic, P. B. J. Thompson, M. Walker, B. E. Griffith, J. V. Hanna and V. Degirmenci, *Appl. Catal. A: Gen.*, 2020, **605**, 117798.
- 12 Y. Román-Leshkov, M. Moliner, J. A. Labinger and M. E. Davis, *Angew. Chem.*, 2010, **122**, 9138–9141.
- 13 G. Li, E. A. Pidko and E. J. M. Hensen, *Catal. Sci. Technol.*, 2014, **4**, 2241–2250.

- 14 R. Fricke, H. Kosslick, G. Lischke and M. Richter, *Chem. Rev.*, 2000, **100**, 2303–2405.
- 15 J. A. Lopez-Sanchez, M. Conte, P. Landon, W. Zhou, J. K. Bartley, S. H. Taylor, A. F. Carley, C. J. Kiely, K. Khalid and G. J. Hutchings, *Catal. Lett.*, 2012, **142**, 1049–1056.
- 16 S. Saravanamurugan, M. Paniagua, J. A. Melero and A. Riisager, *J. Am. Chem. Soc.*, 2013, **135**, 5246–5249.
- 17 N. Rajabbeigi, A. I. Torres, C. M. Lew, B. Elyassi, L. Ren, Z. Wang, H. Je Cho, W. Fan, P. Daoutidis and M. Tsapatsis, *Chem. Eng. Sci.*, 2014, **116**, 235–242.
- 18 R. Gounder and M. E. Davis, *AIChE Journal*, 2013, **59**, 3349–3358.
- 19 M. Demerdash and R. M. Attia, *Zentralbl Mikrobiol*, 1992, **147**, 297–303.
- 20 J. Cui, J. Tan, T. Deng, X. Cui, Y. Zhu and Y. Li, *Green Chem.*, 2016, **18**, 1619–1624.
- 21 F. A. J. Meskens, *Synthesis (Stuttg)*, 1981, **1981**, 501–522.
- 22 D. M. Gao, T. Kobayashi and S. Adachi, *Biosci. Biotechnol. Biochem.*, 2015, **79**, 1005–1010.
- 23 V. F. Taylor, R. E. March, H. P. Longerich and C. J. Stacey, *Int. J. Mass Spectrom.*, 2005, **243**, 71–84.
- 24 Z. Wang, Y. Jiang, O. Lafon, J. Trébosc, K. Duk Kim, C. Stampfl, A. Baiker, J. P. Amoureux and J. Huang, *Nat. Commun.*, 2016, **7**, 13820.
- 25 M. J. Climent, A. Corma, S. Iborra, S. Miquel, J. Primo and F. Rey, *J. Catal.*, 1999, **183**, 76–82.

- 26 S. Saravanamurugan, A. Riisager, E. Taarning and S. Meier, *ChemCatChem*, 2016, **8**, 3107–3111.
- 27 S. Lee, H. Y. Bae and B. List, *Angew Chem. Int. Ed. Engl.*, 2018, **57**, 12162–12166.
- 28 R. S. Shallenberger and L. R. Mattick, *Food Chem.*, 1983, **12**, 159–165.
- 29 T. Barclay, M. Ginic-Markovic, P. Cooper and N. Petrovsky, *J. Excip. Food Chem.*, 2010, **1**, 27–50.
- 30 M. L. Hayes, N. J. Pennings, A. S. Serianni and R. Barker, *J. Am. Chem. Soc.*, 1982, **104**, 6764–6769.
- 31 S. Osanai, in *Glycoscience*, ed. Stütz A.E., Berlin, Heidelberg, 2001, vol. 215, pp. 43–76.
- 32 L. Forster, M. M. M. Kashbor, J. Railton, S. Chansai, C. Hardacre, M. Conte and C. D'Agostino, *J. Catal.*, 2023, **425**, 269–285.
- 33 T. Ennaert, J. Van Aelst, J. Dijkmans, R. De Clercq, W. Schutyser, M. Dusselier, D. Verboekend and B. F. Sels, *Chem. Soc. Rev.*, 2016, **45**, 584–611.
- 34 R. Bermejo-Deval, R. Gounder and M. E. Davis, *ACS Catal.*, 2012, **2**, 2705–2713.
- 35 S. Bhunia, B. Banerjee and A. Bhaumik, *ChemComm.*, 2015, **51**, 5020–5023.
- 36 R. M. N. Kalla, M. R. Kim and I. Kim, *Ind. Eng. Chem. Res.*, 2018, **57**, 11583–11591.
- 37 R. Weingarten, G. A. Tompsett, W. C. Conner and G. W. Huber, *J. Catal.*, 2011, **279**, 174–182.

- 38 A. Platon and W. J. Thomson, *Ind. Eng. Chem. Res.*, 2003, **42**, 5988–5992.
- 39 M. Conte, J. A. Lopez-Sanchez, Q. He, D. J. Morgan, Y. Ryabenkova, J. K. Bartley, A. F. Carley, S. H. Taylor, C. J. Kiely, K. Khalid and G. J. Hutchings, *Catal. Sci. Technol.*, 2012, **2**, 105–112.
- 40 M. M. M. Kashbor, D. Sutarma, J. Railton, N. Sano, P. J. Cumpson, D. Gianolio, G. Cibir, L. Forster, C. D’Agostino, X. Liu, L. Chen, V. Degirmenci and M. Conte, *Appl. Catal. A: Gen.*, 2022, **642**, 118689.
- 41 H. Willemen, D. F. Van De Vondel and G. P. Van Der Kelen, *Inorganica Chim. Acta*, 1979, **34**, 175–180.
- 42 G. Schön, *J. Electron Spectrosc. Relat. Phenom.*, 1973, **2**, 75–86.
- 43 M. Conte, C. J. Davies, D. J. Morgan, T. E. Davies, D. J. Elias, A. F. Carley, P. Johnston and G. J. Hutchings, *J. Catal.*, 2013, **297**, 128–136.
- 44 J. Zhang, S. Nagamatsu, J. Du, C. Tong, H. Fang, D. Deng, X. Liu, K. Asakura and Y. Yuan, *J. Catal.*, 2018, **367**, 16–26.
- 45 Y. Li, Y. Chen, L. Li, J. Gu, W. Zhao, L. Li and J. Shi, *Appl. Catal. A: Gen.*, 2009, **366**, 57–64.
- 46 J. Ma, D. Weng, X. Wu, Z. Si and Z. Wu, *Prog. Nat. Sci.: Mater. Int.*, 2013, **23**, 493–500.
- 47 L. B. McCusker, R. B. Von Dreele, D. E. Cox, D. Louër and P. Scardi, *J. Appl. Crystallogr.*, 1999, **32**, 36–50.
- 48 R. Roy, V. G. Hill and E. F. Osborn, *J. Am. Chem. Soc.*, 1952, **74**, 719–722.

- 49 J. O. Weston, H. Miyamura, T. Yasukawa, D. Sutarma, C. A. Baker, P. K. Singh, M. Bravo-Sanchez, N. Sano, P. J. Cumpson, Y. Ryabenkova, S. Kobayashi and M. Conte, *Catal. Sci. Technol.*, 2017, **7**, 3985–3998.
- 50 L. Botti, R. Navar, S. Tolborg, J. S. Martinez-Espin, D. Padovan, E. Taarning and C. Hammond, *Top. Catal.*, 2019, **62**, 1178–1191.
- 51 P. Wolf, W. C. Liao, T. C. Ong, M. Valla, J. W. Harris, R. Gounder, W. N. P. van der Graaff, E. A. Pidko, E. J. M. Hensen, P. Ferrini, J. Dijkmans, B. Sels, I. Hermans and C. Copéret, *Helv. Chim. Acta*, 2016, **99**, 916–927.
- 52 S. Roy, K. Bakhmutsky, E. Mahmoud, R. F. Lobo and R. J. Gorte, *ACS Catal.*, 2013, **3**, 573–580.
- 53 C. Genovese, M. E. Schuster, E. K. Gibson, D. Gianolio, V. Posligua, R. Grau-Crespo, G. Cibir, P. P. Wells, D. Garai, V. Solokha, S. Krick Calderon, J. J. Velasco-Velez, C. Ampelli, S. Perathoner, G. Held, G. Centi and R. Arrigo, *Nat. Commun.*, 2018, **9**, 935.
- 54 Y.-I. Kim, M.-J. Jung and K.-H. Kim, *Korean. J. Ceram*, 2000, **6**, 354–358.
- 55 S. A. Axon, K. Huddersman and J. Klinowski, *Chem. Phys. Lett.*, 1990, **172**, 398–404.
- 56 N. S. Smirnova, D. A. Shlyapin, O. O. Mironenko, E. A. Anoshkina, V. L. Temerev, N. B. Shitova, D. I. Kochubey and P. G. Tsyurul’Nikov, *J. Mol. Catal. A: Chem.*, 2012, **358**, 152–158.
- 57 N. Senamart, S. Buttha, W. Pantupho, I. Z. Koleva, S. Loiha, H. A. Aleksandrov, J. Wittayakun and G. N. Vayssilov, *J. Porous Mater.*, 2019, **26**, 1227–1240.

Chapter 5. The role of zeolite acidity and porosity toward the catalytic activity of Sn-, Ga-, and Nb-doped zeolite Y, BEA, ZSM-5 and Al-MCM-41 in the isomerisation of glucose to fructose.

5.1. Introduction

Brønsted and Lewis acid sites have been shown to play a critical role in the isomerisation of glucose to fructose and reactions beyond, such as the conversion of fructose to 5-HMF and levulinic acid (section 1.5.4 in Chapter 1). For instance, Lewis acid sites could facilitate the ring-opening of glucose molecules and coordinate with the lone electron pairs in oxygen atoms (O1 and O2) at glucose aldehyde carbons before the isomerisation reaction takes place via an intramolecular hydride shift from the C2 to C1 position in the ring-opened glucose chain¹ (Figure 5.1A). On the other hand, Brønsted acidity was also found to facilitate the conversion of glucose to fructose through the formation of alkyl fructoside intermediates using a two-step protocol in methanol and water media (section 4.2 in Chapter 4). Furthermore, Brønsted acid sites have a crucial role in the dehydration reaction of fructose intermediates to 5-HMF. These acid sites are of vital importance because they facilitate the protonation of the OH hydroxyl group at the anomeric carbon C2 position of fructose. As a result, the hydroxyl group is significantly more susceptible to dehydration, facilitating fructose conversion into 5-HMF. The presence of Brønsted acid sites is essential in promoting this reaction and significantly increasing the efficiency of 5-HMF production² (Figure 5.1B). However, in principle, any proton (H⁺) could potentially be attacked by any hydroxyl group (OH) in the fructose molecule. This will result in a complex mixture containing various reaction products as the final product³. Therefore, selectivity becomes a crucial factor in the dehydration reaction of

fructose into 5-HMF. Consequently, the use of porous materials becomes essential in order to selectively drive the dehydration reaction in specific target hydroxyl groups⁴. Therefore, the information gathered here will also be used to establish structural activity correlations of 5-HMF synthesis.

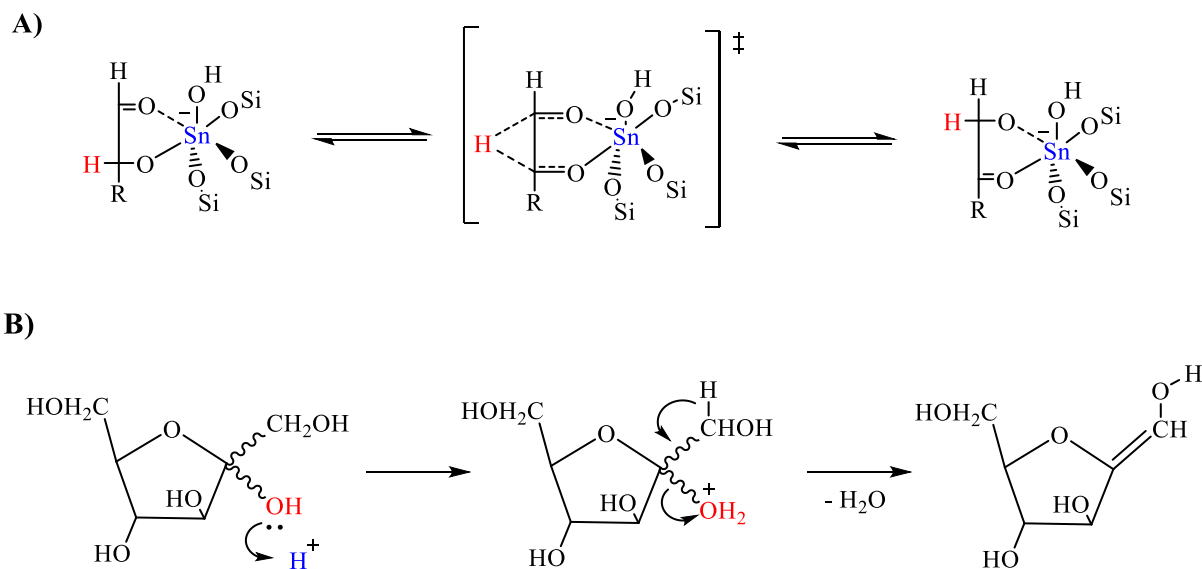


Figure 5.1. Schematic representation of **A)** glucose isomerisation mechanism via 1,2-intramolecular hydride shift in the presence of Sn Lewis active sites⁵, and **B)** the Protonation of OH group at Carbon 2 position of fructose via Brønsted acid sites as the first step of the dehydration reaction⁶.

Given the importance of porous materials in these reactions, it is imperative to study the impact of pore size on the activity of these materials. For instance, glucose molecules in their cyclic form with a molecular size of ~ 0.9 nm require a zeolite framework with a pore size larger than 1 nm to diffuse inside the catalyst pores and reach the active sites⁷. However, the acyclic form of glucose showed to be small enough (~ 0.86 nm) to squeeze and diffuse through the 0.74 nm pores of zeolite Y^{8,9}.

As a consequence, the aims of this chapter are to **1)** gather additional information on the materials involved in the reaction of glucose to fructose by doping zeolite Y, BEA, ZSM-5 and Al-MCM-41 with Sn, Ga and Nb **2)** establish a highly reliable and efficient platform for the synthesis of 5-HMF, drawing upon the insights acquired from this chapter, particularly regarding the structural properties of the materials involved, leading to in the design and development of improved catalysts and reaction systems for the production of 5-HMF.

Niobium-based compounds have attracted significant attention as solid acid catalysts for the production of 5-HMF from glucose and fructose^{10,11}. The exceptional activity of these compounds in aqueous solutions has made them indispensable catalysts for various chemical reactions including sugar dehydration to 5-HMF¹². Therefore, exploring the role of these particular metal species in glucose isomerisation and subsequent fructose dehydration reactions would be highly interesting and worthwhile. As for zeolite-based catalysts, Nb species were doped exclusively on zeolite BEA frameworks for only the purpose of catalysing the dehydration of glucose to 5-HMF. The catalyst showed glucose conversion of 47% and HMF selectivity of 22% under the reaction conditions of 180 °C for 24 h in 5 mL water as a solvent with an M:S molar ratio of 1:2 and using a metal loading of 1.6 wt.%¹¹. However, despite using these metal species on different zeolites for other applications, Nb-doped on the commercially available zeolite Y and their catalytic performance on the isomerisation of glucose to fructose and the dehydration of fructose intermediates to 5-HMF have not been investigated so far. Furthermore, in order to encompass an appropriate range of acidity and porosity, zeolite Y (SiO₂:Al₂O₃ of 5.1), BEA (SiO₂:Al₂O₃ of 25, and 38), ZSM-5 (SiO₂:Al₂O₃ of 23 and 50), and Al-MCM-41 (SiO₂:Al₂O₃ of 28) were used in addition to the previously mentioned catalyst (i.e., zeolite Y (30)). This selection of

zeolite materials was made to provide a comparative basis and gain a deeper understanding of the relative importance of acidity and porosity in glucose isomerisation.

5.2. Catalytic tests in a one-step protocol using water or methanol as a solvent.

Similar to the observations made in section 4.2.1, it has also been found that using water, either in a single-step protocol or in combination with methanol from the beginning of the reaction, does not result in any products formation under the reaction conditions used (reaction temperature in the range of 100 °C, endogenous pressure and a reaction time of up to 2 hours). On the other hand, the use of methanol as a solvent led to a significant increase in the catalytic activity for all catalysts studied (Figures 5.2 and 5.3). In particular, the highest catalytic performances were obtained using large pore zeolites Y and BEA, with zeolites Y ($\text{SiO}_2:\text{Al}_2\text{O}_3$ of 30) and BEA ($\text{SiO}_2:\text{Al}_2\text{O}_3$ of 38) being the best compromise between high glucose conversion and high fructose selectivity, demonstrated through the highest fructose yield in the range of 30% (Table A5 in Appendix A.5). Furthermore, all catalysts showed a closed carbon mass balance in the range of 90 – 100%, within the experimental error.

In the case of zeolite Y, the metal dopant has a negligible effect compared to the impact of pre-existing Al centres, which leads to similar catalytic activity, within the experimental error, for both the parent HY zeolite and Sn-, Ga-, and Nb-doped zeolite Y catalysts. However, zeolite Y with $\text{SiO}_2:\text{Al}_2\text{O}_3$ of 5.1 produced a large amount of methyl fructoside intermediate (~70%), most likely due to the higher Brønsted acidity of this catalyst compared to other catalysts studied. In contrast, doping Sn, Ga, and Nb on BEA and ZSM-5 zeolites significantly increased the catalytic activity. BEA

zeolites demonstrated an increase of 50% and 20% in glucose conversion and fructose selectivity, respectively. Whereas ZSM-5 zeolite catalysts improved glucose conversion by 30% and fructose selectivity by 15%. In ZSM-5 materials, the lower catalytic activity could be attributed to the narrow pore system and large crystal sizes (Table 1.4 in Chapter 1) that have severely limited the diffusion of glucose molecules into the pores of the zeolite¹³ and, in turn, leads to the reactivity being limited to the active sites on the external surface of the catalyst¹⁴. On the other hand, mesoporous aluminosilicate Al-MCM-41 catalysts showed a considerable glucose conversion of 75%, which was further increased up to 90% upon the metal dopant step. The high catalytic activity of conventional Al-MCM-41 compared to undoped BEA and ZSM-5 zeolites can be explained as a result of three factors, which are “the Lewis acidity of the Al site, a proton donor in the form of an Al–O(H)–Si group and a proton acceptor in the form of an Al–OH group”¹⁵.

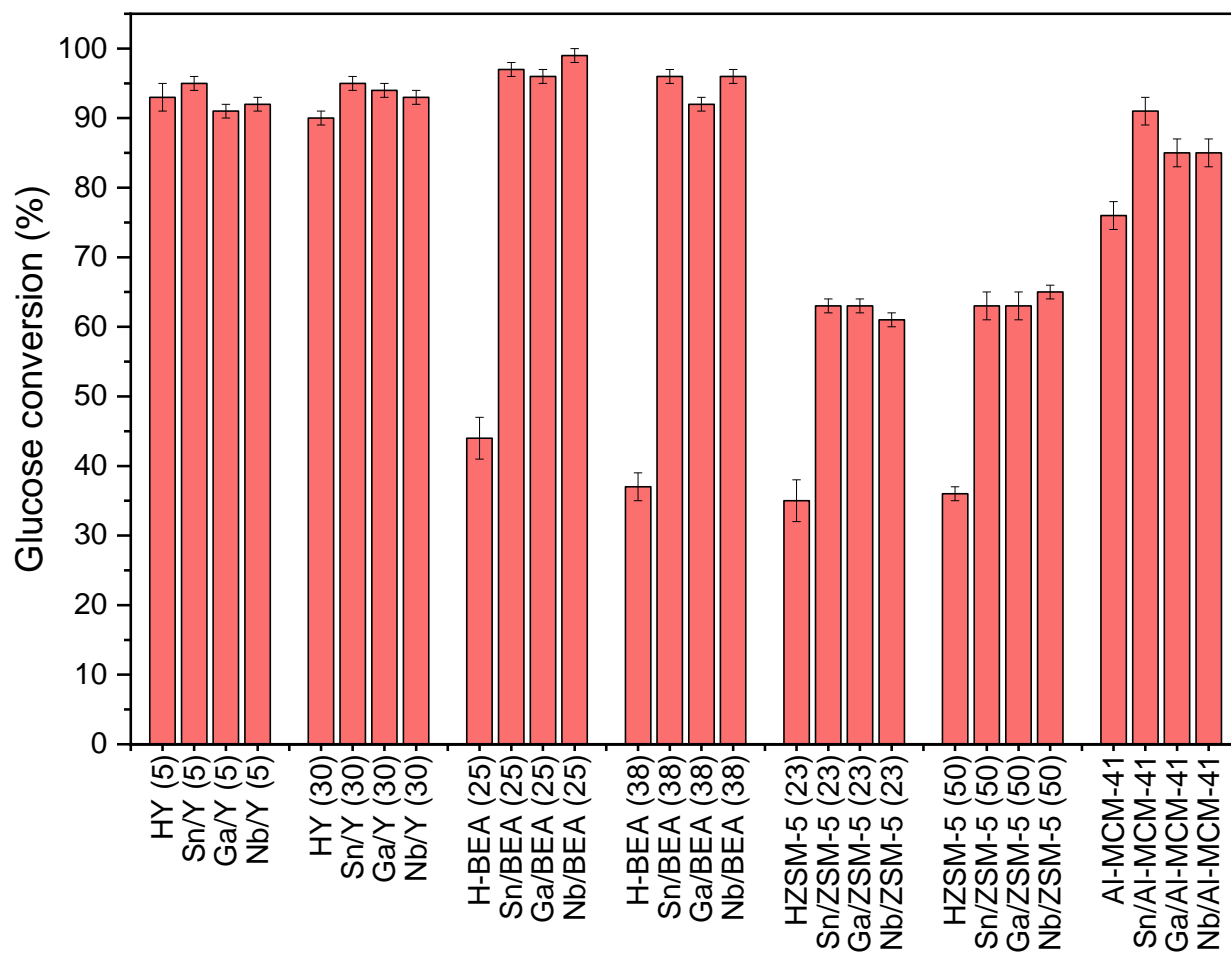


Figure 5.2. Glucose conversions were obtained from the isomerisation reaction of glucose to fructose, which was carried out over various undoped and doped zeolites catalysts using 125 mg of the substrate in 4 mL of CH₃OH at the reaction temperature of 100 °C for 1 h and endogenous pressure using a constant M:S molar ratio M:S = 1:100. Catalytic data of HY (30), Sn/Y (30), and Ga/Y (30) zeolites reported herein are reproduced from Chapter 4. Experimental error is reported as the standard deviation of three repeated measurements.

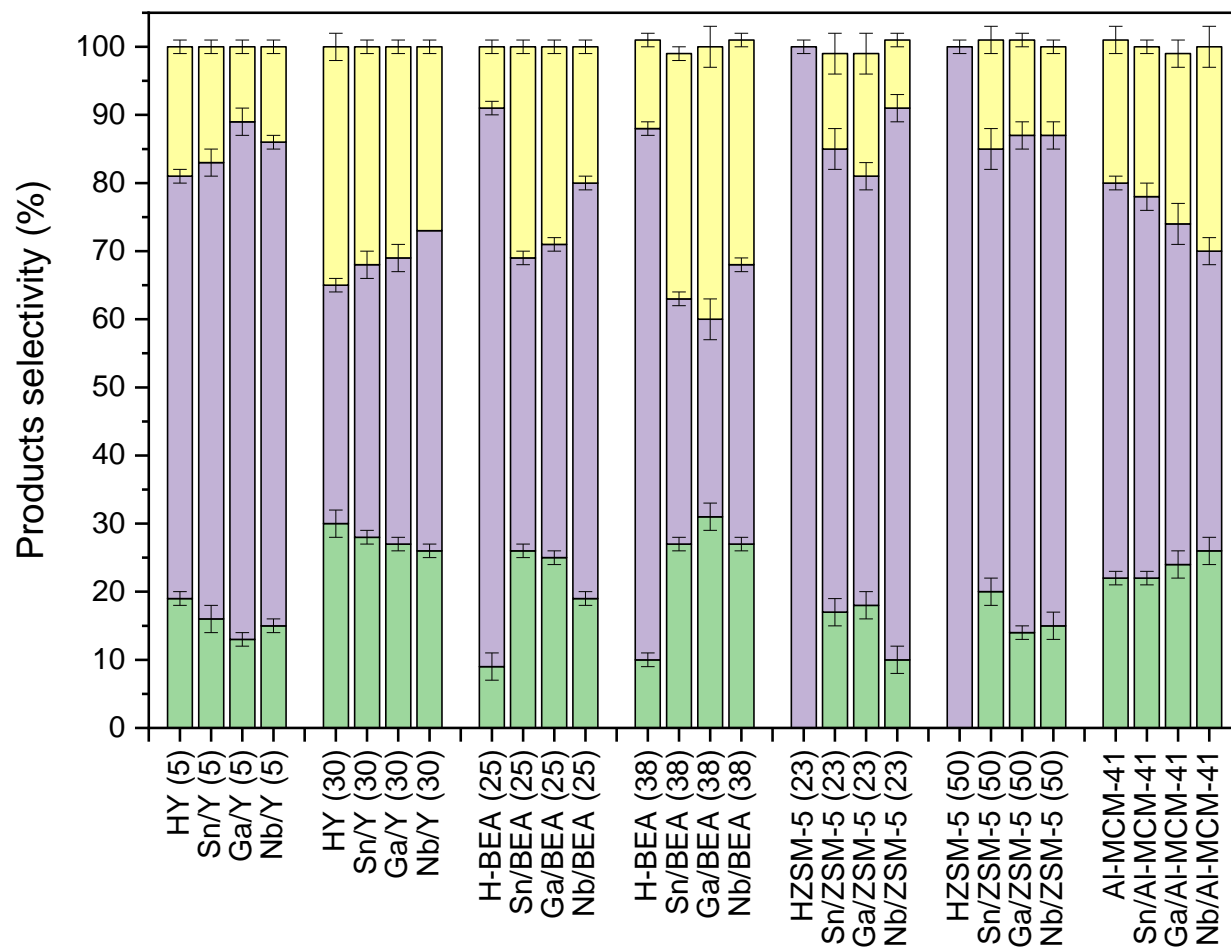


Figure 5.3. Observed product selectivity of fructose (●), methyl fructoside (●) and mannose (●) obtained from the isomerisation reaction of glucose to fructose, which was carried out over various undoped and doped zeolites catalysts using 125 mg of the substrate in 4 mL of CH₃OH at the reaction temperature of 100 °C for 1 h and endogenous pressure using a constant M:S molar ratio M:S = 1:100. Catalytic data of HY (30), Sn/Y (30), and Ga/Y (30) zeolites reported herein are reproduced from Chapter 4.

5.3. Catalytic tests in a two-step protocol by using methanol and water.

In line with the results described in section 4.2.1, the addition of water in the second step of the reaction results in the conversion of methyl fructoside intermediate to the more desirable fructose. The decrease in methyl fructoside upon the step of water addition matches significantly, within experimental error, the formation of fructose, resulting in fructose production of approximately 20 – 65 % depending on the type of catalyst being used. At the same time, the second step of water treatment did not appear to significantly affect glucose conversion and mannose selectivity for all catalysts (either in terms of production or consumption). Sn-, Ga-, and Nb-doped zeolite Y ($\text{SiO}_2:\text{Al}_2\text{O}_3$ of 30) and zeolite BEA ($\text{SiO}_2:\text{Al}_2\text{O}_3$ of 25) showed the most optimal compromise between high glucose conversion and high fructose selectivity, evidenced as having the highest fructose yield in the range of 50 – 60% based on their corresponding carbon mass balance (Table A5 in Appendix A.5).

The catalytic performance of all catalysts tested using two-step reaction protocols in methanol and water (Figures 5.4 and 5.5) showed a similar trend to that obtained using the one-step protocol in methanol. More specifically, the doping of Sn, Ga, and Nb showed no major effect on Zeolite Y. However, this was not the case with Zeolite BEA and ZSM-5, which were strongly affected by this step as observed in the previous section (section 5.2). For Al-MCM-41, the doping of Sn revealed a significant increase in catalytic activity (both in terms of glucose conversion and fructose selectivity). This, in fact, was not the case for Ga/Al-MCM-41 and Nb/Al-MCM-41, which showed no significant difference in catalytic activity to the parent Al-MCM-41. Furthermore, It is also apparent that glucose isomerisation reaction toward fructose demonstrated higher catalytic performance (glucose conversion and fructose yield) with large pore zeolites such as zeolite Y and BEA ($\geq 7 \text{ \AA}$) having a moderate $\text{SiO}_2:\text{Al}_2\text{O}_3$ molar ratio

in the range of 20 – 40. Also, all catalysts exhibited a closed carbon mass balance compatible with 100%, within the experimental error, except for those obtained by zeolite Y catalysts with a $\text{SiO}_2:\text{Al}_2\text{O}_3$ molar ratio of 5.1, which revealed a carbon mass balance in the range of 75%, and Nb-doped BEA zeolite with a $\text{SiO}_2:\text{Al}_2\text{O}_3$ molar ratio of 25 with a CMB value of about 60%, more likely due to catalysts being too acidic, leading to the degradation and polymerization of reactants, intermediates and/or products to humins.

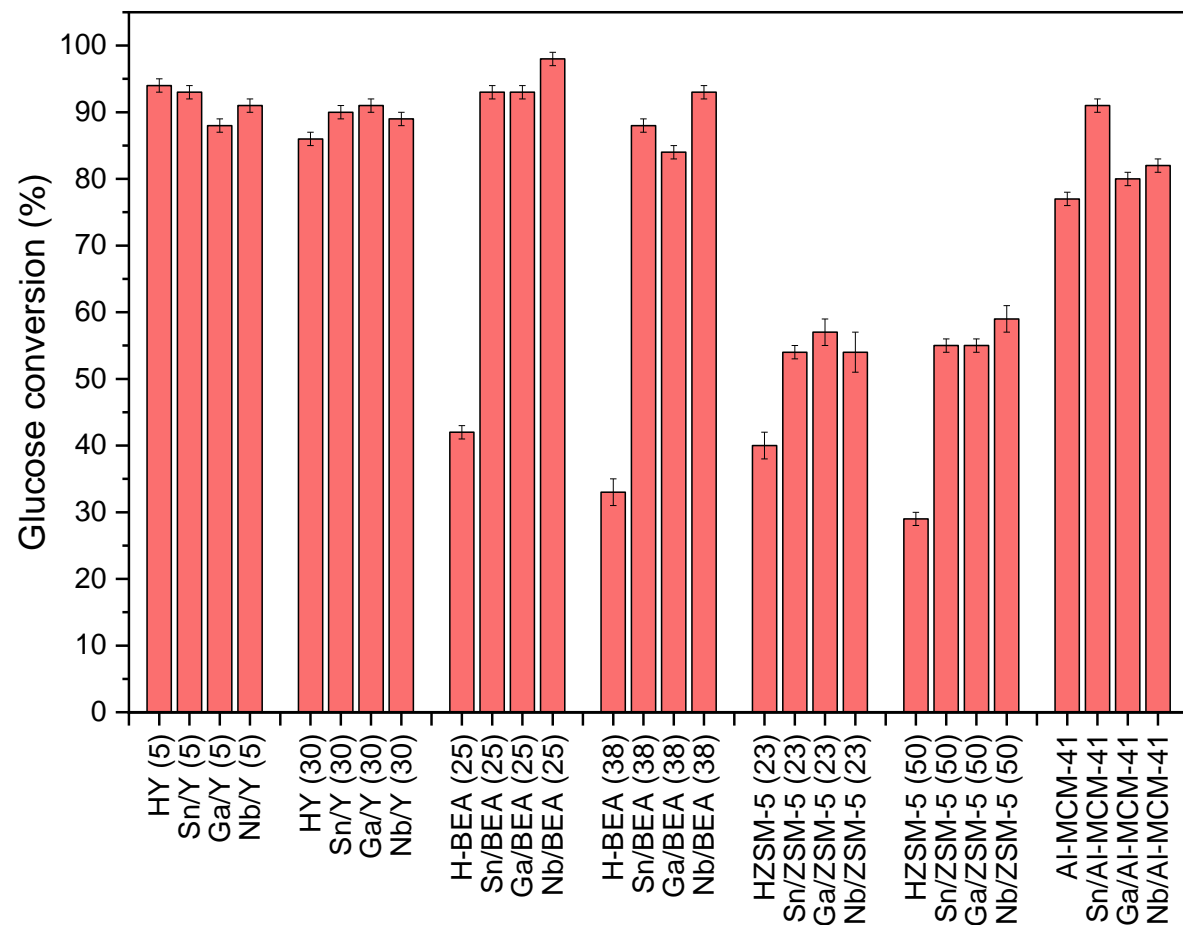


Figure 5.4. Glucose conversions were obtained from the isomerisation reaction of glucose to fructose, which was carried out over various undoped and doped zeolites catalysts using 125 mg of the substrate in 4 mL of CH₃OH at the reaction temperature of 100 °C for 1 h and endogenous pressure and then adding 4 mL of H₂O for an additional reaction time of 1 h at using a constant M:S molar ratio M:S = 1:100. Catalytic data of HY (30), Sn/Y (30), and Ga/Y (30) zeolites reported herein are reproduced from Chapter 4. Experimental error is reported as the standard deviation of three repeated measurements.

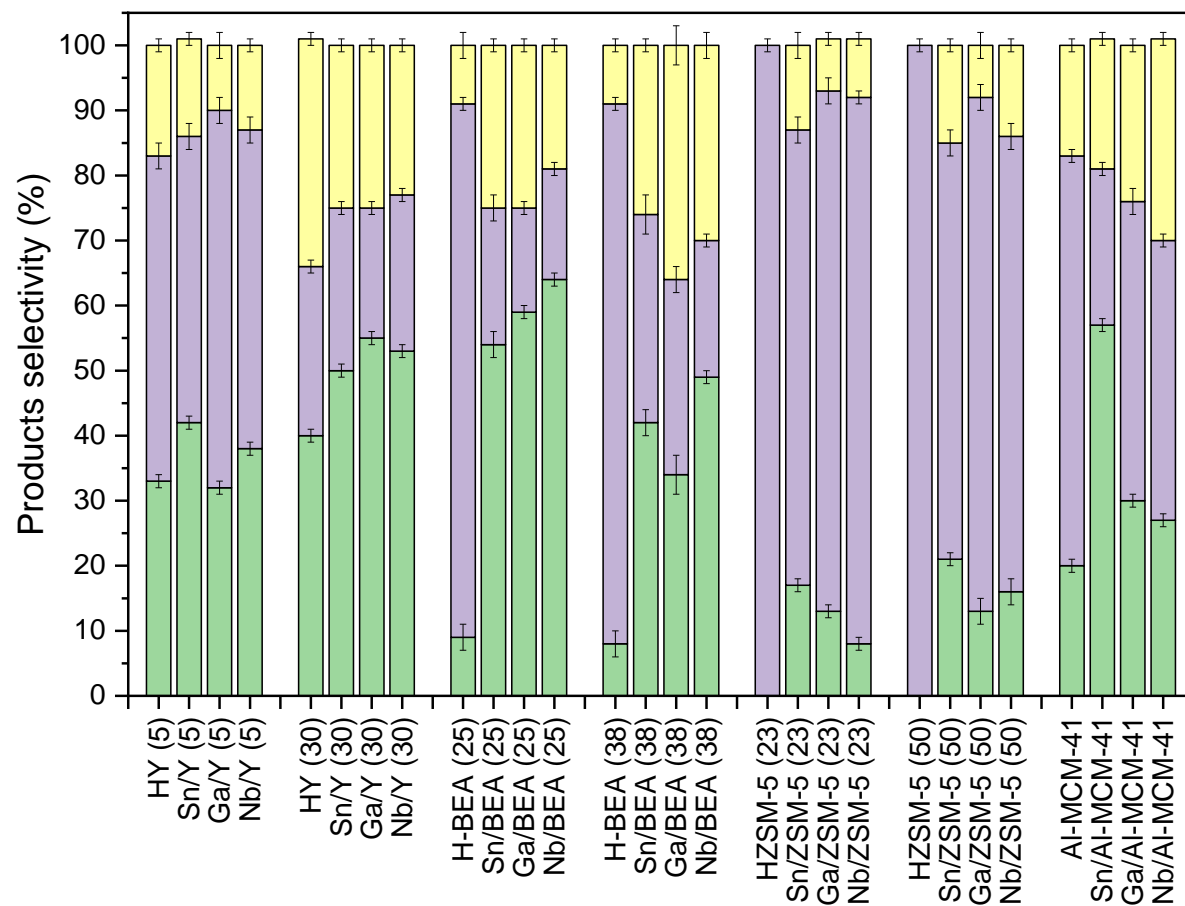


Figure 5.5. Observed product selectivity of fructose (●), methyl fructoside (●) and mannose (●) obtained from the isomerisation reaction of glucose to fructose, which was carried out over various undoped and doped zeolites catalysts using 125 mg of the substrate in 4 mL of CH₃OH at the reaction temperature of 100 °C for 1 h and endogenous pressure and then adding 4 mL of H₂O for an additional reaction time of 1 h at using a constant M:S molar ratio M:S = 1:100. Catalytic data of HY (30), Sn/Y (30), and Ga/Y (30) zeolites reported herein are reproduced from Chapter 4.

5.4. Powder X-ray diffraction.

Powder XRD patterns were collected for parent non-doped and Sn, Ga and Nb-doped zeolite Y, BEA, ZSM-5, and Al-MCM-41 (Figures 5.6 and 5.7) and (Figures A22 – A26 in Appendix A.10) in order to characterise the crystalline structure of the synthesised catalysts and determine the presence of any ion exchange or distortion of the zeolite that could have occurred as a consequence of the preparation protocol used. A Rietveld refinement¹⁶ was carried out (Tables A9 – A14 in Appendix A.10). It can be seen that the XRD patterns of all catalysts studied appear to be virtually identical, with no significant contraction of the unit cell volume being observed in response to variations in the unit cell volume of their parent zeolites with calculated values of 14757 Å³ for HY (5.1), 14363 Å³ for HY (30), 4013 Å³ for H-BEA (25), 3992 Å³ for H-BEA (38), 5382 Å³ for HZSM-5 (23), 5368 Å³ for HZSM-5 (50). This suggests that Sn, Ga, or Nb are not incorporated into the zeolite framework in place of Al - at least within the resolution of the PXRD patterns acquired.

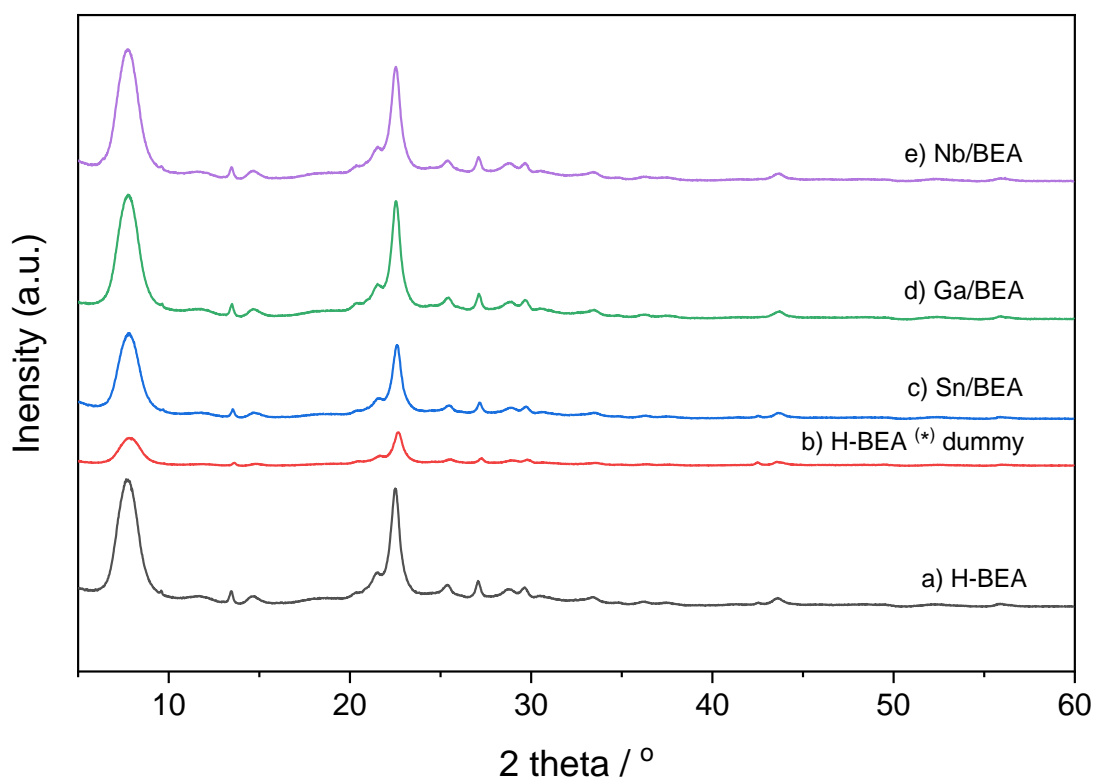


Figure 5.6. X-ray powder diffraction patterns for zeolites: (a) H-BEA as delivered, (b) H-BEA treated as for metal deposition but without any metal dopant, (c) Sn/BEA, (d) Ga/BEA, and (e) Nb/BEA with a $\text{SiO}_2:\text{Al}_2\text{O}_3$ molar ratio of 25 as a representative example. No metal or metal oxide cluster from Sn, Ga or Nb is detected, and all zeolites present a virtually identical pattern.

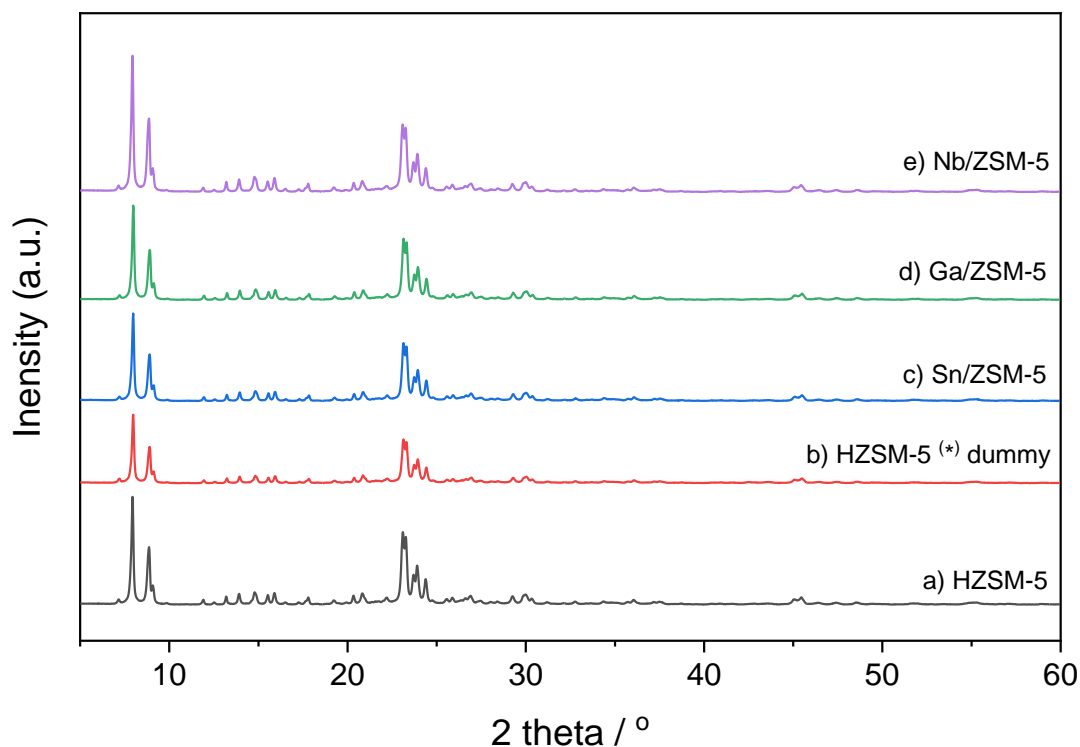


Figure 5.7. X-ray powder diffraction patterns for zeolites: (a) HZSM-5 as delivered, (b) HZSM-5 treated as for metal deposition but without any metal dopant, (c) Sn/ ZSM-5, (d) Ga/ ZSM-5, and (e) Nb/ ZSM-5 with a $\text{SiO}_2:\text{Al}_2\text{O}_3$ molar ratio of 23 as a representative example. No metal or metal oxide cluster from Sn, Ga or Nb is detected, and all zeolites present a virtually identical pattern.

It is important to note that even though Sn, Ga and Nb were confirmed and/or indicated to be present as SnO_2 , Ga_2O_3 and Nb_2O_5 , no characteristic reflections associated with these metal oxides were observed. For SnO_2 ¹⁷, these were expected to be at 26.6, 37.8 and 51.8° 2 θ for the reflections of (110), (200), and (211), respectively, for $\beta\text{-Ga}_2\text{O}_3$ ¹⁸ at 31.2°, 35.9° and 38.1° 2 θ , for the reflections (222), (400) and (411) respectively, and for the orthorhombic phase of Nb_2O_5 ¹⁹ at 22.7, 28.6, 36.7, 46.2, 50.7 and 55.3° 2 θ for the reflections of (001), (180), (200), (181), (002), (380), and (212) respectively.

In addition to the structure and bulk chemical composition, it is important to determine the unit cell parameter (as obtained from XRD data) of Sn-, Ga-, and Nb-doped zeolite Y, BEA, ZSM-5, and Al-MCM-41 catalysts that were prepared using wetness impregnation technique in order to identify metal-zeolite interactions. Metal could be deposited on the external surface of zeolites or trapped within the pores of their frameworks. As a consequence of the two types of metal-zeolite interactions, different catalytic performances are obtained^{20,21}. The expansion or contraction of unit cells is typically used to indicate the substitution of metal in place of Al sites within the zeolite structure based on the metal's size (Specifically, Sn, Ga and Nb) with respect to Al. Whereas the percentage of expansion or contraction, to some extent, depends on the number of metal atoms incorporated into the zeolite structure²². For example, given the relatively larger size of Sn in its ionic form and coordination as compared with Al, an increase in the volume expansion of unit cells is indicative of the successful incorporation of this metal into structural sites²³. However, no significant expansion or contraction of the unit cell was observed with our Sn/BEA (25) and Sn/ZSM-5 (23) catalysts shown in Tables A9 and A10 in Appendix A.10 as well as within those Sn doped on different other supports, such as Y (5.1 and 30), BEA (38), and ZSM-5 (50) reported in (Tables A11 – A14 in Appendix A.10), indicating that the Sn species of our catalysts that were prepared using wetness impregnation are all supported on the outer surface or in the pore/channel of those zeolite catalysts instead of being incorporated into the framework. A similar observation concerning the expansion or contraction of the unit obtained with Sn-doped zeolites has also been found with Ga- and Nb-doped zeolites catalysts. However, HY with a SiO₂:Al₂O₃ molar ratio of 30 showed a strong contraction of -2.7% with respect to HY with a SiO₂:Al₂O₃ molar ratio of 5.1, which corresponds to the dealumination fact practically, it is as there is less Al

in this catalyst. In contrast, a slight borderline contraction of -0.5% and -0.3 for H-BEA (38) and HZSM-5 (50), respectively, was detected. This was compatible with their lower Al contents compared to H-BEA (25) and HZSM-5 (23).

5.5. Acidity measurements.

As confirmed in section 4.2.3, it is evident that acidity characteristics played a key role in the isomerisation of glucose to fructose, resulting in multiple reaction pathways being mediated by Lewis and/or Brønsted acid sites. However, a Brønsted acid pathway showed to be dominant in this reaction under the reaction conditions studied. Therefore, the total Brønsted acidity was determined through a straightforward and statistically robust analytical method of back-titration in order to gain a better understanding of trends in catalytic activity and their correlations with prevalent Brønsted acidity. The results of these acidity measurements for all catalysts are reported in detail in (Table 5.1).

Table 5.1. Total Brønsted acidity of undoped and metal-doped zeolite Y, BEA, ZSM-5 and Al-MCM-41 determined by back-titrations alongside their corresponding $\text{SiO}_2:\text{Al}_2\text{O}_3$ molar ratios. The experimental error is reported as the standard deviation of three repeated measurements.

Zeolite support	Doped Metal	$\text{SiO}_2:\text{Al}_2\text{O}_3$ molar ratio	Total Brønsted ($\text{mmol}\cdot\text{g}^{-1}$)
HY	Parent	5	2.55
	Sn	5	2.52
	Ga	5	2.49
	Nb	5	2.47
HY	Parent	30	1.78
	Sn	30	1.72
	Ga	30	1.70

	Nb	30	1.73
BEA	Parent	25	2.17
	Sn	25	2.15
	Ga	25	2.14
	Nb	25	2.15
BEA	Parent	38	1.58
	Sn	38	1.55
	Ga	38	1.49
	Nb	38	1.54
ZSM5	Parent	23	2.19
	Sn	23	2.16
	Ga	23	2.12
	Nb	23	2.15
ZSM5	Parent	50	1.01
	Sn	50	0.95
	Ga	50	0.92
	Nb	50	0.94
Al-MCM41	Parent	28	2.29
	Sn	28	2.24
	Ga	28	2.19
	Nb	28	2.21

The results of our back titrations indicate a slight decrease in Brønsted acidity values following the metal doping step (Table 5.1). This decrease appears to be compatible, theoretically, with the formation of basic metal oxides (i.e., SnO₂, Ga₂O₃ and Nb₂O₅). However, the difference between the acidity values remains within the experimental error of our method (ca. 0.02 mmol·g⁻¹). Therefore, this difference is not considered statistically significant.

5.5.1. Tentative acidity-activity correlations.

In this section, we will investigate the possibility of correlating the Brønsted acidity values obtained from back-titration with the catalytic activity data for all catalysts. The trends in glucose conversion, fructose and methyl fructoside selectivities and actual yields as a function of total Brønsted acidity are presented in (Figures 5.8 - 5.10).

First of all, in both reactions carried out following the one-step protocol in methanol and the two-step protocol in methanol and water, glucose conversions showed no correlation at all to the total Brønsted acidity of all catalysts, and the conversion values were instead distributed in a random manner (Figures A27 and A28 in Appendix A.11). From the perspective of product selectivity, fructose also did not exhibit any direct relationship with the measured acidity values; again, the data are entirely distributed at random. On the other hand, methyl fructoside selectivity values were clustered together and showed some trend (Figure 5.8); that is, the formation of methyl fructoside increased with the increase of the Brønsted acidity.

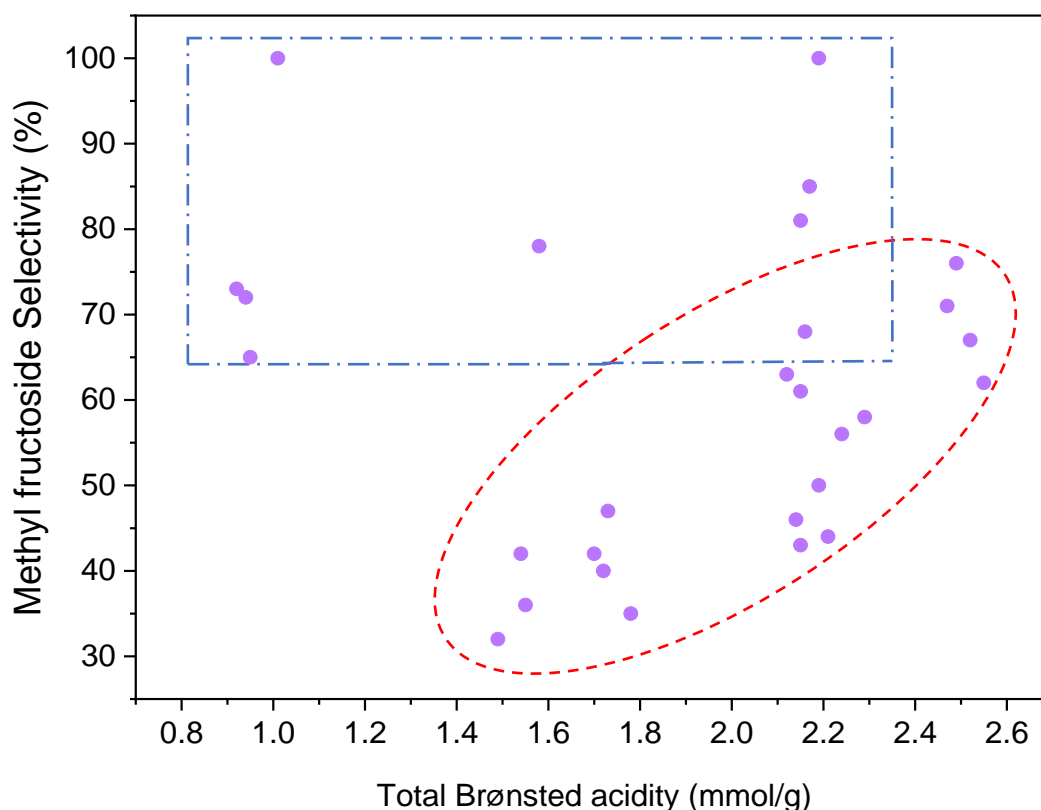


Figure 5.8. The trend of methyl fructoside selectivity with respect to total Brønsted acidity. The reaction was carried out following the one-step protocol in methanol at 100 °C for 1 h and endogenous pressure using a constant M:S molar ratio M:S = 1:100. It seems that the higher the Brønsted acidity, the greater the formation of methyl fructoside. However, some random points could be observed upon using the selectivity values.

As can be seen in Figure 5.8, a tentative correlation between the selectivity of methyl fructoside and total Brønsted acidity was observed (inside the dashed red circle). However, this correlation does not lead to a parabolic shape due to the presence of multiple randomly distributed points (inside the dashed blue square). Due to the lack of clear visual correlation, we carried out the Pearson correlation coefficient test in order to see if any correlation can statistically be observed. However, the test showed a Pearson correlation coefficient value (r) of 0.4, indicating no strong correlation between the two variables. However, since the isomerisation reaction of glucose showed to have three parallel pathways, but with only one of them being a highly rapid

Brønsted pathway toward the formation of methyl fructoside, it would be expected that correlating the product yield instead of selectivity will result in observing a more pronounced trend for this intermediate. In this regard, product yields, calculated based on obtained carbon mass balance, were correlated (Figures 5.9 and 5.10).

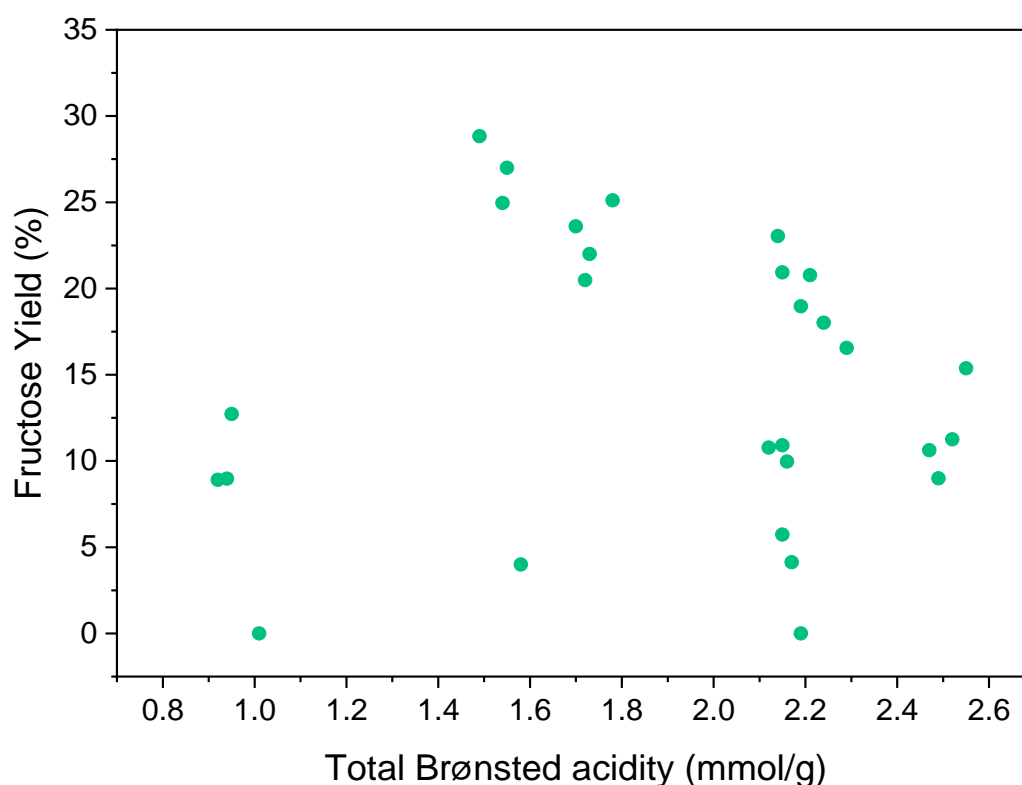


Figure 5.9. The trend of fructose yield as a function of the total Brønsted acidity values. The reaction was carried out following a one-step protocol in methanol at 100 °C for 1 h and endogenous pressure using a constant M:S molar ratio M:S = 1:100. No trend can be seen, and data are randomly distributed.

In line with the results obtained with selectivity, fructose yield from either the one-step reaction in methanol or the two-step reaction in methanol and water did not also show a clear trend with our Brønsted acidity data (Figure 5.9) and (Figure A29 in Appendix A.11). This was further confirmed statistically with the Pearson correlation coefficient value (r) of 0.009 and 0.2 for the correlations of Brønsted acidity with catalytic data obtained from the one-step reaction and two-step reaction, respectively. A possible

explanation for this could be due to the presence of porosity factor (studied in section 5.6), which can significantly affect the trend in fructose yield since the isomerisation reaction takes place largely inside the pores of the zeolite catalyst²⁴. Furthermore, the presence of parallel Lewis acidity reaction routes also contributes significantly to the formation of fructose. Specifically, it is widely accepted that the isomerisation reaction of glucose to fructose is mainly facilitated via the intramolecular hydride shift mechanism from the C2 to C1 positions of glucose in the presence of Lewis acid sites²⁵ (as shown in Figure 5.1a). As a result, correlating the fructose yield with Lewis acidity data might lead to a discernible trend and, hence, could be considered as future work.

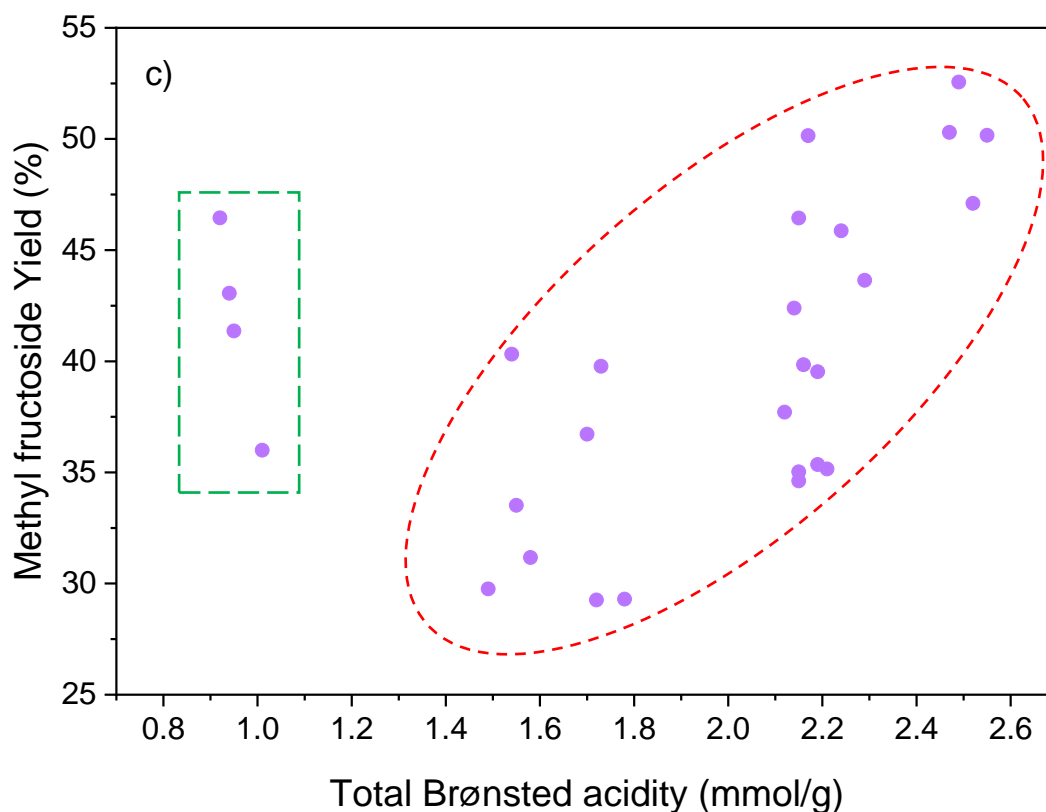


Figure 5.10. The trend of methyl fructoside yield with regard to the total Brønsted acidity values. The reaction was carried out following the one-step protocol in methanol at 100 °C for 1 h and endogenous pressure using a constant M:S molar ratio M:S = 1:100. The higher the Brønsted acidity, the more the formation of methyl fructoside (as shown inside dashed red circle).

In contrast, using the methyl fructoside yield resulted in a parabolic trend and a Pearson correlation coefficient value (r) of 0.7, suggesting a strong correlation between methyl fructoside yields and the total Brønsted acidity, that is, the yield of this intermediate is increased per increase in the total Brønsted acidity (Figure 5.10). However, ZSM-5 (50) catalysts with the lowest Brønsted acidity values in the range of $0.9 - 1 \text{ mmol}\cdot\text{g}^{-1}$ did not follow this trend (inside dashed green rectangle), exhibiting rather high yields of methyl fructoside (ca. 65%). This could be due to their relatively small pore sizes, greatly restricting the entrance of glucose molecules (0.9 nm)⁷ into the pores of these catalysts (0.55 nm)²⁶ and, in turn, limiting the isomerisation reaction of glucose to fructose. Consequently, methyl fructoside was the major product formed using these catalysts since the acid-mediated attack of methanol on fructose does not require pore systems to occur and can take place on the external surface of the catalysts. As a result of this finding and given the importance of porosity characteristics in the isomerisation of glucose to fructose, we decided to investigate further the influence of zeolites' pore size on catalytic data and identify possible trends in catalytic activity as a function of pore diameter.

5.6. Porosity measurements.

BET (Brunauer-Emmett-Teller) and Porosimetry have been used to measure the surface area, pore size and pore volume for a number of our catalysts in order to determine the relative impact of the pore size of zeolites on catalytic performance and to identify possible correlations between the two. Furthermore, to demonstrate that our materials have not been subjected to any potential changes to their zeolite framework caused by the used synthesis process (i.e., wetness impregnation). In fact, the addition of metal centres to zeolites could induce structural changes in the parent

zeolites. This occurs most commonly following the addition of metal centres through the use of ion exchange, which is not the case in incipient wetness impregnation, a synthetic protocol used in this work^{27,28}. In this regard, the textural properties of our main catalysts, namely HY, Sn/Y, Ga/Y and Nb/Y with a SiO₂:Al₂O₃ molar ratio of 30, were determined to confirm that no change in the structure of the parent zeolite has occurred upon the addition of metal centres to its frameworks using incipient wetness impregnation.

The nitrogen adsorption and desorption isotherms of parent HY zeolite and synthesised Sn/Y, Ga/Y and Nb/Y zeolites at 77 K, as shown in Figure 5.10, presented typical types I and IV isotherms²⁹ based on the classification of the International Union of Pure and Applied Chemistry (IUPAC), which indicates the presence of micropores with a pore size of less than 2 nm as well as materials having some mesoporous characteristics with a pore diameter in the range of 2 - 50 nm, respectively. This is evident in hysteresis cycles, which show both condensation and cavitation. As a result of the short vertical hysteresis loops running from $p/p_0 = 0.5$ to 0.99, the materials show the presence of only limited mesoporous volumes. This is also demonstrated by an analysis of the pore distribution (Figures A32 and A33 in Appendix A.12), which indicates that the materials are predominantly microporous with a pore diameter centred at 0.74 nm and also containing mesoporous structures between 20 and 40 nm in size.

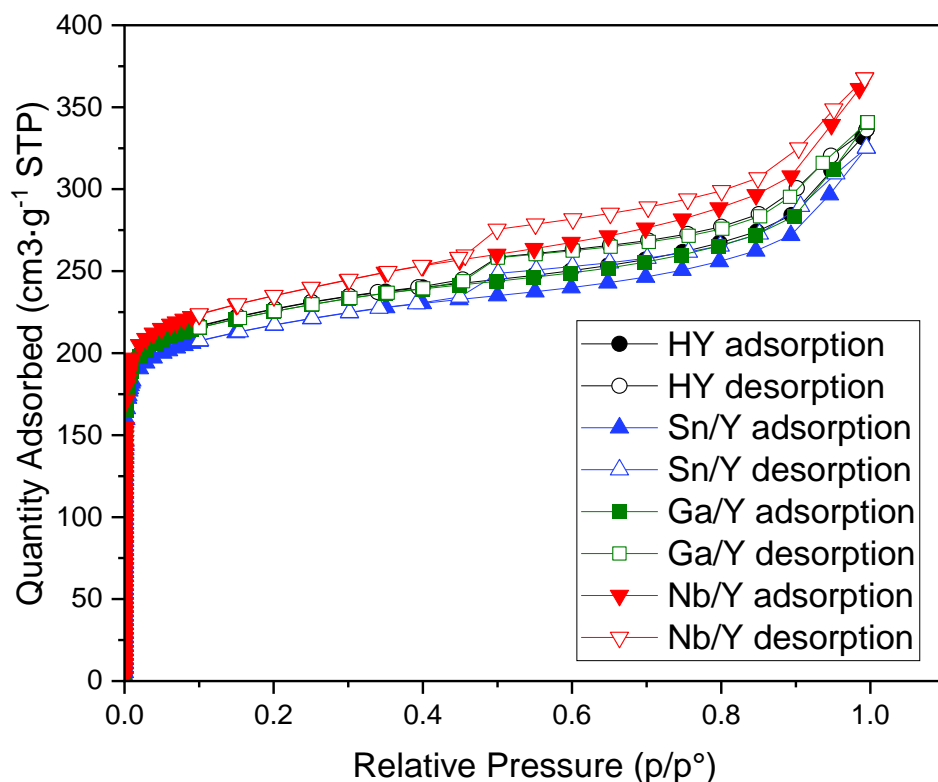


Figure 5.11. N₂ adsorption–desorption isotherm at 77.4 K for (●) parent zeolite HY before doping and doped zeolites (▲) Sn/Y, (■) Ga/Y and (▼) Nb/Y after metal doping through a wetness impregnation protocol. Filled symbols are representative of the adsorption and condensation branch, whereas open symbols are representative of the desorption and cavitation branch.

For the textural properties, the Brunauer–Emmett–Teller (BET) model was applied to determine the specific surface areas, external and micropore areas, whereas t-plots and a Horvarth-Kavazoe model were used to measure the pore volume and pore size distribution. (Table 5.3)

Table 5.3. Textural properties of zeolites for parent zeolite HY and zeolites Sn/Y and Ga/Y doped via an incipient impregnation protocol with a metal loading of 1 wt% for both doped zeolites.

Zeolite	Total surface area^(a) (m²·g⁻¹)	External surface area^(a) (m²·g⁻¹)	Micropore area^(a) (m²·g⁻¹)	Pore Volume^(b) (cm³·g⁻¹)	Channel diameter^(c) (Å)
HY	791	499	292	0.26	7.35
Sn/Y	692	421	271	0.22	7.32
Ga/Y	704	444	260	0.23	7.31
Nb/Y	738	485	254	0.25	7.75

(a) Values calculated from the adoption branch of the adsorption isotherms using BET theory.

(b) Value acquired at the absorption-desorption point using a Barret–Joyner–Halenda (BJH) method.

(c) Value obtained at the absorption-desorption point using a Horvath-Kawazoe method for a cylinder pore geometry.

As a result of these measurements, no changes in textural properties were observed among our materials, within the experimental errors. All specific BET surface areas, external surface areas, and micropores were found in the range of 700 m²·g⁻¹, 450 m²·g⁻¹, and 270 m²·g⁻¹, respectively. Nevertheless, the addition of the metal dopant resulted in slight decreases of approximately 12% in total surface area and 11% in pore volume. This decrease, however, is completely compatible with the deposition method of wetness impregnation used herein, and it also confirms the deposition of a metal dopant, predominantly on the zeolite's exterior surface.

Also, no significant changes in pore size or distribution (Figures A32 and A33 in Appendix A.12) before and after the step of metal deposition or in pressure in

hysteresis cycles to promote condensation and cavitation were detected (Figure 5.11), and all materials showed cylinder-shaped micropores with diameters of 7.4 (Table 5.3), highly consistent with zeolite Y channel containing 12 membered rings³⁰. As a consequence, the synthesis method of metal dopant does not result in any actual changes in the framework characteristics through a change in the coordination or orientation of the zeolite's Al and Si centres.

5.6.1. Porosity-activity correlations.

Additional porosity measurements for a number of our catalysts have been carried out with the aim of identifying correlations between the catalytic activity of our zeolitic materials and the size of their pores. In this context, PET/Porosimetry measurements were carried out for Sn-doped zeolites of Y (5.1), BEA (25), ZSM-5 (23), and Al-MCM-41 (28) as well as Nb-doped zeolite BEA (25) and ZSM-5 (23) since the materials firstly cover appropriate ranges of acidity and porosity in order to provide a comparative basis and have shown the most promising results in terms of fructose yield upon the completion of the reaction. The textural properties of these catalysts are reported in Table 5.4.

Table 5.4. Textural properties of zeolites for parent zeolite Sn/Y (5.1), Sn/BEA (25), Sn/ZSM-5 (23), and Sn/Al-MCM-41 (28) zeolites doped via an incipient impregnation protocol with a metal loading of 1 wt.%.

Zeolite	Total surface area^(a) (m²·g⁻¹)	External surface area^(a) (m²·g⁻¹)	Micropore area^(a) (m²·g⁻¹)	Pore Volume^(b) (cm³·g⁻¹)	Channel diameter^(c) (Å)
Sn/Y (5.1)	655	344	311	0.16	7.1
Sn/BEA (25)	578	394	184	0.09	7.3
Nb/BEA (25)	490	223	267	0.13	6.9
Sn/ZSM-5 (23)	330	103	227	0.11	6.0
Nb/ZSM-5 (23)	328	100	228	0.12	6.2
Sn/Al-MCM-41 (28)	1249	965	not applicable	0.16	11.4

(a) Values calculated from the adoption branch of the adsorption isotherms using BET theory.

(b) Value acquired at the absorption-desorption point using a Barret–Joyner–Halenda (BJH) method.

(c) Value obtained at the absorption-desorption point using a Horvath-Kawazoe method for a cylinder pore geometry.

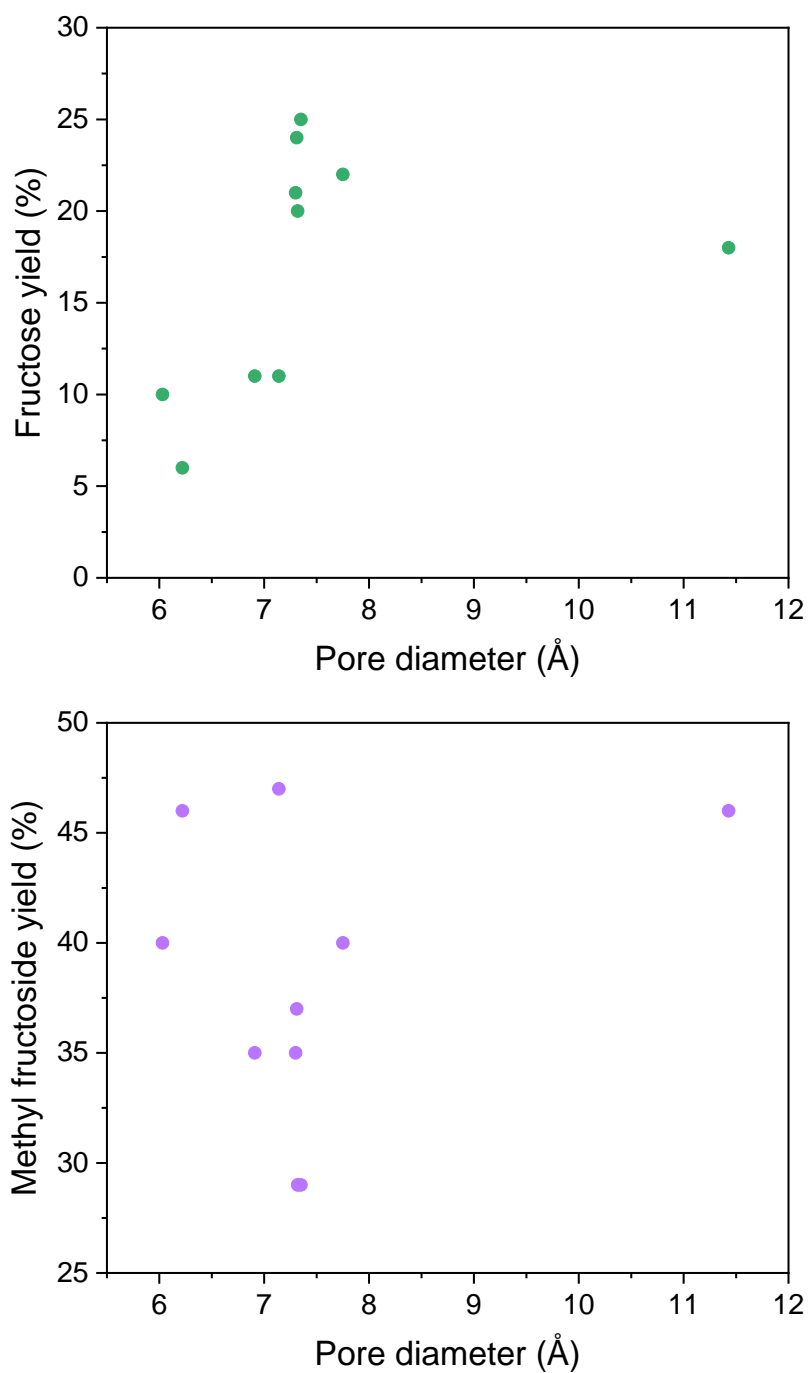


Figure 5.12. Trends of **a)** fructose yield and **b)** methyl fructoside yield as a function of pores diameters (Å). Yields values were obtained from reactions carried out following one-step protocol in methanol for 1 h at a reaction temperature of 100 °C and endogenous pressure using a constant M:S molar ratio M:S = 1:100. Data are randomly distributed, and no clear trend is observed.

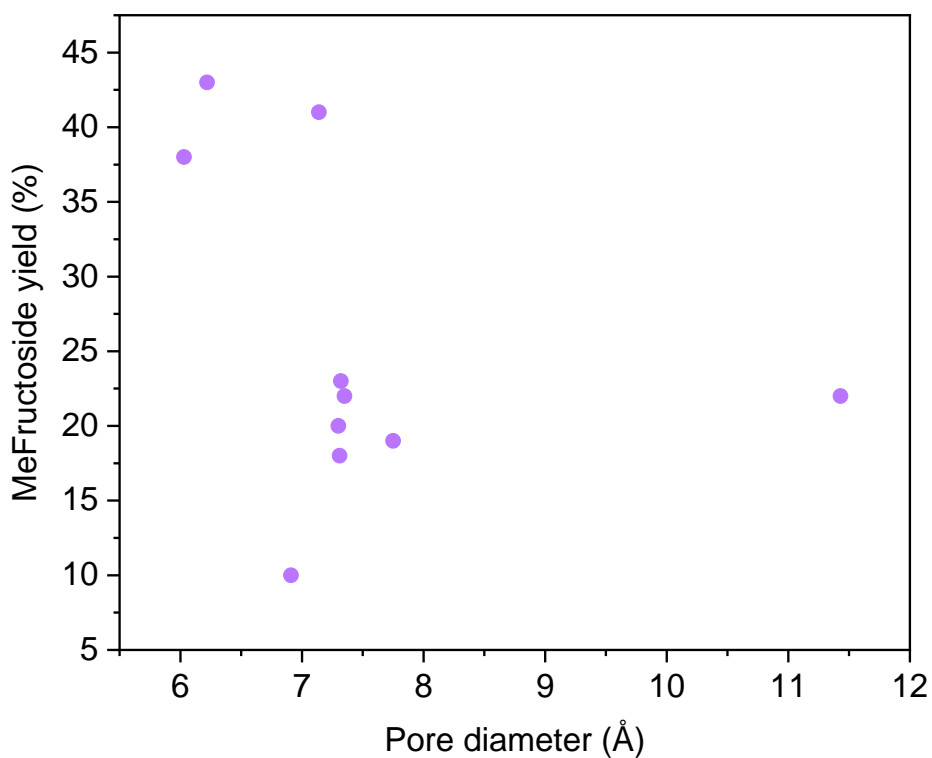
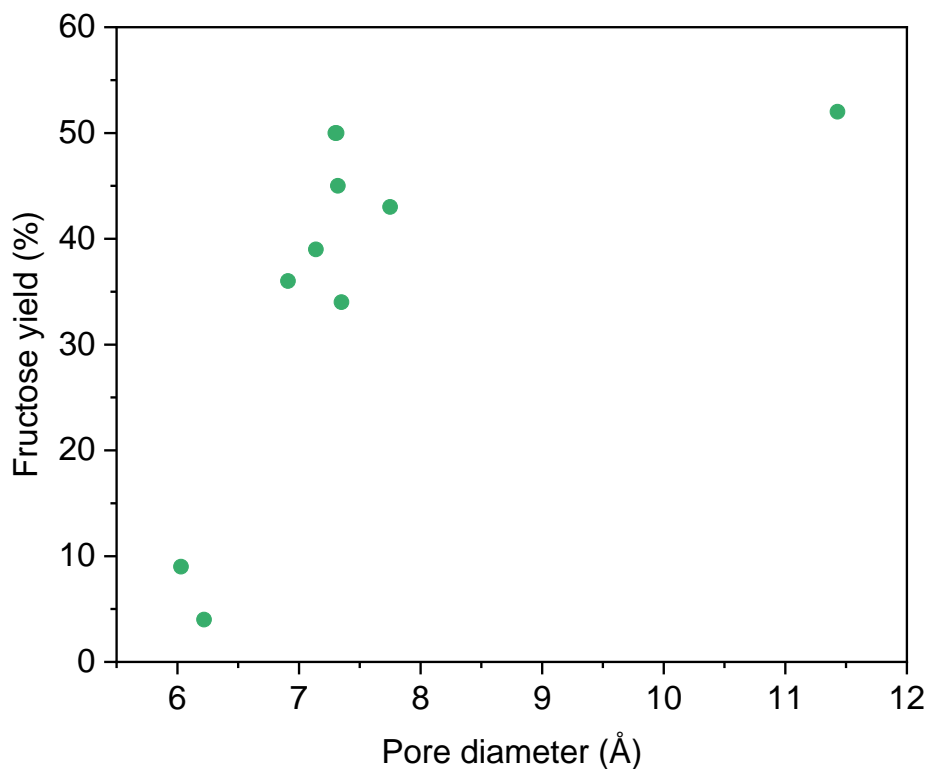


Figure 5.13. Trends of **a)** fructose yield and **b)** methyl fructoside yield as a function of pores diameters (Å). Yields values were obtained from reactions carried out following the two-steps protocol in methanol for 1 h and then adding water for an additional reaction time of 1 h at a reaction temperature of 100 °C and endogenous pressure using a constant M:S molar ratio M:S = 1:100. Data are randomly distributed, and no clear trend is observed.

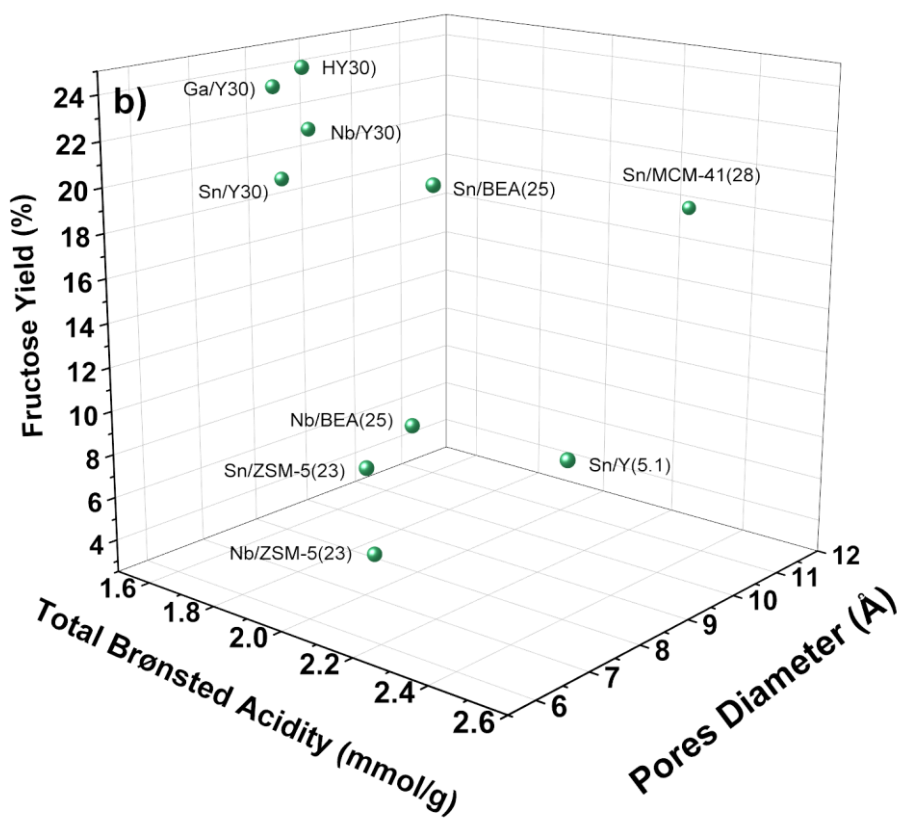
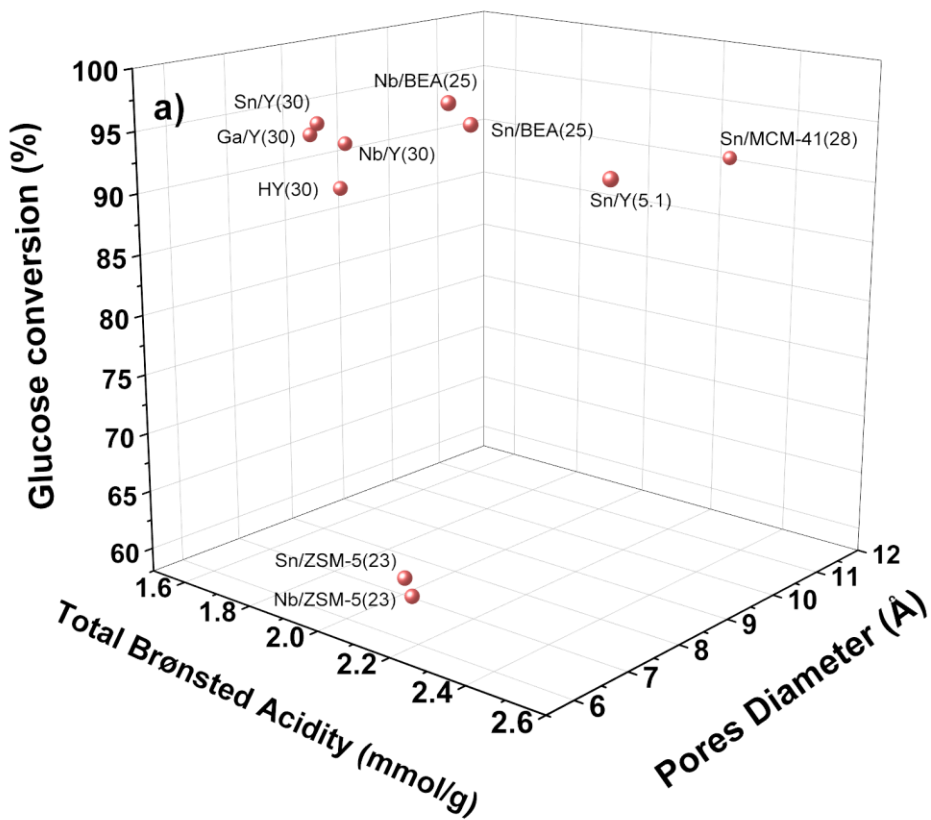
Our porosimetry measurements did not show any direct correlation between catalytic activity in terms of glucose conversion, product selectivity and pores diameters of catalysts studied. A random distribution of the data was instead observed in both reactions carried out following the one-step protocol in methanol and the two-step protocol in methanol and water (Figures A30 and A31 in Appendix A.11). As a consequence, the yield values of fructose and methyl fructoside were also correlated with respect to the pore size of our catalysts in order to identify possible trends in the catalytic activity. However, no clear trend was observed even with yield values and data were randomly distributed (Figures 5.12 and 5.13) with statistical Pearson correlation coefficient values (r) in the range of 0 – 0.5, indicating weak or no correlation between the two data sets (i.e., pore diameter and catalytic activity in terms of glucose conversion, product selectivity and yields). However, as the formation of methyl fructoside is mainly facilitated by Brønsted acidity on the external surface of the zeolite (section 4.2.1.1 in Chapter 4), the pores are really not relevant in this case, and no correlation would be observed. Whereas, in the case of fructose, the lack of correlation can be explained by the fact that a large part of fructose (*ca.* $\geq 30\%$) is formed by the hydrolysis step of methyl fructoside intermediates, which also occur outside the zeolite pores. On the other hand, it was observed that a pore diameter larger than 7 Å could facilitate the diffusion of glucose molecules inside the zeolite pores and allow the isomerisation reaction of glucose to fructose to occur, which results in higher fructose yield formed (Figure 5.12a) as compared to catalysts with smaller pore diameters (≤ 6 Å) such as Sn/ZSM-5 catalyst that leads to a higher yield of methyl fructoside rather than fructose (Figure 5.12b). These observations further proved that our isomerisation reaction has indeed at least two reaction pathways with one being toward the formation of methyl fructoside, which is entirely a Brønsted acid-

catalysed pathway that is occurring on the external surface of the catalyst and does not require pores.

As no clear and direct trends were observed in catalytic activity when correlations were made between catalytic activity and Brønsted acidity and pores diameter individually. It would be worthwhile to correlate our catalytic activity data with both acidity and porosity measurements in a three-dimensional representation.

5.7. 3D acidity-porosity-activity correlations plots.

Given the obtained trends in sections 5.5.1 and 5.6.1, it is evident that the isomerisation reaction of glucose is highly complex and involves multiple pathways that are governed by several factors such as catalyst acidity and porosity. Therefore, selecting a simple parameter that accurately predicts trends in catalytic performance is quite challenging. In this regard, our data were correlated using a three-dimensional relationship between total Brønsted acidity, pore diameter, and catalytic activity. The trends in glucose conversion, fructose yield and methyl fructoside yield depending on both acidity and porosity characteristics are presented in Figures 5.14 and 5.15.



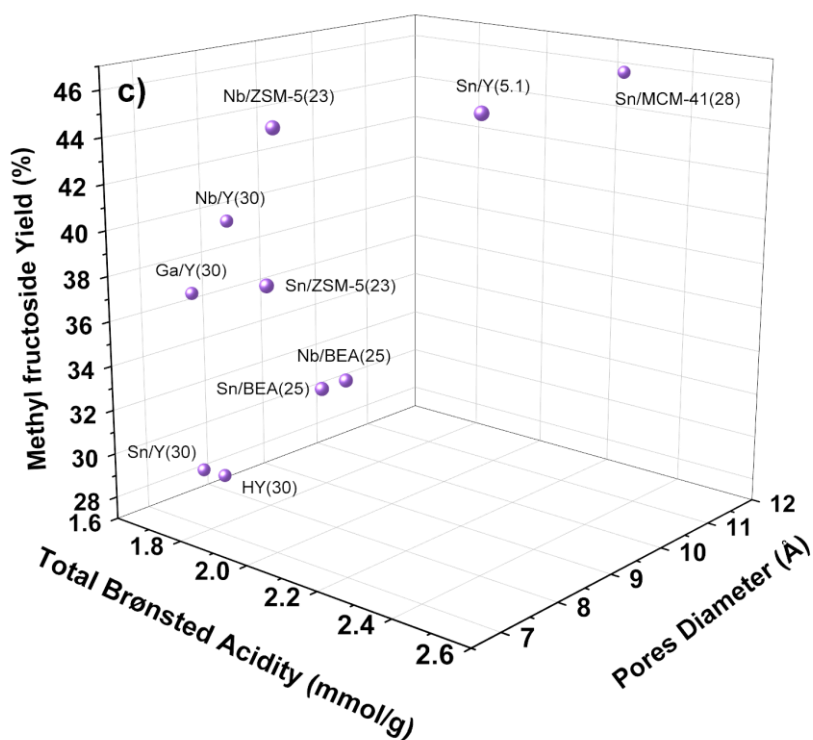
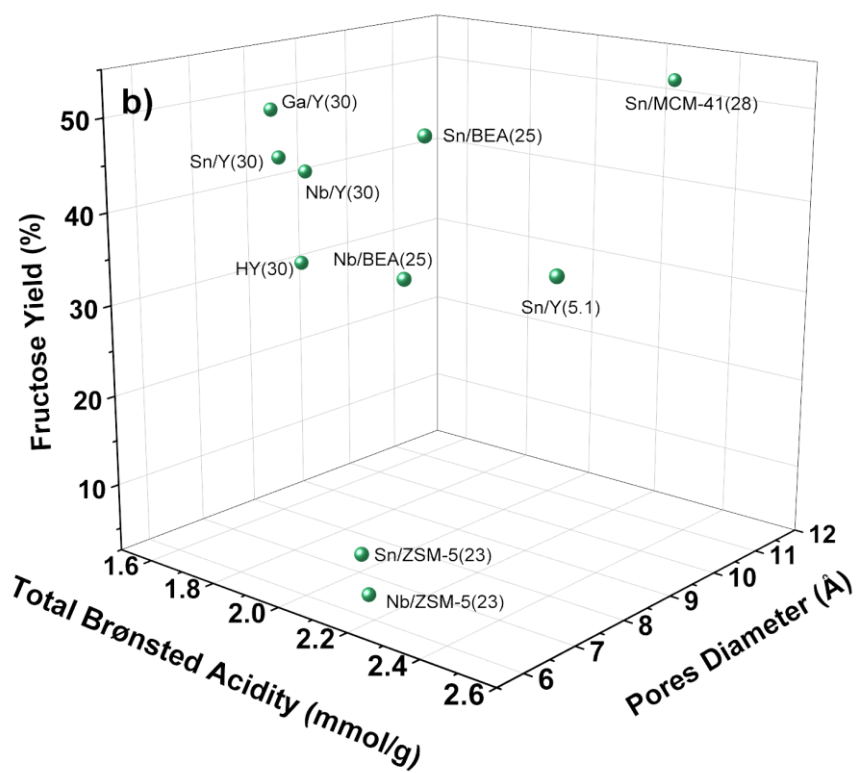
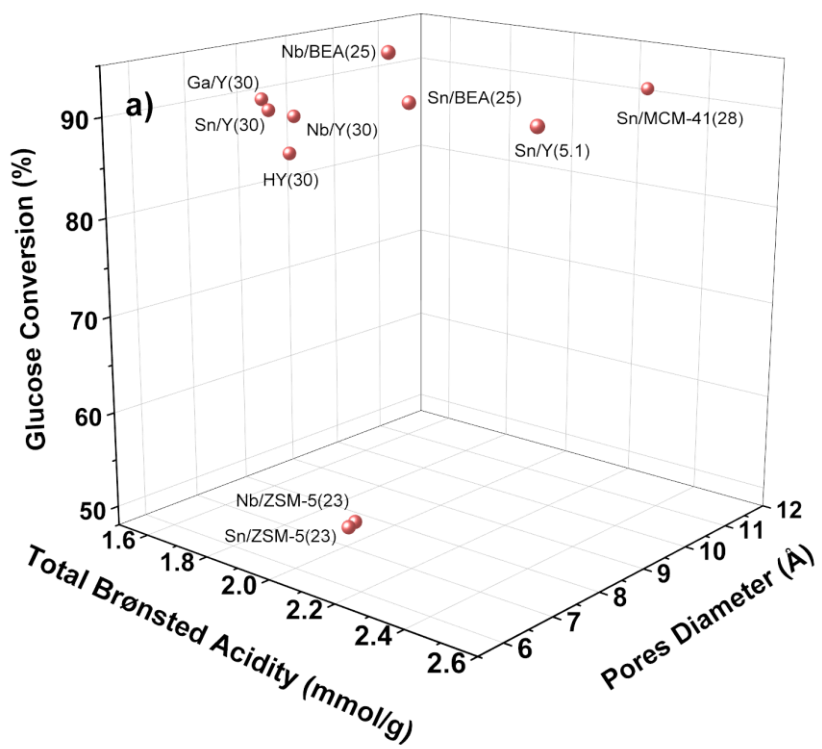


Figure 5.14. Trends in catalytic activity using a three-dimensional correlation between **a)** Glucose conversion, **b)** fructose yield, and **c)** methyl fructoside yield as a function of Brønsted acidity and pores diameter. The reaction was carried out following the one-step protocol in methanol at 100 °C for 1 h and endogenous pressure using a constant M:S molar ratio M:S = 1:100. The number enclosed within the parentheses of the labelling corresponds to the SiO₂:Al₂O₃ molar ratio of zeolite support used.



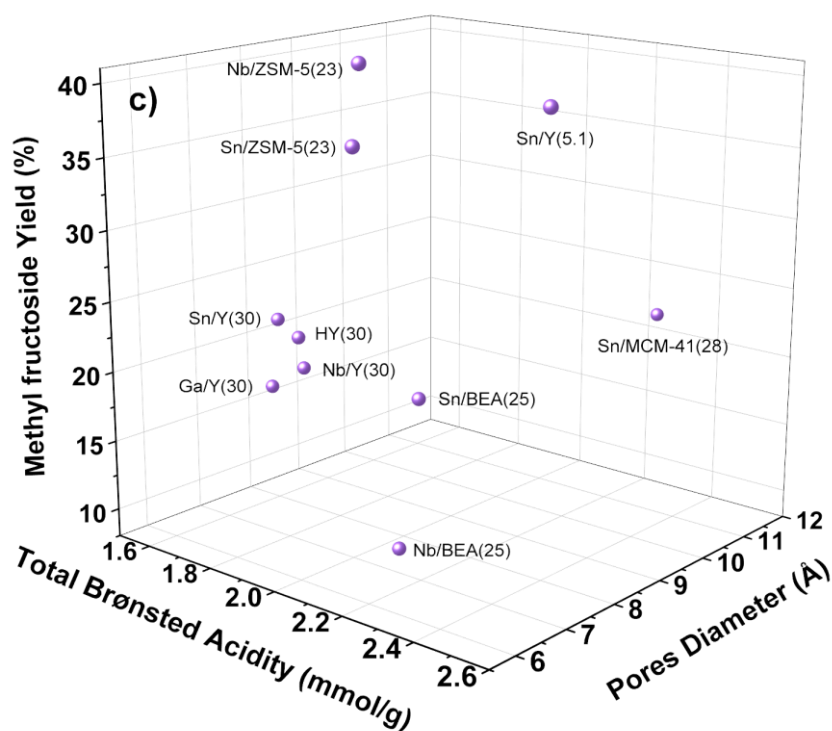


Figure 5.15. Trends in catalytic activity using a three-dimensional correlation of **a)** Glucose conversion, **b)** fructose yield, and **c)** methyl fructoside yield as a function of Brønsted acidity and pores diameter. The reaction was carried out following the two-step protocol in methanol for 1 h and then adding water for an additional reaction time at 100 °C and endogenous pressure using a constant M:S molar ratio M:S = 1:100. The number enclosed within the parentheses of the labelling corresponds to the SiO₂:Al₂O₃ molar ratio of zeolite support used.

As can be seen in Figures 5.14 and 5.15, using three-dimensional correlations between catalytic activity, total Brønsted acidity and pores diameter allowed for the identification of more meaningful trends in the catalytic results. Glucose conversion showed to increase per increase of Brønsted acidity and with catalysts possessing pore diameter larger than 7 Å (Figures 5.14a and 5.15a). Whereas the highest fructose yield ($\geq 50\%$) was obtained by using zeolite catalysts having a Brønsted acidity range of 1.5 – 2.2 mmol·g⁻¹ (Figure 5.15b). on the other hand, the formation of more methyl fructoside ($\sim 45\%$) was obtained by catalysts exhibiting either a high Brønsted acidity value (~ 2.5 mmol·g⁻¹) and/or a small pore diameter smaller than 6 Å (Figures 5.14c and 5.15c). However, the characterisation of more catalytic properties involved in

initiating catalytic activity such as Lewis's acidity would be highly informative in order to identify stronger correlations.

5.8. Conclusion

The roles of zeolite's acidity and porosity in the isomerisation reaction of glucose to fructose were systematically investigated. 1 wt.% Sn, 0.6 wt.% Ga and 0.8 wt.% Nb were added on various zeolite supports with different ranges of acidity and porosity characteristics, including zeolite Y ($\text{SiO}_2:\text{Al}_2\text{O}_3$ molar ratios of 5.1 and 30), BEA ($\text{SiO}_2:\text{Al}_2\text{O}_3$ molar ratios of 25 and 38), ZSM-5 ($\text{SiO}_2:\text{Al}_2\text{O}_3$ molar ratios of 23 and 50), and Al-MCM-41 ($\text{SiO}_2:\text{Al}_2\text{O}_3$ a molar ratio of 28).

The catalytic data showed that large pore zeolites Y and BEA were found to provide the highest catalytic performances with fructose yields of approximately 30% and 60% for reactions followed by a one-step protocol in methanol or a two-step protocol in methanol and water, respectively. As compared to pre-existing Al centres, the effect of the metal dopant is negligible on zeolite Y catalysts. However, this was not the case with BEA, ZSM-5 and Al-MCM-41, for which the doping of Sn, Ga, and Nb significantly enhanced glucose conversion and fructose selectivity. Furthermore, the results showed that a $\text{SiO}_2:\text{Al}_2\text{O}_3$ molar ratio in the range of 20 – 40 provided the best results concerning glucose conversion and fructose yields.

Total Brønsted acidity measurements revealed no direct correlation with glucose conversion, fructose selectivity and yield, and data are completely distributed at random. However, there was a clear positive correlation between the methyl fructoside and the Brønsted acidity. This was expected since this intermediate is mainly formed via a Brønsted acid pathway. In addition, porosity data showed that a pore size larger

than 7 Å is indeed required for the isomerisation reaction to take place inside the pores of the zeolite. In addition, no positive or negative correlation was observed between porosity (pore diameter) and catalytic performance (e.g., glucose conversion, product selectivity, and yield). This lack of correlations could be attributed to the fact that the formation of methyl fructoside and its subsequent hydrolysis to fructose occur mainly on the external surface of the zeolite. Therefore, the pores are not significant in this particular case. On the other hand, the aid in the use of three-dimensional correlations between total Brønsted acidity, porosity, and catalytic activity provided more information to identify clear trends in the obtained catalytic results.

Finally, glucose isomerisation showed to be a complicated reaction that takes place in multiple pathways towards the formation of fructose. As a consequence, it is difficult to assess catalytic performance through a single parameter sufficiently accurately. For this reason, it is imperative that different characteristics of catalysts be evaluated in order to understand the trends in their catalytic performance.

5.9. References

- 1 R. Bermejo-Deval, M. Orazov, R. Gounder, S. J. Hwang and M. E. Davis, *ACS Catal.*, 2014, **4**, 2288–2297.
- 2 G. Yang, E. A. Pidko and E. J. M. Hensen, *J. Catal.*, 2012, **295**, 122–132.
- 3 D. Jung, P. Körner and A. Kruse, *Biomass Convers Biorefin*, 2021, **11**, 1155–1170.
- 4 V. V. Ordonsky, J. Van Der Schaaf, J. C. Schouten and T. A. Nijhuis, *J Catal*, 2012, **287**, 68–75.
- 5 M. Moliner, Y. Román-Leshkov and M. E. Davis, *Proc. Natl. Acad. Sci. U.S.A.*, 2010, **107**, 6164–6168.
- 6 A. S. Amarasekara, L. H. Nguyen, H. Du and R. R. Kommalapati, *SN Appl. Sci.*, 2019, **1**, 964.
- 7 N. A. S. Ramli and N. A. S. Amin, *Appl. Catal. B: Environ.*, 2015, **163**, 487–498.
- 8 R. Netrabukkana, K. Lourvanij and G. L. Rorrer, *Ind. Eng. Chem. Res.*, 1996, **35**, 458–464.
- 9 I. Agirrezabal-Telleria, I. Gandarias and P. L. Arias, *Catal. Today*, 2014, **234**, 42–58.
- 10 P. Carniti, A. Gervasini, S. Biella and A. Auroux, *Catal Today*, 2006, **118**, 373–378.
- 11 N. Candu, M. El Fergani, M. Verziu, B. Cojocaru, B. Jurca, N. Apostol, C. Teodorescu, V. I. Parvulescu and S. M. Coman, *Catal Today*, 2019, **325**, 109–116.

- 12 F. Yang, Q. Liu, X. Bai and Y. Du, *Bioresour Technol*, 2011, **102**, 3424–3429.
- 13 C. M. Osmundsen, M. Spangsborg Holm, S. Dahl and E. Taarning, *Proc. Natl. Acad. Sci. U.S.A.*, 2012, **468**, 2000–2016.
- 14 C. M. Lew, N. Rajabbeigi and M. Tsapatsis, *Microporous Mesoporous Mater.*, 2012, **153**, 55–58.
- 15 L. J. Liu, Z. M. Wang, S. Fu, Z. B. Si, Z. Huang, T. H. Liu, H. Q. Yang and C. W. Hu, *Catal. Sci. Technol.*, 2021, **11**, 1537–1543.
- 16 L. B. Mccusker, R. B. Von Dreele, D. E. Cox, D. Loue and P. Scardi, *J. Appl. Crystallogr.*, 1999, **32**, 36–50.
- 17 M. Conte, C. J. Davies, D. J. Morgan, T. E. Davies, D. J. Elias, A. F. Carley, P. Johnston and G. J. Hutchings, *J. Catal.*, 2013, **297**, 128–136.
- 18 R. Roy, V. G. Hill and E. F. Osborn, *J. Am. Chem. Soc.*, 1952, **74**, 719–722.
- 19 G. Taques Tractz, F. Staciaki da Luz, S. Regina Masetto Antunes, E. do Prado Banczek, M. Taras da Cunha and P. Rogério Pinto Rodrigues, *Sol. Energy*, 2021, **216**, 1–6.
- 20 L. Botti, R. Navar, S. Tolborg, J. S. Martinez-Espin, D. Padovan, E. Taarning and C. Hammond, *Top. Catal.*, 2019, **62**, 1178–1191.
- 21 P. Wolf, W. C. Liao, T. C. Ong, M. Valla, J. W. Harris, R. Gounder, W. N. P. van der Graaff, E. A. Pidko, E. J. M. Hensen, P. Ferrini, J. Dijkmans, B. Sels, I. Hermans and C. Copéret, *Helv. Chim. Acta*, 2016, **99**, 916–927.
- 22 A. Cichocki, J. Datka, A. Olech, Z. Piwowarska and M. Michalik, *J. CHEM. SOC. FARADAY TRANS*, 1990, **86**, 753–756.

- 23 S. Roy, K. Bakhmutsky, E. Mahmoud, R. F. Lobo and R. J. Gorte, *ACS Catal.*, 2013, **3**, 573–580.
- 24 W. N. P. Van Der Graaff, C. H. L. Tempelman, E. A. Pidko and E. J. M. Hensen, *Catal. Sci. Technol.*, 2017, **7**, 3151–3162.
- 25 J. Tang, X. Guo, L. Zhu and C. Hu, *ACS Catal.*, 2015, **5**, 5097–5103.
- 26 B. Sun, Y. Kang, Q. Shi, M. Arowo, Y. Luo, G. Chu and H. Zou, *Can. J. Chem. Eng.*, 2019, **97**, 3063–3073.
- 27 J. A. Lopez-Sanchez, M. Conte, P. Landon, W. Zhou, J. K. Bartley, S. H. Taylor, A. F. Carley, C. J. Kiely, K. Khalid and G. J. Hutchings, *Catal. Lett.*, 2012, **142**, 1049–1056.
- 28 C. Flores, N. Batalha, N. R. Marcilio, V. V. Ordonsky and A. Y. Khodakov, *ChemCatChem*, 2019, **11**, 568–574.
- 29 F. N. Ridha, Y. Yang and P. A. Webley, *Microporous Mesoporous Mater.*, 2009, **117**, 497–507.
- 30 F. C. Hendriks, D. Valencia, P. C. A. Bruijninx and B. M. Weckhuysen, *Phys. Chem. Chem. Phys.*, 2017, **19**, 1857–1867.

Chapter 6. Conversion of fructose to 5-hydroxymethylfurfural (5-HMF) over metals and metal oxides doped zeolite Y in water media.

6.1. Introduction

5-hydroxymethylfurfural (5-HMF) has the potential to serve as a platform chemical for the production of versatile compounds ranging from fine chemicals, polymer monomers, liquid fuels, fuel precursors, and fuel additives to other platform chemicals (Figure 1.3 in Chapter 1), covering a wide range of application demands^{1,2}. For instance, 2,5-furan-dicarboxylic acid (FDCA), a 5-HMF derivative, can be used as a renewable alternative to terephthalic acid during the manufacture of polyethylene terephthalate (PET)³. Furthermore, 2,5-dimethylfuran (DMF), an attractive biofuel candidate produced from 5-HMF by a catalytic hydrogenation process, has received considerable attention due to its numerous advantages, including an ideal boiling point of (92–94 °C), high energy density (30 kJcm⁻³), high research octane number (RON=119), immiscibility with water, and ease of blending with gasoline without requiring major modifications to existing infrastructure or vehicles⁴. To date, numerous studies have demonstrated the use of different carbohydrates, including fructose, glucose, cellulose, starch, sucrose, and inulin, as the initial substrates in the synthesis of 5-HMF molecules^{5–11}. However, fructose is the most prevalent sugar due to its ease of conversion and high selectivity toward the desired 5-HMF by losing three water molecules through a dehydration reaction³.

The dehydration of fructose to 5-HMF has been explored in the literature by using different systems, including aqueous, organic, ionic liquids, and biphasic reaction mediums^{12,13}, and over a wide variety of homogeneous (e.g., mineral acids, heteropoly acids (HPAs), ionic liquids (ILs) and metal chlorides)^{14–16} and heterogeneous

catalysts (e.g., zeolites, metal oxides, ion-exchange resins, mesoporous silica materials, and hydrotalcite-based materials)¹⁷⁻²⁰. In this context, recent attention has been focused on using zeolite catalysts as a result of their advantages compared to other acidic catalysts in sugar dehydration²¹. This explicitly includes the simple separation from products and, thereby, easy recycling of the catalyst compared to the homogeneous catalyst^{22,23} and thermal stability in aqueous solution compared to other heterogeneous catalysts such as Amberlyst resins (< 150 °C)²⁴.

The nature and strength of the acid sites of the catalyst have been found to play a pivotal role in the formation of 5-HMF^{16,18}. For instance, Brønsted acid sites in the case of zeolites and ion-exchange resin showed high selectivity towards 5-HMF in the dehydration of fructose²⁵. Wherein fructose is activated by protonating the OH hydroxyl group at the anomeric carbon C2 position of fructose, followed by sequential dehydration steps to 5-HMF (Figure 6.1)²⁶. In contrast, Lewis acidity could promote the intensive formation of undesirable humins from fructose at the initial stages of the reaction²⁵.

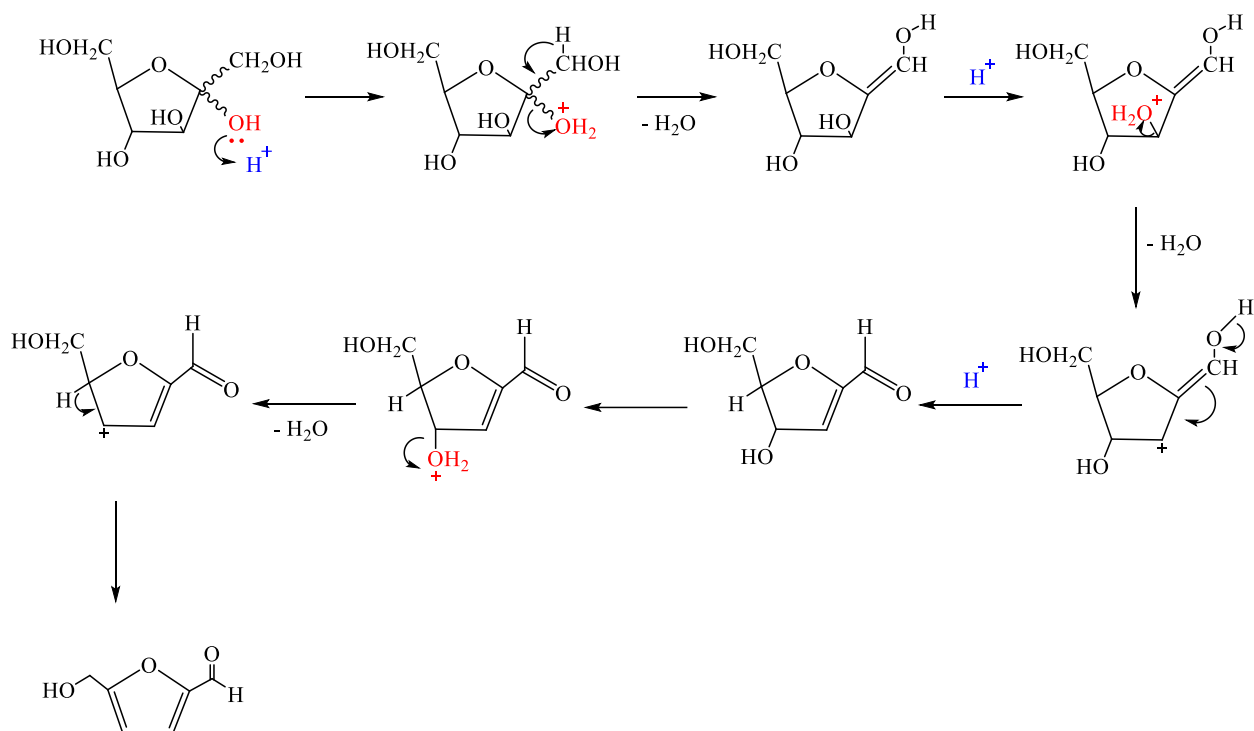


Figure 6.1. A proposed mechanism of Brønsted acid catalysed-reaction of fructose dehydration to 5-HMF. Protonation of the C2 hydroxyl group of the fructose molecule occurs, followed by the loss of a water molecule, resulting in the formation of a carbonium ion. Such intermediate converts into an enol, which is then condensed to form HMF through the release of two additional water molecules²⁷.

Although the synthesis process of 5-HMF has been studied for many years, developing a promising industrial approach to producing this prominent intermediate on a large scale remains a challenge²⁸. This is due to several reasons. For example, the initial reagent (e.g., sugars), intermediates, and the final product (i.e., 5-HMF) can undergo consecutive side reactions such as rehydration, decomposition, polymerisation, and condensation in the presence of water as a reaction medium²⁹ at high reaction temperatures ($> 120\text{ }^{\circ}\text{C}$)³⁰, leading to the formation of other platform chemicals like levulinic and formic acids from the rehydration of 5-HMF¹⁷ and insoluble oligomeric humins as a result of the condensation and cross-polymerisation reactions of initial feedstocks, intermediates and products²⁵, which could lead to a low yield of

the more desirable 5-HMF ($\leq 50\%$)¹². The use of water offers many advantages, including being a green route to produce 5-HMF, reducing solvent costs and providing greater ease of separation and, in turn, making the process easier to scale up^{1,29}. On the other hand, the use of nonaqueous solvents shows a high yield of 5-HMF³¹. For example, 5-HMF yield of (ca. 75%) was obtained from fructose using dimethyl sulfoxide (DMSO) as a reaction media and HY zeolite ($\text{SiO}_2:\text{Al}_2\text{O}_3$ molar ratio of 4.8) as a catalyst at 120 °C for 2 h³². However, this type of solvent has been considered not economically viable for the synthesis of 5-HMF, especially on a large scale³³.

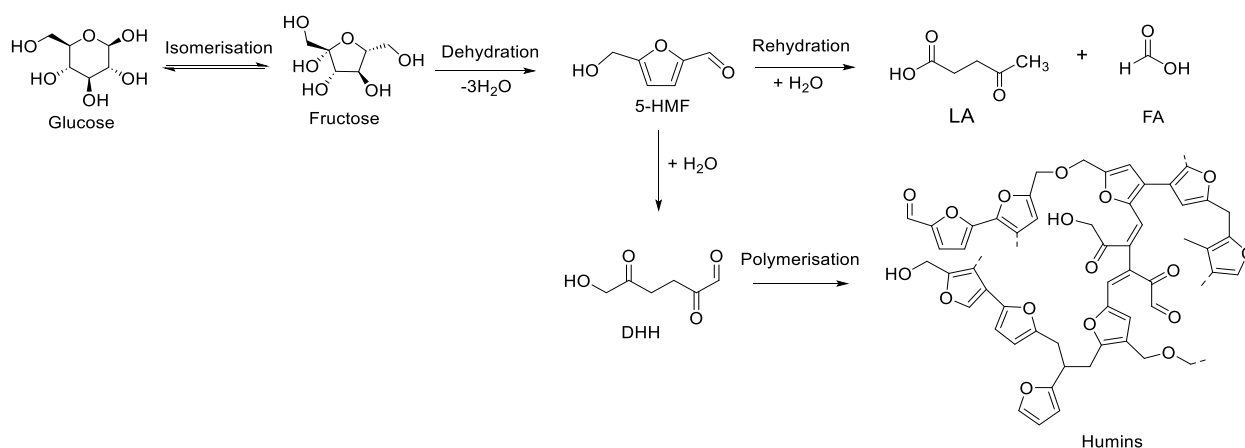


Figure 6.2. Schematic diagram of a proposed reaction pathway toward the formation of Humins through the uncontrollable aldol condensation of glucose, 5-hydroxymethylfurfural (5-HMF) and 2,5-dioxo-6-hydroxy hexanal (DHH)^{34,35}.

In view of this, the aims of this chapter are to **1)** qualitatively and quantitatively identify the products of 5-HMF-containing reaction mixtures by using ¹H-NMR. **2)** preliminary identify the reaction parameters of fructose dehydration by using HCl as a homogeneous Brønsted catalyst to achieve selective fructose conversion to 5-HMF in an aqueous solution using a heterogeneous catalysis system. **3)** synthesise Sn, Ga, Nb, and Fe-doped zeolite Y and test them alongside the parent non-doped zeolite Y

in its acidic form to investigate the synergetic effect of Brønsted and Lewis acid sites in the glucose and fructose dehydration reactions to 5-HMF. **4)** investigate the catalytic activity of MoO_3 , La_2O_3 , CeO_2 , Nb_2O_5 , TiO_2 , and WO_3 , in their bulk metal oxide forms to prove the concept that Brønsted and Lewis acidities are essential characteristics to convert sugars such as glucose and fructose to desirable 5-HMF. **5)** prepare CeO_2 , Nb_2O_5 , and TiO_2 -doped zeolite Y catalysts using a sol-gel technique and study their catalytic performance in the glucose and fructose dehydration reactions to 5-HMF.

6.2. $^1\text{H-NMR}$ characterisation of reaction mixtures.

NMR provides rapid and cheap identification and quantification of samples. As sugar dehydration can typically yield multiple products³⁶, it is, important to accurately determine the individual amount of all possible products in these reactions in order to determine, and afterwards compare the catalytic activity (conversion and selectivity) among all materials studied. In this context, standard solutions of fructose, along with its expected dehydration products, were prepared to assess if ^1H NMR as a viable tool for the characterisation of reaction mixtures of the sugar dehydration (Table 6.1). In this regard, deuterium oxide D_2O was selected as an NMR solvent, to avoid ^1H -containing solvents that would dominate our NMR spectrum³⁷. Moreover, using a solvent that is the deuterated counterpart, the same as the reaction solvent, would be more convenient for method validation to avoid possible immiscibility phenomena. Furthermore, Ethyl acetate ($\text{CH}_3\text{COOCH}_2\text{CH}_3$) [δ 1.2 (t, 3H), δ 1.9 (s, 3H), δ 4.0 (q, 2H)] was chosen as an internal standard in this method owing to several factors that are highly soluble in water (ca. 83 g/L at 20 °C)³⁸, chemically unreactive and highly stable in the reaction solution, so any overestimation of products yield is avoided, resulting in more accurate and reliable measurements and calculations of the yield of

the desired product, and finally, the position of its signal(s) within the NMR spectrum does not overlap with those of major products (Figure 6.4).

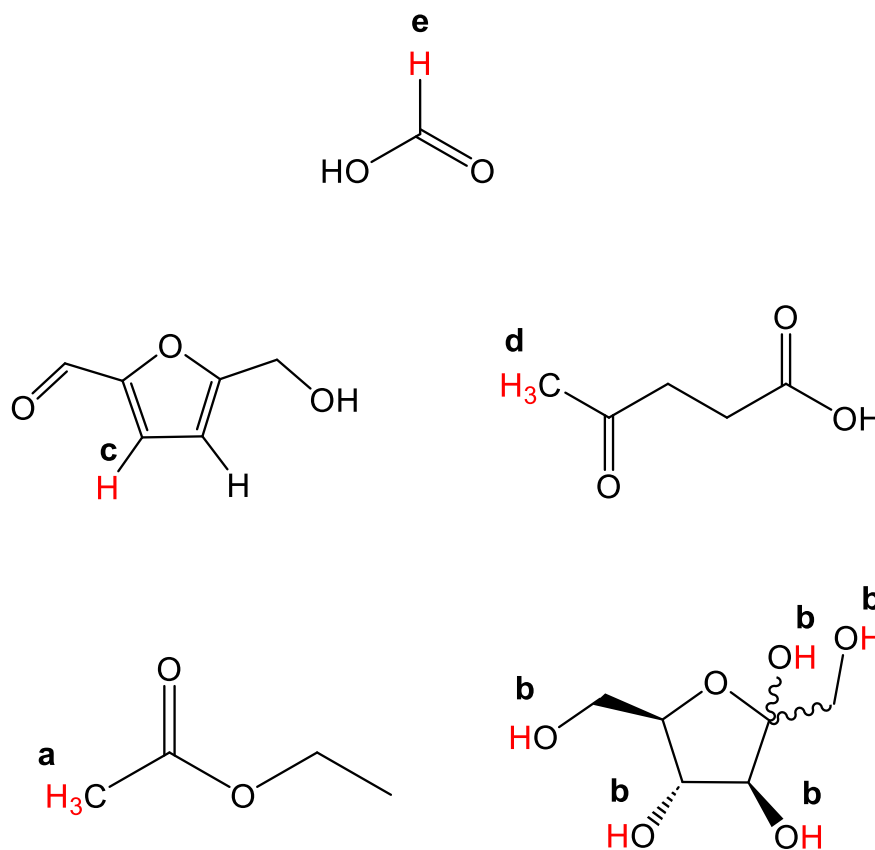


Figure 6.3. Chemical structure of a) ethyl acetate, b) fructose, c) 5-hydroxymethylfurfural, d) levulinic acid, and e) formic acid. Protons labelled in red are the characterisation peaks chosen for each product.

Table 6.1. Calculation of averaged discrepancy of all major products of the fructose dehydration to 5-HMF, a constant discrepancy was observed for each compound. Experimental errors are reported as the standard deviations of three repeated measurements.

compound	Chemical shift δ (ppm)	Expected mole	Average detected moles	Average discrepancy (%)
Fructose	3.4 – 4.0 (CH, m, 12H)	5.50×10^{-5}	4.82×10^{-5}	-12 ± 3
5-HMF	7.4 (CH, d, 1H)	7.93×10^{-5}	8.86×10^{-5}	12 ± 3

Levulinic acid	2.2 (CH ₃ , s, 3H)	8.60×10 ⁻⁵	9.98×10 ⁻⁵	16 ± 3
Formic acid	8.2 (CH, s, 1H)	2.18×10 ⁻⁴	2.21×10 ⁻⁵	1 ± 4

Initially, our proton NMR method was tested using standard solutions of fructose and all expected major products, namely 5-HMF, levulinic and formic acids, in order to determine whether this method would fit our system. As can be seen in (Table 6.1) the NMR analysis of these individual components demonstrated a molar discrepancy in the range of (±15%), which is acceptable considering the integration errors propagation of the NMR method (±5% per component). A common source of such errors can also be sample preparation (in the form of pipetting)³⁹. However, these discrepancies were shown to be constant within three replicates and were therefore applied as correction factors in the cases of mimic and real reaction mixtures.

Table 6.2. The carbon mass balance of three mimic mixtures with a different molar ratio of fructose dehydration components represents different stages of the desired reaction. In all cases, experimental errors are expressed as means standard deviations (n = 3).

Mimic mixture	Component	The moles of each component within the mimic mixtures (mol)	CMB (%)
1	Fructose	1.11×10 ⁻³	95 ± 4
	5-HMF	3.96×10 ⁻⁴	
	Levulinic acid	4.31×10 ⁻⁴	
	Formic acid	2.17×10 ⁻³	
2	Fructose	5.55×10 ⁻⁴	105 ± 6
	5-HMF	7.93×10 ⁻⁴	
	Levulinic acid	8.61×10 ⁻⁴	
	Formic acid	2.17×10 ⁻³	

3	Fructose	2.78×10^{-4}	105 ± 6
	5-HMF	1.59×10^{-3}	
	Levulinic acid	8.61×10^{-4}	
	Formic acid	1.09×10^{-3}	

As shown in Table 6.2, all three mimic reaction mixtures showed a carbon mass balance (calculated using equation Eq.2.12 in Chapter 2) compatible indeed with 100% within the experimental error. As a result, this method will work within a reasonable error at different reaction stages.

The NMR spectrums of the mimic mixture and the actual reaction mixture showed a reasonable match qualitatively (Figure 6.4). The characterisation peaks chosen for each product (H_a. ethyl acetate, H_b. fructose, H_c. 5-HMF, H_d. Levulinic acid, and H_e. Formic acid), reported in (Figure 6.3), were consistent between the mimic and the actual reaction mixtures, which further validates the quantification of the reaction mixtures of glucose and fructose dehydration reaction.

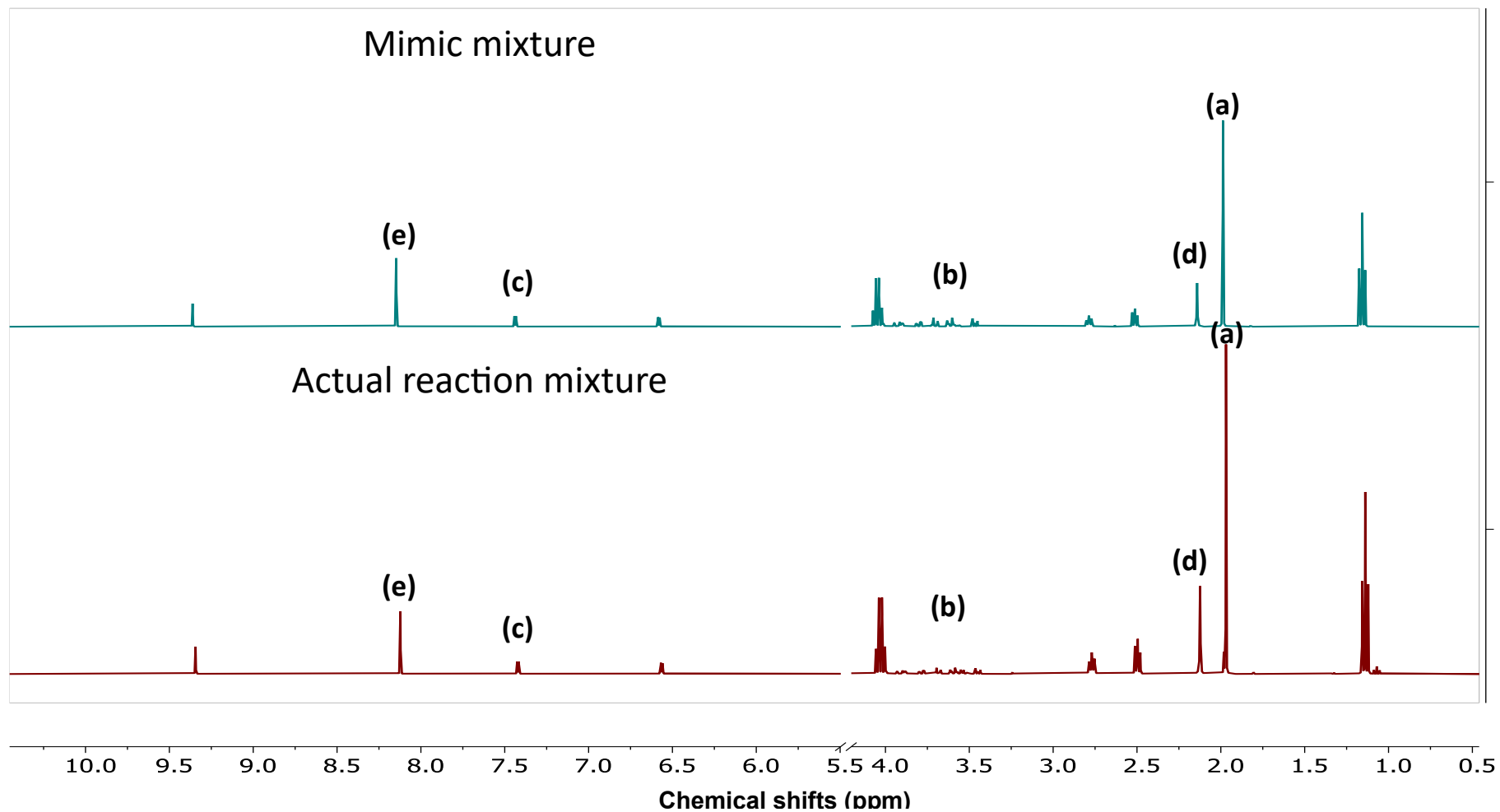


Figure 6.4. NMR spectra of a mimic reaction (●) and the actual reaction mixture of fructose dehydration to 5-HMF (●). One HMF and water peaks were compressed ($\delta = 5.5 - 4.5$ ppm), which will not affect the quantitative analysis.

6.3. Fructose dehydration to 5-HMF using hydrochloric acid as a homogenous catalyst.

In order to achieve a selective fructose dehydration reaction to 5-HMF in aqueous media via a heterogeneous catalyst, a screening of reaction parameters was first conducted using HCl as a homogeneous Brønsted acid catalyst. A kinetic study of the reaction was carried out at a reaction temperature of 100 °C from 10min to 360 min and with a fructose to HCl molar ratio of 1:1 – 1:0.2.

Firstly, a kinetic study of fructose dehydration was carried out by using hydrochloric acid with a fructose-to-HCl molar ratio of 1:1 (Figure 6.5). By accounting for fructose conversion, product selectivity, and carbon mass balance 5-HMF, levulinic acid and formic acid were the main product detected from our fructose dehydration. A complete consumption of fructose was reached in 240 min (Figure 6.5a). 5-HMF showed a pronounced the highest selectivity of 67% in 30 min, followed by a steady increase of Levulinic and formic acid selectivity up to 48% and 51%, respectively, after a reaction time of 240 min (Figure 6.5b). On the other hand, the carbon mass balance (CMB) also demonstrated a decrease of approximately 30% over time as the reaction time approached 360 minutes. This is more likely a consequence of the formation of large amounts of humins, through reactions with 5-HMF, fructose, and their intermediates.

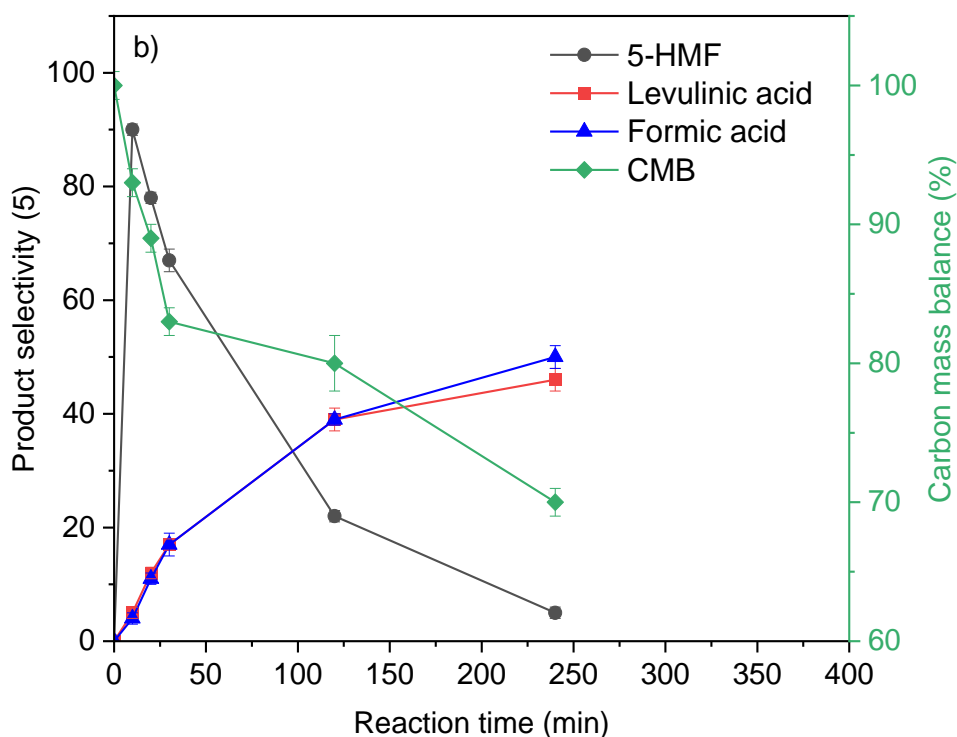
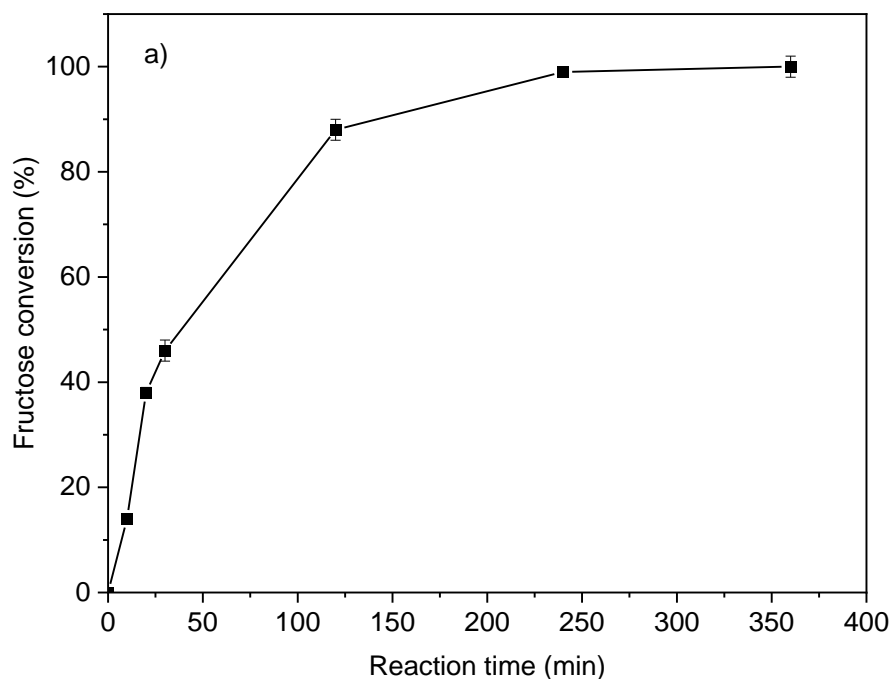


Figure 6.5. a) Fructose conversion, b) product selectivity and CMB obtained from fructose dehydration to 5-HMF in water over HCl (5 mL 100 g·L⁻¹ fructose solution, Fructose: HCl molar ratio of 1:1, 100 °C, time range of 10 – 360 mins, endogenous pressure, and 700 rpm). Experimental errors are presented as the standard deviations of three repeated measurements.

Due to the low yield of 5-HMF ($\leq 30\%$) obtained at a 1:1 fructose to HCl molar ratio and for a reaction time range of 10 – 360 min (Table A15 in Appendix A.13), lower fructose to HCl molar ratios of 1:0.33 and 1:0.2 (Figure 6.4) were also tested in order to determine the effect of Brønsted acidity originating from HCl on the reaction rates of fructose dehydration to 5-HMF and the sequential ring-opening and decomposition of 5-HMF to levulinic and formic acids. Due to the incomplete carbon mass balance obtained in the kinetic tests in (Sections 6.3 and 6.4), data of all products are presented in terms of yield rather than selectivity as considered more representative to determine the relative importance of different fructose to HCl molar ratios.

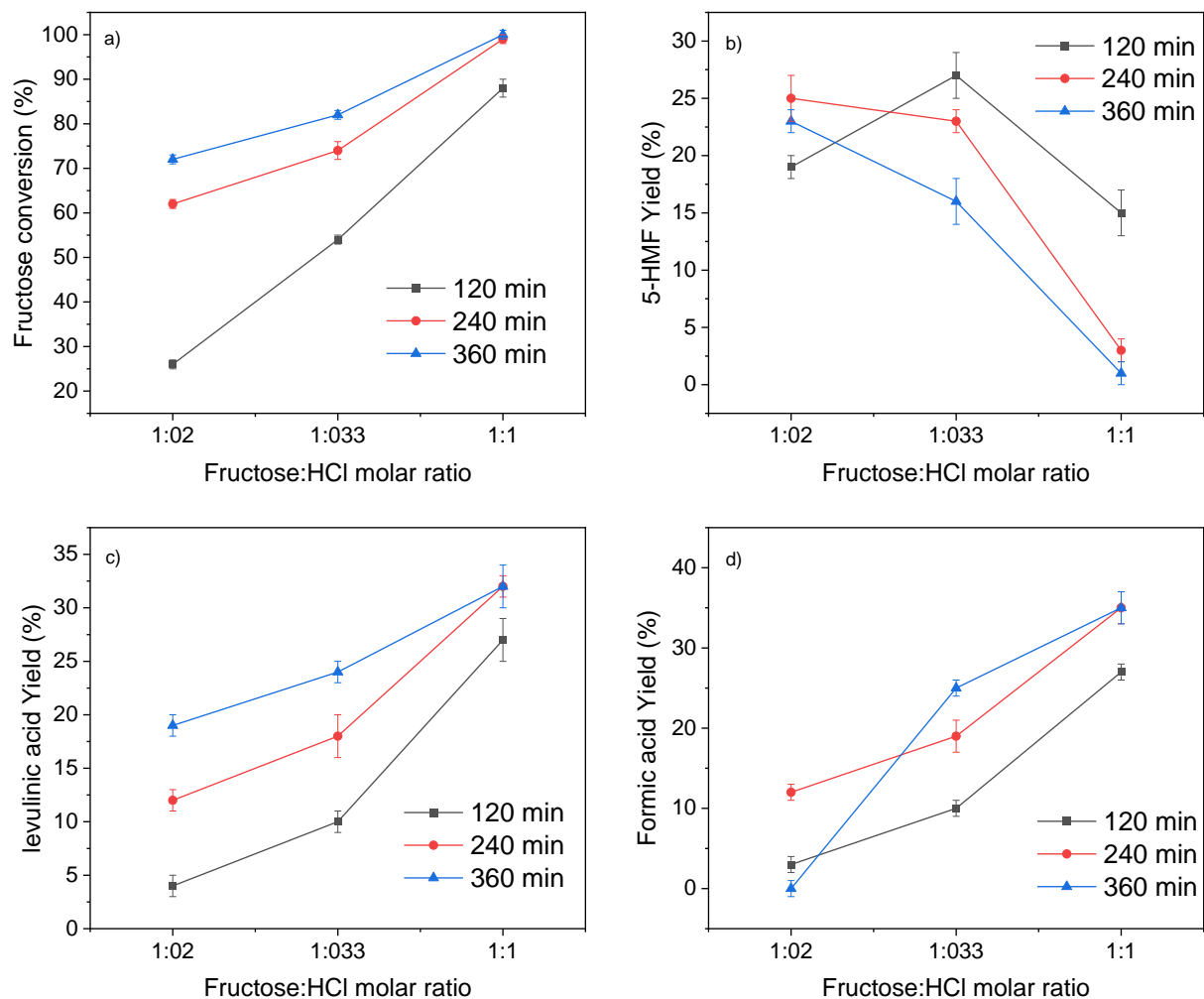


Figure 6.6. a) Fructose conversion, b) 5-HMF yield, c) levulinic acid yield, and d) formic acid yield when using HCl (5 mL of 100 g·L⁻¹ fructose solution, Fructose:HCl molar ratio in the range of 1:1 – 1:0.2, 100 °C, time range of 120 – 360 mins, endogenous pressure, and 700 rpm). Experimental errors are reported as the standard deviations of three independent measurements.

As shown in Figure 6.6a, when fructose to HCl molar ratios of 1:0.33 and 1:0.2 were used, a decrease in the fructose conversion of 30% was observed through different molar ratios. However, this decrease was comparatively accompanied by an increase of 12% in the 5-HMF yield and simultaneously a decrease of 15% in the case of LA and FA yields (Figures 6.6b – d), Among the use of different reaction parameters herein, only the reaction carried out at a molar ratio of 1:0.2 for 120 min displayed an opposite trend regarding 5-HMF yield. A synergistic effect of deficient reaction time and insufficient Brønsted acid concentration being used in this case are the most likely reasons for such findings. Additionally, a stoichiometric excess of formic acid relative to levulinic acid was observed in all cases.

To sum up, the highest 5-HMF yield of 27% obtained over HCl was acquired at two conditions: a molar ratio of 1:1 (30 min) and a molar ratio of 1:0.33 (120 min), resulting in solutions with pH values of 1 and 4, respectively. However, given greener reaction conditions, using less acid would be preferred. Therefore, the latter reaction conditions, that is, a fructose to HCl molar ratio of 1:0.33 for a reaction time of 120 min and with a pH solution of 4, were selected for further investigations of fructose dehydration to 5-HMF over an array of zeolite-based materials as an example of heterogeneous catalysts.

6.4. Fructose dehydration to 5-HMF using metal-doped zeolites as heterogeneous catalyst.

Having confirmed the sufficient reaction conditions (Fructose to HCl molar ratio: 1:0.33, 120 min, 100 °C and endogenous pressure) for our fructose dehydration to 5-HMF, a comprehensive investigation of fructose dehydration reaction was

subsequently carried out using various undoped and metal-doped zeolite Y catalysts was conducted using specified reaction conditions screened from the previous kinetic study (Section 6.3). In particular, the catalytic activity of undoped zeolites Y in their acidic form HY ($\text{SiO}_2:\text{Al}_2\text{O}_5$ molar ratios of 5.1, 30 and 80) was first tested to acquire a like-to-like comparison (acidity: fructose molar ratio 1:3) between the catalytic activities obtained by homogeneous catalyst (HCl) and Heterogeneous catalyst (HY zeolite). However, It has been observed that no products were formed under our reaction conditions (100 °C, 2h, endogenous pressure, and M:S of 1:3). However, this could be explained by multiple reasons: **1)** site-blocking effects by strong adsorption inside the pores of the zeolite⁴⁰ or by active metal sites (e.g., Al species in case of undoped zeolite) on its external surface⁴¹, **2)** the use of insufficient reaction conditions such as temperature, reaction time or catalyst's acidity to trigger the reaction heterogeneously. In other words, catalysts also possess their own activation temperature to initiate specific reactions efficiently. For example, a reaction temperature in the range of 120 – 165 °C is needed to allow the reaction of fructose dehydration to take place over zeolites as heterogeneous catalysts^{42,43}.

In this context, the reaction was carried out at a reaction temperature of 140 °C and with different metal-to-substrate molar ratios ranging from 1:3 to 1:300 (Figure 6.7). As expected, a higher reaction temperature significantly promoted the fructose dehydration reaction. This means that a reaction temperature of 100 °C was not enough to activate our catalysts in order to facilitate the fructose dehydration to 5-HMF under other reaction conditions.

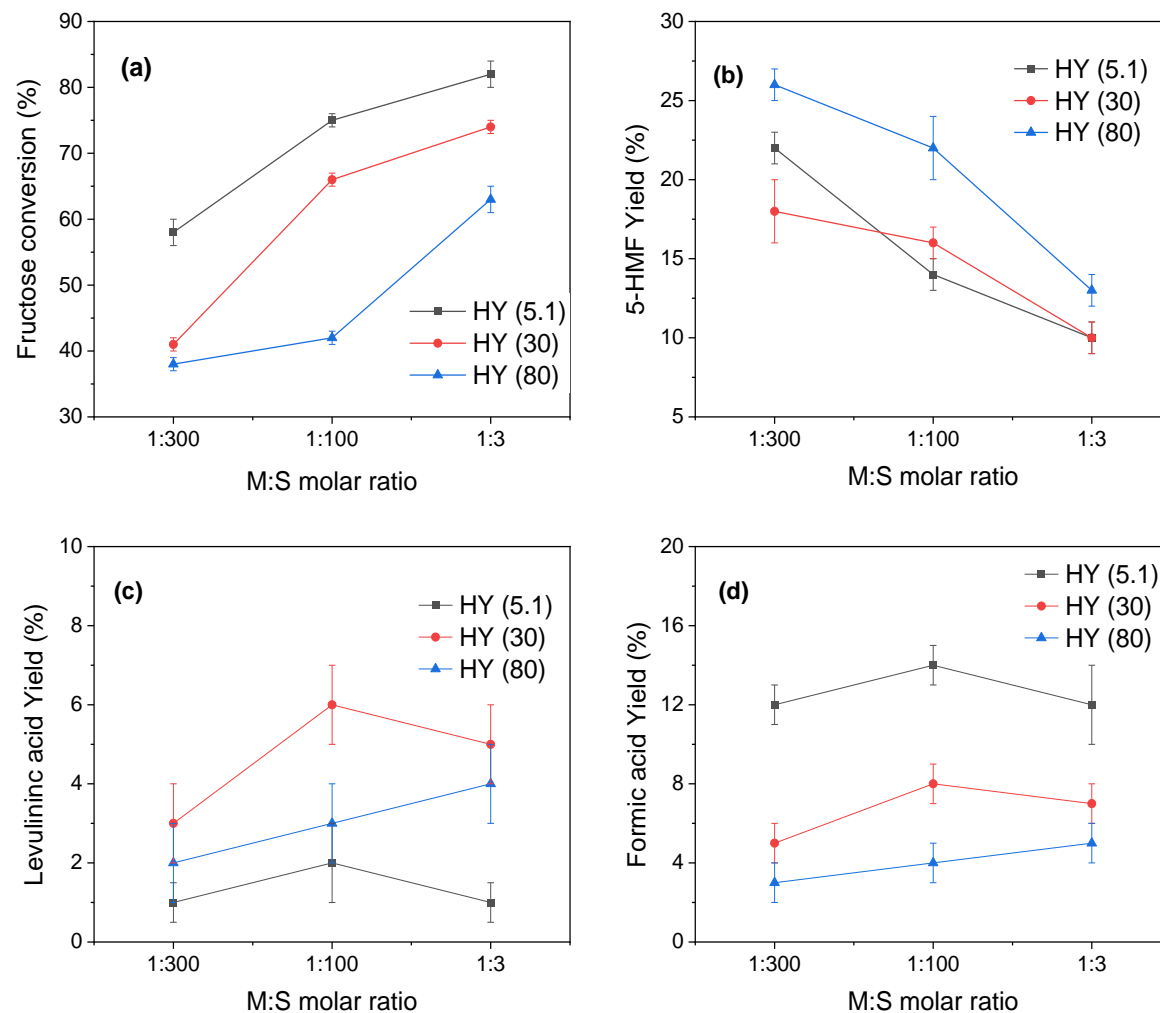


Figure 6.7. **a)** Fructose conversion, **b)** 5-HMF yield, **c)** levulinic acid yield, and **d)** formic acid yield when using undoped HY zeolite catalysts with different $\text{SiO}_2:\text{Al}_2\text{O}_3$ molar ratios of 5.1, 30, and 80 (5 mL of $100 \text{ g}\cdot\text{L}^{-1}$ fructose solution, M:S in the range of 1:3 – 1:300, 140°C , 2h, endogenous pressure, and 700 rpm). Experimental errors are reported as the standard deviations of three repeated measurements.

At first, the reaction was carried out at M:S of 1:3 as considered more representative of a molar ratio of 1:1 between the homogeneous catalyst of HCl and the heterogeneous catalyst of HY zeolite. This showed high fructose conversions of 63%, 74%, and 82% for HY (80), HY (30) and HY (5.1), respectively, with the latter being consistent with the conversion obtained by HCl under similar reaction conditions. However, at this metal-to-substrate ratio, a low carbon mass balance of ($\leq 35\%$) was detected (Table A16 in Appendix A.13), leading to low yields of 5-HMF, LA and FA up to 15%, 5%, and 12%, respectively (Figure 6.7b – d). This would be indicative of either the formation of insoluble organic polymer humins or the decomposition of formic acid to carbon dioxide and water. However, a decrease in M:S molar ratio to 1:100 and 1:300 leads to a gradual increase of 12% in 5-HMF yields (Figure 6.7b). Furthermore, no increase in equimolar levulinic and formic acid yields was simultaneously observed, suggesting that sequential decomposition of 5-HMF was not favoured at a low M:S molar ratio of 1:300 under our reaction condition.

The ratio of Brønsted to Lewis acid sites has proven to play a crucial role in determining the production of 5-HMF from sugar molecules⁴⁴. In order to investigate different heterogeneous systems using zeolite-based materials, HY doped with 1wt% of Sn, Ga, Nb, or Fe - here denoted as Sn/Y, Ga/Y, Nb/Y, and Fe/Y, respectively, were synthesised and their catalytic performance was tested for the reaction of fructose dehydration to 5-HMF. Since a multi-functional catalyst offers substantial advantages compared to a single-function catalyst, it would be advantageous to test the catalytic activity of Sn, Ga, and Nb-doped zeolite Y for reactions beyond the isomerisation of glucose to fructose. In principle, the concept of multi-functional catalysts refers to catalysts containing multiple active sites, some of which can catalyse a specific reaction, and other parts capable of catalysing another reaction, which results in

materials with catalytic performance unattainable with traditional single-functional catalysts⁴⁵. The incorporation of metals (e.g., Sn, Ga, and Nb) acting as Lewis acid sites can facilitate the catalytic isomerisation of glucose to fructose, whereas the Brønsted acid function, that is, tetra-coordinated aluminium sites (Al^{IV}) with bridging OH groups in the zeolite framework, can dehydrate fructose to produce 5-HMF⁴⁶. In addition to the metals that have been tested in previous chapters, iron-based compounds have gained significant attention as solid acid catalysts to catalyse the conversion of hexose sugars (e.g., glucose and fructose) to 5-HMF and levulinic acid due to their relatively low cost and toxicity⁴⁷. For example, Fe/Y have previously been shown to promote the catalytic conversion of glucose to levulinic acid under mild conditions, leading to a yield value of 62% at 180 °C after a reaction time of 180 min⁴⁸. Therefore, it would be valuable to test such a catalyst for fructose dehydration to 5-HMF under our specified reaction conditions. The results of these catalytic tests are reported in detail in (Table 6.3).

Table 6.3. Catalytic tests for the fructose dehydration to 5-HMF in water using 1wt% of Sn/Y, Ga/Y, Nb/Y, and Fe/Y catalysts. The tests were carried out using 500 mg of the substrate in 5 mL of H₂O at 140 °C for 2 h and endogenous pressure with an M:S molar ratio of 1:300. Experimental errors are reported as the standard deviations of three repeated measurements.

SiO ₂ :Al ₂ O ₃ molar ratio	Catalyst	Fructose conversion (%)	Selectivity (%)			CMB (%)
			5-HMF	LA	FA	
5.1	HY	58 ± 4	65 ± 2	1 ± 1	35 ± 2	58 ± 3
	Sn/Y	68 ± 3	60 ± 1	4 ± 1	36 ± 2	52 ± 2
	Ga/Y	48 ± 4	69 ± 1	1 ± 1	29 ± 2	73 ± 4
	Nb/Y	58 ± 2	64 ± 2	3 ± 1	32 ± 2	62 ± 2
	Fe/Y	60 ± 2	69 ± 1	2 ± 1	29 ± 1	60 ± 3
80	HY	38 ± 4	84 ± 2	6 ± 1	11 ± 2	83 ± 4

Sn/Y	61 ± 1	81 ± 1	7 ± 1	12 ± 1	70 ± 2
Ga/Y	72 ± 3	76 ± 1	7 ± 1	18 ± 1	55 ± 4
Nb/Y	69 ± 1	82 ± 1	7 ± 2	12 ± 2	64 ± 2
Fe/Y	52 ± 4	90 ± 1	2 ± 1	8 ± 1	79 ± 1

In particular, when the reaction is carried out over zeolite Y with a SiO₂:Al₂O₃ molar ratio of 5.1, it would seem that the introduction of metal dopant has a trivial effect compared to a non-doped material, at the reaction conditions used, with maximum 5-HMF yield of 25% (Table A17 in Appendix A.13) at around 60% fructose conversion. Carbon mass balance in the range of 60% was also obtained for all catalysts at this SiO₂:Al₂O₃ molar ratio, more likely due to the decomposition of formic acid to carbon dioxide and water⁴⁹. However, there seem to be differences in the case of Ga/Y (5.1) with a carbon mass balance of 73%, possibly due to their distinct Lewis acidity characteristic.

In contrast, there was an apparent effect with a significant increase in the fructose conversion in the case of metal dopant on the zeolite support with a SiO₂:Al₂O₃ molar ratio of 80. The use of zeolite Y at this SiO₂:Al₂O₃ molar ratio resulted in an increase of 20% in the 5-HMF selectivity. Also, there was a considerable increase in carbon mass balance compared to those obtained at a higher SiO₂:Al₂O₃ molar ratio, except Ga/Y, which revealed a decrease in carbon mass balance from 75% to 55% when a SiO₂:Al₂O₃ molar ratio of 80 was used, probably promoting the formation of insoluble undesirable humins being facilitated via strong Lewis acid sites due to the presence of Ga species within zeolite Y framework (see section 4.7.1 in Chapter 4). Furthermore, it was observable that the metal dopant could express Lewis acidity when less acidic zeolite Y with a SiO₂:Al₂O₃ molar ratio of 80. For instance, Sn-, Ga, Nb- and Fe-doped zeolite Y (80) showed a molar ratio of the metal dopant with respect

to Al centres of 2.13, 3.62, 2.72, and 4.57, respectively, compared with 0.17, 0.29, 0.22, and 0.36 for Sn-, Ga, Nb- and Fe-doped zeolite Y (5.1).

Although fructose dehydration to 5-HMF, in principle, is Brønsted acid sites dependent. From our data, the reaction proved to be more selective towards the production of 5-HMF over undoped and doped zeolite Y catalysts possessing less Brønsted acidity at a molar SiO₂:Al₂O₃ ratio of 80 with Fe/Y (80), showing the highest 5-HMF selectivity of 90%, resulting in the highest 5-HMF yield of 37% based on carbon mass balance (Table A17 in Appendix A.13) among all catalysts studied. These results prompted us to study and identify possible acidity-activity correlations for these catalysts by the mean of Brønsted acidity measurements and assess if any ion exchange or distortion of the zeolite could have occurred as a consequence of the preparation method used by powder XRD analysis.

Furthermore, the reaction was also carried out at a higher M:S molar ratio of 1:100 (Table 6.4). It was observed that increasing M:S molar ratio led to a decrease in 5-HMF selectivity and comparatively an increase in levulinic and formic acid selectivity.

Table 6.4. Catalytic tests for the fructose dehydration to 5-HMF in water using 1wt% of Sn/Y, Ga/Y, Nb/Y, and Fe/Y catalysts. The tests were carried out using 500 mg of the substrate in 5 mL of H₂O at 140 °C for 2 h and endogenous pressure with an M:S molar ratio of 1:100. Experimental errors are reported as the standard deviations of three repeated measurements.

SiO ₂ :Al ₂ O ₃ molar ratio	Catalyst	Fructose conversion (%)	Selectivity (%)			CMB (%)
			5-HMF	LA	FA	
5.1	HY	75 ± 1	46 ± 2	8 ± 2	46 ± 2	40 ± 1
	Sn/Y	92 ± 2	32 ± 2	6 ± 1	62 ± 2	36 ± 3
	Ga/Y	79 ± 2	48 ± 1	8 ± 1	43 ± 1	37 ± 1
	Nb/Y	80 ± 3	46 ± 1	5 ± 2	49 ± 2	32 ± 2

	Fe/Y	42 ± 1	38 ± 2	11 ± 1	50 ± 2	100 ± 1
80	HY	42 ± 1	75 ± 1	11 ± 1	13 ± 1	70 ± 1
	Sn/Y	55 ± 2	59 ± 1	15 ± 2	26 ± 2	81 ± 2
	Ga/Y	66 ± 1	63 ± 2	11 ± 2	26 ± 1	60 ± 2
	Nb/Y	62 ± 3	65 ± 1	13 ± 1	22 ± 1	73 ± 3
	Fe/Y	39 ± 2	87 ± 2	4 ± 1	8 ± 2	89 ± 2

6.4.1. Brønsted acidity measurements.

Due to the importance of Brønsted acidity to correlate our data, the Brønsted acidity of all catalysts was measured in order to identify potential correlations between Brønsted acidity and catalytic activity. In this regard, the total Brønsted acidity was measured using a back-titration protocol (described in section 2.7.2.1 in the experimental chapter).

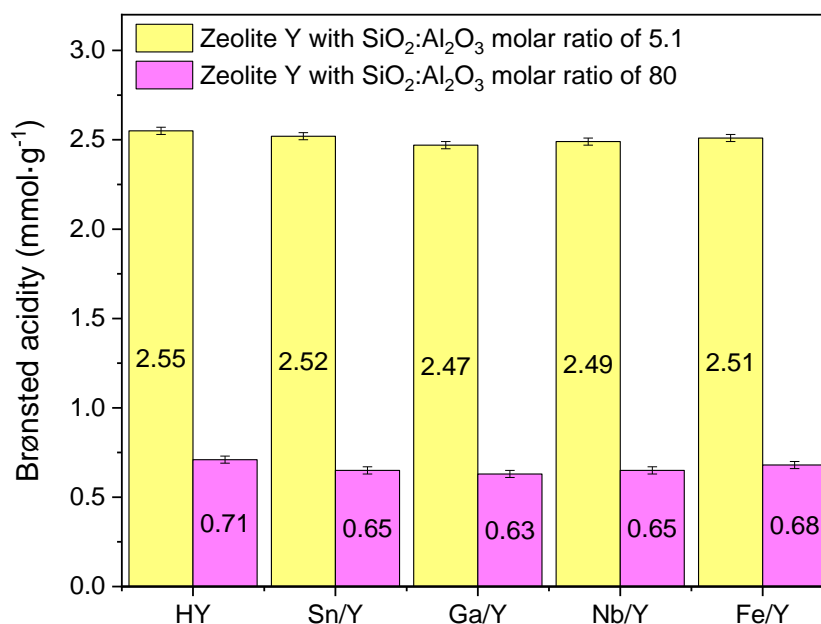


Figure 6.8. Total Brønsted acidity of HY, Sn/Y, Ga/Y, Nb/Y, and Fe/Y with different silica-to-alumina molar ratios of 5.1 and 80, determined by acid-base back-titrations. There is a direct correlation between the Brønsted acidity values and the amount of Al species within the catalyst. Experimental errors are expressed as the standard deviations of three repeated measurements.

Our back titration measurements show a decrease in Brønsted acidity upon the metal doping step (Figure 6.8). This decrease was consistent, in theory, with a decrease in Brønsted acidity associated with the formation of basic metal oxides. It should be noted, however, that the difference between these values is within the experimental error of our method (ca. $0.02 \text{ mmol}\cdot\text{g}^{-1}$). Therefore, we do not consider this difference to be statistically significant.

Given possible acidity-activity correlations, the catalytic activity of zeolites (5.1) was a function of total Brønsted acidity, with the catalyst possessing the highest Brønsted acidity being the most active in terms of fructose conversion. Furthermore, the same observations were found concerning 5-HMF selectivity and yields, except for HY, following an opposite trend. Similar findings were reported in the literature⁴⁸, which was explained by catalytic activity being more comparable in terms of the acid sites per unit surface area rather than the ratio of Brønsted to Lewis acid sites. In contrast, the catalytic activity of zeolites (80) was not found to be a function of total Brønsted acidity. The catalyst with the highest Lewis acidity was instead the most active in terms of fructose conversion. On a *per-site* basis, the fructose conversion decreased as follows: Ga/Y > Nb/Y > Sn/Y > Fe/Y > HY. An increase in the relative number of Brønsted to Lewis acid sites leads to a decrease in the catalytic activity. In contrast, the 5-HMF selectivity showed an opposite trend compared to fructose conversion. Consequently, the catalyst with the highest catalytic activity in terms of fructose conversion shows the lowest selectivity for 5-HMF production. Weingarten et al. reported similar results in the aqueous-phase dehydration of xylose to furfural⁴⁴.

6.4.2. Powder X-ray diffraction.

In order to obtain structural information regarding our catalysts, powder XRD patterns were collected for zeolite HY, Sn/Y, Ga/Y, Nb/Y, and Fe/Y with $\text{SiO}_2:\text{Al}_2\text{O}_3$ molar ratio of 5.1 and 80 (Figures 6.9 and 6.10) in order to characterise the crystalline structure of the prepared catalysts and to determine if any ion exchange or distortion of the zeolite could have resulted from the preparation procedure used. A Rietveld refinement⁵⁰ was performed (Tables 6.5 and 6.6). As shown in the XRD patterns, Sn/Y, Ga/Y, Nb/Y, and Fe/Y exhibit virtually identical patterns and no significant expansion or contraction of the unit cell volume has been observed as a result of variations in the unit cell volume of the parent zeolite HY (calculated values 14757 \AA^3 for HY (5.1) and 14219 \AA^3 for HY (80)). Based on these data, it is unlikely that Sn, Ga, Nb, or Fe would be incorporated into the zeolite framework in place of Al - at least within the resolution of the acquired PXRD patterns.

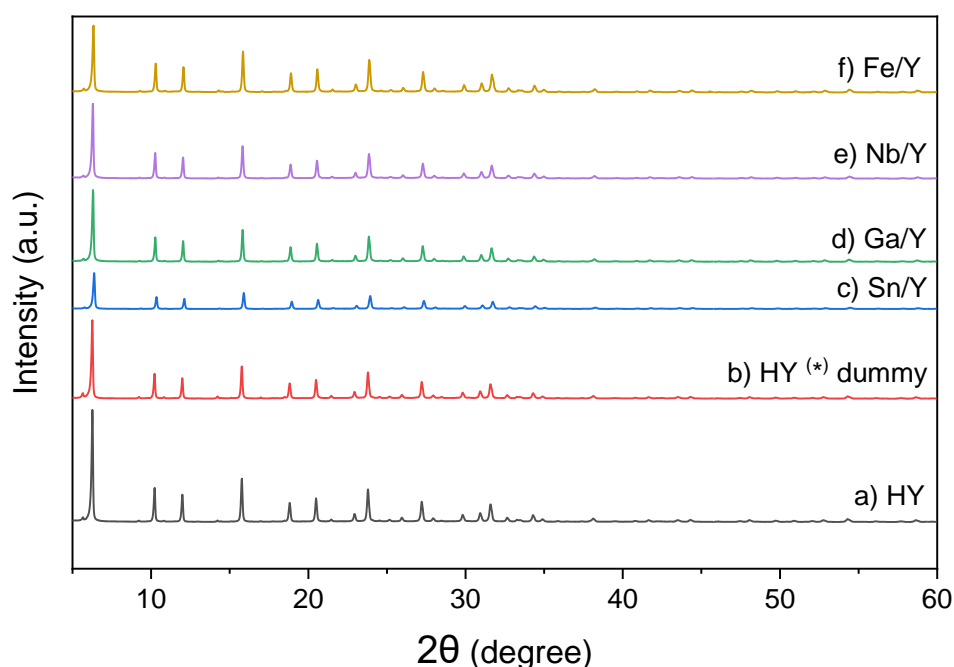


Figure 6.9. X-ray powder diffraction patterns for zeolites with a $\text{SiO}_2:\text{Al}_2\text{O}_3$ molar ratio of 5.1: (a) HY as delivered, (b) HY treated as for metal deposition but without any metal dopant, (c)

Sn/Y, (d) Ga/Y, (e) Nb/Y, and (f) Fe/Y. No metal or metal oxide cluster from Sn, Ga, Nb or Fe is detected, and all zeolites present a virtually identical pattern.

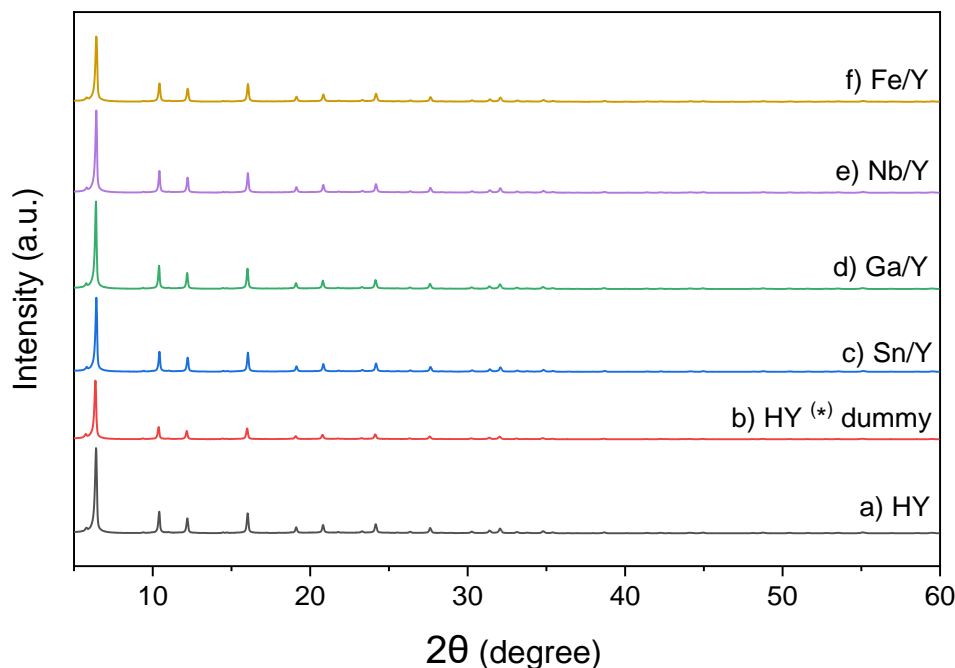


Figure 6.10. X-ray powder diffraction patterns for zeolites with a $\text{SiO}_2:\text{Al}_2\text{O}_3$ molar ratio of 80: (a) HY as delivered, (b) HY treated as for metal deposition but without any metal dopant, (c) Sn/Y, (d) Ga/Y, (e) Nb/Y, and (f) Fe/Y. No metal or metal oxide cluster from Sn, Ga, Nb or Fe is detected, and all zeolites present a virtually identical pattern.

It is important to note that even though Sn, Ga, Nb and Fe were indicated to be present as SnO_2 , Ga_2O_3 , Nb_2O_5 , and Fe_2O_3 , no characteristic reflections associated with these metal oxides were observed. For SnO_2 ⁵¹, these were expected to be at 26.6, 37.8 and 51.8° 2θ for the reflections of (110), (200), and (211), respectively, for $\beta\text{-Ga}_2\text{O}_3$ ⁵² at 31.2°, 35.9° and 38.1° 2θ , for the reflections (222), (400) and (411) respectively, for the orthorhombic phase of Nb_2O_5 ⁵³ at 22.7, 28.6, 36.7, 46.2, 50.7 and 55.3° 2θ for the reflections of (001), (180), (200), (181), (002), (380), and (212) respectively, and for $\alpha\text{-Fe}_2\text{O}_3$ ⁵⁴ at 24.2, 33.2, 35.7, 40.9, 49.5, 54.2, and 57.7° 2θ for reflections of (012), (104), (110), (113), (024), (116), and (018) respectively.

Aside from the structure and bulk chemical composition, it is essential to know the unit cell parameter (acquired from XRD data) of Sn, Ga, Nb, and Fe-doped zeolite Y catalysts prepared via wetness impregnation technique in order to identify the metal-zeolite interactions. Several studies have demonstrated that metal might be deposited over the surface of zeolite or trapped within its framework, wherein the two types of metal-zeolite interactions result in different catalytic performances^{55,56}. The substitution of metal in place of Al sites within the zeolite matrix is generally indicated by the unit cell's expansion or contraction based on the metal's size (in our case, Sn, Ga, Nb, and Fe) compared to Al. In contrast, the percentage of expansion or contraction is, to some extent, dependent on the number of metal atoms being incorporated into the zeolite⁵⁷. For instance, due to the larger size of Sn in its ionic form and coordination compared to Al, an increase in the unit cell's volume expansion indicates the successful incorporation of this metal into structural sites⁵⁸. However, no expansion of the unit cell was observed with our Sn/Y catalysts (Tables A17 and A18 in Appendix A.14), indicating that the Sn species of our catalysts prepared by wetness impregnation were not embedded into the framework of these zeolite catalysts but instead were supported on their surface or within their pores/channels. Identical observations to Sn/Y were found regarding the expansion or contraction of the unit cell of Ga, Nb, and Fe doped on both zeolites Y at SiO₂:Al₂O₃ molar ratios of 5.1 and 80. However, a strong contraction of -3.6% of HY with a SiO₂:Al₂O₃ molar ratio of 80 with respect to HY with a SiO₂:Al₂O₃ molar ratio of 5.1 was detected, which corresponds to the dealumination fact practically, it is as there is less Al in this catalyst.

6.5. Glucose and Fructose dehydration to 5-HMF using pure metal oxides as heterogeneous catalysts.

Given the importance of the acidity characteristic in this research work and to gather additional information on the roles of Brønsted and Lewis acid sites in reactions beyond glucose isomerisation. Glucose and fructose dehydration reactions were carried out over CeO_2 , MoO_3 , La_2O_3 , WO_3 , Nb_2O_5 and TiO_2 in their bulk metal oxide forms in order to prove the concept that Brønsted and Lewis acid sites are essential characteristics to convert these sugar molecules to desirable 5-HMF. Since these metal oxides exhibit different acidity characteristics at their surface levels, they should behave differently in terms of their reactivity toward the formation of 5-HMF. For instance, CeO_2 can rapidly interchange in the oxidation state ($\text{Ce}^{4+} \rightleftharpoons \text{Ce}^{3+}$)⁵⁹, which results in the release of oxygen, and the reaction to undergo an oxidation step⁶⁰; thus, a high conversion would be expected in this case, but toward an undesirable carboxylic acid product (Figure 6.11).

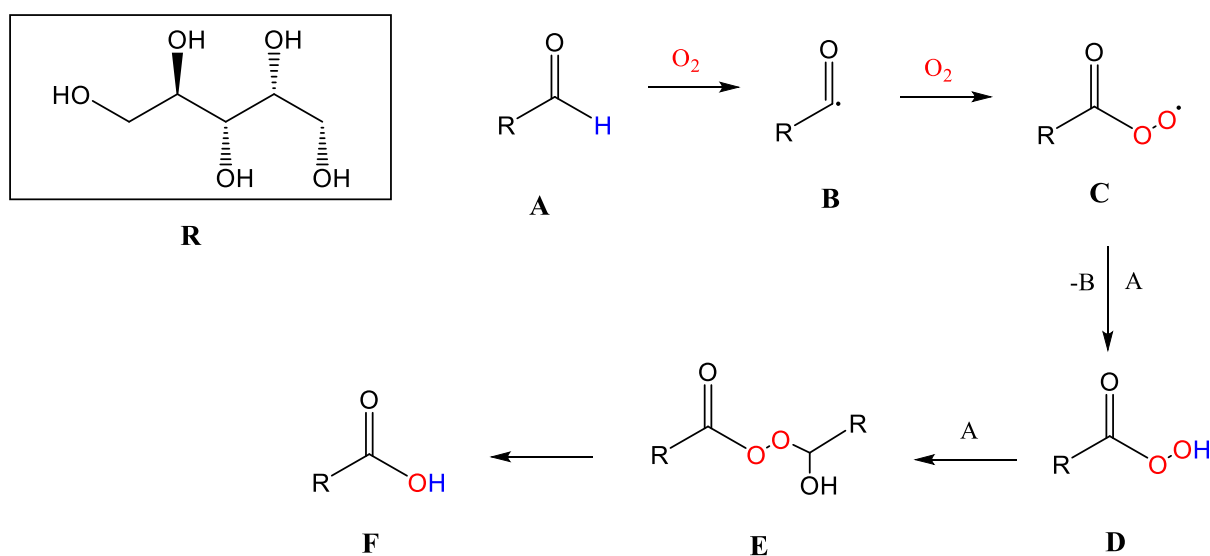


Figure 6.11. Schematic representation of the chemical mechanism of aldehyde oxidation reaction with oxygen to form a carboxylic acid. The reaction proceeds through the initial

hydrogen atom abstraction (HAA) from an aldehyde **A** to form acyl radical **B**. A subsequent reaction between **B** and O₂ results in the formation of acyl peroxy radical **C**. HAA from a second equivalent of **A** leads to the formation of peracid **D** and chain carrier **B**. Using intermediate **E**, peracid **D** is converted to carboxylic acid **F** via a Baeyer-Villiger reaction⁶¹.

In contrast, transition metal oxides such as MoO₃, La₂O₃, WO₃, and Nb₂O₅ typically possess both Lewis acid sites (coordinatively unsaturated sites) and Brønsted acid sites (acidic hydroxyl group on the surface of the bare oxide), making them suitable for heterogeneous pathway reaction of glucose and fructose dehydration to 5-HMF^{62,63}. For example, niobium pentoxide (Nb₂O₅) possesses an Nb-O bond that is highly polarised in distorted NbO₆ octahedra and NbO₄ tetrahedra, which in turn leads to both Brønsted acid sites (surface OH group) and Lewis acidic sites (coordinately unsaturated Nb⁵⁺) within its distorted polyhedron structure⁶⁴. whereas the Brønsted and Lewis acid sites on the surface of molybdenum trioxide (MoO₃) are presented in the form of the octahedrally coordinated MoO₃ species⁶⁵ and Mo-OH⁶⁶, respectively. The bare lanthanum oxide (La₂O₃) metal oxide exhibits Brønsted acid sites (surface OH group)⁶⁷ and Lewis acid sites (unsaturated La³⁺ and La³⁺-OH sites)⁶⁸. In addition, tungsten trioxide (WO₃) contains coordinatively unsaturated W⁶⁺ species acting as Lewis acid sites and terminal W-O bonds that can be protonated easily to form terminal hydroxyl groups (-OH) on its surface, which serve as Brønsted acid sites⁶⁹. On the other hand, rutile titanium dioxide (TiO₂) was reported to have a low amount and density of acidic sites (15 μmol·g⁻¹ and 2.5 μmol·m², respectively)⁷⁰. Consequently, it would be expected not to show any reactivity to obtain 5-HMF. The catalytic results of glucose and fructose dehydration reactions to 5-HMF over pure metal oxides are presented in (Figures 6.12 – 6.15).

6.5.1. Glucose dehydration to 5-HMF.

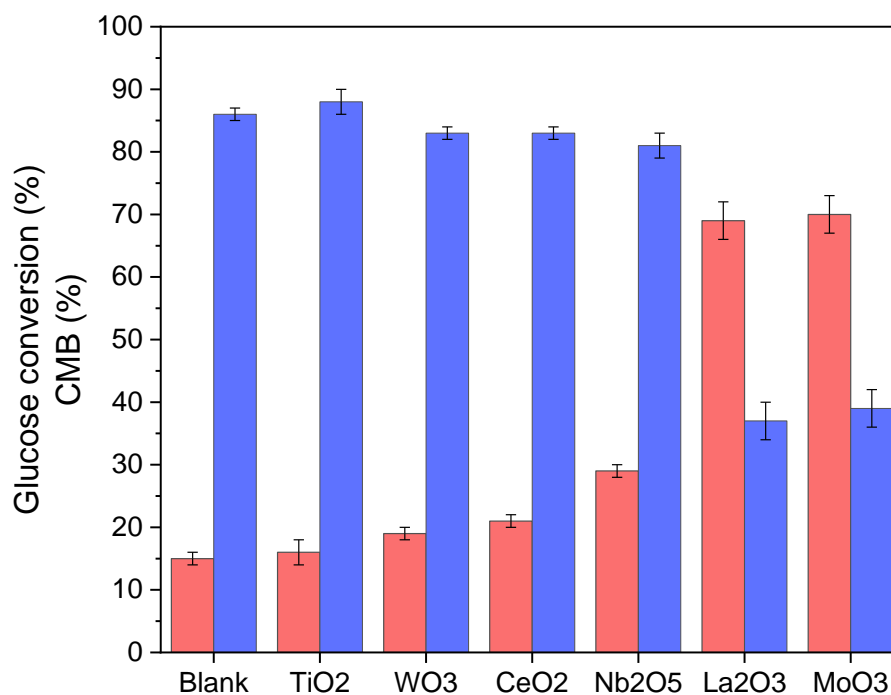


Figure 6.12. Glucose conversion (●) and carbon mass balance (●) were obtained from the dehydration reaction of glucose to 5-HMF, which was carried out by using various pure metal oxides (5 mL 100 g·L⁻¹ fructose solution, M:S of 1:10, 140 °C, 2h, endogenous pressure, 700 rpm). The blank sample represents reaction conduction in the absence of the catalyst. Experimental errors are reported as the standard deviations of three repeated measurements.

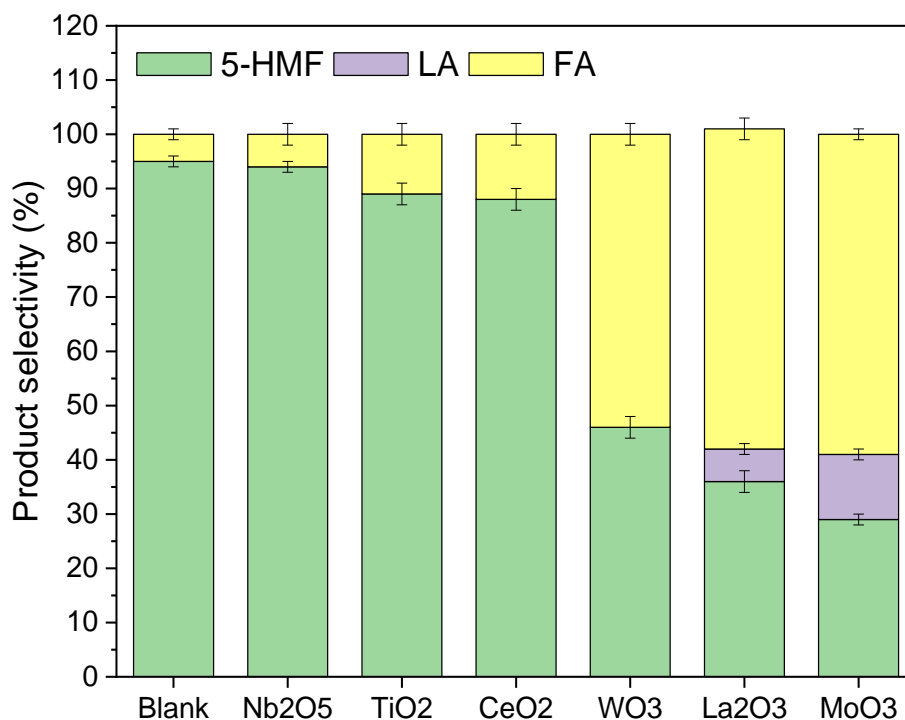


Figure 6.13. Observed product selectivity of 5-hydroxymethylfurfural (5-HMF), levulinic acid (LA) and formic acid (FA) obtained from the dehydration reaction of glucose to 5-HMF, which was carried out by using various pure metal oxides (5 mL 100 g·L⁻¹ fructose solution, M:S of 1:10, 140 °C, 2h, endogenous pressure, 700 rpm). The blank sample represents reaction conduction in the absence of the catalyst.

The dehydration of glucose to 5-HMF was studied in the presence of different metal oxides (Figures 6.12 and 6.13). The performance of the blank test was examined to assess the reactivity of these metal oxides since this might also contribute to the conversion of glucose into 5-HMF. However, under our reaction conditions, a glucose conversion of 15% was detected when no catalyst was used, which could be obtained as a result of the acidity of the water at 140 °C (Figure 6.12). As compared to the blank test in the absence of a catalyst, TiO₂, WO₃, and CeO₂ showed no improvement in the catalytic activity. In contrast, the presence of Nb₂O₅ enhanced glucose conversion by up to 29%. In addition, La₂O₃ and MoO₃ were both found to be highly active, exhibiting a glucose conversion of 70%, but this was toward other by-products, mainly formic

acids (Figure 6.13). Furthermore, incomplete carbon mass balance was also observed with these metal oxides, indicating the presence of consecutive rehydration reactions toward formic acid and its sequential decomposition to carbon dioxide and water. On the other hand, Nb₂O₅, TiO₂, WO₃, and CeO₂ showed no detectable levulinic acid and only a small amount of formic acid (< 15%). However, with WO₃, only 5-HMF and formic acid were formed with selectivity values of 46% and 54%, respectively.

To conclude, the catalytic activity toward the formation of 5-HMF from glucose decreased in the following order: Nb₂O₅ > CeO₂ > WO₃ > La₂O₃ > MoO₃ > TiO₂, with Nb₂O₅ showing the highest catalytic activity with 5-HMF yields of 21% (Table 6.7). However, all of these metal oxides did not show any promising results in catalysing the dehydration reaction of glucose to 5-HMF compared to the reaction carried out in the absence of a catalyst.

Table 6.7. Product **yields** of 5-hydroxymethylfurfural (5-HMF), levulinic acid (LA) and formic acid (FA) obtained from the dehydration reaction of glucose to HMF, which was carried out by using various pure metal oxides (5 mL 100 g·L⁻¹ fructose solution, M:S of 1:10, 140 °C, 2h, endogenous pressure, 700 rpm). The blank sample represents reaction conduction in the absence of the catalyst.

Catalyst	Yield (%)		
	5-HMF	levulinic acid	formic acid
Blank	12	n.d.	4
Nb ₂ O ₅	22	n.d.	1
TiO ₂	13	n.d.	2
CeO ₂	15	n.d.	2
WO ₃	7	n.d.	9
La ₂ O ₃	9	1	15
MoO ₃	8	1	16

6.5.2. Fructose dehydration to 5-HMF.

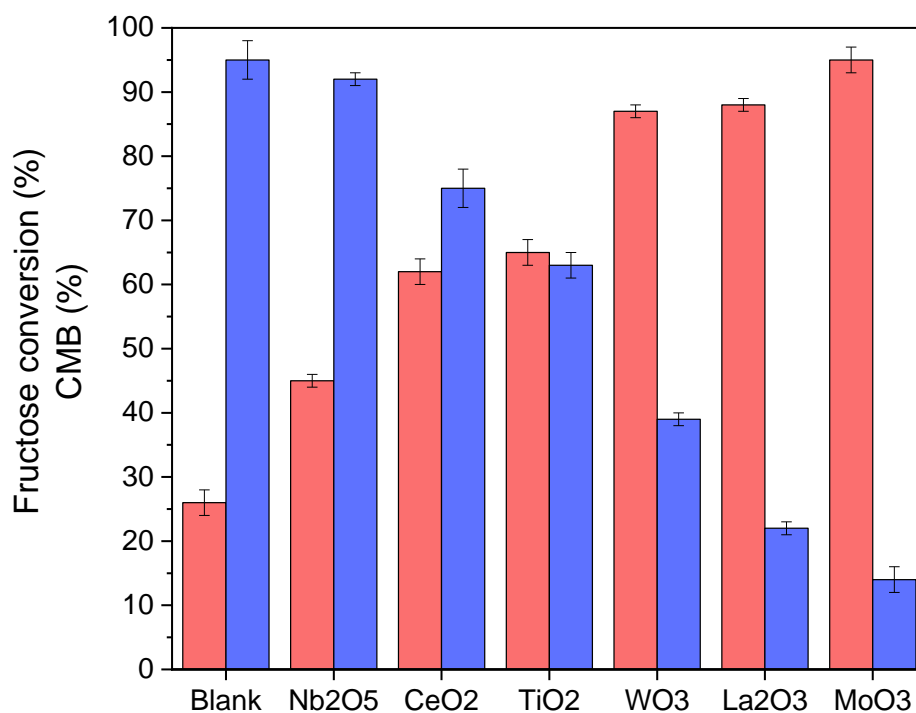


Figure 6.14. Fructose conversion (●) and carbon mass balance (●) obtained from the dehydration reaction of fructose to 5-HMF, which was carried out by using various pure metal oxides (5 mL 100 g·L⁻¹ fructose solution, M:S of 1:10, 140 °C, 2h, endogenous pressure, 700 rpm). The blank sample represents reaction conduction in the absence of the catalyst. Experimental errors are reported as the standard deviations of three repeated measurements.

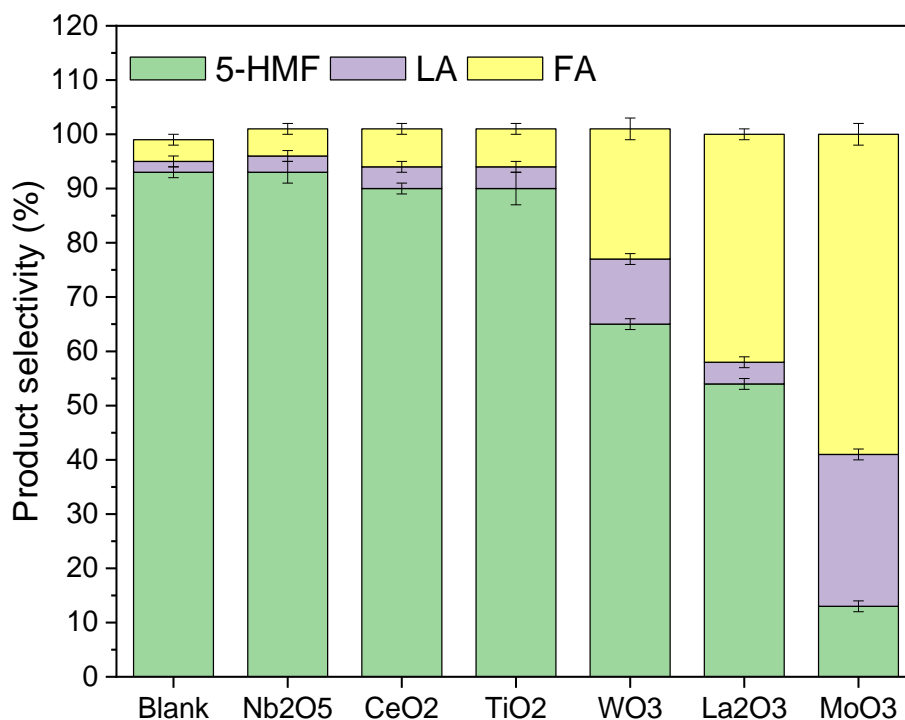


Figure 6.15. Observed product selectivity of 5-hydroxymethylfurfural (5-HMF), levulinic acid (LA) and formic acid (FA) obtained from the dehydration reaction of fructose to 5-HMF, which was carried out by using various pure metal oxides (5 mL 100 g·L⁻¹ fructose solution, M:S of 1:10, 140 °C, 2h, endogenous pressure, 700 rpm). The blank sample represents reaction conduction in the absence of the catalyst.

As expected, using fructose as feedstock significantly promoted the dehydration reaction toward 5-HMF⁷¹ (see Figure 6.1). In particular, a fructose conversion of 26% was observed when no catalyst was used under the same reaction conditions used with glucose dehydration. However, this was dramatically enhanced when pure metal oxides were used as catalysts, showing fructose conversions in the range of 45% - 95% (Figure 6.14). However, this increase in the conversion was paralleled by a gradual decrease in the carbon mass balance for all metal oxides (Figure 6.14). In this regard, carbon mass balance (CMB) values of ($\leq 75\%$) were observed, except for Nb₂O₅, which showed a CMB of 92%, consistent, within the experimental error, with the that obtained from the blank test. As a result, Nb₂O₅ appears to be the most

selective catalyst toward the formation of 5-hydroxymethylfurfural (5-HMF) among all metal oxides studied herein. In comparison with the blank test in the absence of a catalyst, Nb₂O₅, CeO₂, and TiO₂ did not affect the formation of 5-HMF with 90% selectivity obtained (Figure 6.15), and a similar product distribution with a slight but detectable increase in the Formic acid (FA) selectivity with CeO₂ and TiO₂. In contrast, a significant decrease in the 5-HMF selectivity, accompanied by an increase in the selectivity of equimolar levulinic acid (LA) and formic acid (FA), was observed for WO₃, La₂O₃ and MoO₃, with the latter being the most selective toward the sequential rehydration toward other by-products of LA and FA acids. In general, the catalytic activity toward the formation of 5-HMF from fructose decreased in terms of yield as follows: CeO₂ > Nb₂O₅ > TiO₂ > WO₃ > La₂O₃ > MoO₃, with CeO₂, Nb₂O₅ and TiO₂ showing the highest catalytic activity with yields of 42%, 39%, and 37% respectively (Table 6.8). It is also obvious that glucose has been found to be a relatively inert molecule in dehydration toward 5-HMF with conversion values of (\leq 20%), primarily due to the high stability of its 6-membered ring structure. Alternatively, fructose, an isomer of glucose with a 5-membered ring, proved to be more thermodynamically favourable toward the formation of 5-HMF via a dehydration reaction, showing conversions in the range of (45 - 90%), which is due to the fact that the C-2-OH group within this molecule can easily be protonated, leading to the stabilization of the furanic ring and, in turn, promoting the dehydration step toward the formation of 5-HMF⁷¹.

Table 6.8. product yields of 5-hydroxymethylfurfural (5-HMF), levulinic acid (LA) and formic acid (FA) obtained from the dehydration reaction of fructose to 5-HMF, which was carried out by using various pure metal oxides (5 mL 100 g·L⁻¹ fructose solution, M:S of 1:10, 140 °C, 2h, endogenous pressure, 700 rpm). The blank sample represents reaction conduction in the absence of the catalyst.

Catalyst	Yield (%)		
	5-HMF	levulinic acid	formic acid
Blank	23	0	4
Nb ₂ O ₅	39	1	2
CeO ₂	42	2	3
TiO ₂	37	2	3
WO ₃	22	4	8
La ₂ O ₃	10	0	8
MoO ₃	2	1	8

In general, the catalytic activity of the metal oxides studied did not show any predictable trend for their acidity characteristics. Probably as multiple and sometimes opposite factors are operating simultaneously. For example, most of these metal oxides were used in the form of very light and fine powders, which could lead to the diffusion of the substrate to the surface of the catalyst from mass transfer limitations in liquid reactions^{48,72}. On the other hand, the finer the powder, the higher the total surface area. In this context, the use of bulk metal oxides in the form of pellets of given diameters could be considered as a future work.

6.5.3. Control test for external mass transfer limitations

In order to rule out any diffusion effect from external mass transfer limitations discussed in previous sections (6.5.1 and 6.5.2), a control test on the effect of the stirring rate and the amount of catalyst to conversion is systematically studied for Nb₂O₅ as the material showing the highest carbon mass balance and in turn the lowest formation of by-products. In this regard, catalytic tests using varying mixing stirring

rates in the range of 200 to 1000 rpm did not show any effect for both glucose and fructose dehydration reactions, meaning that no diffusion limitation is associated, and a kinetic regime governs the reaction in this case. On the other hand, a change in M:S ratio from 1:20 to 2:1 showed significantly different results in the dehydration reaction of fructose (Figure 6.16). As can be seen, the fructose conversion is increasing per increased number of active centres, which also indicates that the reaction is carried out under a kinetic regime, and the external diffusion limitation effects (mass transfer) are negligible. However, a change in M:S ratio from 1:20 to 2:1 resulted in constant glucose conversions of 25% (Figure 6.17) within the experimental error. This could be either due to diffusion limitation, or the glucose conversion is already at maximum.

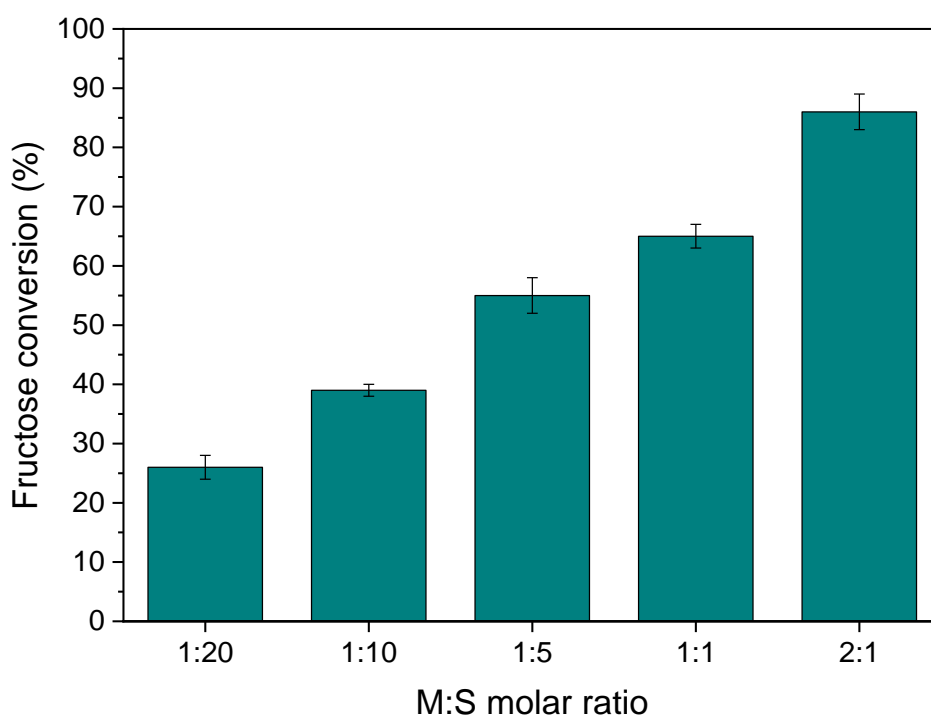


Figure 6.16. Representative diffusion (external mass transfer) control test for the effect on fructose conversion by varying a metal-to-substrate molar ratio for Nb_2O_5 for a reaction in water (5 mL $100 \text{ g}\cdot\text{L}^{-1}$ fructose solution, M:S of 1:10, $140 \text{ }^\circ\text{C}$, 2h, 700 rpm).

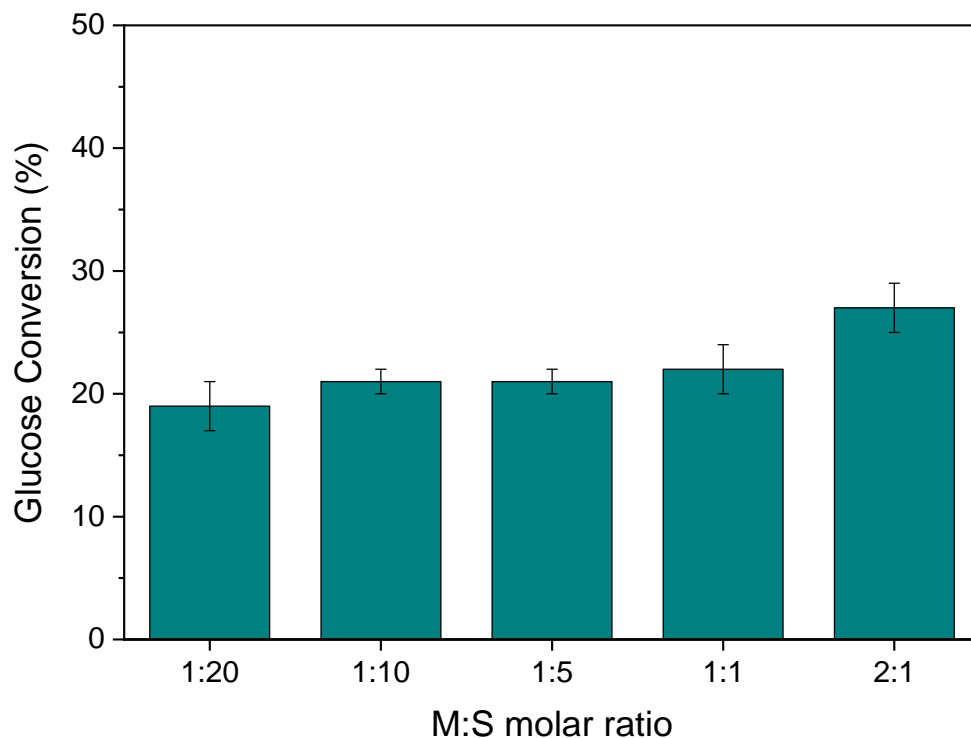


Figure 6.17. Representative diffusion (external mass transfer) control test for the effect on glucose conversion by varying a metal-to-substrate molar ratio for Nb_2O_5 for a reaction in water (5 mL $100 \text{ g}\cdot\text{L}^{-1}$ fructose solution, M:S of 1:10, 140°C , 2h, 700 rpm).

6.6. Glucose and fructose dehydration to 5-HMF using metal oxide-doped zeolite Y as a heterogeneous catalyst.

In view of their results reported in section 6.5, metal oxides of CeO_2 , Nb_2O_5 and TiO_2 were selected to be further doped on zeolite Y ($\text{SiO}_2:\text{Al}_2\text{O}_3$ molar ratio of 80) using a sol-gel protocol described in (Section 2.2.2) with the aim of enhancing the formation rate of desired HMF from glucose and fructose. In principle, the dispersion of metal oxides on zeolite supports would result in numerous advantages, including a larger surface area, which would increase the number of active sites available for the catalytic reaction, improve the accessibility of the surface-active site, which can improve catalytic activity and selectivity since metal oxides are commonly found on

the surface of zeolites either in the form of nanoparticles or clusters and also afford good resistance to sintering, which can decrease the active surface area and, in turn, decrease the catalytic activity. Furthermore, compared to bare metal oxides, zeolite supports can offer a confined environment for metal oxide, which can affect the product selectivity of catalytic reactions. For example, the pores of zeolites differ in size and shape, which can affect the adsorption and reaction of certain molecules⁷³. In this context, glucose and fructose dehydration reactions were carried at a reaction temperature of 140 °C for a reaction time of 2 h, endogenous pressure, and M:S molar ratios of 1:100 and 1:300. The conversion of glucose and fructose and the selectivity for 5-HMF, levulinic and formic acids during the dehydration of sugar molecules in an aqueous medium over TiO₂/Y, Nb₂O₅/Y, and CeO₂/Y catalysts are reported in Tables 6.6 and 6.7.

6.6.1. Glucose dehydration to 5-HMF.

As compared to undoped HY zeolite, the deposition of CeO₂, Nb₂O₅ and TiO₂ on zeolite Y did not significantly improve the activity. Glucose conversions of 20% and 10% were observed with reactions carried out with M:S ratios of 1:100 and 1:300, respectively (Table 6.6), indicating that the doping step of these metal oxides on zeolite has no considerable effect on the reaction rate. In addition, the 5-HMF selectivity was also unaffected by CeO₂, whereas slightly increased to nearly 35% with Nb₂O₅ and TiO₂ at an M:S molar ratio of 1:100. In contrast, when an M:S molar ratio of 1:300 was used, the 5-HMF selectivity was drastically increased to the range of 55 - 73% (Table 6.9). Although an M:S molar ratio of 1:300 showed a slightly lower glucose conversion than 1:100, it, however, resulted in substantially higher 5-HMF selectivity simply

because sequential rehydration to ring opening and decomposition reactions to levulinic and formic acid seem not favoured at this M:S molar ratio.

Table 6.9. Catalytic tests for the glucose dehydration to 5-HMF using undoped and doped zeolite Y 1wt.% of TiO₂, Nb₂O₅, and CeO₂. The tests were carried out using 500 mg of the substrate in 5 mL of H₂O at constant reaction conditions of 140 °C for 2 h and endogenous pressure with M:S molar ratios of 1:100 and 1:300. Experimental errors are reported as the standard deviations of three repeated measurements.

M:S molar ratio	Catalyst	Glucose conversion (%)	Selectivity (%)			CMB (%)
			5-HMF	LA	FA	
1:100	HY	19 ± 1	22 ± 2	21 ± 1	57 ± 1	82 ± 2
	TiO ₂ /Y	15 ± 1	32 ± 1	19 ± 2	49 ± 1	89 ± 1
	Nb ₂ O ₅ /Y	17 ± 1	37 ± 2	19 ± 1	44 ± 1	91 ± 2
	CeO ₂ /Y	12 ± 2	21 ± 1	7 ± 1	72 ± 1	90 ± 2
1:300	HY	12 ± 1	47 ± 2	16 ± 1	38 ± 1	89 ± 2
	TiO ₂ /Y	13 ± 1	70 ± 1	9 ± 1	19 ± 1	88 ± 1
	Nb ₂ O ₅ /Y	14 ± 2	73 ± 2	8 ± 2	23 ± 2	86 ± 1
	CeO ₂ /Y	11 ± 1	55 ± 2	11 ± 2	35 ± 1	93 ± 2

Compared with their bare metal oxide counterparts, TiO₂/Y, Nb₂O₅/Y, and CeO₂/Y showed no statistically significant difference in the conversion rate. This could be because the metal oxides were not sufficiently deposited on the zeolite support, or more simply, glucose conversion is already at maximum under the reaction conditions used. Evidence of consistent glucose conversion ($\leq 20\%$) obtained under similar reaction conditions was found in the literature over a variety of heterogeneous catalysts, supporting the latter hypothesis^{74,75}. While 5-HMF selectivity decreased appreciably in the range of 60% by doping CeO₂, Nb₂O₅, and TiO₂ on the zeolite Y for the reaction conducted at 1:100 and 25% for the reaction carried out at 1:300. This decrease in 5-HMF selectivity could be explained by the regular pore size of HY

zeolite, which makes it difficult for the formed HMF to diffuse out and, in turn, leads to its rehydration to levulinic and formic acids that are diffused much more readily out of the zeolite structure²⁹.

6.6.2. Fructose dehydration to 5-HMF.

In the case of fructose dehydration, the doping of CeO₂, Nb₂O₅ and TiO₂ on zeolite Y led to an improved fructose conversion with a slight or no increase found in 5-HMF selectivity as compared to undoped HY zeolite using both M:S ratios of 1:100 and 1:300 (Table 6.6). When the reaction was carried out at an M:S ratio of 1:100, CeO₂/Y demonstrated the highest catalytic activity in terms of reaction rate. However, this was accompanied by a low carbon mass balance of 49%, suggesting that CeO₂/Y is highly reactive but toward undesirable by-products such as formic acid.

TiO₂/Y and Nb₂O₅/Y, on the other hand, showed 5-HMF selectivity of 76% and 80%, respectively, with a CMB of nearly 80%, indicating to be more selective towards the formation of desirable 5-HMF. Furthermore, TiO₂/Y and Nb₂O₅/Y did not exhibit a dramatic change in catalytic activity when the reaction was carried out at an M:S ratio of 1:300, whereas the CeO₂/Y catalyst demonstrated a significant increase in 5-HMF selectivity of 25% and CMB of 35% in comparison with activity data obtained at a 1:100 M:S ratio (Table 6.10).

Table 6.10. Catalytic tests for the fructose dehydration to 5-HMF using undoped and doped zeolite Y with 1wt.% of TiO₂, Nb₂O₅, and CeO₂. The tests were carried out using 500 mg of the substrate in 5 mL of H₂O at constant reaction conditions of 140 °C for 2 h and endogenous pressure with M:S molar ratios of 1:100 and 1:300. In all cases, data are reported as means standard deviations (n = 3).

M:S molar ratio	Catalyst	Fructose Conversion (%)	Selectivity (%)			CMB (%)
			5-HMF	LA	FA	
1:100	HY	42 ± 1	75 ± 2	11 ± 1	13 ± 2	70 ± 2
	TiO ₂ /Y	56 ± 2	76 ± 2	12 ± 1	12 ± 1	78 ± 1
	Nb ₂ O ₅ /Y	61 ± 2	80 ± 1	12 ± 2	8 ± 2	77 ± 2
	CeO ₂ /Y	77 ± 3	60 ± 2	11 ± 1	29 ± 2	49 ± 3
1:300	HY	38 ± 1	84 ± 1	6 ± 1	11 ± 2	83 ± 1
	TiO ₂ /Y	46 ± 2	84 ± 2	6 ± 1	11 ± 2	82 ± 2
	Nb ₂ O ₅ /Y	50 ± 2	85 ± 1	5 ± 1	10 ± 1	89 ± 1
	CeO ₂ /Y	51 ± 4	85 ± 2	4 ± 1	12 ± 2	84 ± 3

In comparison with pure metal oxides, fructose conversion was slightly enhanced by 10 - 15%. Whereas 5-HMF selectivity was significantly decreased by 15% in the case of Nb₂O₅/Y and TiO₂/Y, as well as 30% in the case of CeO₂/Y with an M:S molar ratio of 1:100. However, using a lower M:S ratio of 1:300 result in a slight decrease in fructose conversion for the blank and the corresponded metal oxides, but it also increases the carbon mass balance and in turn lead to a reaction mixture which is less rich in fructose but purer. Among all catalysts studied herein, Nb₂O₅/Y exhibited the highest catalytic activity toward the formation of 5-HMF with a yield of 38% at both M:S ratios of 1:100 and 1:300 (Table A16 in Appendix A.13). Our results showed that an M:S molar ratio of 1:300 was the most suitable for the synthesis of 5-HMF from glucose and fructose. In this regard, increasing the M:S molar ratio does not necessarily lead to an improvement in catalytic activity toward desired products.

This data prompted us to compare the catalytic activity of Nb/Y prepared by the impregnation protocol described in (Section 2.2.1) and Nb₂O₅/Y prepared by the sol-gel method reported in (Section 2.2.2) to determine the consequence of using different preparation methods on the formation of 5-HMF from fructose using niobium-based catalysts (Figure 6.18).

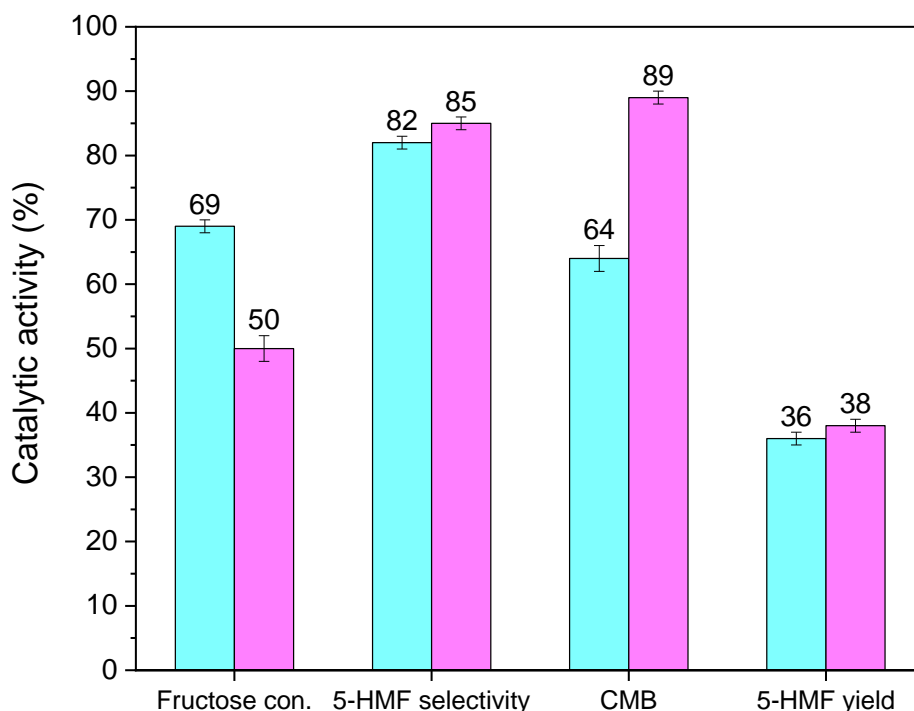


Figure 6.18. the catalytic activity of fructose conversion, 5-HMF selectivity, carbon mass balance (CMB), and 5-HMF yields for 1 wt.% of Nb/Y catalyst prepared by impregnation method (●) and Nb₂O₅/Y catalyst prepared by sol-gel method (●) in the dehydration reaction of fructose to 5-HMF. In all cases, the reaction was carried out at a reaction temperature of 140 °C for 2 hours, with endogenous pressure and an M:S ratio of 1:300. Experimental errors are expressed as the standard deviations of three repeated measurements.

As can be seen in Figure 6.18, the Nb/Y catalyst synthesised by the impregnation method showed a higher fructose conversion of 69% compared to the 50% obtained by Nb₂O₅/Y, which was prepared by the sol-gel protocol. However, these conversion rates were accompanied by carbon mass balances of 64% and 89% after reactions

were carried out over Nb/Y and Nb₂O₅/Y zeolites, respectively. Although there was no statistically significant difference in the yield of 5-HMF observed from both catalysts. It is apparent that Nb₂O₅/Y prepared by the sol-gel protocol revealed a purer route towards the desired 5-HMF under our reaction conditions.

6.6.3. Control test on the synergistic effect of HY and Nb₂O₅/Y zeolite catalysts for glucose dehydration to 5-HMF.

In order to further confirm the role of Nb₂O₅/Y zeolite catalyst in achieving a more selective route toward 5-HMF formation, a control test using a two-step reaction protocol was carried out in an aqueous solution. The glucose isomerisation was first conducted over undoped zeolite Y in its acidic form (SiO₂:Al₂O₃ molar ratio of 80) in order to convert glucose into fructose, and then fructose intermediate is dehydrated to 5-HMF over Nb₂O₅/Y zeolite catalyst.

Table 6.11. Catalytic tests for the glucose dehydration to 5-HMF using undoped and doped zeolite Y 1wt.% of Nb₂O₅. The tests were carried out using 500 mg of the substrate in 5 mL of H₂O at constant reaction conditions of 140 °C for 2 h and endogenous pressure with M:S molar ratios of 1:100 and 1:300. Experimental errors are reported as the standard deviations of three repeated measurements.

M:S molar ratio	Time (h)	Catalyst	Glucose conversion (%)	Selectivity (%)			CMB (%)
				5-HMF	LA	FA	
1:100	2	HY	19 ± 1	22 ± 2	21 ± 1	57 ± 1	82 ± 2
	4	HY	29 ± 1	20 ± 2	18 ± 1	62 ± 2	76 ± 3
	4	HY Nb ₂ O ₅ /Y	38 ± 1	29 ± 2	27 ± 2	44 ± 1	76 ± 2
1:300	2	HY	12 ± 1	47 ± 2	16 ± 1	38 ± 1	89 ± 2
	4	HY	15 ± 2	52 ± 2	11 ± 1	36 ± 2	81 ± 1

4	HY Nb ₂ O ₅ /Y	23 ± 1	61 ± 2	9 ± 2	30 ± 1	81 ± 2
---	---	--------	--------	-------	--------	--------

As shown in Table 6.11, glucose conversion was only increased by 10% with the increase in reaction time for reactions at the M:S ratio of 1:100, whereas 5-HMF selectivity was almost unaffected by the change of the reaction time, and a consistent product distribution within the experimental error could be obtained with the varied reaction time. However, the use of HY and Nb₂O₅/Y together showed a slight improvement in catalytic activity, with glucose conversion and 5-HMF selectivity increased by 10%. It is indeed the presence of Nb₂O₅ species in the zeolite catalyst that contributes to this noticeable increase in catalytic activity toward the formation of more 5-HMF. This confirms that Nb₂O₅/Y zeolite produces 5-HMF from glucose in a purer and more selective manner compared to the Nb/Y catalyst.

6.6.4. Powder X-ray diffraction.

To obtain relevant structural information and determine the activity-structure correlations, powder XRD patterns were collected for zeolite HY, TiO₂/Y, Nb₂O₅/Y, and CeO₂/Y with SiO₂:Al₂O₃ molar ratio of 80 (Figure 6.19) to characterise the crystalline structure of the prepared catalysts and to identify if any ion exchange or distortion of the zeolite could have occurred during the preparation procedure used. A Rietveld refinement⁵⁰ was carried out (Table A19 in Appendix A.15). As shown in the XRD patterns, HY, TiO₂/Y, Nb₂O₅/Y, and CeO₂/Y exhibit nearly identical PXRD patterns and no significant expansion in the unit cell volume has been observed as a consequence of the variations in the unit cell volume of the parent zeolite HY (determined as 14219 Å³). In view of this, it is unlikely for TiO₂, Nb₂O₅, or CeO₂ to be incorporated into the

zeolite framework as a substitution for Al - at least within the resolution of the acquired PXRD patterns.

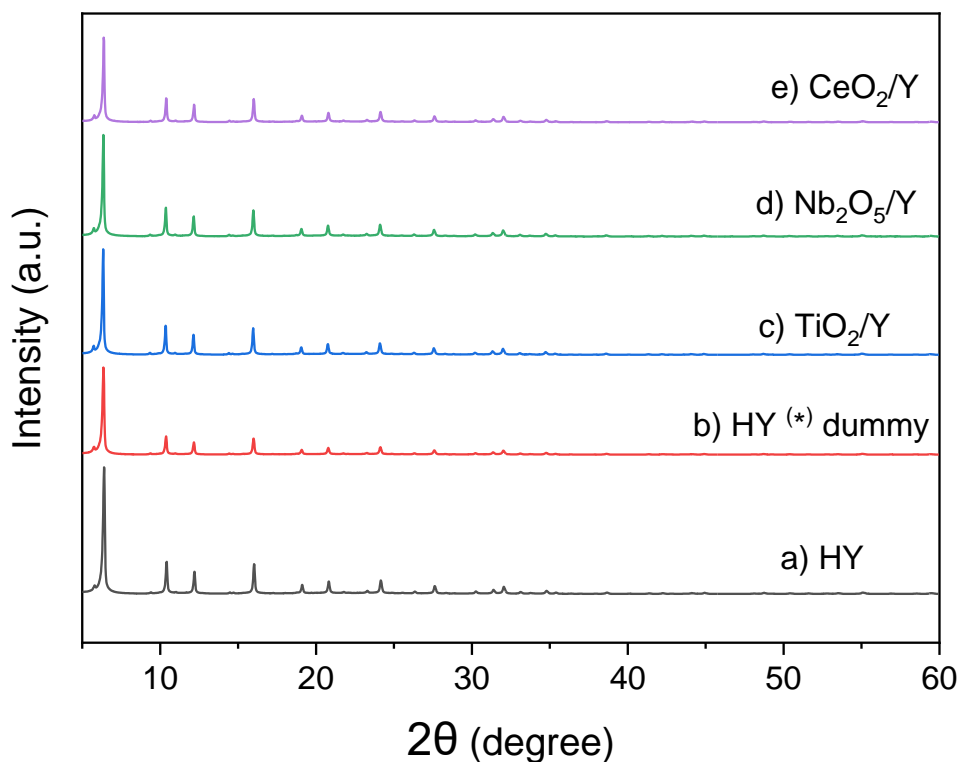


Figure 6.19. X-ray powder diffraction patterns for zeolites with a $\text{SiO}_2:\text{Al}_2\text{O}_3$ molar ratio of 80: (a) HY as delivered, (b) HY treated as for metal deposition but without any metal dopant, (c) TiO_2/Y , (d) $\text{Nb}_2\text{O}_5/\text{Y}$, and (e) CeO_2/Y . No metal or metal oxide cluster from Ti, Nb or Ce is detected, and all zeolites present a virtually identical pattern.

As can be seen in figure 6.19, no evident XRD pattern indicative of TiO_2 , Nb_2O_5 , or CeO_2 was observed. For rutile TiO_2 ⁷⁶, these were expected to be at 26.9, 35.7, 53.7, 68.4, 69.4 2θ for reflection of (110), (101), (211), (301), and (112) respectively. For the orthorhombic phase of Nb_2O_5 ⁵³, these were expected to be at 22.7, 28.6, 36.7, 46.2, 50.7 and 55.3° 2θ for the reflections of (001), (180), (200), (181), (002), (380), and (212) respectively. For CeO_2 ⁷⁷, these were expected to be at 28.5, 33.1, 47.5, 56.3, 2θ for reflections of (111), (200), (220), and (311) respectively.

In addition to understanding the structure and overall chemical composition, determining the unit cell parameter (obtained from XRD data) of TiO₂-, Nb₂O₅-, or CeO₂-doped zeolite Y catalysts, prepared using the sol-gel technique, is important to identify the interactions between these metal oxides and the zeolite. Numerous studies have provided evidence indicating that active species (metals or metal oxides) can be either deposited on the surface of zeolite or trapped within its framework. These two types of metal-zeolite interactions yield distinct catalytic performances^{55,56}. The substitution of metals in the zeolite matrix, replacing Al sites, is typically characterized by the expansion or contraction of the unit cell, depending on the larger/smaller size of the metal (in this case Ti, Nb, and Ce) compared to Al. On the other hand, the percentage of expansion/contraction is, to some extent, dependent on the number of metal atoms being incorporated into the zeolite⁵⁷. For instance, due to the larger size of Ti, Nb, and Ce in their ionic form and coordination compared to Al, an increase in the unit cell's volume expansion indicates the successful incorporation of these metals into structural sites⁷⁸⁻⁸¹. Nevertheless, our catalysts (as shown in Table A19 in Appendix A.15) did not exhibit any significant expansion of the unit cell, indicating that the Ti, Nb, and Ce species in our catalysts, prepared through sol-gel, were not incorporated into the framework of the zeolite catalysts. Instead, they were found to be supported on the catalyst's surface or located within its pores/channels.

6.7. Conclusion

The catalytic dehydration of glucose and fructose to 5-HMF in an aqueous medium was investigated using an array of heterogeneous catalysts ranging from undoped zeolites, metal-doped zeolites, and pure metal oxides to metal oxides-doped zeolite. Wherein the characterisation of sugars conversions and the distribution of their

products in the actual reaction mixture was quantified by the mean of a rapid and efficient proton NMR method in order to evaluate the catalytic activity of our materials and provide guidance on the catalyst design for the industrial production of 5-HMF.

Screening the reaction parameters by HCl as a homogeneous Brønsted catalyst showed that the best compromise between high fructose conversion and high 5-HMF selectivity, demonstrated through the highest 5-HMF yield of 27%, which is obtained at ratios of 1:1 and 1:0.33 for reaction times of 30 min and 120 min, respectively, with greater emphasis placed on the latter reaction conditions (Fructose to HCl molar ratio: 1:0.33, 120 min, 100 °C, endogenous pressure and a pH solution of 4), resulting in a more sustainable process.

A reaction temperature of 140 °C showed to be more appropriate than 100 °C for the catalytic fructose dehydration to 5-HMF over Sn, Ga, Nb, and Fe containing zeolite Y as heterogeneous catalysts. Whereas Using an M:S molar ratio of 1:3 revealed a higher conversion of 70% but toward the formation of undesirable products instead. However, decreasing the M:S molar ratio to 1:300 leads to an increase in 5-HMF yield to 26%, which was significantly increased up to 37% when Sn, Ga, Nb, and Fe were doped on zeolite Y with a SiO₂:Al₂O₃ molar ratio 80. In all cases, catalysts with SiO₂:Al₂O₃ molar ratio of 80 and an M:S molar ratio of 1:300 was found to promote 5-HMF formation under our reaction conditions.

Brønsted acidity measurements revealed two different trends with regard to the acidity-activity correlation. Catalysts with zeolite Y at a SiO₂:Al₂O₃ molar ratio of 5.1 exhibited a direct correlation between the catalytic activity and Brønsted acidity measurements. In contrast, an opposite trend was observed with zeolite Y at a

SiO₂:Al₂O₃ molar ratio of 80, with the catalyst possessing the highest Lewis acidity being the most active.

An array of bulk metal oxides with different acidity characteristics were also tested for the glucose and fructose dehydration reactions in order to prove the necessity of Brønsted and Lewis acid sites to convert these sugar molecules to 5-HMF. TiO₂, Nb₂O₅, WO₃, and CeO₂ showed low activity with glucose conversion (< 30%) and the highest 5-HMF yield of 21% was obtained over Nb₂O₅. Whereas La₂O₃ and MoO₃ were found to be highly active with glucose conversions of 70% but toward levulinic and formic acid. However, Fructose as the initial substrate showed significantly higher catalytic activity in terms of 5-HMF yield, with CeO₂, Nb₂O₅ and TiO₂ being the most active catalysts yielding 42%, 39%, and 37%, respectively.

Furthermore, TiO₂, Nb₂O₅, and CeO₂ were doped on zeolite Y (SiO₂:Al₂O₃ ratio of 80), aiming to improve the yield of desired 5-HMF. However, no statistically significant difference was observed by doing these metal oxides on zeolite Y compared to data obtained by their pure metal oxides. With a yield of 38% from fructose, Nb₂O₅/Y prepared by the sol-gel method exhibited a purer route toward the formation of 5-HMF than Nb/Y prepared by the impregnation protocol.

6.8. References

- 1 Q. Hou, X. Qi, M. Zhen, H. Qian, Y. Nie, C. Bai, S. Zhang, X. Bai and M. Ju, *Green Chem.*, 2021, **23**, 119–231.
- 2 S. Wang, T. L. Eberhardt, D. Guo, J. Feng and H. Pan, *Renew. Energy*, 2022, **190**, 1–10.
- 3 B. Agarwal, K. Kailasam, R. S. Sangwan and S. Elumalai, *Renew. Sustain. Energy Rev.*, 2018, **82**, 2408–2425.
- 4 T. Thananattananachon and T. B. Rauchfuss, *Angew. Chem.*, 2010, **122**, 6766–6768.
- 5 M. A. A. B. A. Rani, N. A. Karim and S. K. Kamarudin, *Int. J. Energy Res.*, 2022, **46**, 577–633.
- 6 B. R. Caes, R. E. Teixeira, K. G. Knapp and R. T. Raines, *ACS Sustain. Chem. Eng.*, 2015, **3**, 2591–2605.
- 7 F. Yang, Q. Liu, X. Bai and Y. Du, *Bioresour. Technol.*, 2011, **102**, 3424–3429.
- 8 V. V. Ordonsky, J. Van Der Schaaf, J. C. Schouten and T. A. Nijhuis, *J. Catal.*, 2012, **287**, 68–75.
- 9 M. M. Özer, Y. Jia, Z. Zhang, J. R. Thompson and H. H. Weitering, *Science (1979)*, 2007, **316**, 1594–1597.
- 10 S. Lima, P. Neves, M. M. Antunes, M. Pillinger, N. Ignatyev and A. A. Valente, *Appl. Catal. A: Gen.*, 2009, **363**, 93–99.
- 11 A. Takagaki, M. Ohara, S. Nishimura and K. Ebitani, *ChemComm.*, 2009, 6276–6278.

- 12 K. Świątek, M. P. Olszewski and A. Kruse, *Glob. Change Biol. Bioenergy*, 2022, **14**, 681–693.
- 13 G. Portillo Perez, A. Mukherjee and M. J. Dumont, *J. Ind. Eng. Chem.*, 2019, **70**, 1–34.
- 14 P. Zhou and Z. Zhang, *Catal. Sci. Technol.*, 2016, **6**, 3694–3712.
- 15 X. Zhang, D. Zhang, Z. Sun, L. Xue, X. Wang and Z. Jiang, *Appl. Catal. B: Environ.*, 2016, **196**, 50–56.
- 16 Y. Zhao, K. Lu, H. Xu, L. Zhu and S. Wang, *Renew. Sustain. Energy Rev.*, 2021, **139**, 110706.
- 17 R. Karinen, K. Vilonen and M. Niemelä, *ChemSusChem*, 2011, **4**, 1002–1016.
- 18 T. Wang, M. W. Nolte and B. H. Shanks, *Green Chem.*, 2014, **16**, 548–572.
- 19 M. E. Davis, *Top. Catal.*, 2015, **58**, 405–409.
- 20 L. Wang, H. Guo, Q. Xie, J. Wang, B. Hou, L. Jia, J. Cui and D. Li, *Appl. Catal. A: Gen.*, 2019, **572**, 51–60.
- 21 J. S. Kruger, V. Choudhary, V. Nikolakis and D. G. Vlachos, *ACS Catal.*, 2013, **3**, 1279–1291.
- 22 C. Moreau, R. Durand, S. Razigade, J. Duhamet, P. Faugeras, P. Rivalier, P. Ros and G. Avignon, *Appl. Catal. A: Gen.*, 1996, **145**, 211–224.
- 23 Y. Qiao, N. Theyssen and Z. Hou, *Recyclable Catalysis*, 2015, **2**, 36–60.
- 24 J. Guilera, E. Ramírez, C. Fité, M. Iborra and J. Tejero, *Appl. Catal. A: Gen.*, 2013, **467**, 301–309.

- 25 V. v. Ordonsky, J. van der Schaaf, J. C. Schouten and T. A. Nijhuis, *ChemSusChem*, 2012, **5**, 1812–1819.
- 26 G. Yang, E. A. Pidko and E. J. M. Hensen, *J. Catal.*, 2012, **295**, 122–132.
- 27 A. S. Amarasekara, L. H. Nguyen, H. Du and R. R. Kommalapati, *SN Appl. Sci.*, 2019, **1**, 964.
- 28 J. Slak, B. Pomeroy, A. Kostyniuk, M. Grilc and B. Likozar, *Chem. Eng. J.*, 2022, **429**, 132325.
- 29 J. P. V. Lima, P. T. A. Campos, M. F. Paiva, J. J. Linares, S. C. L. Dias and J. A. Dias, *Chemistry (Switzerland)*, 2021, **3**, 1189–1202.
- 30 Z. Xu, Y. Yang, P. Yan, Z. Xia, X. Liu and Z. C. Zhang, *RSC Adv.*, 2020, **10**, 34732–34737.
- 31 R. J. Van Putten, J. C. Van Der Waal, E. De Jong, C. B. Rasrendra, H. J. Heeres and J. G. De Vries, *Chem. Rev.*, 2013, **113**, 1499–1597.
- 32 K. ichi Shimizu, R. Uozumi and A. Satsuma, *Catal. Commun.*, 2009, **10**, 1849–1853.
- 33 S. Kunnikuruvan and N. N. Nair, *ACS Catal.*, 2019, **9**, 7250–7263.
- 34 J. C. Velasco Calderón, J. S. Arora and S. H. Mushrif, *ACS Omega*, 2022, **7**, 44786–44795.
- 35 L. Filiciotto, A. M. Balu, A. A. Romero, E. Rodríguez-Castellón, J. C. Van Der Waal and R. Luque, *Green Chem.*, 2017, **19**, 4423–4434.
- 36 P. Carniti, A. Gervasini and M. Marzo, *Catal. Commun.*, 2011, **12**, 1122–1126.

- 37 K. E. Haslauer, D. Hemmler, P. Schmitt-Kopplin and S. S. Heinzmann, *Anal. Chem.*, 2019, **91**, 11063–11069.
- 38 A. P. Altshuller and H. E. Everson, *J. Am. Chem. Soc.*, 1953, **75**, 1727–1727.
- 39 S. Sokolenko and M. G. Aucoin, *BMC Syst. Biol.*, 2015, **9**, 51.
- 40 R. Gounder and M. E. Davis, *AIChE Journal*, 2013, **59**, 3349–3358.
- 41 R. Bermejo-Deval, R. Gounder and M. E. Davis, *ACS Catal.*, 2012, **2**, 2705–2713.
- 42 B. F. M. Kuster, *Starch - Stärke*, 1990, **42**, 314–321.
- 43 P. Dornath and W. Fan, *Microporous Mesoporous Mater.*, 2014, **191**, 10–17.
- 44 R. Weingarten, G. A. Tompsett, W. C. Conner and G. W. Huber, *J. Catal.*, 2011, **279**, 174–182.
- 45 U. Díaz and A. Corma, *Chem. Eur. J.*, 2018, **24**, 3944–3958.
- 46 K. Saenluang, A. Thivasasith, P. Dugkhuntod, P. Pornsetmetakul, S. Salakhum, S. Namuangruk and C. Wattanakit, *Catalysts*, 2020, **10**, 1–12.
- 47 Hongbo Du, F. Deng, R. R. Kommalapati and A. S. Amarasekara, *Renew. Sustain. Energy Rev.*, 2020, **134**, 110292.
- 48 N. A. S. Ramli and N. A. S. Amin, *Appl. Catal. B: Environ.*, 2015, **163**, 487–498.
- 49 Gy. Popova, L. Zakharov and T. Andrushkevich, *React. Kinet. Catal. Lett.*, 1999, **66**, 251–256.
- 50 L. B. Mccusker, R. B. Von Dreele, D. E. Cox, D. Loue and P. Scardi, *J. Appl. Crystallogr.*, 1999, **32**, 36–50.

- 51 M. Conte, C. J. Davies, D. J. Morgan, T. E. Davies, D. J. Elias, A. F. Carley, P. Johnston and G. J. Hutchings, *J. Catal.*, 2013, **297**, 128–136.
- 52 R. Roy, V. G. Hill and E. F. Osborn, *J. Am. Chem. Soc.*, 1952, **74**, 719–722.
- 53 G. Taques Tractz, F. Staciaki da Luz, S. Regina Masetto Antunes, E. do Prado Banczek, M. Taras da Cunha and P. Rogério Pinto Rodrigues, *Sol. Energy*, 2021, **216**, 1–6.
- 54 O. A. Bulavchenko, Z. S. Vinokurov, A. A. Saraev, A. M. Tsapina, A. L. Trigub, E. Y. Gerasimov, A. Y. Gladky, A. v. Fedorov, V. A. Yakovlev and V. v. Kaichev, *Inorg Chem*, 2019, **58**, 4842–4850.
- 55 L. Botti, R. Navar, S. Tolborg, J. S. Martinez-Espin, D. Padovan, E. Taarning and C. Hammond, *Top. Catal.*, 2019, **62**, 1178–1191.
- 56 P. Wolf, W. C. Liao, T. C. Ong, M. Valla, J. W. Harris, R. Gounder, W. N. P. van der Graaff, E. A. Pidko, E. J. M. Hensen, P. Ferrini, J. Dijkmans, B. Sels, I. Hermans and C. Copéret, *Helv. Chim. Acta*, 2016, **99**, 916–927.
- 57 A. Cichocki, J. Datka, A. Olech, Z. Piwowarska and M. Michalik, *J. CHEM. SOC. FARADAY TRANS*, 1990, **86**, 753–756.
- 58 S. Roy, K. Bakhmutsky, E. Mahmoud, R. F. Lobo and R. J. Gorte, *ACS Catal.*, 2013, **3**, 573–580.
- 59 M. Zakrzewski, O. Shtyka, R. Ciesielski, A. Kedziora, W. Maniukiewicz, N. Arcab and T. Maniecki, *Mater.*, 2021, **14**, 7581.
- 60 S. Shao, C. Liu, X. Xiang, X. Li, H. Zhang, R. Xiao and Y. Cai, *Renew. Energy*, 2021, **177**, 1372–1381.

- 61 A. Maity, S. M. Hyun and D. C. Powers, *Nat. Chem.*, 2018, **10**, 200–204.
- 62 E. I. García-López, F. R. Pomilla, B. Megna, M. L. Testa, L. F. Liotta and G. Marci, *Nanomater.*, 2021, **11**, 1821.
- 63 K.-I. Seri, Y. Inoue and H. Ishida, *Bull. Chem. Soc. Jpn.*, 2001, **74**, 1145–1150.
- 64 A. Sahani, R. S. Rao, A. Vadakkayil, M. Santhosh, M. Mummoothi, M. Karthick and C. R. Ramanathan, *J. Chem. Sci.*, 2021, **133**, 4.
- 65 Y. Liu, X. Ma, S. Wang and J. Gong, *Appl. Catal. B: Environ.*, 2007, **77**, 125–134.
- 66 H. Belatel, H. Al-Kandari, F. Al-Khorafi, A. Katrib and F. Garin, *Appl. Catal. A: Gen.*, 2004, **275**, 141–147.
- 67 G. A. H. Mekhemer, *Phys. Chem. Chem. Phys.*, 2002, **4**, 5400–5405.
- 68 F. S. Al-Sultan, S. N. Basahel and K. Narasimharao, *Fuel*, 2018, **233**, 796–804.
- 69 C. Martín, P. Malet, G. Solana and V. Rives, *J. Phys. Chem. B.*, 1998, **102**, 2759–2768.
- 70 M. Watanabe, Y. Aizawa, T. Iida, R. Nishimura and H. Inomata, *Appl. Catal. A: Gen.*, 2005, **295**, 150–156.
- 71 A. A. Marianou, C. M. Michailof, A. Pineda, E. F. Iliopoulou, K. S. Triantafyllidis and A. A. Lappas, *Appl. Catal. A: Gen.*, 2018, **555**, 75–87.
- 72 C. Aellig and I. Hermans, *ChemSusChem*, 2012, **5**, 1737–1742.
- 73 T. Andana, K. G. Rappé, F. Gao, J. Szanyi, X. Pereira-Hernandez and Y. Wang, *Appl. Catal. B: Environ.*, 2021, **291**, 120054.
- 74 R. L. de Souza, H. Yu, F. Rataboul and N. Essayem, *Challenges*, 2012, **3**, 212–232.

- 75 M. Watanabe, Y. Aizawa, T. Iida, R. Nishimura and H. Inomata, *Appl. Catal. A: Gen.*, 2005, **295**, 150–156.
- 76 Y. Masuda and K. Kato, *J. Ceram. Soc. Jpn.*, 2009, **117**, 373–376.
- 77 H. Li, F. Meng, J. Gong, Z. Fan and R. Qin, *J. Alloys Compd.*, 2017, **722**, 489–498.
- 78 R. Millini, G. Perego, D. Berti, W. O. Parker, A. Carati and G. Bellussi, *Microporous Mesoporous Mater.*, 2000, **35–36**, 387–403.
- 79 M. El Fergani, N. Candu, S. M. Coman and V. I. Parvulescu, *Molecules*, 2017, **22**, 2218.
- 80 S. Dzwigaj, Y. Millot, C. Méthivier and M. Che, *Microporous Mesoporous Mater.*, 2010, **130**, 162–166.
- 81 B. Tang, W. Dai, X. Sun, G. Wu, L. Li, N. Guan and M. Hunger, *Cuihua Xuebao, Chinese J. Catal.*, 2015, **36**, 801–805.

Chapter 7. Conclusion and future work.

7.1. Conclusion

This research project has made significant progress in the following areas: i) evaluation of sugar solubilities and their potential implications for the catalytic activity of our materials, ii) characterisation of reaction intermediates formed during glucose isomerisation over zeolite-based catalysts in both methanol and water, iii) elucidation on the role of Lewis and Brønsted acid sites in glucose isomerisation and identification of their respective reaction pathways and iv) provide preliminary data for future work by highly efficient zeolite-based catalysts for glucose and fructose dehydration to produce platform chemicals such as 5-HMF.

In light of this, the major achievements of this research project can be summarised below.

7.1.1 Solubility of sugars.

A reliable and efficient HPLC analysis method was developed to address the significant variations in the literature regarding the solubility values of sugars obtained from different analytical methods, this method relies on determining the saturation point of sugar solutions for accurate quantification of glucose, fructose, and mannose solubilities in water, methanol, ethanol, 1-propanol, and isopropanol at room temperature. This approach is intended to identify the possible implications of this important property on catalytic activity and establish a robust platform to ensure the reliability of catalytic tests. Specifically, errors in solubility can bias the catalytic results both in terms of conversion and selectivity. solubility which besides compromising experiments per se with misleading results could significantly limit the reproducibility of data among different laboratories and impede the development of catalysts by

design. Our solubility measurements did not show any significant implications toward the catalytic activity, this allowed us to confidently derive data from glucose isomerisation and fructose dehydration under the various reaction conditions studied.

7.1.2 Identification of reaction intermediates.

In view of the conflicting evidence in the literature concerning the formation of alkyl-sugar species, an extensive analysis was carried out to investigate the mass spectroscopic fragmentation patterns of methyl glucoside and methyl fructoside intermediates. In this regard, two distinct peaks of fragmentation patterns of $m/z = 217$ corresponding to an anomeric mixture of methyl glucoside and methyl fructoside were identified. One has a retention time of nearly 0.45 minutes on the LC column, comparable with the standard methyl fructoside. Whereas the second peak, with an LC retention time of approximately 0.6 minutes, most likely represents methyl glucoside. As a consequence, we concluded that at least two independent reaction pathways are involved during the isomerisation reaction in methanol: 1) a Lewis-catalysed pathway for the conversion of glucose to fructose and 2) a Brønsted-catalysed pathway toward the formation of methyl fructoside and methyl glucoside intermediates. Therefore, it is evident that an accurate characterisation of a reaction mixture is a fundamental step and requisite to provide insight into reaction mechanisms and, in turn, to promote catalyst rational design.

7.1.3 Glucose to fructose isomerisation by Sn and Ga doped zeolites.

The isomerisation of glucose to fructose has been successfully achieved with HY, Sn/Y, and Ga/Y zeolites under mild reaction conditions (100 °C, endogenous pressure, 1-2 hours). These catalysts showed comparable performance in converting glucose into fructose, methyl fructoside, and mannose in methanol as a solvent using a one-step reaction protocol and methanol followed by water as a solvent in a two-step

reaction protocol. The conversion of glucose exceeded 90%, while a selectivity towards fructose up to 55% under optimal reaction conditions in a two-step reaction. In the presence of methanol as a solvent, large amounts of methyl fructoside intermediate (ca. 70 %) were formed through a reaction pathway mediated via Brønsted acid centres. By conducting catalytic tests using fructose and mannose as substrates in methanol, it was observed that glucose, fructose, and mannose are in equilibrium with fructose through a hydride shift mediated by Lewis acid sites. Consequently, the conversion of glucose in methanol occurs through three distinct reaction pathways: (i) a Lewis acid-catalysed pathway, converting glucose to fructose and then mannose, (ii) the reverse reaction, and (iii) a Brønsted acid pathway, where fructose is transformed into methyl fructose. In contrast, the initial presence of water as a solvent in the reaction quenched the catalytic activity of HY, Sn/Y, and Ga/Y zeolites. This loss of activity was a consequence of the strong water adsorption within the pores of the zeolites and/or the site-blocking of metal Lewis acid sites that initiate the isomerisation reaction. However, if water is, instead, added after the reaction step in methanol, this solvent could promote the hydrolysis of methyl fructoside intermediates to fructose with a formation from ca. 40 to 70% of the desired product for the catalytic tests carried out at 100 and 120 °C in all cases, suggesting that the Brønsted acid pathway is dominant for this reaction. This likely explains the similar catalytic performance observed among the studied catalysts.

7.1.4 Characterisation of zeolites for the glucose to fructose isomerisation.

As per our detailed structure characterisation, Ga/Y and Sn/Y exhibited significantly different structures, with Sn/Y consisting mainly of SnO₂ clusters outside the zeolite crystals and Ga/Y consisting of highly dispersed Ga species inside the pores.

Although Brønsted acidity and porosity played a significant role in the obtained catalytic data, establishing detailed and accurate correlations between catalytic performance and a single parameter proved to be challenging. Therefore, identifying and ascertaining potential trends in the catalytic activity of different catalysts requires the investigation of various catalyst properties.

7.1.5 Synthesis of 5-HMF.

In order to accomplish the selective dehydration of fructose to 5-HMF in aqueous media using a heterogeneous catalyst, different reaction parameters of this reaction were screened using HCl as a Brønsted acid homogeneous catalyst. The results demonstrated that fructose to HCl molar ratio of 1:0.33, 2h, 100 °C, endogenous pressure, and a pH 4 for the solution were the best compromise between high fructose conversion and high 5-HMF selectivity, with the highest 5-HMF yield of 27%. However, A reaction temperature of (≥ 140 °C) could significantly promote the fructose dehydration reaction compared to 100 °C, which proved insufficient to activate our heterogeneous catalyst (i.e., HY zeolite) to facilitate the dehydration reaction toward 5-HMF under the reaction conditions studied.

Furthermore, A wide range of heterogeneous catalysts, including undoped zeolite Y, metal-doped zeolite Y, pure metal oxides, and metal oxide-doped zeolite Y, were assessed in the catalytic dehydration of fructose and/or glucose to 5-HMF in aqueous media. An M:S molar ratio of 1:3 revealed a higher conversion of 70% but toward the formation of unwanted by-products such as LA and FA. However, decreasing the M:S molar ratio to 1:300 promotes the catalytic activity toward 5-HMF, especially with Sn,

Ga, Nb, or Fe -doped zeolite Y ($\text{SiO}_2:\text{Al}_2\text{O}_3$ molar ratio 80) that exhibited HMF yield of ($\geq 30\%$).

7.1.6 Isomerisation and dehydration mediated by metal oxides.

In addition, an array of bulk metal oxides having different acidity levels were tested for the catalytic dehydration of glucose and fructose in aqueous media ($140\text{ }^\circ\text{C}$, 2h, endogenous pressure and an M:S molar ratio of 1:10) in order to prove the concept that Brønsted and Lewis acid sites are essential to convert these sugar molecules to 5-HMF. TiO_2 , Nb_2O_5 , WO_3 , and CeO_2 showed low activity with glucose conversion ($\leq 30\%$), with Nb_2O_5 demonstrating the highest 5-HMF yield (21%). La_2O_3 and MoO_3 were highly active with glucose conversions of 70% but toward levulinic and formic acids. Alternatively, fructose as a substrate displayed significantly higher catalytic activity concerning 5-HMF yield, with CeO_2 , Nb_2O_5 and TiO_2 exhibiting the highest yields of 42%, 39%, and 37%, respectively. Also, the deposition of TiO_2 , Nb_2O_5 , and CeO_2 on zeolite Y (80) showed no statistically significant difference in the catalytic activity to their bare metal oxide counterparts and a 5-HMF yield in the range of 40% was also obtained.

In conclusion, the results of these studies have significantly enhanced our understanding of sugar transformations, their underlying reaction mechanisms, and the development of efficient catalysts for the conversion of glucose and fructose into platform chemicals such as 5-HMF.

7.2. Future work.

While this research project has contributed significantly to our knowledge of biomass valorisation and Lewis acid zeolite-based catalysts, there are still several challenges

that need to be addressed before we can successfully develop commercially viable heterogeneous Lewis acid catalysts for the catalytic conversion of glucose to 5-HMF via the formation of fructose intermediates.

For example, we successfully identified two distinguishable fragmentation patterns corresponding to $m/z = 217$, representing an anomeric mixture of methyl glucoside and methyl fructoside. However, the formation and decomposition mechanisms of these intermediates under used reaction conditions were not fully elucidated. Therefore, it is vitally important to conduct further research in this domain to explore the intricate nature of these processes. As a result, we can gain a better understanding of this process and develop strategies to promote the formation of desirable fructose, thereby providing the basis for future developments in this field.

Furthermore, using NMR relaxation measurements, the potential solvent effects of water, methanol and ethanol on the catalytic performance of our materials in the isomerisation reaction of glucose to fructose were investigated. However, the current study does not encompass specific analysis or considerations regarding the potential nucleophilic effects of these solvents on our substrates. For instance, the reactivity of the solvents towards the substrates could influence the overall reaction kinetics and selectivity through the formation of undesired by-products. Furthermore, the nucleophilicity of the solvent could have an impact on the stability of our catalyst or other intermediates involved in the reaction. A nucleophilic attack by the solvent could result in the deactivation of the catalyst or the formation of stable complexes, thereby altering catalytic activity. Given these potential implications, it is highly beneficial to consider the nucleophilic effects of these solvents on our substrates. Therefore, it is recommended to investigate further the significance of these effects to gain a more comprehensive understanding of how solvents impact catalytic activity. Such

exploration could provide valuable insights into the complex interaction between solvents and the catalytic system.

If then considering the complexity of diverse catalytic systems, an assessment of catalytic performance based solely on a single parameter is challenging. Therefore, it is crucial to evaluate various catalyst characteristics in order to understand trends in their catalytic performance in a comprehensive manner. For instance, by considering additional factors such as Lewis acidity alongside the previously measured Brønsted acidity and catalyst porosity, we can obtain a more holistic perspective and a deeper understanding of how our catalysts operate under different conditions. This more integrated approach would enable us to identify more accurate multi-dimensional correlations, leading to an enhanced comprehension of catalyst functionality. Through this, a deeper understanding of the complex relationship between catalyst properties and their performance can be gained, ultimately resulting in a more accurate prediction of catalyst behaviour.

The catalytic performance of doped zeolite catalysts for fructose dehydration to HMF was studied under constant reaction parameters. Therefore, considering the effects of reaction parameters, such as temperature, pressure, and catalyst loading on the performance of these catalysts aiming to achieve elevated conversion rates and selectivity of the desired product would be a highly recommended approach for this part.

In this context, metal oxides were predominantly used in finely powdered forms, possibly leading to substrate diffusion to the catalyst surface due to limitations in mass transfer during liquid reactions. Conversely, finer powders offer a larger total surface area. Hence, future research in this area could involve the use of bulk metal oxides in

the form of pellets with specific diameters for the selective dehydration of sugars to 5-HMF, aiming to surpass the current catalytic performance and achieve higher levels of efficiency.

Last but not least, based on the catalytic data obtained in this project using glucose and fructose as the reaction substrates, investigate the effect of different biomass feedstocks (e.g., lignocellulosic materials or agricultural residues such as corn stover, wheat straw, and wood chips) on the catalytic performance of ideal catalysts such as Nb/Y(80) and Nb₂O₅/Y is highly recommended. This investigation seeks to validate the broad applicability of the catalysts and explore the effects of feedstock composition, impurities, and pre-treatment methods on the catalytic activity and selectivity of the desired product. The ultimate objective is to develop highly adaptable catalysts capable of efficiently processing diverse biomass feedstocks. Likewise, it would also be highly beneficial to examine the universal applicability of the most promising materials in catalysing reactions beyond sugar transformations such as the conversion of 5-HMF to Benzene and its derivatives, such as toluene, xylenes, and ethylbenzene. These compounds are in high industrial demand due to their extensive use as essential raw materials in manufacturing chemicals, plastics, synthetic fibres, rubber, dyes, and pharmaceuticals.

Appendix

A.1 Calibration Curves of Glucose, Fructose and Mannose in Aqueous Solution.

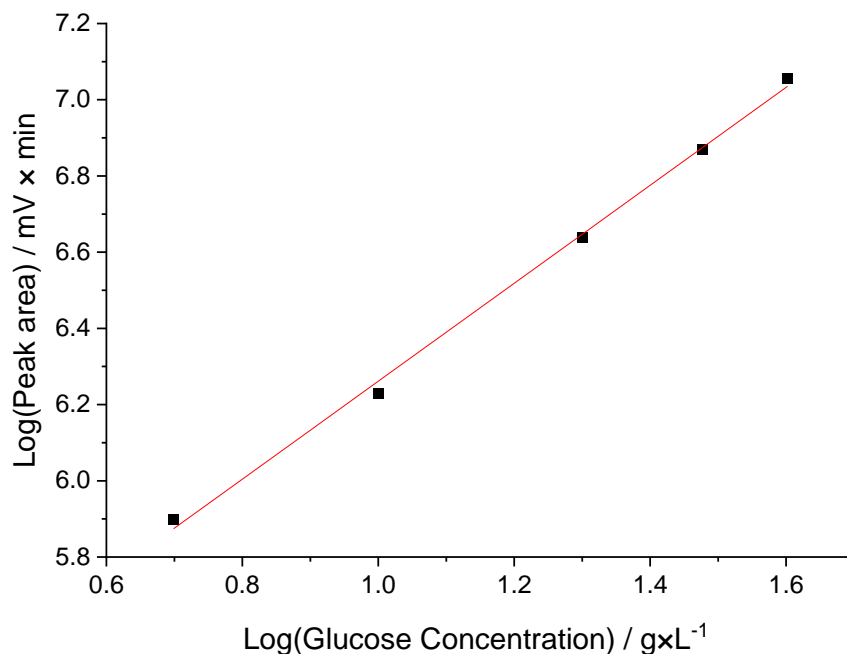


Figure A1. Calibration curve of glucose solutions with concentrations ranging from 5 g·L⁻¹ to 40 g·L⁻¹ (0.02 – 0.22 mol·L⁻¹). Regression parameters of 1.28 ± 0.04 and 4.98 ± 0.05 for the slope and intercept of the regression line were obtained and used in the calculation of glucose conversion and product selectivity values for the isomerisation reaction.

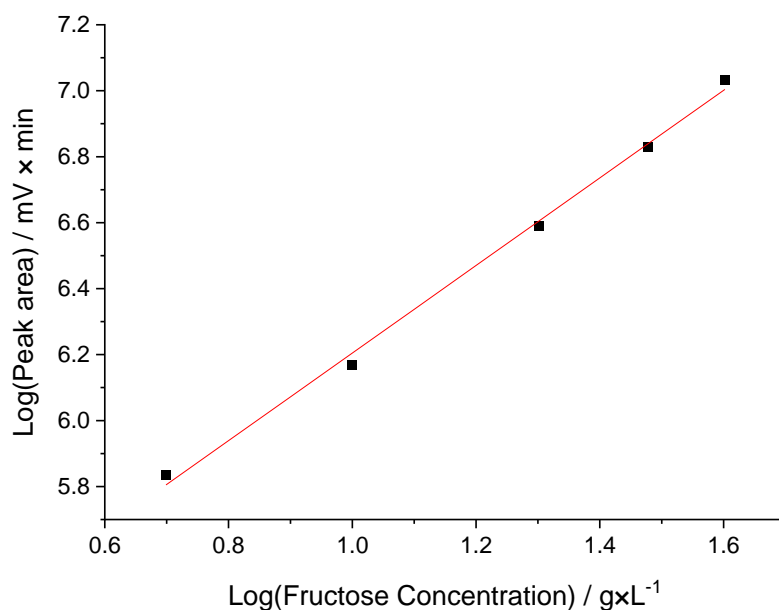


Figure A2. Calibration curve of fructose solutions with concentrations ranging from $5 \text{ g}\cdot\text{L}^{-1}$ to $40 \text{ g}\cdot\text{L}^{-1}$ ($0.02 - 0.22 \text{ mol}\cdot\text{L}^{-1}$). Regression parameters of 1.33 ± 0.04 and 4.88 ± 0.05 for the slope and intercept of the regression line were obtained and used in the calculation of glucose conversion and product selectivity values for the isomerisation reaction.

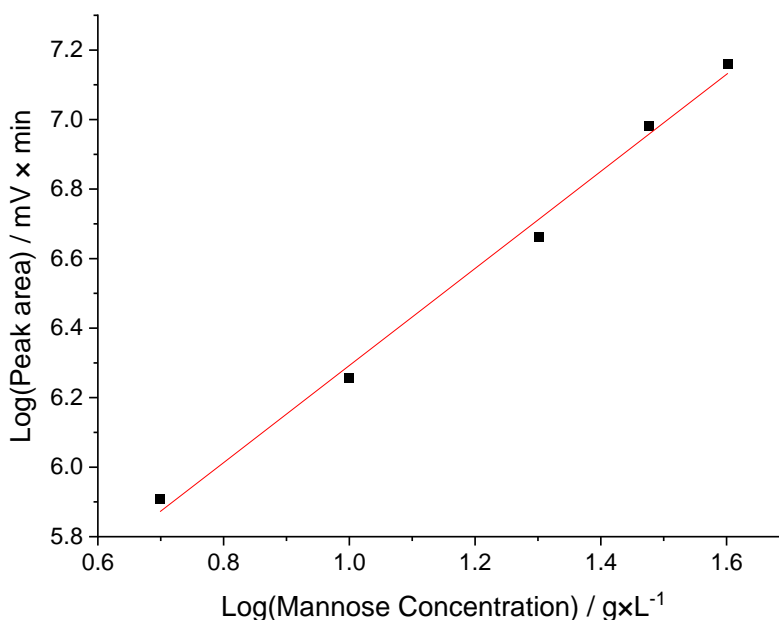


Figure A3. Calibration curve of mannose solutions with concentrations ranging from $5 \text{ g}\cdot\text{L}^{-1}$ to $40 \text{ g}\cdot\text{L}^{-1}$ ($0.02 - 0.22 \text{ mol}\cdot\text{L}^{-1}$). Regression parameters of 1.40 ± 0.06 and 4.90 ± 0.08 for the slope and intercept of the regression line were obtained and used in the calculation of glucose conversion and product selectivity values for the isomerisation reaction.

A2. ¹H-NMR Spectra of Fructose Dehydration Reaction Mixture.

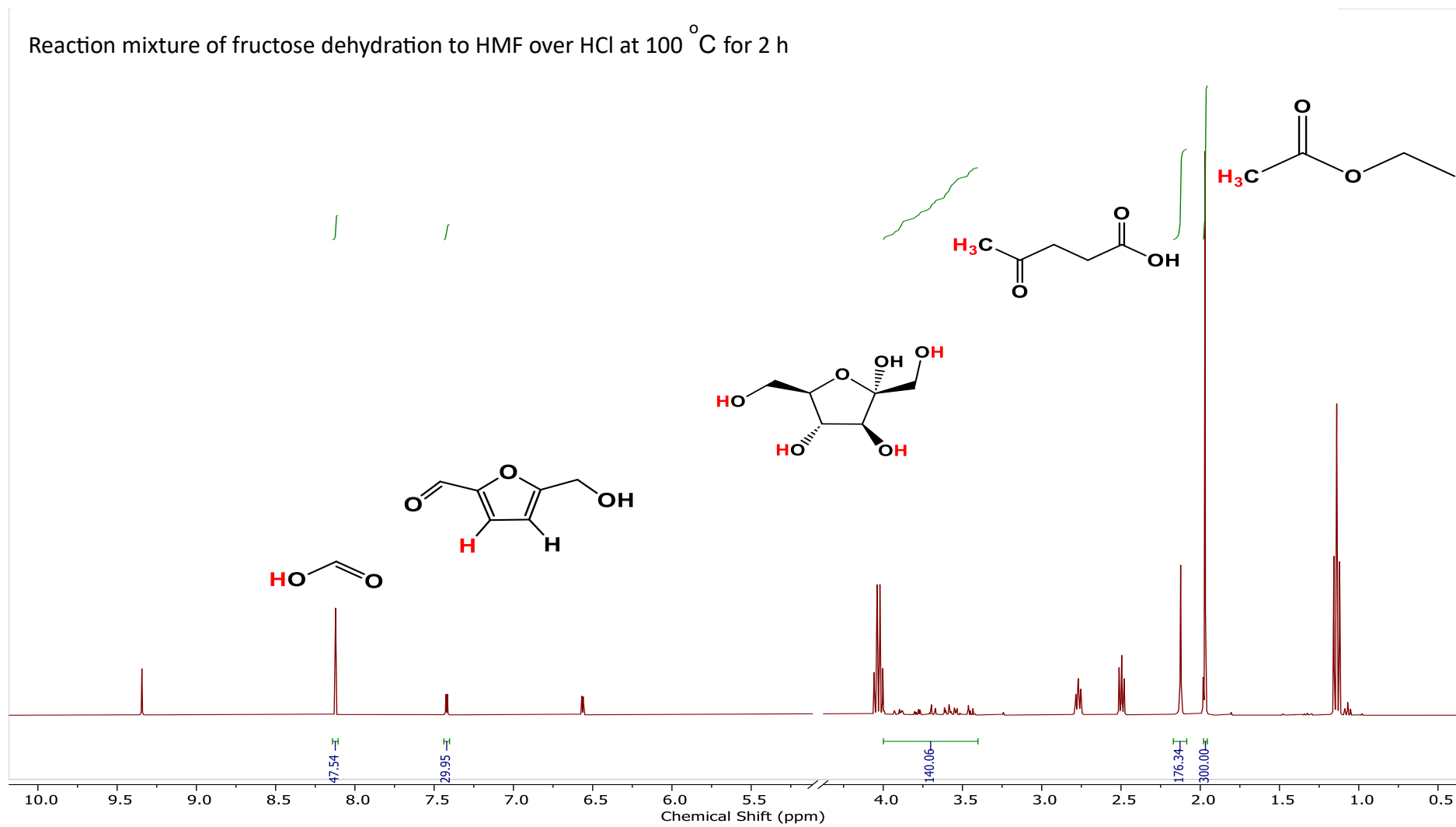


Figure A4. Representative example of fructose dehydration reaction mixture obtained by HCl at 100 °C for 2 h using an M:S molar ratio of 1:1.

A.3 Solubility Determination of Sugars by HPLC Diagram Method.

The solubility of glucose, fructose, and mannose in water, methanol, ethanol, 1-propanol and isopropanol was measured at room temperature using HPLC diagrams, which measure the solubility upon the saturation point of a solution via the intersection of two observed regression lines.

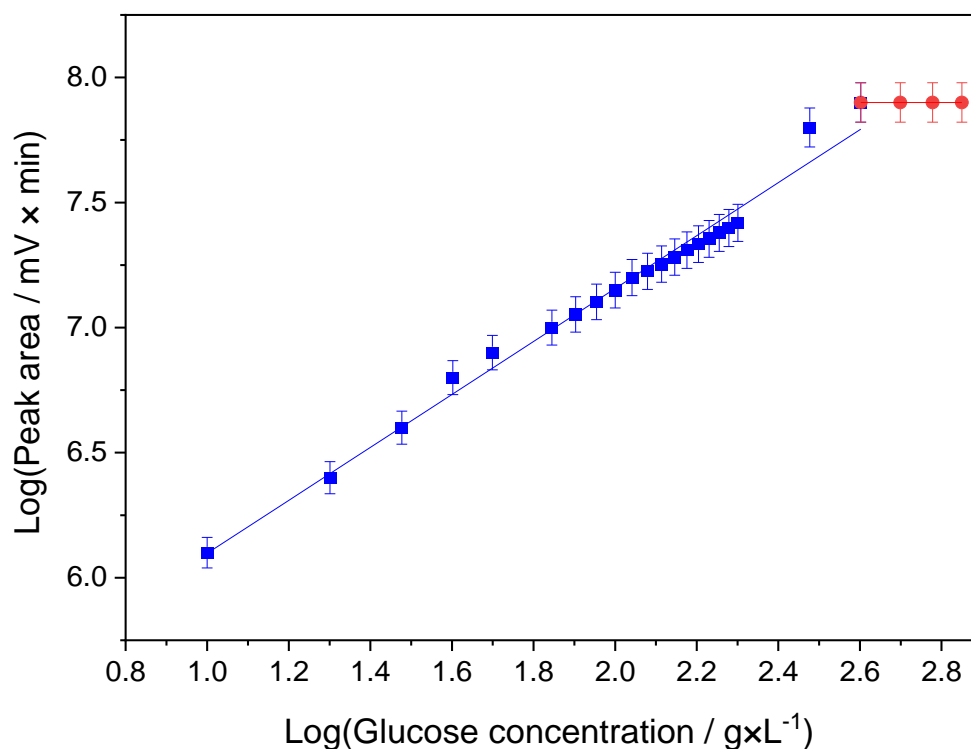


Figure A5. HPLC solubility diagram of glucose in water ($10 - 600 \text{ g}\cdot\text{L}^{-1}$). A linear correlation between an HPLC peak area and the sample concentration is expected within the solubility limit (■), whereas as expected a constant saturation value was detected upon saturation and by analysing the surfactant solution (●).

Regression parameters of 1.05 ± 0.05 and 5.04 ± 0.05 for the slope and intercept of the regression line before the saturation point (blue line), as well as regression parameters of $(-1.16 \times 10^{-29} \pm 6.81)$ and $7.90 \pm 1.86 \times 10^{-14}$ for the slope and intercept of the regression line after the saturation point (red line) were obtained and used in the calculation of solubility values.

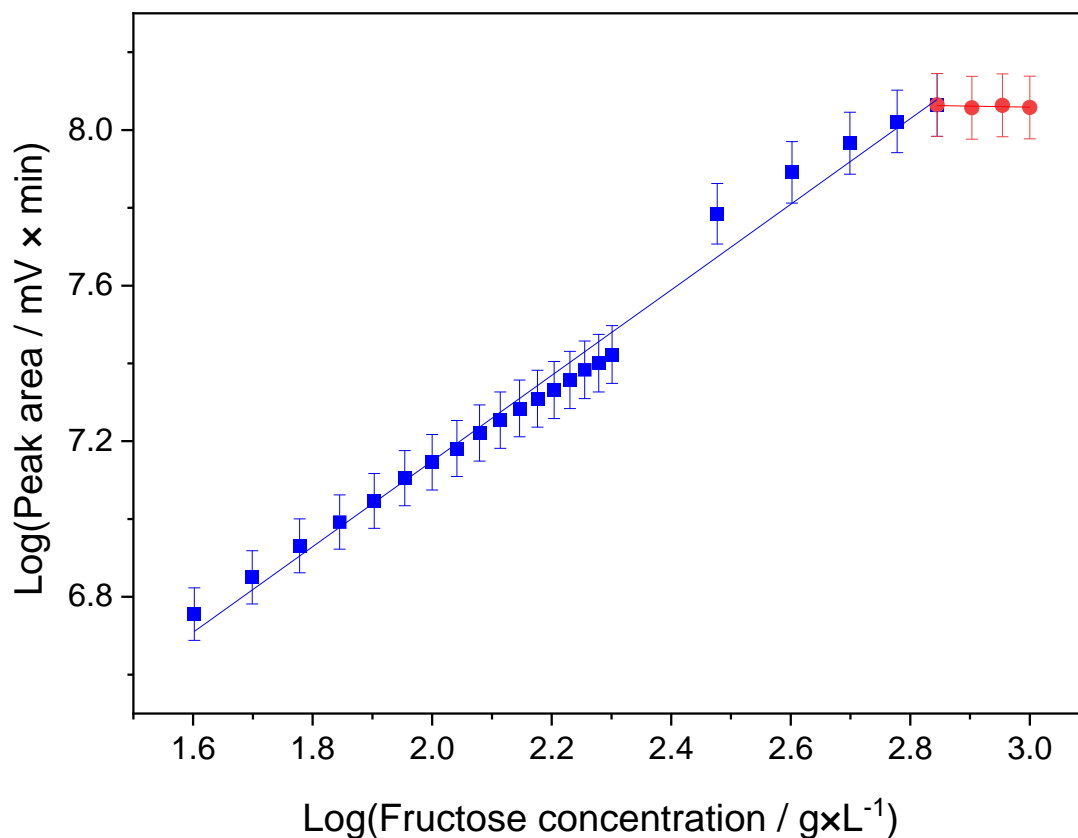


Figure A6. HPLC solubility diagram of fructose in water ($10 - 1000 \text{ g}\cdot\text{L}^{-1}$). A linear correlation between an HPLC peak area and the sample concentration is expected within the solubility limit (■), whereas as expected a constant saturation value was detected upon saturation and by analysing the surfactant solution (●).

Regression parameters of 1.10 ± 0.03 and 4.95 ± 0.06 for the slope and intercept of the regression line before the saturation point (blue line), as well as regression parameters of (-0.03 ± 0.03) and 8.14 ± 0.10 for the slope and intercept of the regression line after the saturation point (red line) were obtained and used in the calculation of solubility values.

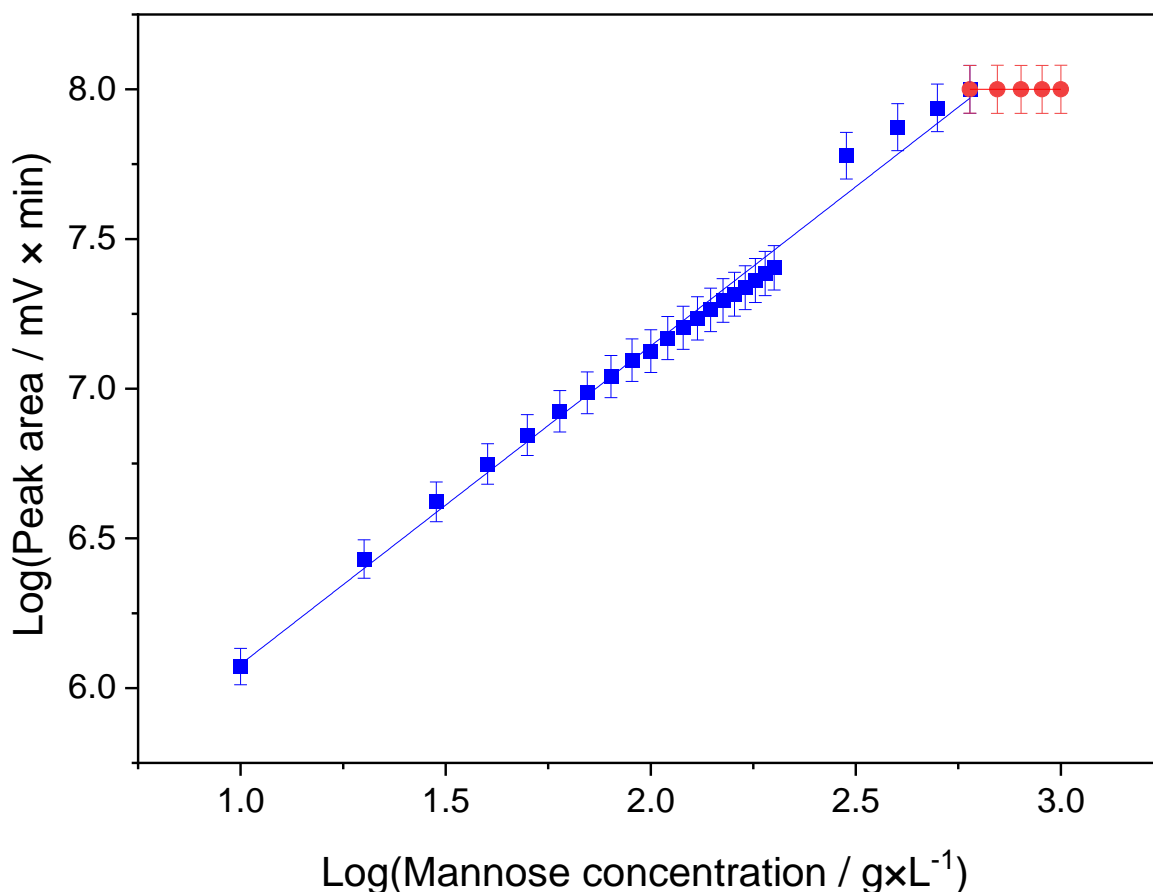


Figure A7. HPLC solubility diagram of mannose in water (10 – 1000 g·L⁻¹). A linear correlation between an HPLC peak area and the sample concentration is expected within the solubility limit (■), whereas as expected a constant saturation value was detected upon saturation and by analysing the surfactant solution (●).

Regression parameters of 1.06 ± 0.02 and 5.01 ± 0.04 for the slope and intercept of the regression line before the saturation point (blue line), as well as regression parameters of $(-5.18 \times 10^{-15} \pm 2.22 \times 10^{-15})$ and $8.00 \pm 6.51 \times 10^{-15}$ for the slope and intercept of the regression line after the saturation point (red line) were obtained and used in the calculation of solubility values.

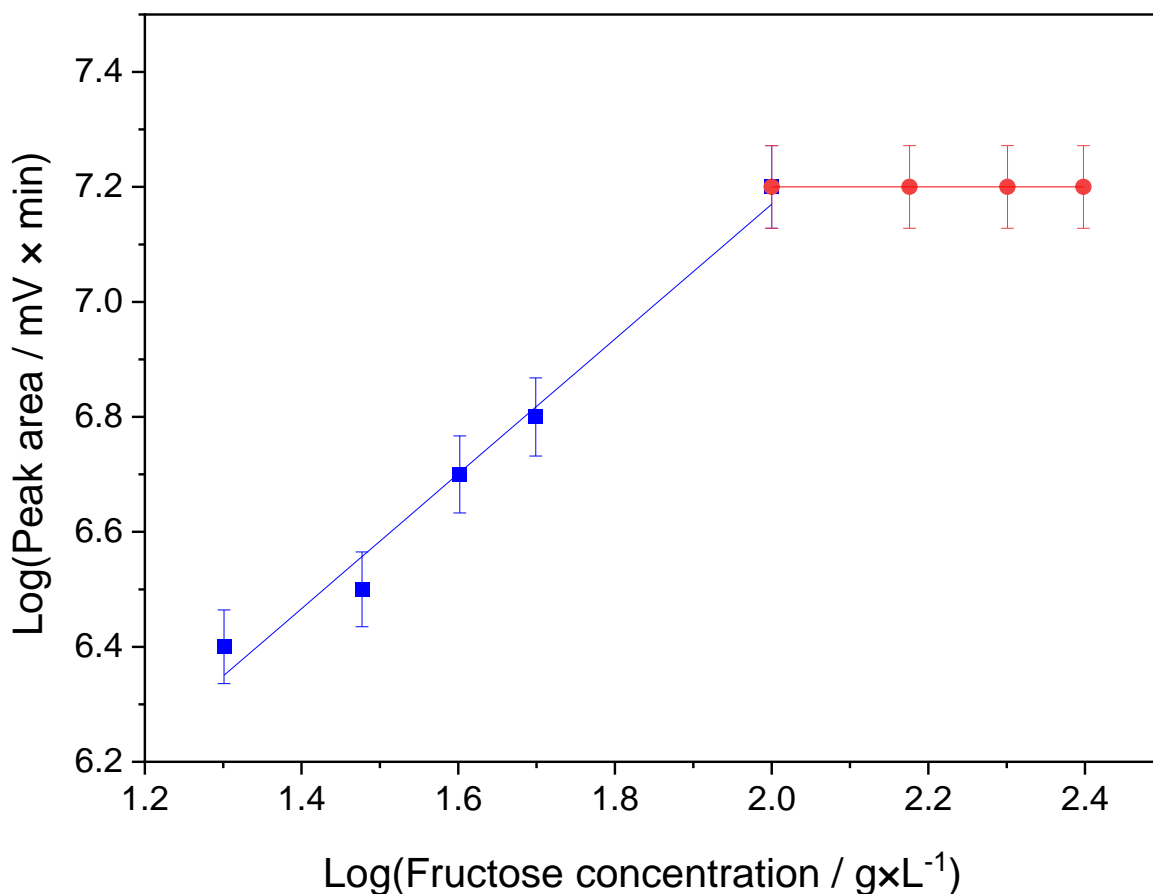


Figure A8. HPLC solubility diagram of fructose in methanol (10 – 250 g·L⁻¹). A linear correlation between an HPLC peak area and the sample concentration is expected within the solubility limit (■), whereas as expected a constant saturation value was detected upon saturation and by analysing the surfactant solution (●).

Regression parameters of 1.17 ± 0.09 and 4.82 ± 0.15 for the slope and intercept of the regression line before the saturation point (blue line), as well as regression parameters of $(0.00 \pm 4.22 \times 10^{-15})$ and $7.92 \pm 9.39 \times 10^{-15}$ for the slope and intercept of the regression line after the saturation point (red line) were obtained and used in the calculation of solubility values.

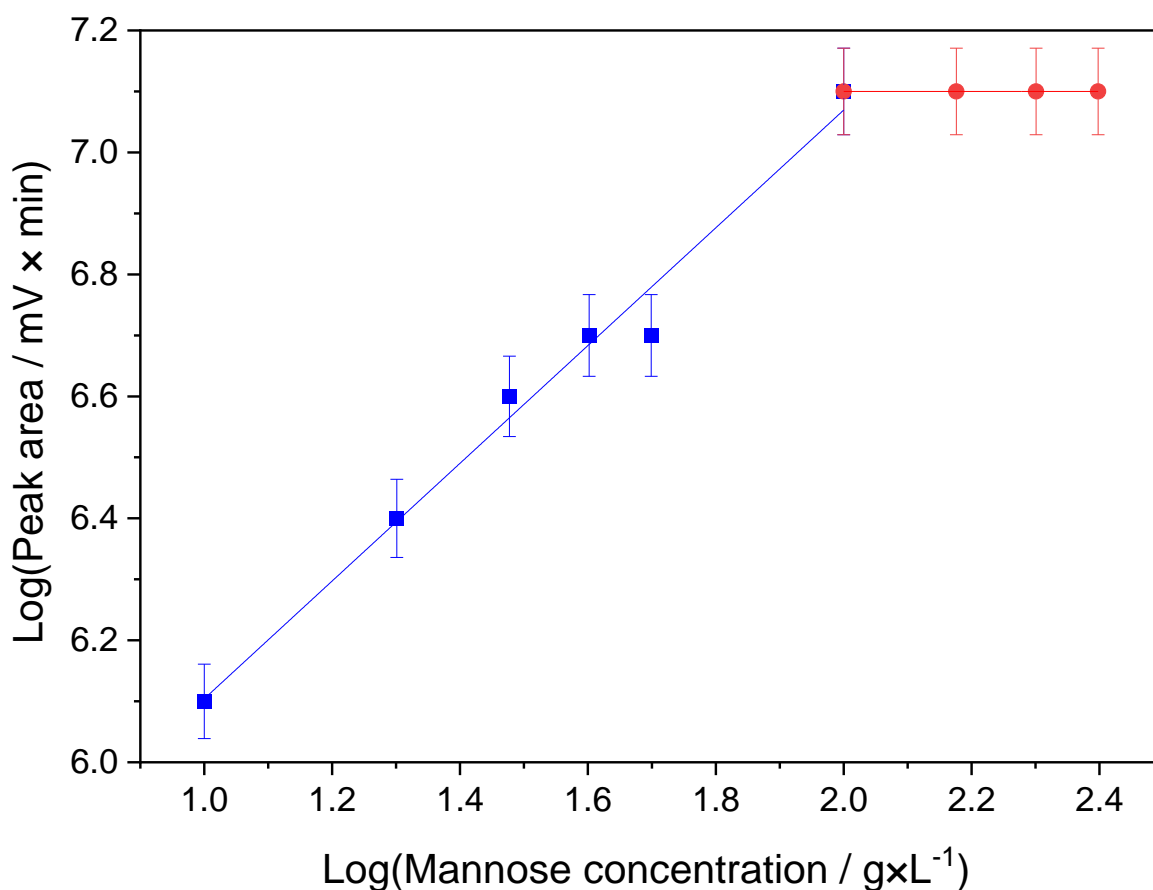


Figure A9. HPLC solubility diagram of mannose in methanol (10 – 250 g·L⁻¹). A linear correlation between an HPLC peak area and the sample concentration is expected within the solubility limit (■), whereas as expected a constant saturation value was detected upon saturation and by analysing the surfactant solution (●).

Regression parameters of 0.96 ± 0.06 and 5.14 ± 0.09 for the slope and intercept of the regression line before the saturation point (blue line), as well as regression parameters of $(4.98 \times 10^{-15} \pm 2.19 \times 10^{-15})$ and $7.10 \pm 4.88 \times 10^{-15}$ for the slope and intercept of the regression line after the saturation point (red line) were obtained and used in the calculation of solubility values.

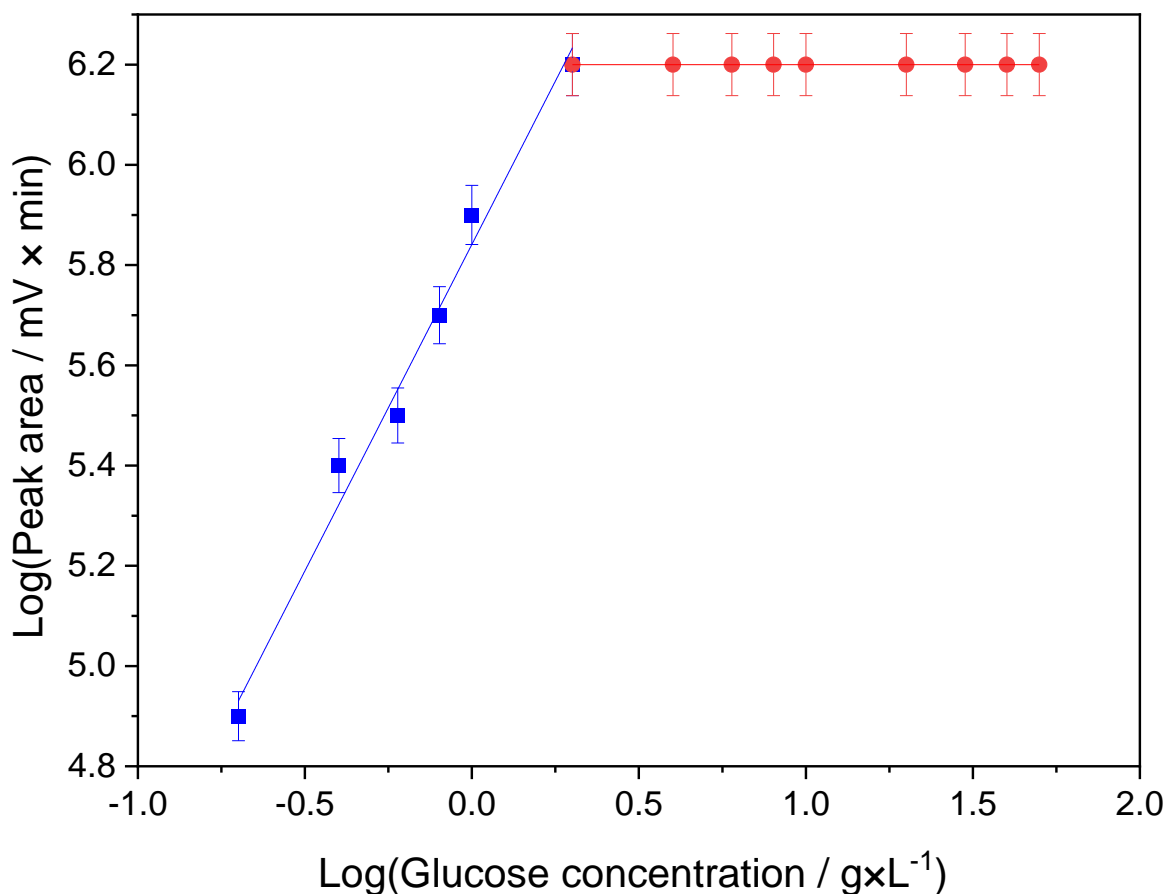


Figure A10. HPLC solubility diagram of glucose in ethanol ($0.2 - 50 \text{ g}\cdot\text{L}^{-1}$). A linear correlation between an HPLC peak area and the sample concentration is expected within the solubility limit (■), whereas as expected a constant saturation value was detected upon saturation and by analysing the surfactant solution (●).

Regression parameters of 1.30 ± 0.08 and 5.84 ± 0.03 for the slope and intercept of the regression line before the saturation point (blue line), as well as regression parameters of $(-1.12 \times 10^{-30} \pm 7.45 \times 10^{-16})$ and $6.20 \pm 8.68 \times 10^{-16}$ for the slope and intercept of the regression line after the saturation point (red line) were obtained and used in the calculation of solubility values.

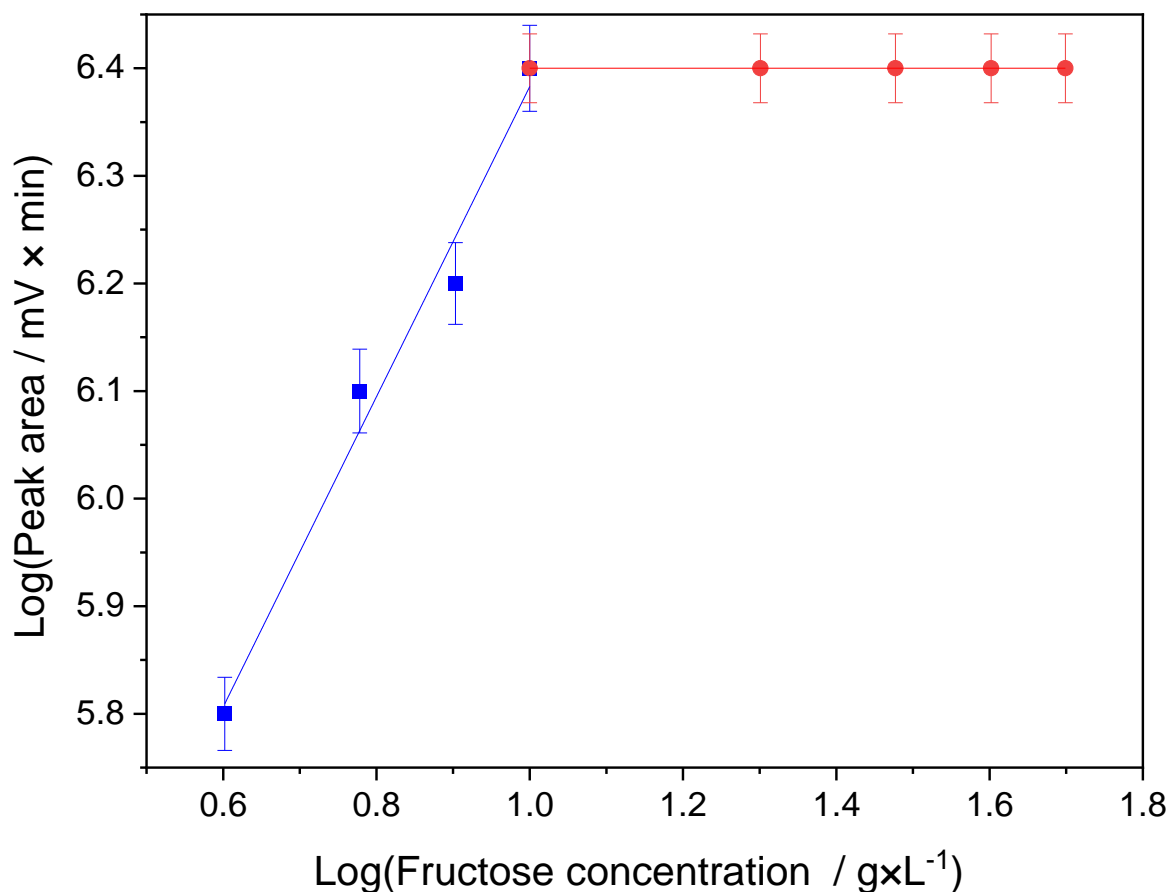


Figure A11. HPLC solubility diagram of fructose in ethanol ($2 - 50 \text{ g}\cdot\text{L}^{-1}$). A linear correlation between an HPLC peak area and the sample concentration is expected within the solubility limit (■), whereas as expected a constant saturation value was detected upon saturation and by analysing the surfactant solution (●).

Regression parameters of 1.44 ± 0.14 and 4.94 ± 0.12 for the slope and intercept of the regression line before the saturation point (blue line), as well as regression parameters of $(2.77 \times 10^{-15} \pm 1.03 \times 10^{-15})$ and $6.40 \pm 1.47 \times 10^{-15}$ for the slope and intercept of the regression line after the saturation point (red line) were obtained and used in the calculation of solubility values.

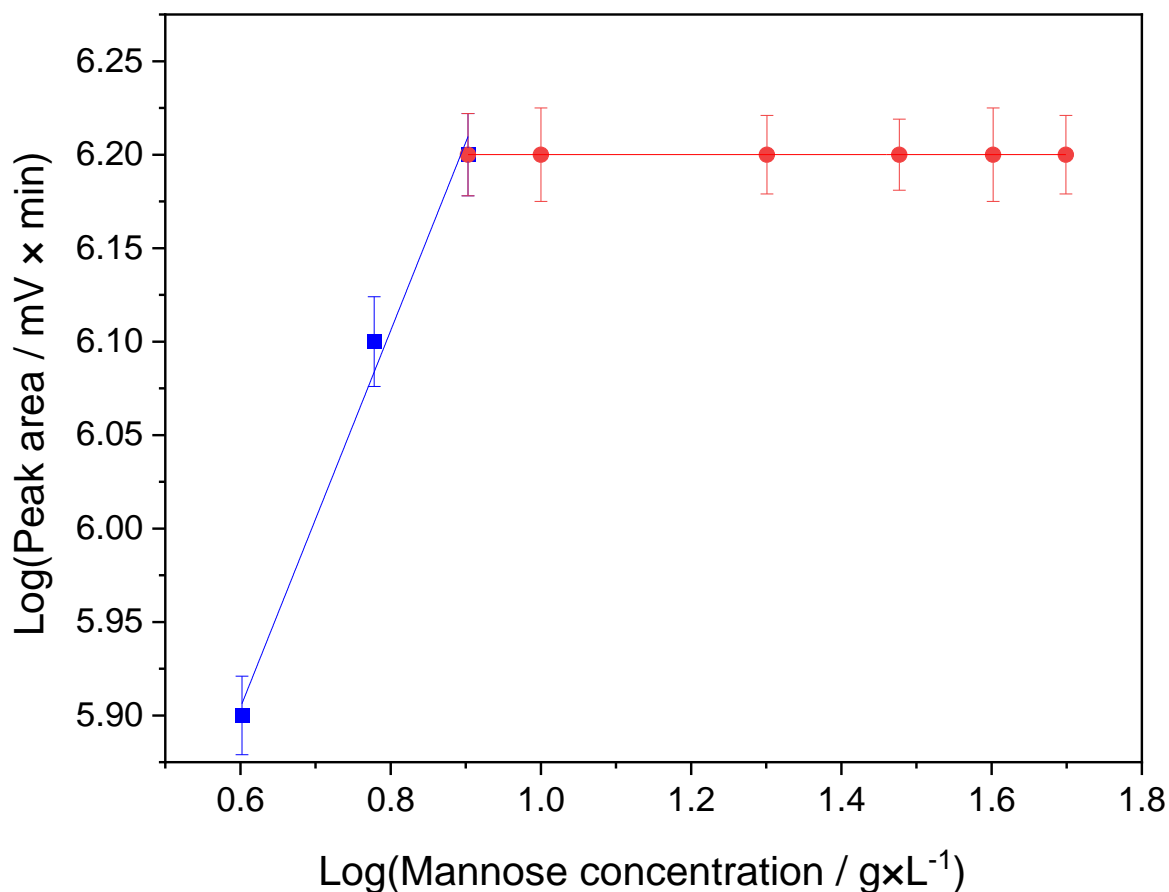


Figure A12. HPLC solubility diagram of mannose in ethanol (2 – 50 g·L⁻¹). A linear correlation between an HPLC peak area and the sample concentration is expected within the solubility limit (■), whereas as expected a constant saturation value was detected upon saturation and by analysing the surfactant solution (●).

Regression parameters of 1.01 ± 0.09 and 5.30 ± 0.07 for the slope and intercept of the regression line before the saturation point (blue line), as well as regression parameters of $(8.34 \times 10^{-31} \pm 1.50 \times 10^{-15})$ and $6.20 \pm 2.05 \times 10^{-15}$ for the slope and intercept of the regression line after the saturation point (red line) were obtained and used in the calculation of solubility values.

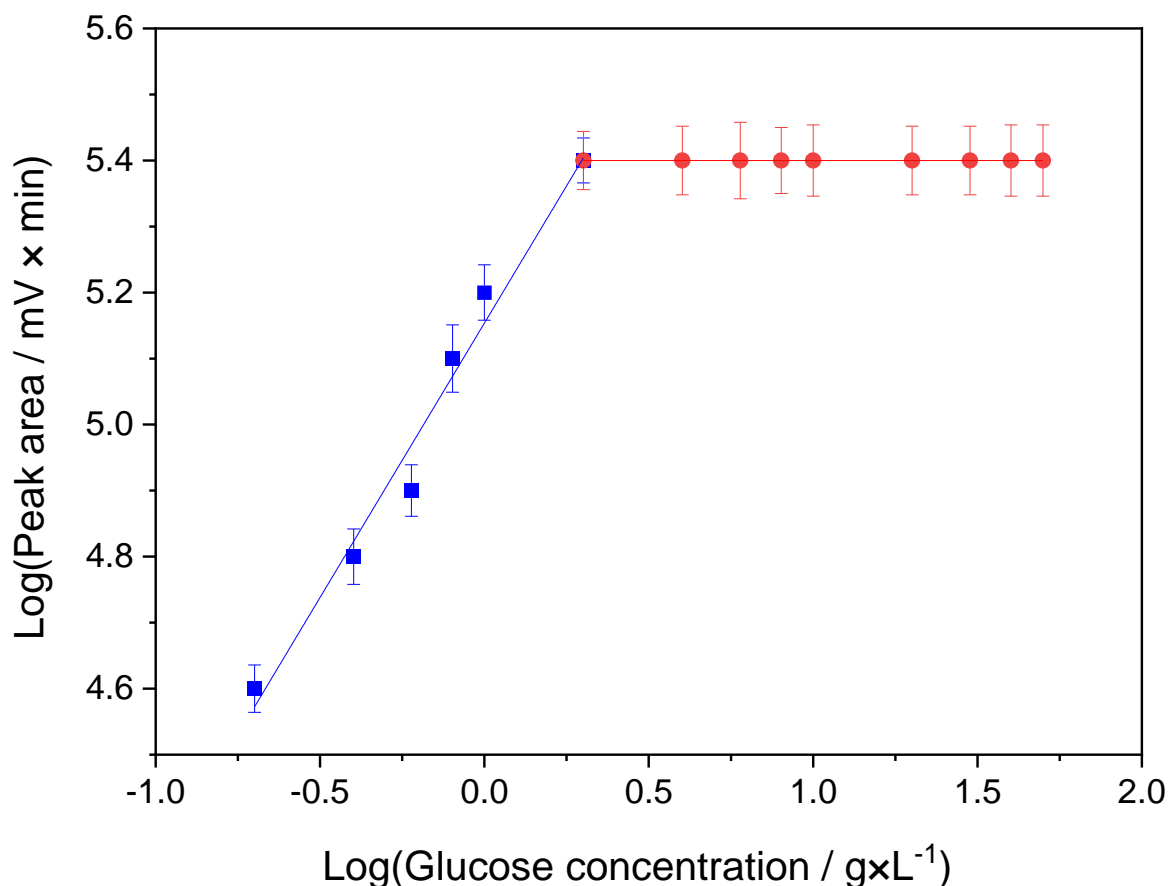


Figure A13. HPLC solubility diagram of glucose in 1-propanol ($0.2 - 50 \text{ g}\cdot\text{L}^{-1}$). A linear correlation between an HPLC peak area and the sample concentration is expected within the solubility limit (■), whereas as expected a constant saturation value was detected upon saturation and by analysing the surfactant solution (●).

Regression parameters of 0.83 ± 0.06 and 5.15 ± 0.02 for the slope and intercept of the regression line before the saturation point (blue line), as well as regression parameters of $(1.61 \times 10^{-31} \pm 7.45 \times 10^{-15})$ and $5.40 \pm 8.68 \times 10^{-16}$ for the slope and intercept of the regression line after the saturation point (red line) were obtained and used in the calculation of solubility values.

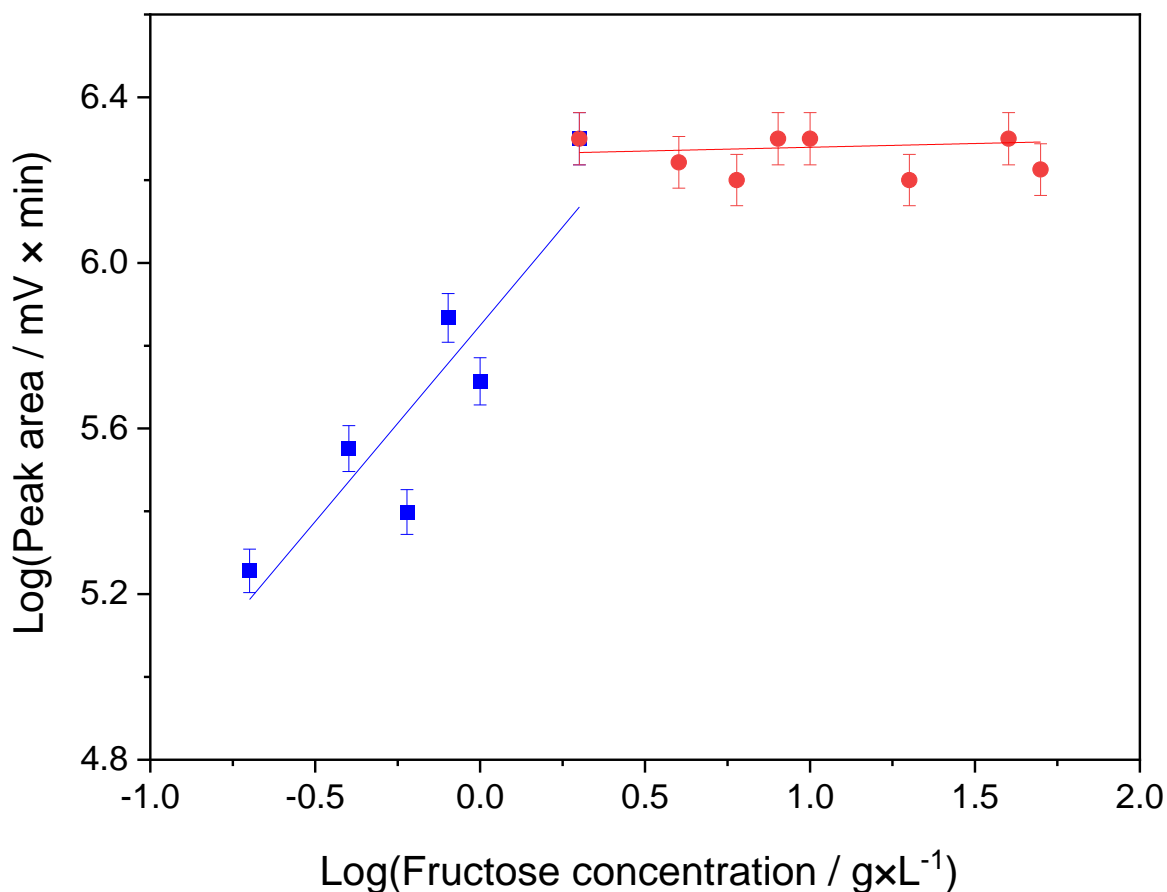


Figure A14. HPLC solubility diagram of fructose in 1-propanol ($0.2 - 50 \text{ g}\cdot\text{L}^{-1}$). A linear correlation between an HPLC peak area and the sample concentration is expected within the solubility limit (■), whereas as expected a constant saturation value was detected upon saturation and by analysing the surfactant solution (●).

Regression parameters of 0.96 ± 0.20 and 5.85 ± 0.09 for the slope and intercept of the regression line before the saturation point (blue line), as well as regression parameters of 0.02 ± 0.07 and 6.26 ± 0.09 for the slope and intercept of the regression line after the saturation point (red line) were obtained and used in the calculation of solubility values.

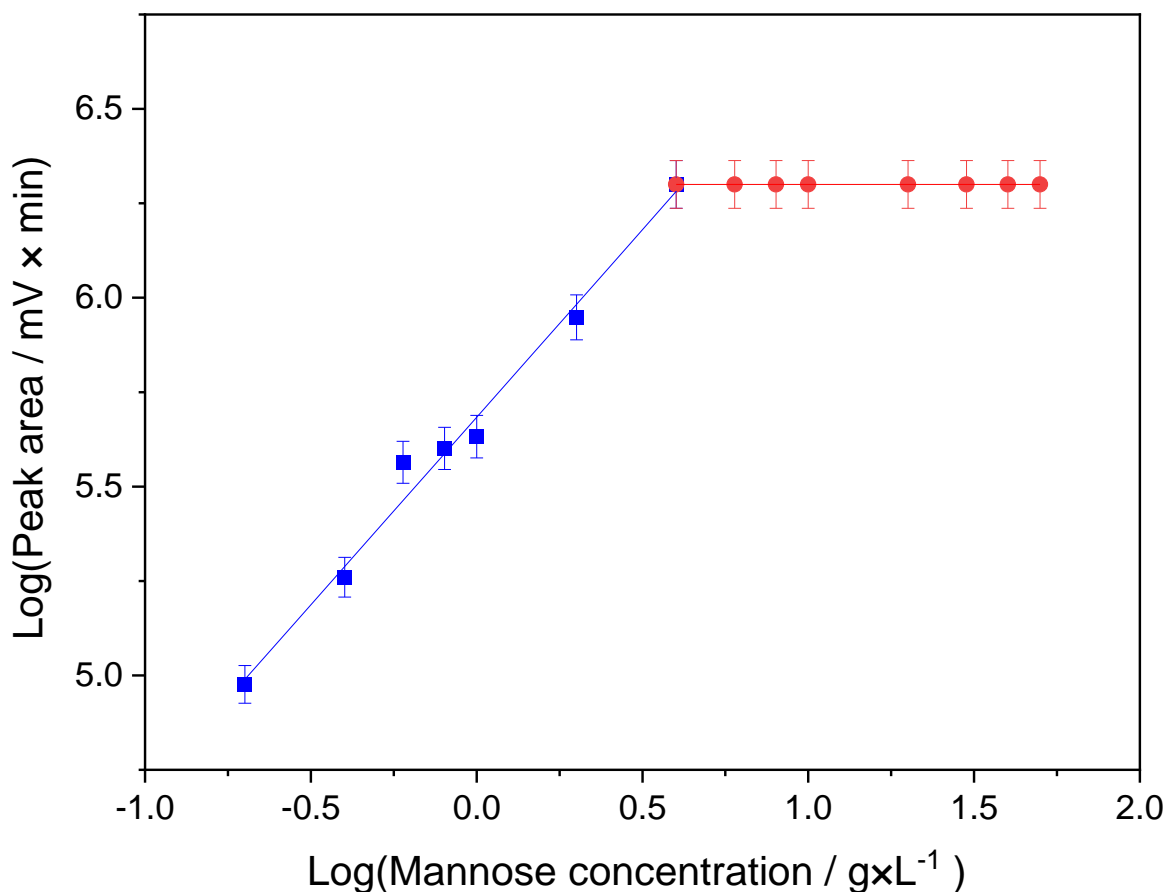


Figure A15. HPLC solubility diagram of mannose in 1-propanol (0.2 – 50 g·L⁻¹). A linear correlation between an HPLC peak area and the sample concentration is expected within the solubility limit (■), whereas as expected a constant saturation value was detected upon saturation and by analysing the surfactant solution (●).

Regression parameters of 0.99 ± 0.05 and 5.68 ± 0.02 for the slope and intercept of the regression line before the saturation point (blue line), as well as regression parameters of $(-8.68 \times 10^{-31} \pm 9.55 \times 10^{-16})$ and $6.30 \pm 1.17 \times 10^{-15}$ for the slope and intercept of the regression line after the saturation point (red line) were obtained and used in the calculation of solubility values.

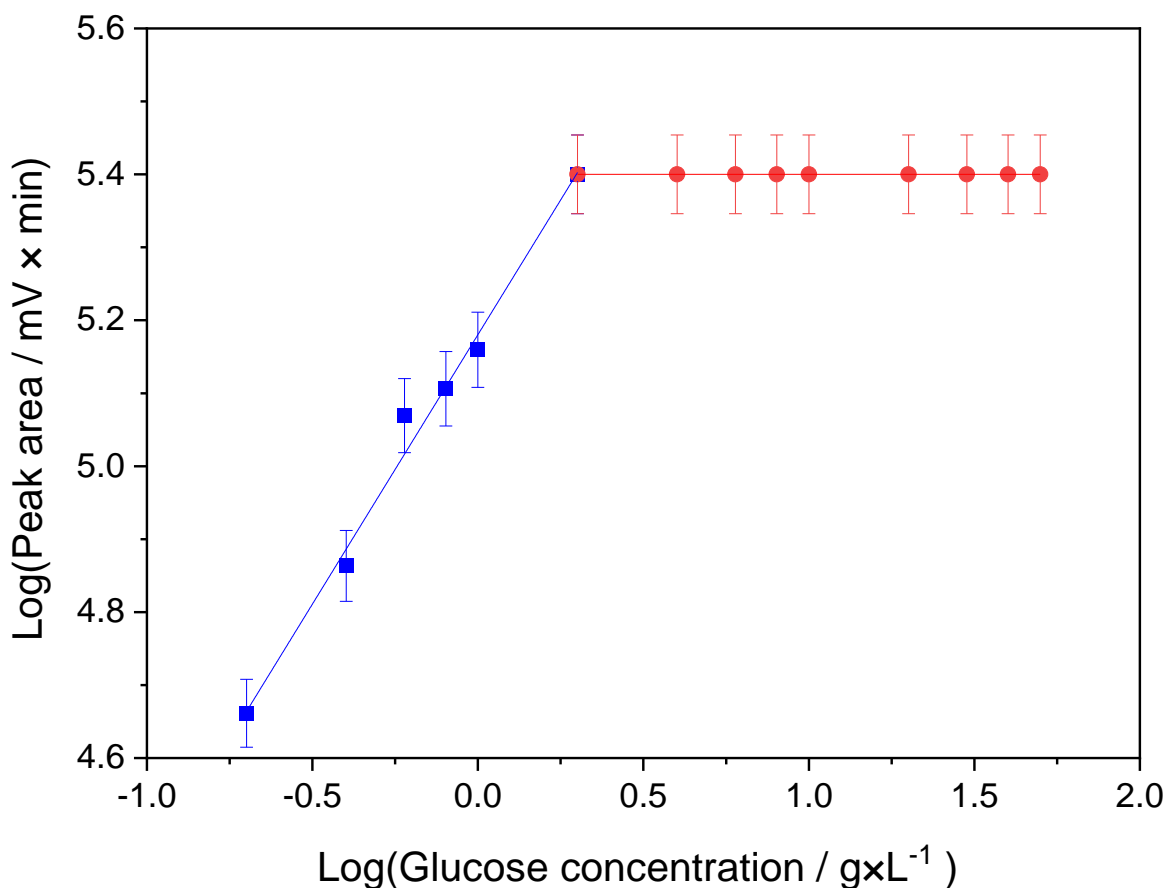


Figure A16. HPLC solubility diagram of glucose in 2-propanol ($0.2 - 50 \text{ g}\cdot\text{L}^{-1}$). A linear correlation between an HPLC peak area and the sample concentration is expected within the solubility limit (■), whereas as expected a constant saturation value was detected upon saturation and by analysing the surfactant solution (●).

Regression parameters of 0.74 ± 0.04 and 5.18 ± 0.01 for the slope and intercept of the regression line before the saturation point (blue line), as well as regression parameters of $(-1.61 \times 10^{-31} \pm 7.45 \times 10^{-16})$ and $5.40 \pm 8.68 \times 10^{-16}$ for the slope and intercept of the regression line after the saturation point (red line) were obtained and used in the calculation of solubility values.

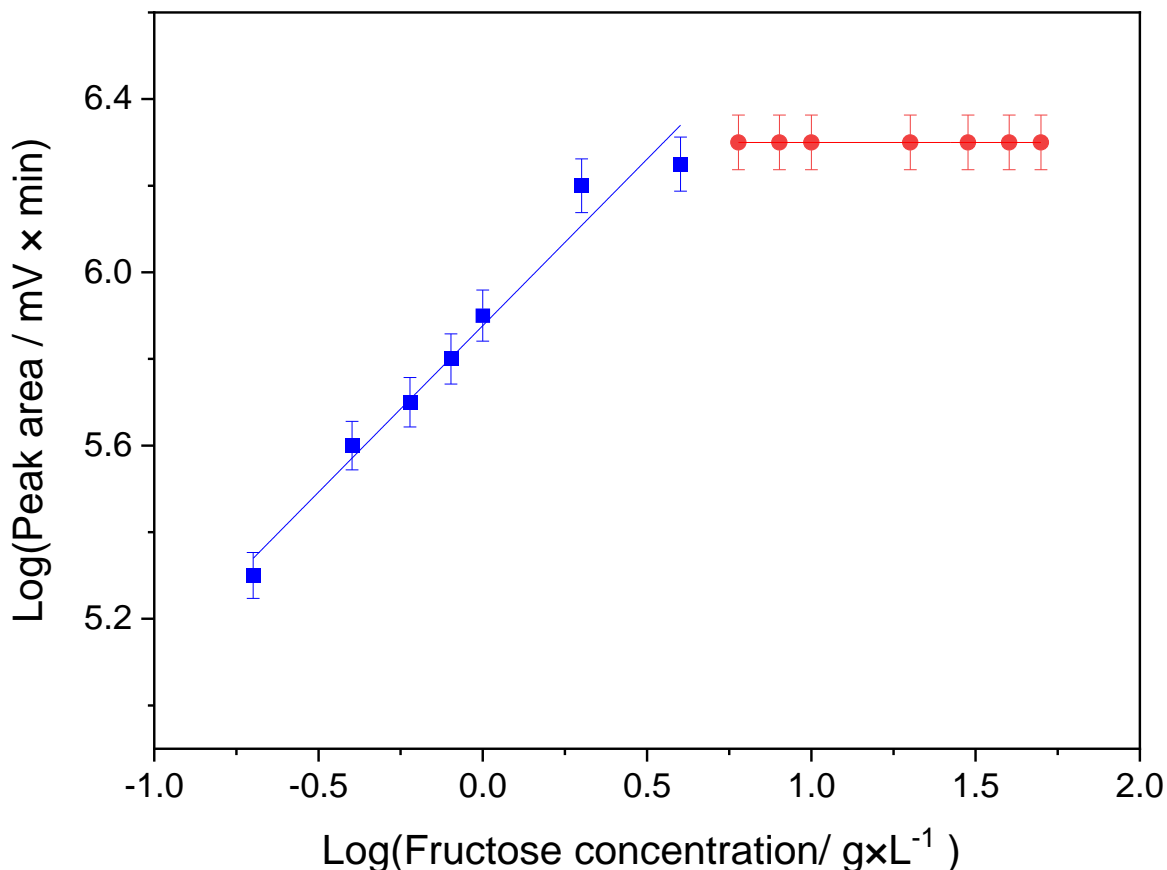


Figure A17. HPLC solubility diagram of fructose in 2-propanol ($0.2 - 50 \text{ g}\cdot\text{L}^{-1}$). A linear correlation between an HPLC peak area and the sample concentration is expected within the solubility limit (■), whereas as expected a constant saturation value was detected upon saturation and by analysing the surfactant solution (●).

Regression parameters of 0.77 ± 0.06 and 5.88 ± 0.02 for the slope and intercept of the regression line before the saturation point (blue line), as well as regression parameters of $(2.85 \times 10^{-15} \pm 1.81 \times 10^{-15})$ and $6.30 \pm 2.34 \times 10^{-15}$ for the slope and intercept of the regression line after the saturation point (red line) were obtained and used in the calculation of solubility values.

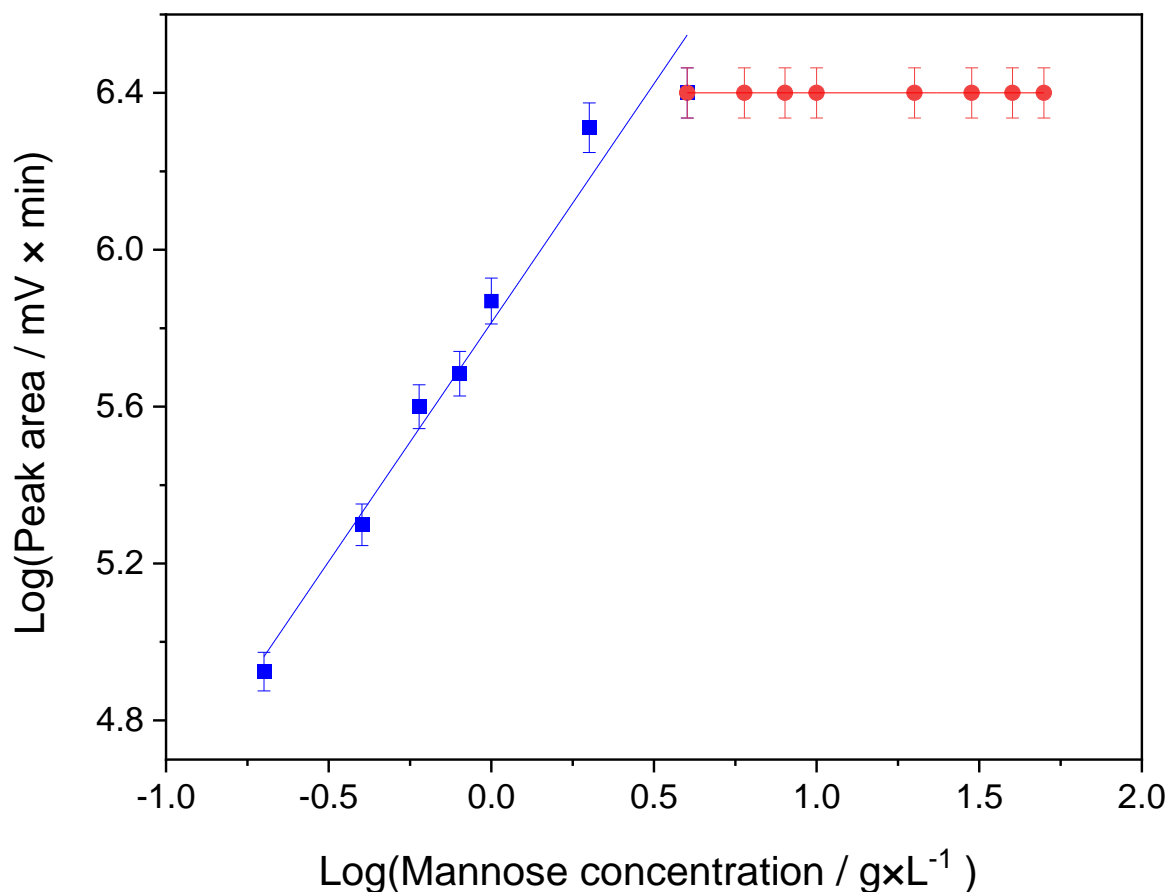


Figure A18. HPLC solubility diagram of mannose in 2-propanol (0.2 – 50 g·L⁻¹). A linear correlation between an HPLC peak area and the sample concentration is expected within the solubility limit (■), whereas as expected a constant saturation value was detected upon saturation and by analysing the surfactant solution (●).

Regression parameters of 1.22 ± 0.08 and 5.81 ± 0.04 for the slope and intercept of the regression line before the saturation point (blue line), as well as regression parameters of 0.00 ± 0.00 and 6.40 ± 0.00 for the slope and intercept of the regression line after the saturation point (red line), were obtained and used in the calculation of solubility values.

A.4 Density Determinations of Saturated Sugar Solutions in Water and Alcohols.

Table A1. Density measurements of sugar solutions at their saturation points in water, methanol, ethanol, 1-propanol, and 2-propanol at room temperature together with the density of pure solvents.

solvent	Density of pure solvents (g·mL ⁻¹)	Sugar	Density of sugar solution (g·mL ⁻¹)
Water	1.000 ± 0.005	Glucose	1.136 ± 0.003
		Fructose	1.192 ± 0.006
		Mannose	1.182 ± 0.005
Methanol	0.750 ± 0.002	Glucose	0.760 ± 0.006
		Fructose	0.776 ± 0.001
		Mannose	0.773 ± 0.001
Ethanol	0.755 ± 0.003	Glucose	0.758 ± 0.003
		Fructose	0.761 ± 0.004
		Mannose	0.760 ± 0.010
1-propanol	0.763 ± 0.001	Glucose	0.770 ± 0.002
		Fructose	0.779 ± 0.002
		Mannose	0.779 ± 0.002
2-propanol	0.750 ± 0.002	Glucose	0.757 ± 0.002
		Fructose	0.770 ± 0.001
		Mannose	0.757 ± 0.002

A.5 Catalytic Activity Data for Glucose Isomerisation Reaction in Yields.

Table A2. Catalytic tests with yield data for the isomerization of glucose to fructose in methanol, using HY, Sn/Y and Ga/Y catalysts. The tests were carried out using 125 mg of the substrate in 4 mL of CH₃OH at the specified reaction temperature for 1 h and endogenous pressure using a constant metal-to-substrate molar ratio M:S = 1:100.

T (°C)	Catalyst	Yield (%)		
		Fructose	Methyl Fructoside	Mannose
120	HY	19	34	19
100	HY	27	31	32
90	HY	14	44	9
80	HY	7	38	3
120	Sn/Y	17	33	15
100	Sn/Y	22	32	26
90	Sn/Y	13	46	7
80	Sn/Y	13	34	3
120	Ga/Y	15	21	13

100	Ga/Y	23	36	27
90	Ga/Y	13	40	5
80	Ga/Y	9	42	3

Table A3. Catalytic tests with data in yields for the isomerization of glucose to fructose in methanol followed by the addition of water in a two-step procedure using HY, Sn/Y and Ga/Y catalysts. The tests were carried out using 125 mg of the substrate in 4 mL of CH₃OH at a reaction temperature for 1 h and endogenous pressure, and then adding 4 mL of H₂O for an additional reaction time of 1 h at a constant metal-to-substrate molar ratio M:S = 1:100.

T (°C)	Catalyst	Yield (%)		
		Fructose	Methyl Fructoside	Mannose
120	HY	40	13	21
100	HY	32	21	27
90	HY	16	39	9
80	HY	9	28	2
120	Sn/Y	34	12	15
100	Sn/Y	35	17	17
90	Sn/Y	14	39	6
80	Sn/Y	12	33	1
120	Ga/Y	41	8	13
100	Ga/Y	47	17	21
90	Ga/Y	14	36	4
80	Ga/Y	9	42	3

Table A4. Catalytic tests with data for the isomerization of glucose to fructose followed a one-step reaction protocol in methanol and a two-step protocol in methanol followed by adding water using HY, Sn/Y and Ga/Y catalysts. The tests were carried out using 125 mg of the substrate in 4 mL of CH₃OH at a reaction temperature at specified reaction times in min and endogenous pressure, and then adding 4 mL of H₂O for the specified reaction time (min) at a constant metal-to-substrate molar ratio M:S = 1:100

catalyst	One-step reaction Protocol					
	Time (min)	Glucose conversion (%)	Selectivity (%)			CMB (%)
			Fructose	MeFructoside	Mannose	
HY	10	61	6	84	9	102
	20	67	14	67	19	102
	30	77	20	53	26	101
	40	86	25	43	32	97
	50	87	26	41	33	96
	60	90	30	35	36	109

	120	89	29	35	37	102	
	Two steps reaction Protocol						
	10	86	34	29	37	99	
	20	88	39	25	36	94	
	30	88	39	25	36	93	
	40	86	38	26	36	92	
	50	86	38	26	36	92	
	60	86	40	26	35	93	
	120	81	31	40	30	95	
	One-step reaction Protocol						
Sn/Y	10	62	8	80	12	102	
	20	85	16	63	21	103	
	30	90	22	51	27	99	
	40	93	24	46	30	94	
	50	93	25	45	30	92	
	60	95	28	40	32	84	
	120	92	27	42	32	89	
		Two steps reaction Protocol					
	10	94	43	25	32	76	
	20	93	50	19	32	77	
	30	93	50	21	30	75	
	40	92	49	22	29	77	
	50	91	49	23	28	81	
	60	90	50	25	25	77	
	120	84	40	39	21	83	
	One-step reaction Protocol						
Ga/Y	10	61	5	87	7	99	
	20	74	11	74	15	105	
	30	84	18	59	18	104	
	40	90	21	53	26	101	
	50	94	26	43	32	95	
	60	94	27	42	31	91	
	120	94	26	43	31	89	
		Two steps reaction Protocol					
	10	93	38	31	30	83	
	20	92	50	20	29	82	
	30	91	51	21	28	82	
	40	92	51	21	28	84	
	50	90	51	22	27	87	
	60	91	55	20	25	93	
	120	85	47	31	23	88	

Table A5. Catalytic tests with data in yields for the isomerisation of glucose to fructose followed a one-step reaction protocol in methanol and a two-step protocol in methanol and water using various zeolite-based catalysts. The tests were carried out using 125 mg of the substrate in 4 mL of CH₃OH at a reaction temperature at specified reaction times in min and endogenous pressure, and then adding 4 mL of H₂O for the specified reaction time (min) at a constant metal-to-substrate molar ratio M:S = 1:100

Catalyst	Yield (%)					
	One step			Two steps		
	Fructose	MeF	Mannose	Fructose	MeF	Mannose
HY 5	17	55	17	27	41	14
Sn/Y 5	13	55	14	29	30	10
Ga/Y 5	10	61	9	21	39	7
Nb/Y 5	12	58	11	27	34	9
HY 30	29	33	33	32	21	28
Sn/Y 30	22	32	26	35	17	17
Ga/Y 30	23	36	27	47	17	21
Nb/Y 30	22	39	23	43	19	19
H-Beta 25	4	38	4	4	35	4
Sn/beta 25	23	39	28	42	16	19
Ga/beta 25	24	44	28	53	14	22
Nb/beta 25	16	50	16	36	10	11
H-Beta 38	4	30	5	3	30	3
Sn/beta 38	25	34	34	34	26	21
Ga/beta 38	30	28	38	26	23	28
Nb/beta 38	25	38	30	43	19	27
HZSM-5 23	0	35	0	0	40	0
Sn/ZSM-5 23	10	40	8	9	35	7
Ga/ZSM-5 23	11	38	11	7	41	4
Nb/ZSM-5 23	6	46	6	4	43	5
HZSM-5 50	0	36	0	0	32	0
Sn/ZSM-5 50	12	39	10	12	36	8
Ga/ZSM-5 50	9	46	9	7	44	4
Nb/ZSM-5 50	9	44	8	9	38	8
Al-MCM-41	17	45	16	15	48	13
Sn/Al-MCM-41	21	54	21	47	20	16
Ga/Al-MCM-41	21	45	22	22	34	18
Nb/Al-MCM-41	23	40	27	21	33	24

A.6 Powder X-ray Diffraction of Sn-, Ga-doped on SiO₂ and Al₂O₃.

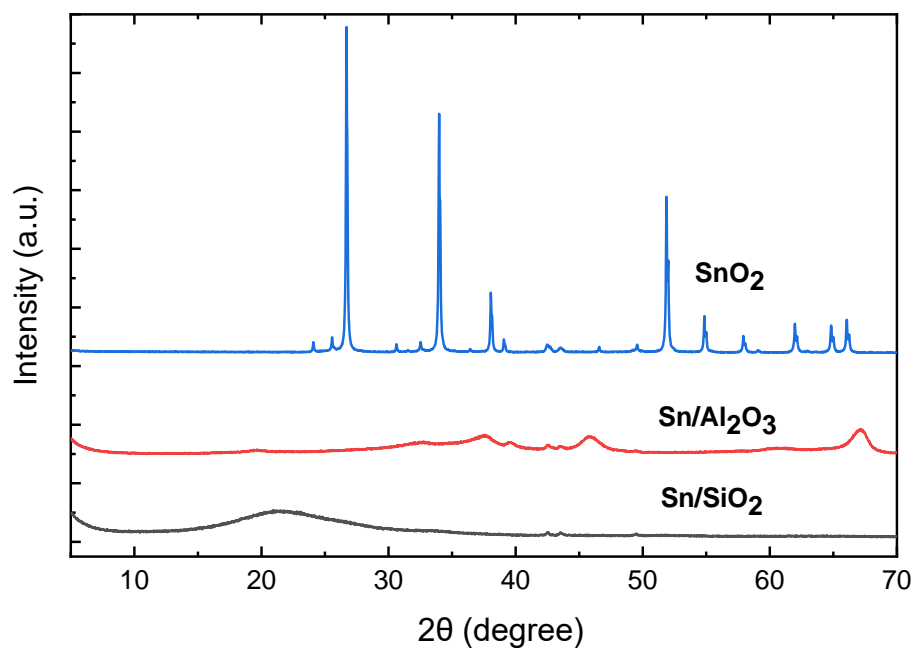


Figure A19. XRPD patterns of control test materials: (a) Sn/SiO₂ and (b) Sn/Al₂O₃, both prepared *via* wetness impregnation, and (c) SnO₂ for pattern comparison.

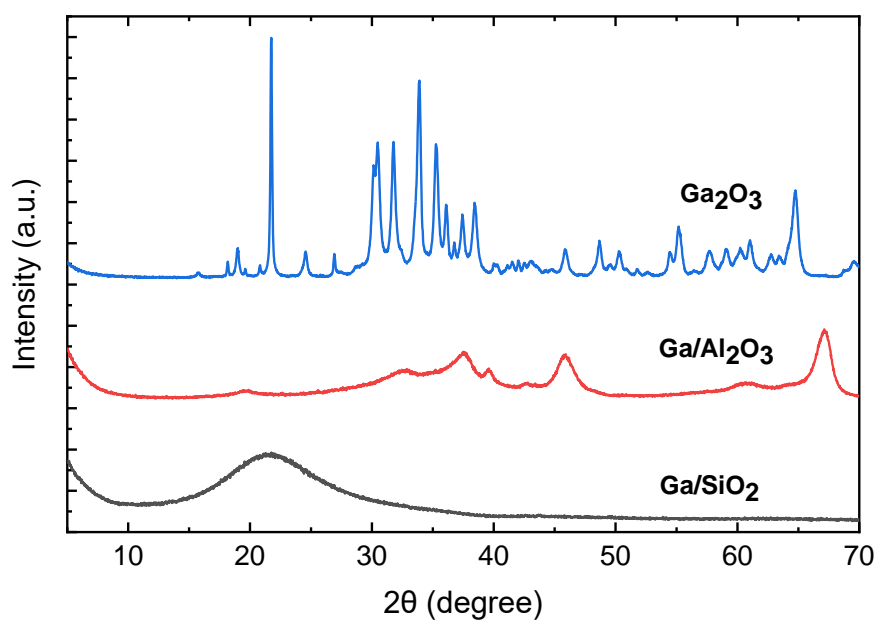


Figure A20. XRPD patterns of control test materials: (a) Ga/SiO₂ and (b) Ga/Al₂O₃, both prepared *via* wetness impregnation and (c) Ga₂O₃ for pattern comparison.

A.7 Diffuse Reflectance Infrared Fourier Transform (DRIFT) Spectroscopy Measurements.

In situ DRIFTS measurements were performed with a Bruker Vertex 70 FTIR spectrometer equipped with a liquid N₂-cooled detector. Approximately 25 mg of the catalyst sample of interest was placed in a ceramic crucible in the DRIFTS cell. Prior to the experiments, the catalyst was pre-treated by heating in Ar with a total flow rate of 50 cm³ min⁻¹ up to 400 °C for 1 h and then cooled down in flowing Ar to 35 °C. The IR spectrum of the catalyst at 35 °C under flowing Ar was taken as a background.

Gaseous pyridine in Ar then flowed over the catalyst with a total flow rate of 50 cm³ min⁻¹ (Ar flow = 30 cm³ min⁻¹, pyridine flow = 20 cm³ min⁻¹) for 60 minutes. The temperature of the DRIFTS cell was then increased in increments of up to 150 °C. The use of pyridine was preferred to the use of ammonia as the latter can decompose over Al centres in the presence of residual oxygen¹.

In situ DRIFTS spectra were recorded with a resolution of 4 cm⁻¹ and with the accumulation of 128 scans every 60 s during transient switches. The DRIFTS spectra were analysed using the OPUS software.

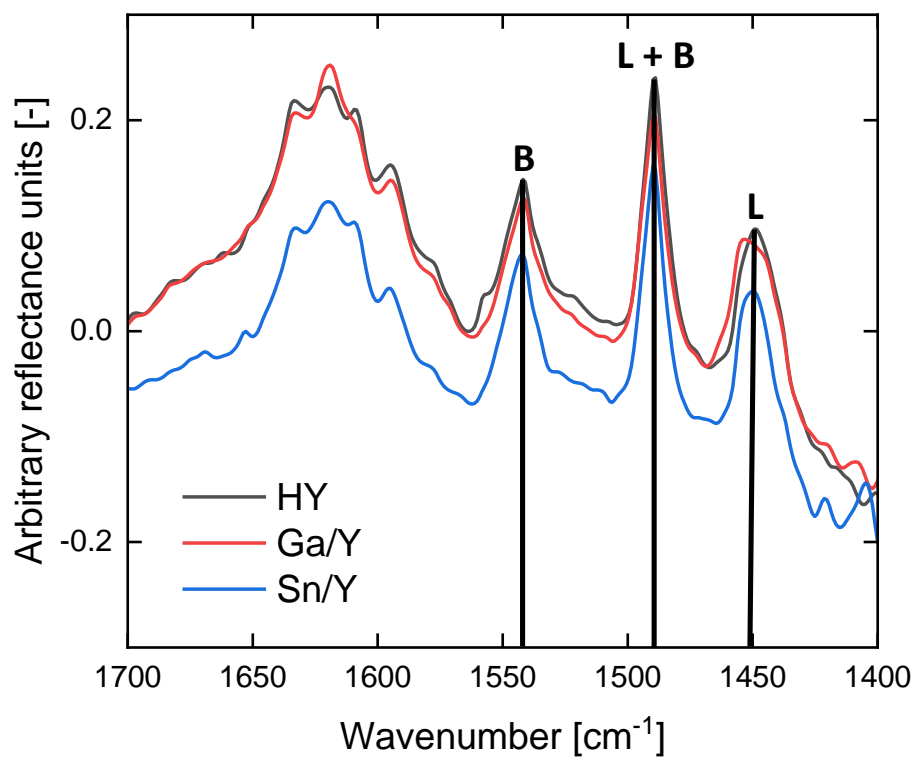


Figure A21. DRIFT spectra of HY (black line), Sn/Y (blue line) and Ga/Y (red line). The samples were pre-treated with Ar and then adsorbed with pyridine at 150 °C. Black lines represent the band position for Brønsted acids sites (B), Lewis acid sites (L) and combined Brønsted and Lewis (B + L) acid sites².

A.8 Unit cell calculations of powder X-ray patterns for HY, Sn/Y and Ga/Y zeolites.

Table A6. Rietveld refinement of HY, as delivered, dummy HY, Sn/Y and Ga/Y with SiO₂:Al₂O₃ molar ratio of 30. Fitting parameters were: zero shift; scale factor; B overall; unit cell parameters: *a*, *b*, *c*, α , β , γ ; profile parameters: U, V, W and asymmetry peak shape 1. The sign (+) stands for an expansion and the sign (-) stands for a contraction with respect to the undoped zeolite.

Material	Unit cell parameters					Expansion or contraction
	<i>a</i> (Å) ± 0.001	<i>b</i> (Å) ± 0.001	<i>c</i> (Å) ± 0.001	$\alpha = \beta = \gamma = 90^\circ \pm 0.001$	<i>V</i> (Å ³) ± 1	
HY	24.308	24.308	24.308	90.00	14363	--
HY-dummy (*)	24.290	24.290	24.290	90.00	14330	- 0.2
Sn/Y	24.299	24.299	24.299	90.00	14346	- 0.1
Ga/Y	24.304	24.304	24.304	90.00	14356	0.0

(*) HY zeolite is treated for metal doping but without adding any metal.

A.9 EXFAS data analysis for Sn/Y and Ga/Y zeolites.

Table A7. EXFAS data analysis for Sn/Y. Fitting parameters for Sn/Y data using a SnO₂ model for incorporating Sn over the zeolite structure.

Main EXAFS contributions	CN	EXAFS Distance (Å)	XRD distance (Å)	σ^2 Debye-Waller (Å ²)	S ₀ ²	ΔE_0 (eV)	R-factor
Sn – O	6	2.048 (5)	2.057	0.0042 (6)	0.90 (4)	4.6 (5)	0.026
Sn – Sn	2	3.22 (2)	3.201	0.0089 (7)	0.90 (4)	4.6 (5)	0.026
Sn – Sn	8	3.722 (8)	3.712	0.0089 (7)	0.90 (4)	4.6 (5)	0.026
Sn – Sn	4	4.73 (3)	4.737	0.0089 (7)	0.90 (4)	4.6 (5)	0.026

Table A8. EXFAS data analysis for Ga/Y. Fitting parameters for Ga/Y data using a Ga model with Ga species incorporated into the zeolite framework.

Main EXAFS contributions	CN	EXAFS Distance (Å)	XRD distance Yzeolite (Å)	XRD distance Ga T _d site Ga ₂ O ₃ (Å)	σ^2 Debye-Waller (Å ²)	S ₀ ²	ΔE_0 (eV)	R-factor
Ga – O	2	1.83 (1)	1.628 (Si-O)	1.833 (Ga-O)	0.008 (1)	1.2 (1)	2 (1)	0.021
Ga – O	2	1.86 (1)	1.658 (Si-O)	1.863 (Ga-O)	0.02 (7)	1.2 (1)	2 (1)	0.021
Ga - Si/Al (69/31%)	4	3.3 (2)	3.103/3.136 (Si-Si/Al)	3.037/3.289 (Ga-Ga)	0.02 (7)	1.2 (1)	2 (1)	0.021

A.10 Powder X-ray Diffraction of Sn-, Ga- and Nb-doped Zeolite Y (5.1 and 30), zeolite beta (38), ZSM-5 (50) and MCM-41.

Table A9. Rietveld refinement of HY as delivered, dummy Sn-, Ga-, and Nb-doped on zeolite BEA with a SiO₂:Al₂O₃ molar ratio of 25, alongside their parent undoped zeolites. Fitting parameters were: zero shift; scale factor; B overall; unit cell parameters: *a*, *b*, *c*, α , β , γ ; profile parameters: U, V, W and asymmetry peak shape 1. The sign (+) stands for an expansion and the sign (-) stands for a contraction with respect to the undoped zeolite.

Material	Unit cell parameters					Expansion or contraction
	<i>a</i> (Å)	<i>b</i> (Å)	<i>c</i> (Å)	$\alpha = \beta = \gamma = 90^\circ \pm 0.001$	<i>V</i> (Å ³) ± 1	
H-BEA	12.37 \pm 0.01	12.37 \pm 0.01	26.23 \pm 0.04	90.00	4013	--
H-BEA-dummy (*)	12.36 \pm 0.01	12.36 \pm 0.01	26.22 \pm 0.04	90.00	4003	- 0.2
Sn/BEA	12.33 \pm 0.01	12.33 \pm 0.01	26.16 \pm 0.04	90.00	3977	- 0.9
Ga/BEA	12.35 \pm 0.01	12.35 \pm 0.01	26.22 \pm 0.04	90.00	4002	- 0.3
Nb/BEA	12.35 \pm 0.01	12.35 \pm 0.01	26.19 \pm 0.04	90.00	3996	- 0.4

(*) H-BEA zeolite is treated for metal doping but without adding any metal.

Table A10. Rietveld refinement of HY as delivered, dummy Sn-, Ga-, and Nb-doped on ZSM-5 zeolite with a SiO₂:Al₂O₃ molar ratio of 23, alongside their parent undoped zeolites. Fitting parameters were: zero shift; scale factor; B overall; unit cell parameters: *a*, *b*, *c*, α , β , γ ; profile parameters: U, V, W and asymmetry peak shape 1. The sign (+) stands for an expansion and the sign (-) stands for a contraction with respect to the undoped zeolite.

Material	Unit cell parameters					Expansion or contraction
	<i>a</i> (Å)	<i>b</i> (Å)	<i>c</i> (Å)	$\alpha = \beta = \gamma = 90^\circ \pm 0.001$	<i>V</i> (Å ³) ± 1	
HZSM-5	20.102 \pm 0.004	20.102 \pm 0.004	20.102 \pm 0.003	90.00	5382	--
HZSM-5-dummy (*)	20.105 \pm 0.004	19.934 \pm 0.004	13.426 \pm 0.003	90.00	5382	0.0
Sn/ZSM-5	20.089 \pm 0.004	20.089 \pm 0.004	20.089 \pm 0.003	90.00	5380	0.0
Ga/ZSM-5	20.104 \pm 0.004	19.940 \pm 0.004	13.426 \pm 0.003	90.00	5382	0.0
Nb/ZSM-5	20.104 \pm 0.004	19.937 \pm 0.004	13.411 \pm 0.003	90.00	5375	- 0.1

(*) HZSM-5 zeolite is treated for metal doping but without adding any metal.

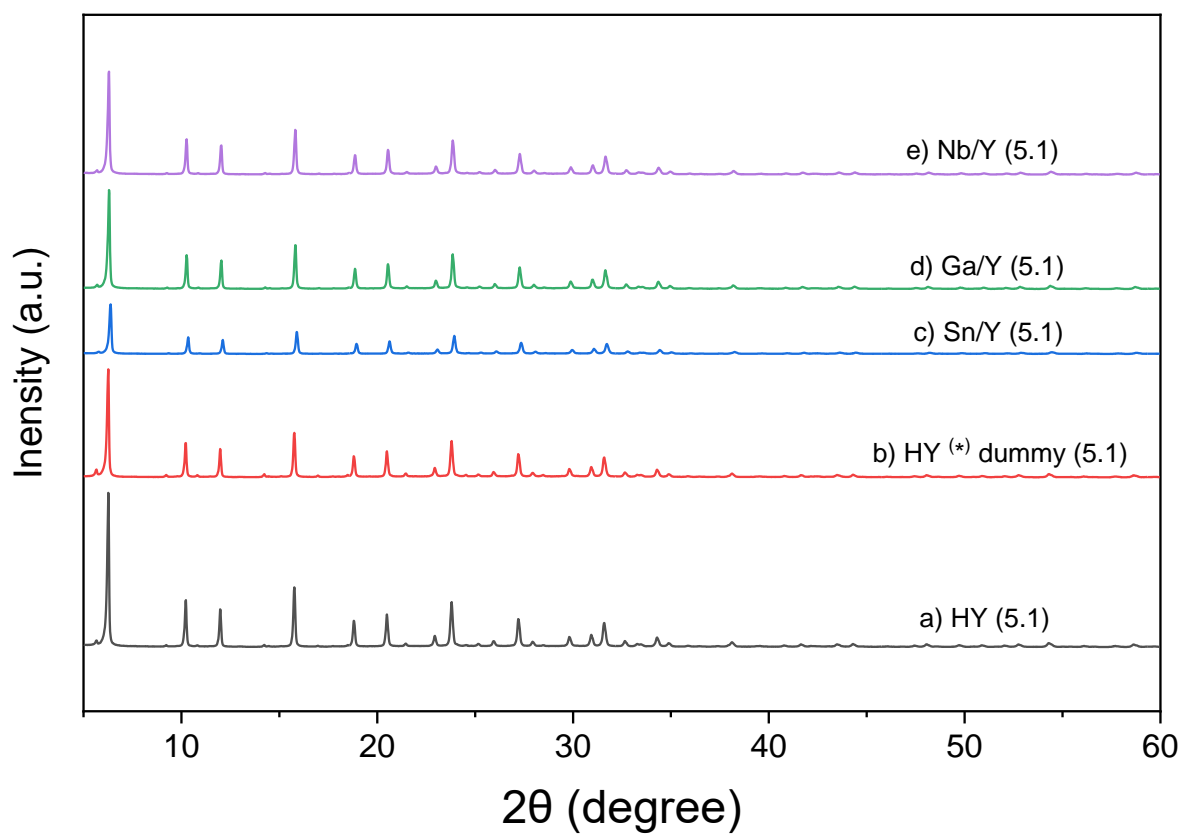


Figure A22. X-ray powder diffraction patterns for zeolites: (a) HY as delivered, (b) HY treated as for metal deposition but without any metal dopant, (c) Sn/Y, (d) Ga/Y, and (e) Nb/Y with a $\text{SiO}_2:\text{Al}_2\text{O}_3$ molar ratio of 5.1. No metal or metal oxide cluster from Sn, Ga or Nb is detected, and all zeolites present a virtually identical pattern.

Table A11. Rietveld refinement of HY as delivered, dummy HY, Sn/Y, Ga/Y, and Nb/Y with a SiO₂:Al₂O₃ molar ratio of 5.1. Fitting parameters were: zero shift; scale factor; B overall; unit cell parameters: *a*, *b*, *c*, α , β , γ ; profile parameters: U, V, W and asymmetry peak shape 1. The sign (+) stands for an expansion and the sign (-) stands for a contraction with respect to the undoped zeolite.

Material	Unit cell parameters					Expansion or contraction
	<i>a</i> (Å) ± 0.001	<i>b</i> (Å) ± 0.001	<i>c</i> (Å) ± 0.001	$\alpha = \beta = \gamma = 90^\circ \pm 0.001$	<i>V</i> (Å ³) ± 1	
HY	24.528	24.528	24.528	90.00	14757	--
HY-dummy (*)	24.522	24.522	24.522	90.00	14745	- 0.1
Sn/Y	24.509	24.509	24.509	90.00	14723	- 0.2
Ga/Y	24.507	24.507	24.507	90.00	14719	- 0.3
Nb/Y	24.487	24.487	24.487	90.00	14683	- 0.5

(*) HY zeolite is treated for metal doping but without adding any metal.

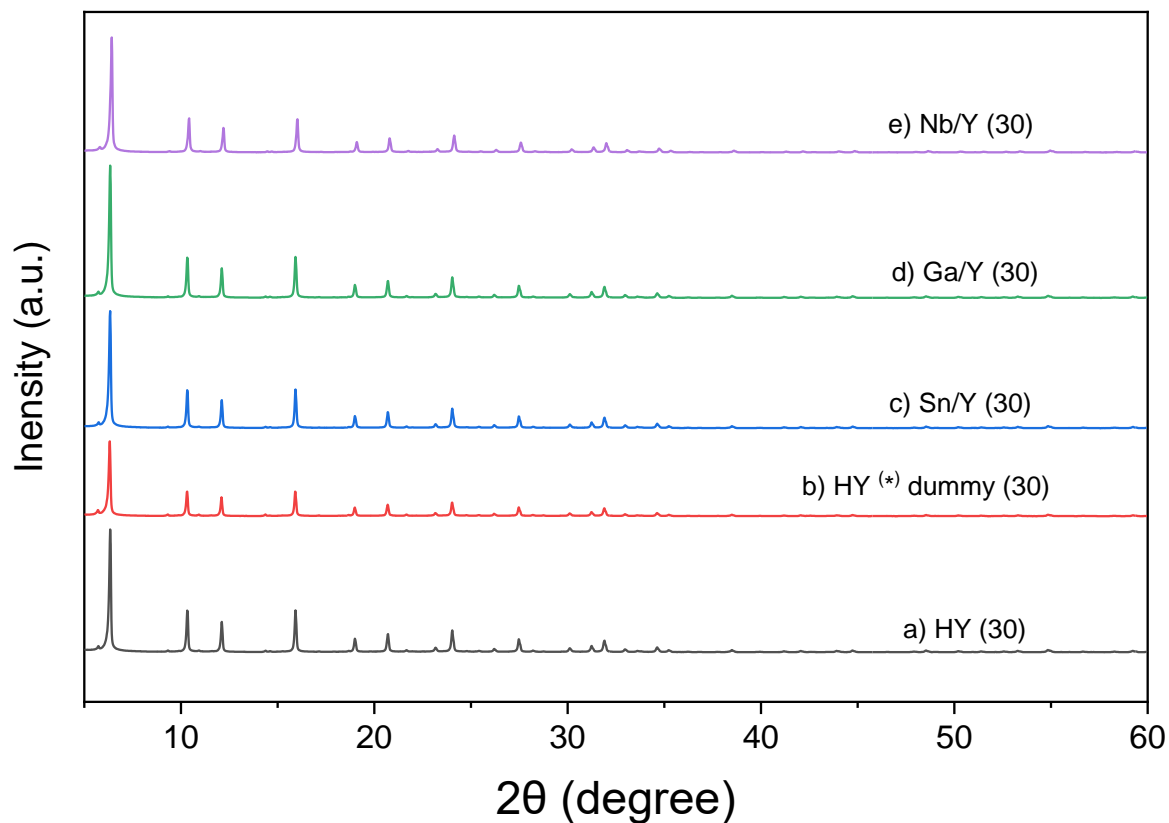


Figure A23. X-ray powder diffraction patterns for zeolites: (a) HY as delivered, (b) HY treated as for metal deposition but without any metal dopant, (c) Sn/Y, (d) Ga/Y, and (e) Nb/Y with a $\text{SiO}_2:\text{Al}_2\text{O}_3$ molar ratio of 30. No metal or metal oxide cluster from Sn, Ga or Nb is detected, and all zeolites present a virtually identical pattern.

Table A12. Rietveld refinement of HY, as delivered, dummy HY, Sn/Y, Ga/Y, and Nb/Y with a SiO₂:Al₂O₃ molar ratio of 30. Fitting parameters were: zero shift; scale factor; B overall; unit cell parameters: a, b, c, α , β , γ ; profile parameters: U, V, W and asymmetry peak shape 1. The sign (+) stands for an expansion and the sign (-) stands for a contraction with respect to the undoped zeolite.

Material	Unit cell parameters					Expansion or contraction
	a (Å) \pm 0.001	b (Å) \pm 0.001	c (Å) \pm 0.001	$\alpha = \beta = \gamma = 90^\circ \pm 0.001$	V (Å ³) \pm 1	
HY	24.308	24.308	24.308	90.00	14363	--
HY-dummy (*)	24.290	24.290	24.290	90.00	14330	- 0.2
Sn/Y	24.299	24.299	24.299	90.00	14346	- 0.1
Ga/Y	24.304	24.304	24.304	90.00	14356	0.0
Nb/Y	24.283	24.283	24.283	90.00	14319	- 0.3

(*) HY zeolite is treated for metal doping but without adding any metal.

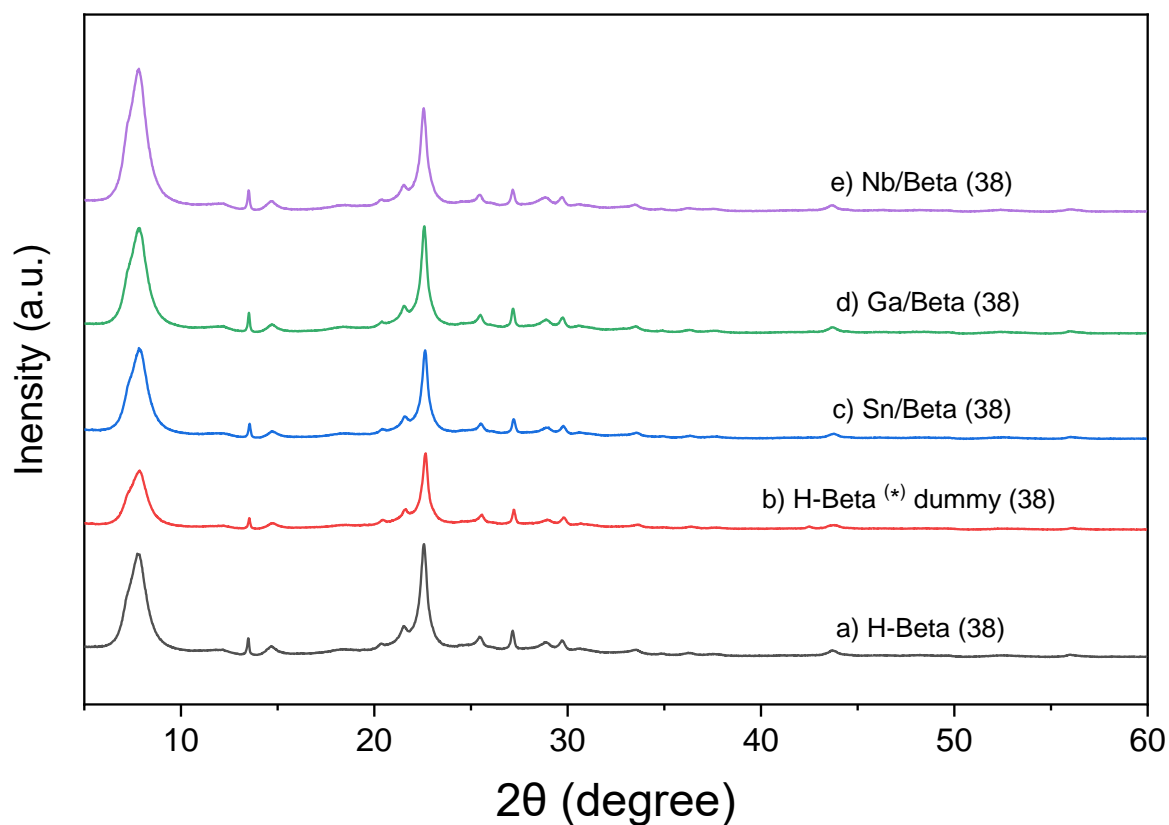


Figure A24. X-ray powder diffraction patterns for zeolites: (a) H-Beta as delivered, (b) H-Beta treated as for metal deposition but without any metal dopant, (c) Sn/Beta, (d) Ga/Beta, and (e) Nb/Beta with a $\text{SiO}_2:\text{Al}_2\text{O}_3$ molar ratio of 38. No metal or metal oxide cluster from Sn, Ga or Nb is detected, and all zeolites present a virtually identical pattern.

Table 4.13. Rietveld refinement of H-beta, as delivered, dummy HY, Sn/beta, Ga/beta, and Nb/beta with a SiO₂:Al₂O₃ molar ratio of 38. Fitting parameters were: zero shift; scale factor; B overall; unit cell parameters: a, b, c, α , β , γ ; profile parameters: U, V, W and asymmetry peak shape 1. The sign (+) stands for an expansion and the sign (-) stands for a contraction with respect to the undoped zeolite.

Material	Unit cell parameters					Expansion or contraction
	a (Å) ± 0.01	b (Å) ± 0.01	c (Å) ± 0.04	$\alpha = \beta = \gamma = 90.0 \pm 0.001$	V (Å ³) ± 1	
H-Beta	12.344	12.344	26.195	90.00	3992	--
H-Beta-dummy (*)	12.317	12.317	26.160	90.00	3969	- 0.6
Sn/Beta	12.335	12.335	26.185	90.00	3984	- 0.2
Ga/Beta	12.350	12.350	26.211	90.00	3998	0.2
Nb/Beta	12.350	12.350	26.200	90.00	3996	0.1

(*) H-Beta zeolite is treated for metal doping but without adding any metal.

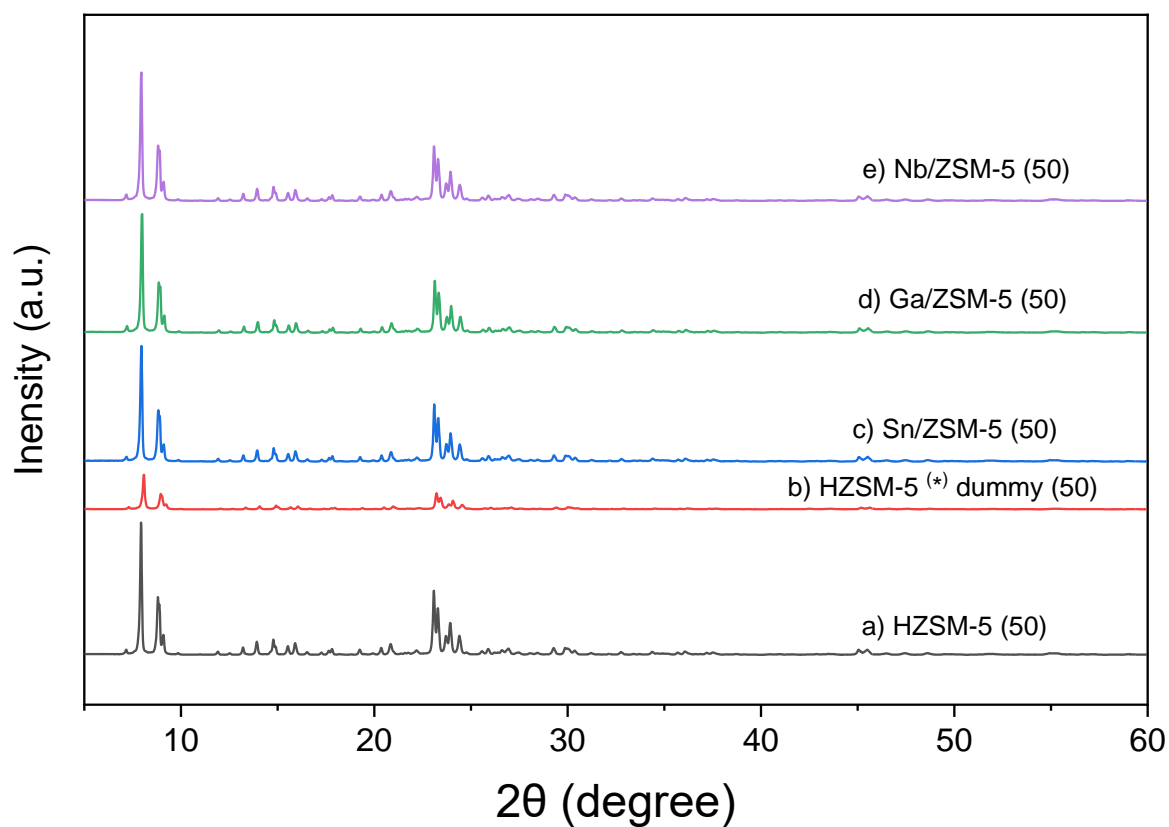


Figure A25. X-ray powder diffraction patterns for zeolites: (a) HZSM-5 as delivered, (b) HZSM-5 treated as for metal deposition but without any metal dopant, (c) Sn/ ZSM-5, (d) Ga/ ZSM-5, and (e) Nb/ ZSM-5 with a $\text{SiO}_2:\text{Al}_2\text{O}_3$ molar ratio of 50. No metal or metal oxide cluster from Sn, Ga or Nb is detected, and all zeolites present a virtually identical pattern.

Table A14. Rietveld refinement of HZSM-5, as delivered, dummy HZSM-5, Sn/ZSM-5, Ga/ZSM-5, and Nb/ZSM-5 with a SiO₂:Al₂O₃ molar ratio of 50. Fitting parameters were: zero shift; scale factor; B overall; unit cell parameters: a, b, c, α , β , γ ; profile parameters: U, V, W and asymmetry peak shape 1. The sign (+) stands for an expansion and the sign (-) stands for a contraction with respect to the undoped zeolite.

Material	Unit cell parameters					Expansion or contraction
	a (Å) \pm 0.003	b (Å) \pm 0.002	c (Å) \pm 0.002	$\alpha = \beta = \gamma = 90^\circ \pm 0.001$	V (Å ³) \pm 1	
HZSM-5	20.106	19.917	13.406	90.00	5368	--
HZSM-5-dummy (*)	20.111	19.919	13.402	90.00	5368	0.0
Sn/ZSM-5	20.096	19.908	13.401	90.00	5361	- 0.1
Ga/ZSM-5	20.100	19.913	13.404	90.00	5365	- 0.1
Nb/ZSM-5	20.102	19.910	13.399	90.00	5363	- 0.1

(*) HZSM-5 zeolite is treated for metal doping but without adding any metal.

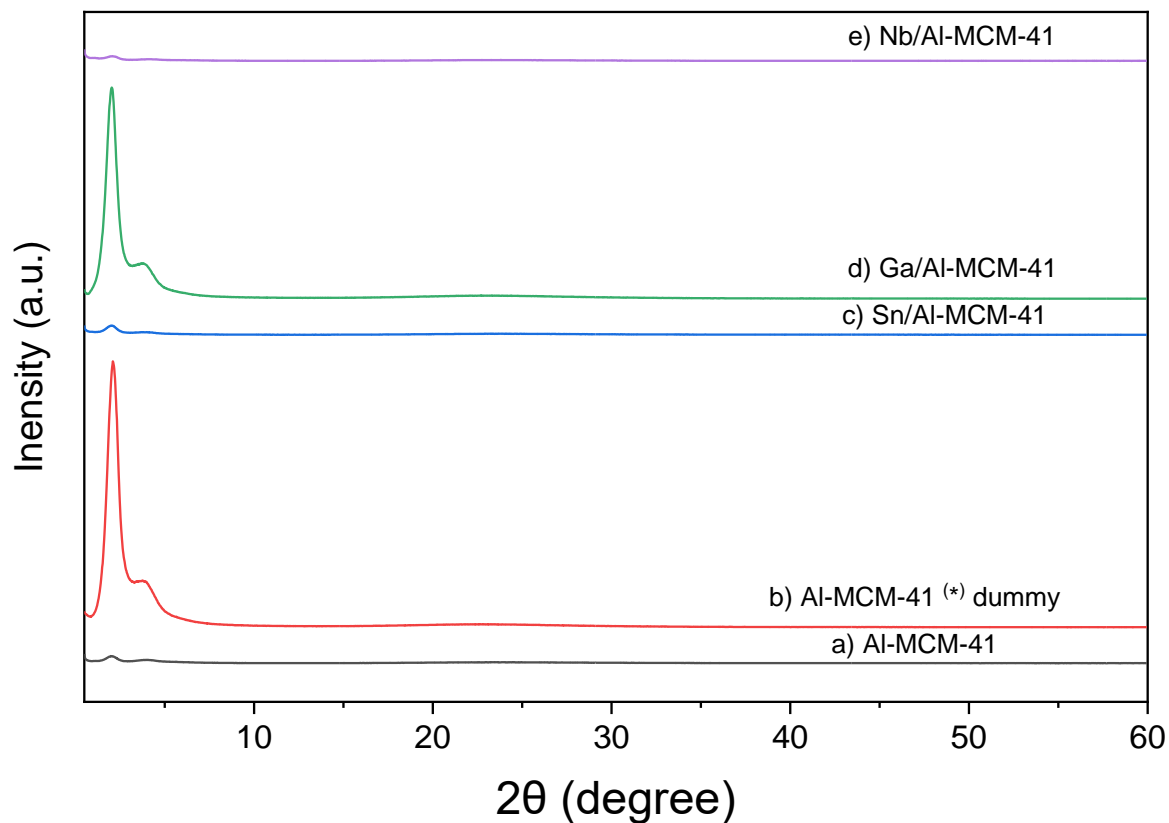


Figure A26. X-ray powder diffraction patterns for zeolites: (a) Al-MCM-41 as delivered, (b) Al-MCM-41 treated as for metal deposition but without any metal dopant, (c) Sn/Al-MCM-41, (d) Ga/Al-MCM-41, and (e) Nb/Al-MCM-41 with a $\text{SiO}_2:\text{Al}_2\text{O}_3$ molar ratio of 28. No metal or metal oxide cluster from Sn, Ga or Nb is detected, and all zeolites present a virtually identical pattern. No refinement is possible for Al-MCM-41 catalysts as it has one peak only.

A.11 Trends in Catalytic Activity as a Function of Acidity and Porosity.

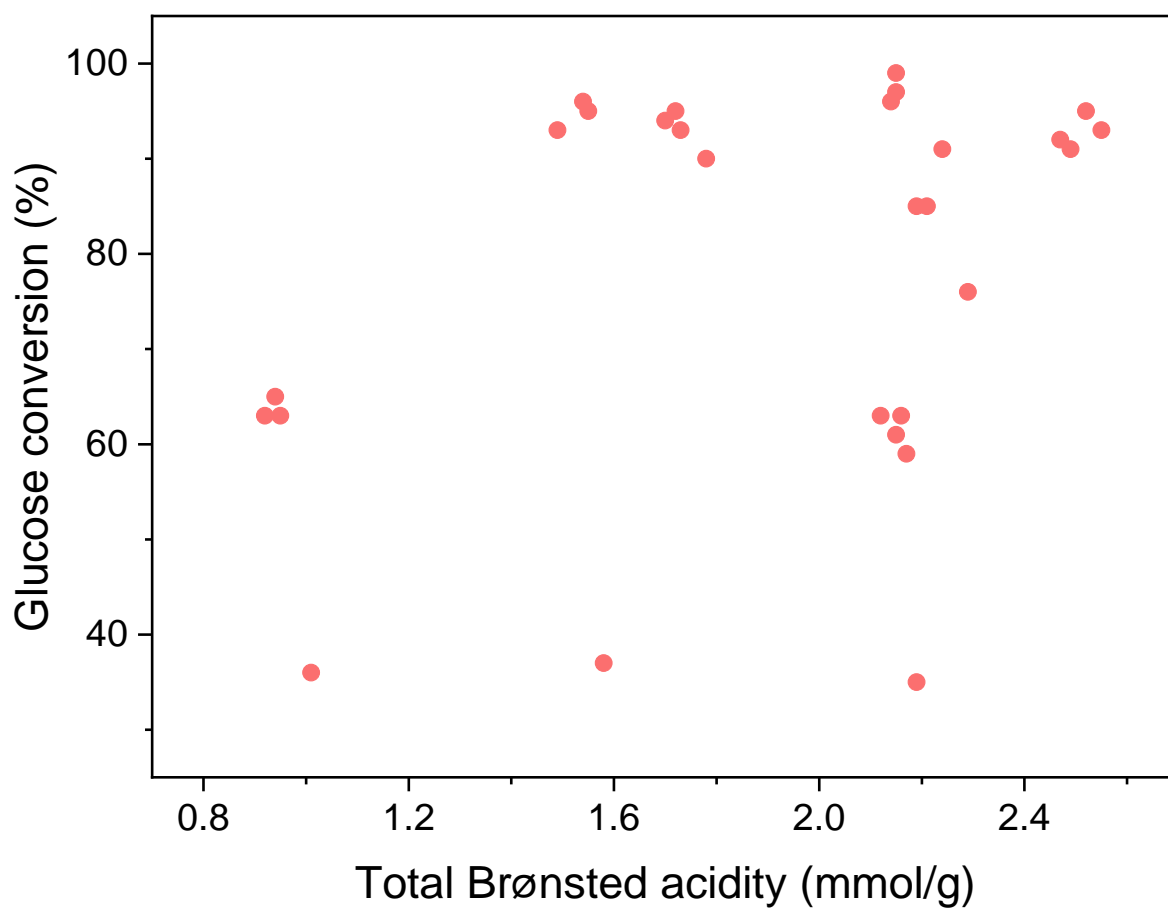


Figure A27. The trend of glucose conversion with respect to total Brønsted acidity. The reaction was carried out following the one-step protocol in methanol at 100 °C for 1 h and endogenous pressure using a constant M:S molar ratio M:S = 1:100. No clear trend is detected in conversion values and data are randomly distributed.

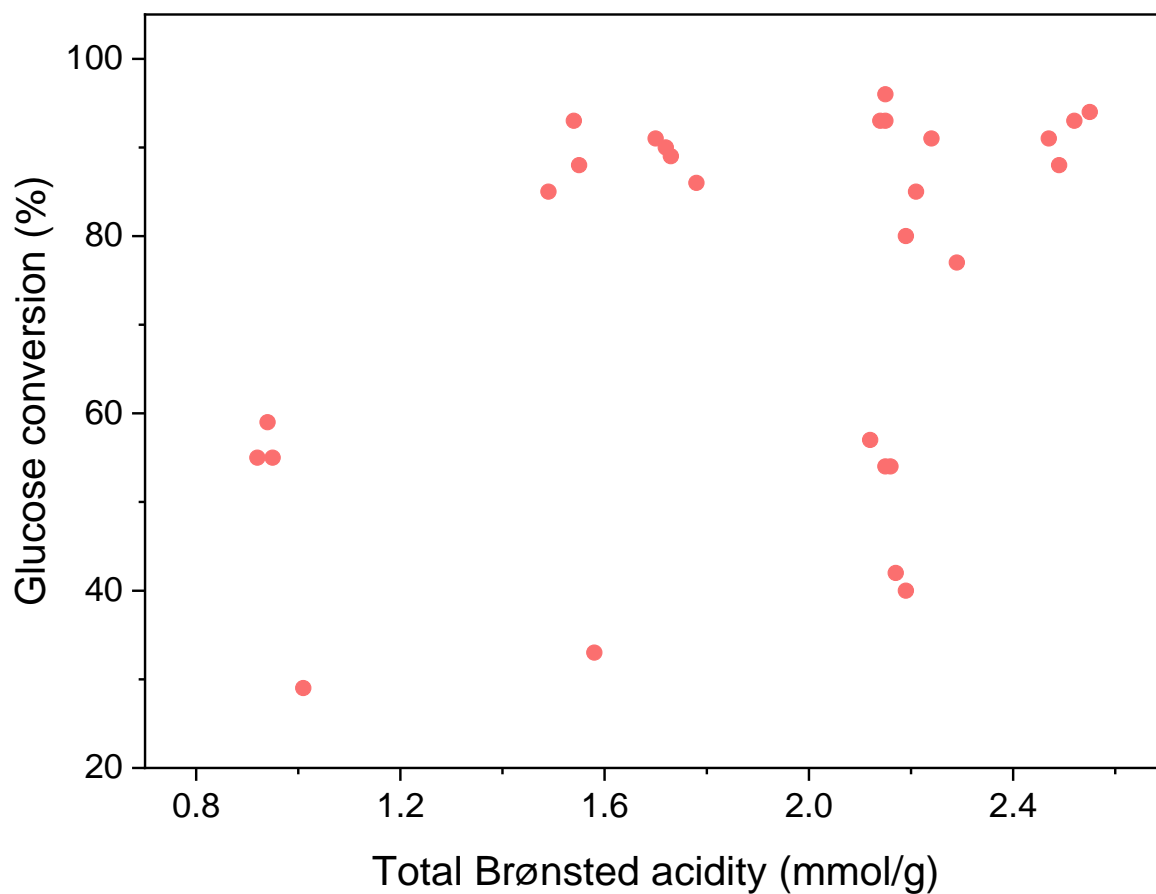


Figure A28. The trend of glucose conversion with respect to total Brønsted acidity. The reaction was carried out following the two-step protocol in methanol and water at 100 °C for 1 h and endogenous pressure using a constant M:S molar ratio M:S = 1:100. No clear trend is detected in conversion values and data are randomly distributed.

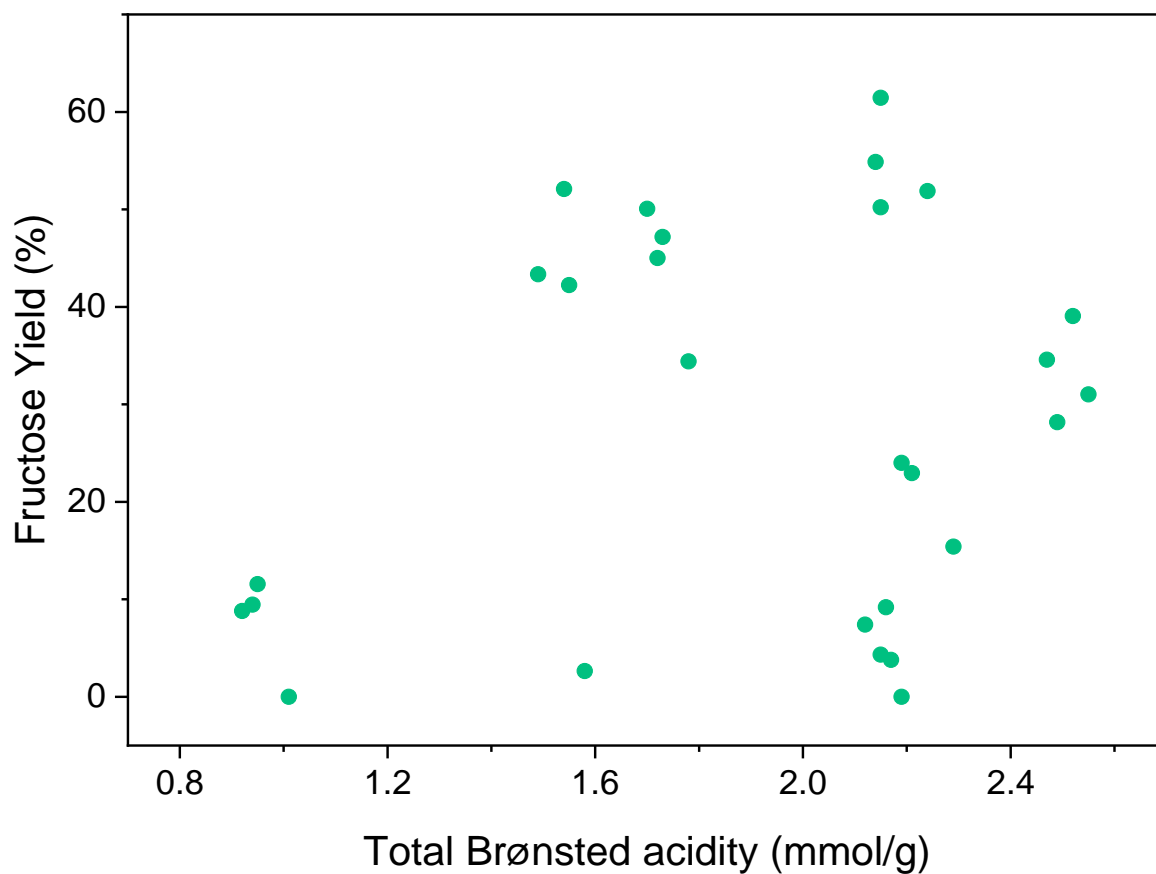


Figure A29. The trend of fructose yield with respect to total Brønsted acidity. The reaction was carried out following the two-step protocol in methanol and water at 100 °C for 1 h and endogenous pressure using a constant M:S molar ratio M:S = 1:100. No clear trend is detected in conversion values and data are randomly distributed.

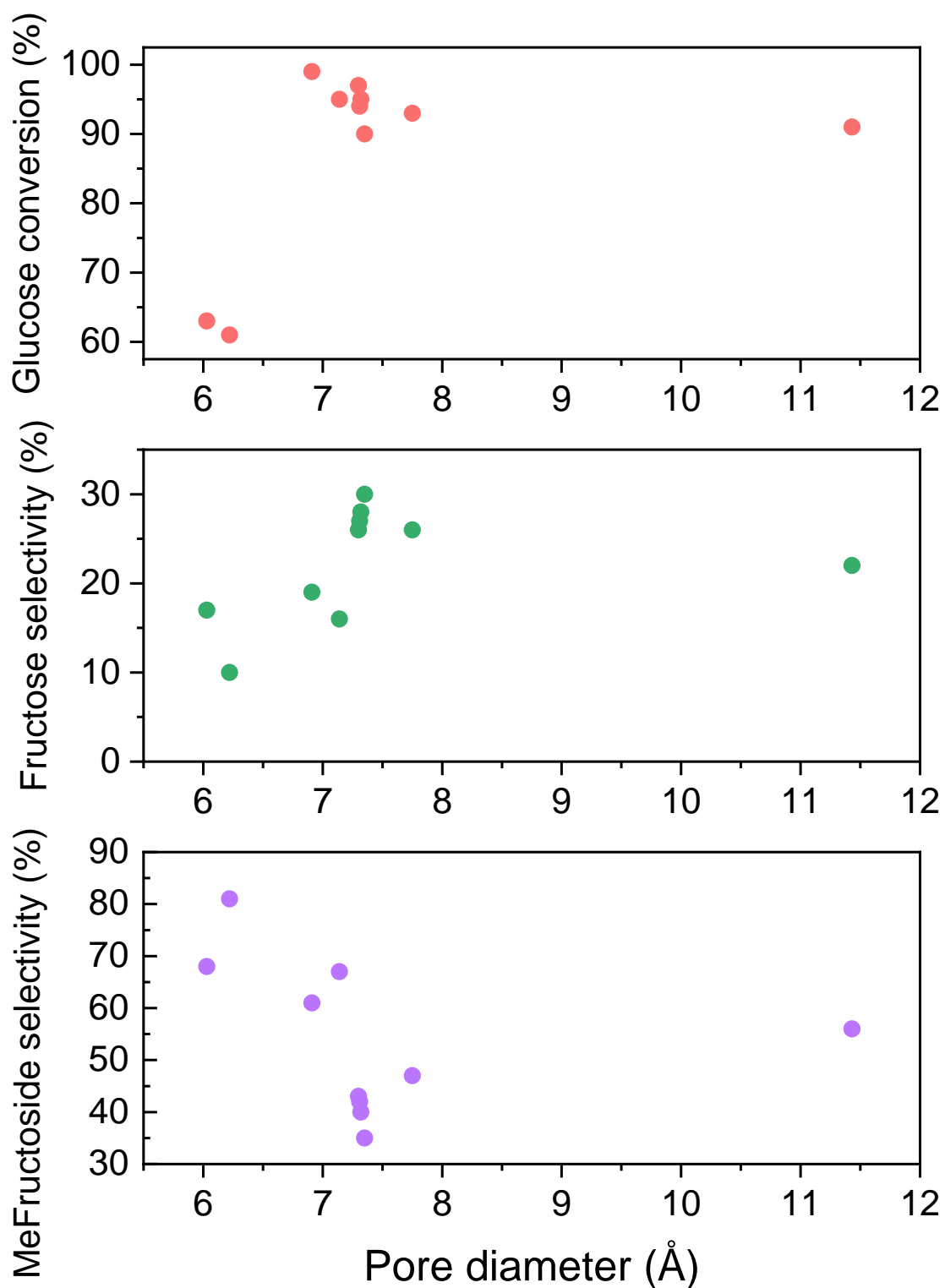


Figure A30. Trends of **a)** glucose conversion, **b)** fructose selectivity and **c)** methyl fructoside selectivity as a function of pores diameters (Å). Reactions carried out following the one-step protocol in methanol for 1 h at 100 °C and endogenous pressure using a constant M:S molar ratio M:S = 1:100. Data are randomly distributed, and no clear trend is observed.

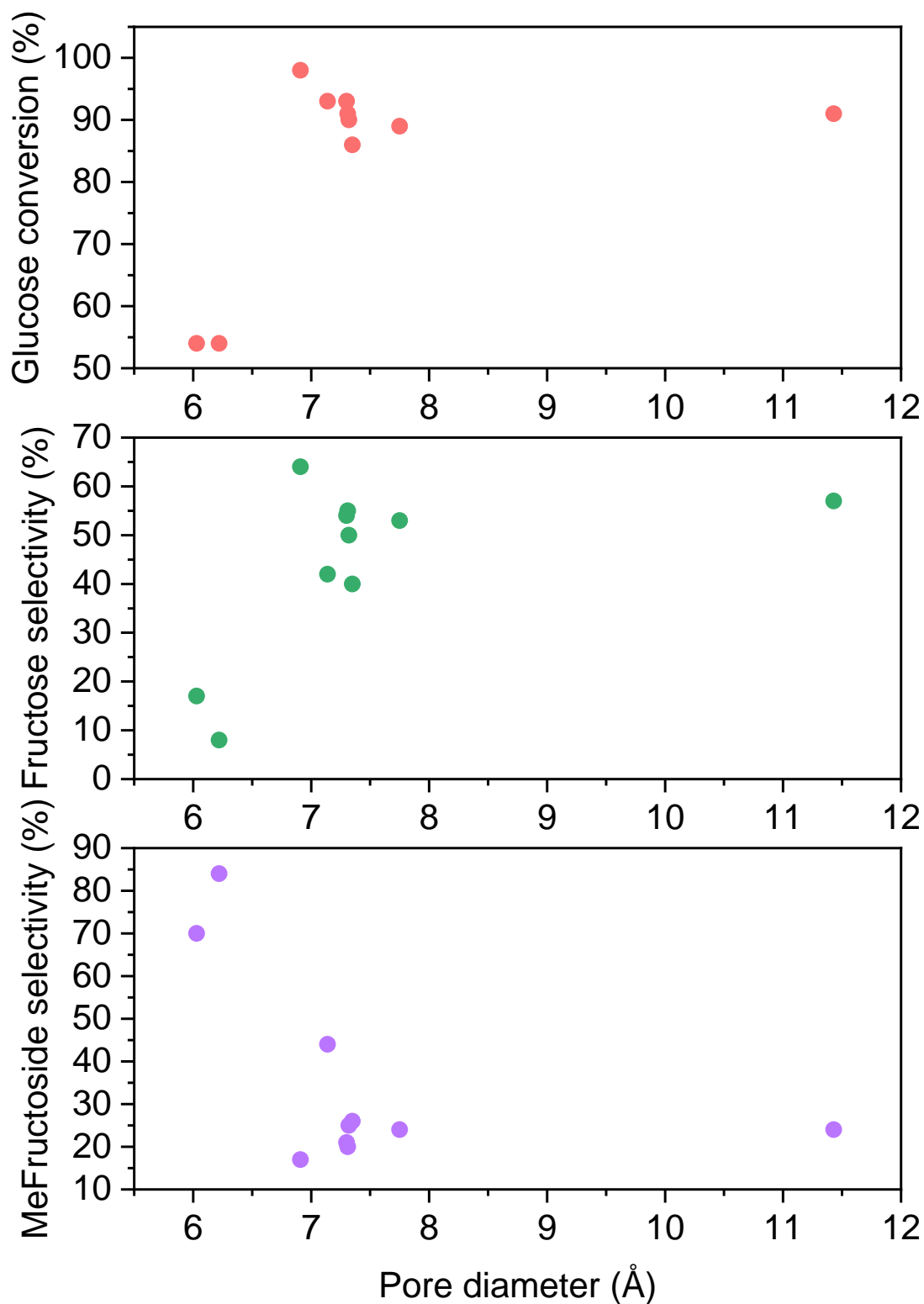


Figure A31. Trends of **a)** glucose conversion, **b)** fructose selectivity and **c)** methyl fructoside selectivity as a function of pores diameters (Å). Reactions carried out following the two-step protocol in methanol for 1 h and water for an additional 1 h at 100 °C and endogenous pressure using a constant M:S molar ratio M:S = 1:100. Data are randomly distributed, and no clear trend is observed.

A.12 The Analysis of Pore Distribution.

The hysteresis cycles were used to determine the isotherm type and the external and microporous areas of the zeolites. t-plots were used to determine the pore volume, with a Barrett-Joyner-Halenda (BJH) procedure for the determination of the pore distribution³, and the use of a Horvath-Kawazoe model⁴ for the fine fitting of the diameter of the microporous component of the zeolite Y framework.

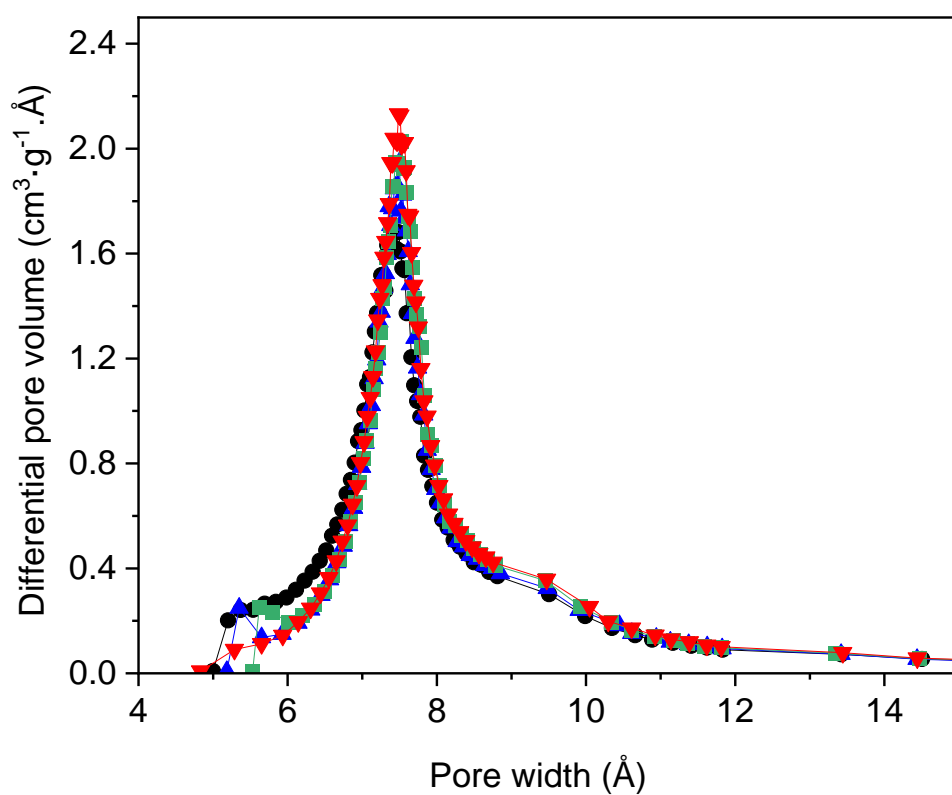


Figure A32. Normalized differential pore volume for (●) zeolite HY before doping, and zeolites (▲) Sn/Y, (■) Ga/Y and (▼) Nb/Y after metal doping via a wetness impregnation protocol. Profile fitting by using a Horvath-Kawazoe.

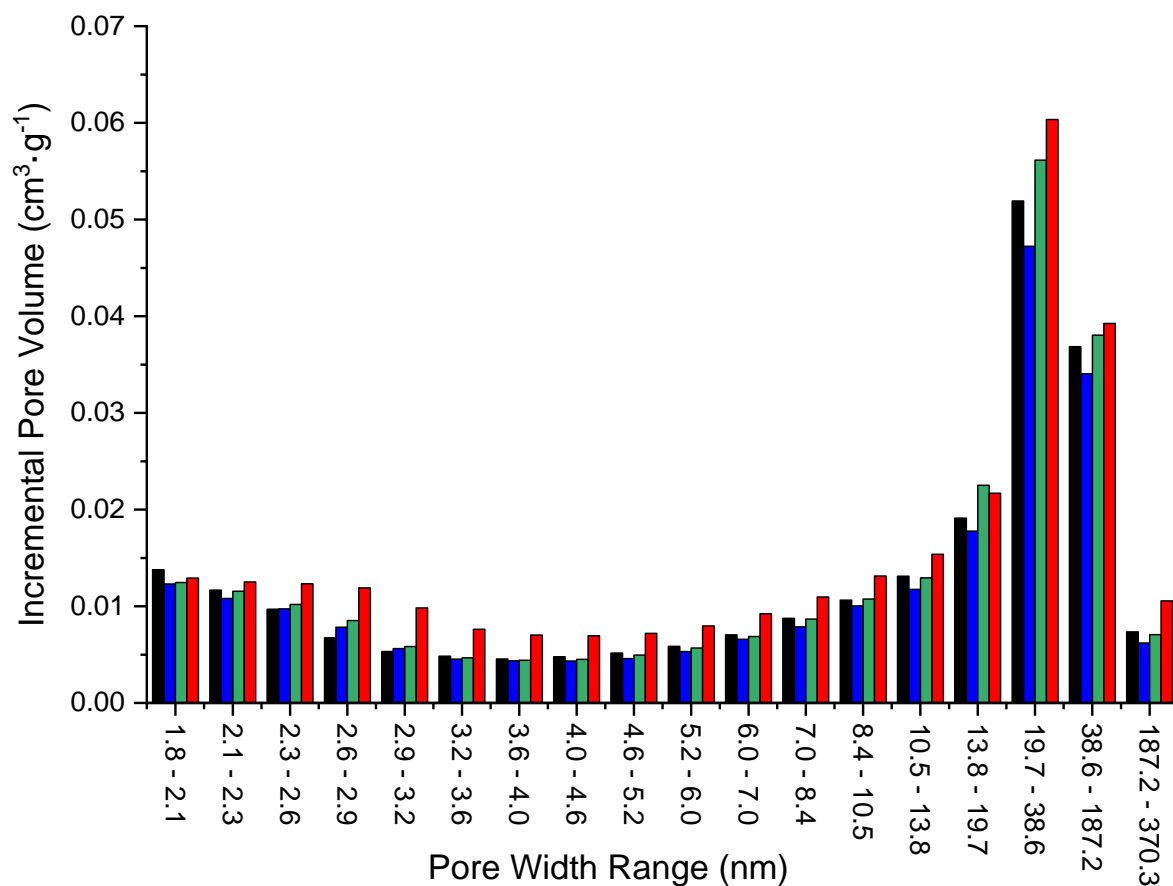


Figure A33. Incremental pore volume by BJH model for (■) zeolite HY before doping, and zeolites (■) Sn/Y, (■) Ga/Y and (■) Nb/Y after metal doping via a wetness impregnation protocol. Profile fitting by using a Horvath-Kawazoe.

A.13 Catalytic Activity Data for Glucose and Fructose Dehydration Reaction in Yields.

Table A13. Catalytic data in yields for the fructose dehydration to 5-HMF in water, using HCl. The tests were carried out using 500 mg of the substrate in 5 mL of H₂O at 100 °C for the specified reaction time and endogenous pressure using a constant metal-to-substrate molar ratio of 1:1.

Reaction time (min)	Yield (%)		
	5-HMF	Levulinic acid	Formic acid
10	12	1	1
20	24	4	3
30	27	7	7
120	15	27	27
240	3	32	35
360	1	33	35

Table A14. Catalytic data of HY zeolites in their acidic forms for the fructose dehydration to 5-HMF in water. The tests were carried out using 500 mg of the substrate in 5 mL of H₂O at 140 °C for 2 h and endogenous pressure using the specified metal-to-substrate molar ratios.

Catalyst	M:S molar ratio	Fructose conversion (%)	Selectivity (%)			CMB (%)
			5-HMF	Levulinic acid	Formic acid	
HY (5.1)	1:3	82	43	6	51	28
	1:100	75	46	8	46	40
	1:300	58	65	1	35	58
HY (30)	1:3	74	46	23	31	30
	1:100	66	54	19	27	46
	1:300	41	69	12	19	70
HY (80)	1:3	63	59	16	24	35
	1:100	42	75	11	13	70
	1:300	38	84	6	11	83

Table A15. Catalytic data in yields for dehydration reaction of fructose to 5-HMF in water using undoped HY and doped Sn, Ga, Nb, and Fe catalysts with 1 wt.%. The tests were carried out using 500 mg of the substrate in 5 mL of H₂O at 140 °C for 2 h and endogenous pressure with an M:S molar ratio of 1:300.

Catalyst	SiO ₂ :Al ₂ O ₃ molar ratio	Yield (%)		
		5-HMF	Levulinic acid	Formic acid
HY	5.1	22	0	12
Sn/Y		21	1	13
Ga/Y		24	0	10
Nb/Y		23	1	12
Fe/Y		25	1	10
HY	80	26	2	3
Sn/Y		35	3	5
Ga/Y		30	3	7
Nb/Y		36	3	5
Fe/Y		37	1	3

Table A16. Catalytic data in yields for fructose dehydration to 5-HMF using undoped and doped zeolite Y with 1wt.% of TiO₂, Nb₂O₅, and CeO₂. The tests were carried out using 500 mg of the substrate in 5 mL of H₂O at 140 °C for 2 h and endogenous pressure with M:S molar ratios of 1:100 and 1:300.

Catalyst	M:S molar ratio	Yield (%)		
		5-HMF	Levulinic acid	Formic acid
HY	1:100	22	3	4
TiO ₂ /Y		35	5	3
Nb ₂ O ₅ /Y		33	5	8
CeO ₂ /Y		23	4	11
HY	1:300	26	2	3
TiO ₂ /Y		34	2	5
Nb ₂ O ₅ /Y		35	2	4
CeO ₂ /Y		36	2	5

A.14 Unit cell calculations of powder X-ray patterns for HY, Sn/Y, Ga/Y, Nb/Y, and Fe/Y zeolites.

Table A17. Rietveld refinement of HY as delivered, dummy HY, Sn/Y, Ga/Y, Nb/Y, and Fe/Y with a SiO₂:Al₂O₃ molar ratio of 5.1. Fitting parameters were: zero shift; scale factor; B overall; unit cell parameters: *a*, *b*, *c*, α , β , γ ; profile parameters: U, V, W and asymmetry peak shape 1. The sign (+) stands for an expansion and the sign (-) stands for a contraction with respect to the undoped zeolite.

Material	Unit cell parameters					V expansion or contraction (%)
	<i>a</i> (Å) ± 0.001	<i>b</i> (Å) ± 0.001	<i>c</i> (Å) ± 0.001	$\alpha = \beta = \gamma = 90^\circ \pm 0.001$	V (Å ³) ± 1	
HY	24.528	24.528	24.528	90.00	14757	--
HY-dummy (*)	24.522	24.522	24.522	90.00	14745	- 0.1
Sn/Y	24.509	24.509	24.509	90.00	14723	- 0.2
Ga/Y	24.507	24.507	24.507	90.00	14719	- 0.3
Nb/Y	24.487	24.487	24.487	90.00	14683	- 0.5
Fe/Y	24.508	24.508	24.508	90.00	14721	- 0.2

(*) HY zeolite is treated for metal doping but without adding any metal.

Table 18. Rietveld refinement of HY as delivered, dummy HY, Sn/Y, Ga/Y, Nb/Y, and Fe/Y with a SiO₂:Al₂O₃ molar ratio of 80. Fitting parameters were: zero shift; scale factor; B overall; unit cell parameters: *a*, *b*, *c*, α , β , γ ; profile parameters: U, V, W and asymmetry peak shape 1. The sign (+) stands for an expansion and the sign (-) stands for a contraction with respect to the undoped zeolite.

Material	Unit cell parameters					V expansion or contraction (%)
	<i>a</i> (Å) ± 0.001	<i>b</i> (Å) ± 0.001	<i>c</i> (Å) ± 0.001	$\alpha = \beta = \gamma = 90^\circ \pm 0.001$	V (Å ³) ± 1	
HY	24.227	24.227	24.227	90.00	14219	--
HY-dummy (*)	24.205	24.205	24.205	90.00	14181	- 0.3
Sn/Y	24.222	24.222	24.222	90.00	14211	- 0.1
Ga/Y	24.224	24.224	24.224	90.00	14215	0.0
Nb/Y	24.221	24.221	24.221	90.00	14209	- 0.1
Fe/Y	24.225	24.225	24.225	90.00	14216	0.0

(*) HY zeolite is treated for metal doping but without adding any metal.

A.15 Unit cell calculations of powder X-ray patterns for HY, TiO₂/Y, Nb₂O₅/Y, and CeO₂/Y zeolites.

Table A19. Rietveld refinement of HY as delivered, dummy HY, TiO₂/Y, Nb₂O₅/Y, and CeO₂/Y with a SiO₂:Al₂O₃ molar ratio of 80. Fitting parameters were: zero shift; scale factor; B overall; unit cell parameters: *a*, *b*, *c*, α , β , γ ; profile parameters: U, V, W and asymmetry peak shape 1. The sign (+) stands for an expansion and the sign (-) stands for a contraction with respect to the undoped zeolite.

Material	Unit cell parameters					V expansion or contraction (%)
	<i>a</i> (Å) ± 0.001	<i>b</i> (Å) ± 0.001	<i>c</i> (Å) ± 0.001	$\alpha = \beta = \gamma = 90^\circ \pm 0.001$	V (Å ³) ± 1	
HY	24.227	24.227	24.227	90.00	14219	--
HY-dummy (*)	24.205	24.205	24.205	90.00	14181	- 0.3
TiO ₂ /Y	24.230	24.230	24.230	90.00	14219	0.1
Nb ₂ O ₅ /Y	24.230	24.230	24.230	90.00	14221	0.0
CeO ₂ /Y	24.230	24.230	24.230	90.00	14223	0.3

(*) HY zeolite is treated for metal doping but without adding any metal.

A.16 References

- 1 P. R. Davies and N. G. Newton, *Surf. Sci.*, 2003, 546, 149–158.
- 2 M. M. M. Kashbor, D. Sutarma, J. Railton, N. Sano, P. J. Cumpson, D. Gianolio, G. Cibin, L. Forster, C. D'Agostino, X. Liu, L. Chen, V. Degirmenci and M. Conte, *Appl. Catal. A: Gen.*, 2022, 642, 118689.
- 3 E. P. Barrett, L. G. Joyner, P. P. Halenda Vol, R. -RnAtn Apj and R. A. Vn-Rn Atn Ac, *J. Am. Chem. Soc.*, 1951, 73, 373–380.
- 4 A. Galarneau, D. Desplantier, R. Dutartre and F. Di Renzo, *Microporous Mesoporous Mater.*, 1999, 27, 297–308.